

*LEPTONIC DECAYS OF NEUTRAL B MESONS IN THE
THREE-SPURION TWO-HIGGS-DOUBLET MODEL*

Zur Erlangung des akademischen Grades eines
DOKTORS DER NATURWISSENSCHAFTEN (Dr. rer. nat.)
von der KIT-Fakultät für Physik
des Karlsruher Instituts für Technologie (KIT)

angenommene

DISSERTATION

von

M.SC. MARTIN LANG,
geboren am 14.10.1994 in Wuppertal

Tag der mündlichen Prüfung:

24. November 2023

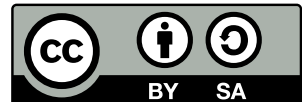
Erster Gutachter:

Prof. Dr. Ulrich Nierste

Zweiter Gutachter:

Prof. Dr. Matthias Steinhauser

This work is licensed under a Creative Commons “Attribution-ShareAlike 4.0 International” license.



A copy of this license can be retrieved from <https://creativecommons.org/licenses/by-sa/4.0/deed.en>.

Copyright ©2024

Abstract

Leptonic decays of neutral B mesons, $B_{q=d,s} \rightarrow l^+l^-$, are extremely rare processes in the Standard Model of particle physics and therefore provide an ideal probe for potential models of new physics. In this thesis, we introduce a two-Higgs-doublet model, extending the so-called type-II model, with flavour-changing couplings of the heavy neutral Higgs bosons in the up-type quark sector, the *three-spurion* two-Higgs-doublet model without discrete \mathbb{Z}_2 symmetry. We compute the Wilson coefficients for the effective theory description of the decays $B_q \rightarrow l^+l^-$ including two-loop next-to-leading order QCD corrections. The renormalisation of this model for the process under consideration is discussed with emphasis on the conceptual differences to the popular \mathbb{Z}_2 -symmetric two-Higgs-doublet models. Relevant constraints from flavour physics and collider experiments are presented and bounds on the most prominent couplings are derived. In particular, we show that even tiny values of some of these couplings have profound consequences for observables such as the branching ratio for $B_s \rightarrow \mu^+\mu^-$.

Zusammenfassung

Leptonische Zerfälle $B_{q=d,s} \rightarrow l^+l^-$ neutraler B -Mesonen sind im Standardmodell der Teilchenphysik stark unterdrückt und stellen daher einen idealen Prüfstand für Modelle neuer Physik dar. In dieser Arbeit wird ein das sogenannte Typ-II-Modell erweiterndes Zwei-Higgs-Dublett-Modell vorgestellt, welches im up-artigen Quark-Sektor flavourändernde Yukawa-Kopplungen der schweren neutralen Higgs-Bosonen beinhaltet. Dieses Modell wird als *Drei-Spurion-Modell* ohne diskrete \mathbb{Z}_2 -Symmetrie bezeichnet. Die zur Beschreibung mittels einer effektiven Feldtheorie benötigten Wilson-Koeffizienten für $B_q \rightarrow l^+l^-$ werden in dieser Arbeit zur nächstführenden Zwei-Schleifen-Ordnung in QCD berechnet. Besonderes Augenmerk wird auf die Renormierung des vorgestellten Modells im Kontext dieser Zerfälle gelegt, insbesondere auf die konzeptionellen Unterschiede zu den besser bekannten \mathbb{Z}_2 -symmetrischen Modellen. Weiter werden relevante Einschränkungen aus der Flavour-Physik und von Beschleuniger-Experimenten präsentiert und daraus Informationen über den erlaubten Parameterbereich der am stärksten eingehenden Kopplungen abgeleitet. Insbesondere wird in dieser Dissertation gezeigt, dass selbst sehr kleine Werte mancher dieser Kopplungen beträchtlichen Einfluss auf Observablen wie das Zerfallsverhältnis in $B_s \rightarrow \mu^+\mu^-$ haben können.

Contents

Abstract	5
Zusammenfassung	5
1. Introduction	11
2. Two-Higgs-Doublet Models	13
2.1. Scalar sector	14
2.2. The Yukawa sector of the general two-Higgs-doublet model	15
2.2.1. The different classical types of 2HDMs	19
2.3. The three-spurion 2HDM of type III	22
3. The rare decays $B_q \rightarrow l^+l^-$	25
3.1. The effective Lagrangian	25
3.2. The decay rate	29
3.3. Status of experiment	31
4. $B_q \rightarrow l^+l^-$ in the two-Higgs-doublet model of type II	35
4.1. Computational setup	35
4.1.1. Feynman rules	35
4.1.2. Feynman graph generation, symbolic expressions, and mapping onto topologies	36
4.1.3. FORM code, projectors, and integration	37
4.2. Computation of the Wilson coefficients in the Standard Model	39
4.2.1. Box diagrams	41
4.2.2. Z-penguin diagrams	43
4.2.3. Self-energy diagrams	44
4.2.4. Next-to-leading order QCD corrections	46
4.3. Wilson coefficients in the Two-Higgs-Doublet Model of type II	48
4.3.1. Contributions to C_A and C'_A	48
4.3.2. The Wilson coefficients $C_S^{(\prime)}$ and $C_P^{(\prime)}$	53
4.4. Scale dependence and branching ratio in the type-II 2HDM	56
5. Additional Wilson coefficients in the three-spurion two-Higgs-doublet model	59
5.1. Higgs-boson box diagrams	59
5.2. Higgs-Z-boson penguin diagrams	61
5.2.1. Hierarchy between the flavour-changing Yukawa couplings	64
5.2.2. Higgs-Z-boson penguin at next-to-leading order	65

5.3.	Leading terms in $\tan\beta$: self-energy diagrams	66
5.4.	Renormalisation of the three-spurion 2HDM: spurion expansion	68
5.5.	Renormalisation of $C_{S,P,\tan^3\beta}^{(\prime),(0),\text{III}}$	71
5.6.	The Wilson coefficients $C_{S,P}^{(\prime),\text{III}}$: subleading $\tan\beta$ orders	75
5.7.	Leading terms of Y_i	82
5.8.	A general observation on the structure of the counterterms in the three-spurion 2HDM	83
5.9.	The decay $B_d \rightarrow \mu^+\mu^-$	84
6.	Phenomenology of g^u	85
6.1.	Collider Higgs searches	85
6.2.	Perturbativity of the quartic couplings and the Higgs-boson mass spectrum	88
6.3.	Perturbativity of Yukawa couplings	88
6.4.	$b \rightarrow s\gamma$	89
6.5.	$B_s-\bar{B}_s$ mixing	94
6.6.	The branching ratio $\mathcal{B}(B_s \rightarrow \mu^+\mu^-)$	102
6.6.1.	The coupling g_{ct}	103
6.6.2.	The coupling g_{tc}	105
6.6.3.	The coupling g_{sb}	107
6.6.4.	The couplings g_{ct} and g_{sb}	109
6.7.	$B_d \rightarrow \mu^+\mu^-$	109
6.8.	Summary	114
7.	Conclusion and outlook	115
A.	The UFOReader module for tapir	117
A.1.	Propagators	119
A.2.	Vertices	119
B.	The effective $\Delta B = \Delta S = 1$ vertices	123
C.	Supplementary figures and equations	129
D.	Numerical input	135

Abbreviations

1LPI	one-light-particle-irreducible
1LPR	one-light-particle-reducible
1PI	one-particle-irreducible
2HDM	two-Higgs-doublet model
ATLAS	A Toroidal LHC Apparatus
CKM	Cabibbo-Kobayashi-Maskawa
CMS	Compact Muon Solenoid
CP	charge-parity
EFT	effective field theory
EW	electroweak
FCNC	flavour-changing neutral current
HL-LHC	high-luminosity phase of the Large Hadron Collider
hMSSM	habemus MSSM?
IR	infrared
LHC	Large Hadron Collider
LHCb	Large Hadron Collider beauty
LO	leading order
MFV	minimal flavour violation
MS	minimal subtraction
$\overline{\text{MS}}$	modified minimal subtraction
MSSM	minimal supersymmetric standard model
NLO	next-to-leading order
NP	new physics
NNLO	next-to-next-to-leading order
OPE	operator product expansion
PDG	Particle Data Group
QCD	quantum chromodynamics
RGE	renormalisation-group evolution

SM	Standard Model
UFO	Universal Feynman Output
UV	ultraviolet
VEV	vacuum expectation value

1. Introduction

Decays of mesons containing a beauty (bottom) quark and one light up, down, or strange quark, so-called B mesons, offer unique insights into the mechanisms governing the weak interactions of the Standard Model (SM) of particle physics. The fact that in the SM all flavour-changing transitions are mediated by the heavy W^\pm bosons implies, for example, that decay processes of neutral mesons into leptons, which change both the beauty and strangeness quantum numbers by one unit, cannot arise through tree-level Feynman diagrams. Instead, their amplitudes are of order G_F^2 in the perturbative expansion in the weak Fermi coupling $G_F \approx 1.166 \times 10^{-5} \text{ GeV}^{-2}$, compared to e.g. the tree-level $B^+ \equiv B_u \rightarrow \tau \nu_\tau$ decay, which is of order G_F . An additional suppression that affects all weak decays of B mesons is due to the smallness of the off-diagonal elements V_{cb} and V_{ts} of the Cabibbo-Kobayashi-Maskawa (CKM) matrix that parameterise transitions between the third and second generations of quarks. The resulting branching fraction $\mathcal{B}(B_s \rightarrow \mu^+ \mu^-) \equiv \Gamma(B_s \rightarrow \mu^+ \mu^-) / \Gamma_{\text{total}}(B_s)$ for the decay into muons is of order $3 \cdot 10^{-9}$, making the decay extremely rare in the SM, whose branching fraction has nevertheless been precisely measured in the ongoing experiments CMS and LHCb at the Large Hadron Collider (LHC).

These experiments, together with the ATLAS experiment at the LHC and the Belle and Belle II experiments in Japan, continue to confirm the SM of particle physics as arguably the most adequate theory of elementary particle interactions constructed so far. A major milestone in the scientific agenda of the LHC programme has certainly been achieved in 2012 with the discovery of a scalar boson with mass of around 125 GeV [1, 2]. Hitherto, the measured properties of this boson agree with those of the *Higgs boson* predicted in the 1960s, marking the completion of the SM in terms of its particle content. The tremendous scope of experimental analyses and an equally broad range of theory predictions at increasing accuracy pave the way for an unprecedented quantitative understanding of the interactions of fundamental particles. These analyses find that the SM is generally in good shape. However, several anomalies—discrepancies between the theoretical expectation based on the SM on the one hand and experimental observations on the other hand—, in particular in the flavour sector, slightly point at shortcomings of the SM and continue to spark interest in explanations beyond the SM. For example, the branching ratio for $B_s \rightarrow \mu^+ \mu^-$ averaged by the Particle Data Group (PDG) in 2022 was given by $\mathcal{B}(B_s \rightarrow \mu^+ \mu^-) = 3.01 \pm 0.35$ [3], falling slightly short of the SM prediction. Other anomalies in processes involving B -meson decays into particles containing second-generation quarks, are also found by experimental analyses, for example in $b \rightarrow sl^+ l^-$ decays and decays into charmed mesons.

Typically, explanations beyond the SM require the introduction of additional particles and new couplings. Unfortunately, there is no definite guidance from theory principles as to which possible theory beyond the SM is realised. It is up to experiments to determine which additional particles occur in Nature and thus rule out most theories invoked to explain these anomalies.

However, so far no undisputed direct observation of additional elementary particles has been accomplished in current and past experiments, so that the number of theories is vast.

Yet, some beyond-SM theories are related more closely to the SM than others, and may therefore be considered less exotic. One example of these theories are the so-called *two-Higgs-doublet models (2HDMs)*. They feature one more Higgs doublet in addition to the one present in the SM and have in total five Higgs bosons, two of which are charged. Furthermore, the Yukawa interactions with fermions are in general much more diverse due to the additional free parameters. Of special historical interest have been a class of 2HDMs in which the interactions of the additional neutral Higgs bosons with fermions are proportional to the ones of the SM Higgs boson. In particular, these models have the appealing property that the mixing of neutral B mesons into their antiparticles is a loop-suppressed process as in the SM, allowing the additional Higgs bosons to be relatively light and in principle observable at the current LHC-based experiments. The absence of any direct observation of such bosons so far pushes the lower mass bounds to higher values at which there is no particular phenomenological reason why these tailored 2HDMs should take precedence over the more general case which allows tree-level flavour-changing couplings of neutral Higgs bosons.

In this thesis, we consider rare leptonic B_q -meson decays, where q denotes a strange or down quark, in the context of a 2HDM that features flavour-changing couplings of neutral Higgs bosons in the up-type quark sector. We call this model—a restriction of the most general 2HDM—the *three-spurion* 2HDM for reasons that will be outlined within the thesis. For the description of leptonic B -meson decays the phenomenologically interesting variant of the three-spurion model is an extension of the so-called *type-II* 2HDM. Since only the decay $B_s \rightarrow \mu^+\mu^-$ has been observed of all six lepton-flavour conserving decays $B_{d,s} \rightarrow e^+e^-, \mu^+\mu^-, \tau^+\tau^-$ so far, this decay will be the main focus in the discussion of current phenomenological constraints. The Wilson coefficients of the effective operators entering the theoretical description of the branching ratio are calculated including next-to-leading order (NLO) quantum chromodynamics (QCD) corrections arising at two loops.

The remainder of the thesis is structured as follows. An introduction to two-Higgs-doublet models (2HDMs) is presented in Chapter 2, with a focus on the aspects the most relevant for this thesis. Chapter 3 is devoted to the discussion of the decays $B_q \rightarrow l^+l^-$ and the setup of an effective field theory (EFT) framework for the description of the decay amplitude, as well as a brief summary of the current experimental status. The computation of the Wilson coefficients involves several subtle aspects, and we therefore present the computation within the limiting type-II 2HDM separately in Chapter 4, with emphasis on some of the technical aspects that are common for all computations, including the three-spurion model. Chapter 5 is devoted to an in-depth presentation of the actual computation of the additional effects occurring in the three-spurion 2HDM. In particular, we discuss the renormalisation of this type of 2HDM, which substantially differs from that of the underlying type-II model. The three-spurion 2HDM introduces a number of a priori free parameters in the quark Yukawa sector. Observables such as the branching ratio for $B_q \rightarrow \mu^+\mu^-$, the mixing of B_q mesons and their antiparticles, as well as the rare radiative decays $b \rightarrow q\gamma$ can be used in order to constrain the parameter space. We will present and discuss a number of constraints of that kind in Chapter 6. Finally, conclusions are drawn in Chapter 7.

2. Two-Higgs-Doublet Models

This chapter serves as an introduction to some relevant properties of two-Higgs-doublet models (2HDMs). We will discuss the scalar sector and new particles that these models entail, including their mass eigenstates, as well as the Yukawa sector. The material presented in this chapter mostly follows Ref. [4].

In the Standard Model (SM) of particle physics, a single Higgs doublet field [5–10] is introduced that serves multiple purposes at once. Firstly, it provides the necessary contribution to maintain unitarity in the scattering of longitudinally polarised massive vector bosons even at high energies, which in its own right is a strong motivation for a Higgs doublet. Secondly, after spontaneous symmetry breaking it generates the masses of these massive vector bosons by providing the would-be Goldstone bosons that propagate alongside the vector bosons, constituting the third, longitudinal component. Finally, it also allows for Yukawa terms in the Lagrangian which reduce to Dirac mass terms for the fermions, once the electroweak $SU(2)_L \times U(1)_Y$ gauge symmetry is spontaneously broken to its electromagnetic $U(1)_Q$ subgroup. This thesis deals with a number of phenomena arising from the second and third aspects listed above.

The SM Higgs doublet can be parameterised as

$$\Phi_{\text{SM}} \equiv \begin{pmatrix} \phi_{\text{SM}}^+ \\ \phi_{\text{SM}}^0 \end{pmatrix} \equiv \begin{pmatrix} G^+ \\ \frac{1}{\sqrt{2}} (v_{\text{SM}} + h_{\text{SM}} + iG^0) \end{pmatrix} \quad (2.1)$$

in terms of the neutral physical Higgs boson h_{SM} and the three would-be Goldstone bosons G^\pm and G^0 . The Higgs potential

$$V(\Phi_{\text{SM}}) = -\mu^2 \Phi_{\text{SM}}^\dagger \Phi_{\text{SM}} + \lambda \left(\Phi_{\text{SM}}^\dagger \Phi_{\text{SM}} \right)^2 \quad (2.2)$$

attains its minimum at the Higgs vacuum expectation value (VEV), $\langle \phi_{\text{SM}}^0 \rangle = \frac{v_{\text{SM}}}{\sqrt{2}}$, where $v_{\text{SM}} \approx 246$ GeV. In the SM Higgs potential the parameters $\mu^2 > 0$ and $\lambda > 0$ are real. The would-be Goldstone bosons are subsequently absorbed by the W^\pm and Z bosons and give rise to their masses. Furthermore, since Φ_{SM} transforms as a doublet under $SU(2)_L$, it can be used to write down gauge-invariant Yukawa terms coupling the left-handed fermion doublets to right-handed $SU(2)_L$ singlets. After spontaneous symmetry breaking these Yukawa couplings appear as mass terms in the broken phase. The fermion mass eigenstates are in general not aligned with the flavour eigenstates that participate in the electroweak interactions. This misalignment is characterised by the CKM matrix which allows couplings between different generations of quarks and thus gives rise to a plethora of interesting phenomena in the field of flavour physics. We will not present further details of the SM Higgs doublet and its physical implications here since our following discussion of the Higgs fields in the two-Higgs-doublet model is presented in a basis that makes the Standard Model part explicit.

In a two-Higgs-doublet model (2HDM), two Higgs doublets are introduced,

$$H_u \equiv \begin{pmatrix} H_u^+ \\ H_u^0 \end{pmatrix} = \begin{pmatrix} H_u^+ \\ \frac{v_u + \text{Re } H_u^0 + i \text{Im } H_u^0}{\sqrt{2}} \end{pmatrix}, \quad H_d \equiv \begin{pmatrix} H_d^+ \\ H_d^0 \end{pmatrix} = \begin{pmatrix} H_d^+ \\ \frac{v_d + \text{Re } H_d^0 + i \text{Im } H_d^0}{\sqrt{2}} \end{pmatrix}. \quad (2.3)$$

Within this thesis we choose the scalar potential such that the VEVs are real and in the lower components, i.e. charge-parity (CP) conserving and charge-neutral,

$$\langle H_{u,d}^0 \rangle = \frac{v_{u,d}}{\sqrt{2}}. \quad (2.4)$$

In general, neither H_u nor H_d is identical to the SM Higgs doublet Φ_{SM} . The VEVs need to satisfy the condition

$$v_u^2 + v_d^2 = v_{\text{SM}}^2, \quad (2.5)$$

in order to reproduce the correct masses of the electroweak gauge bosons. In the presence of a second Higgs doublet, the most general renormalisable (i.e. containing up to quartic terms in the fields) scalar potential is given by [4]

$$\begin{aligned} V_{2\text{HDM}} = & m_{11}^2 (H_u^\dagger H_u) + m_{22}^2 (H_d^\dagger H_d) - (m_{12}^2 (H_u^\dagger H_d) + \text{h.c.}) \\ & + \frac{\lambda_1}{2} (H_u^\dagger H_u)^2 + \frac{\lambda_2}{2} (H_d^\dagger H_d)^2 + \lambda_3 (H_u^\dagger H_u) (H_d^\dagger H_d) + \lambda_4 (H_u^\dagger H_d) (H_d^\dagger H_u) \\ & + \left[\frac{\lambda_5}{2} (H_u^\dagger H_d)^2 + \lambda_6 (H_u^\dagger H_u) (H_u^\dagger H_d) + \lambda_7 (H_u^\dagger H_d) (H_d^\dagger H_d) + \text{h.c.} \right]. \end{aligned} \quad (2.6)$$

Hermiticity of the Lagrangian enforces m_{ii}^2 and $\lambda_{1,2,3,4} \in \mathbb{R}$, while m_{12}^2 and $\lambda_{5,6,7}$ can be complex parameters. In total, the scalar sector of the 2HDM comprises 14 real parameters. However, only 11 out of these parameters are physical [4]. Within this thesis, we will restrict ourselves to a CP-conserving potential, in which also m_{12}^2 and $\lambda_{5,6,7}$ are real couplings. In this case the neutral fields have well-defined CP quantum numbers.

2.1. Scalar sector

The mass matrix of charged scalar particles has a zero eigenvalue for the pseudo-Goldstone boson that is absorbed into the charged W boson. Another massive charged scalar boson, H^\pm , remains, with mass given by

$$M_{H^\pm}^2 = m_{12}^2 \frac{v_{\text{SM}}^2}{v_u v_d} - [\lambda_4 + \lambda_5] \frac{v_{\text{SM}}^2}{2} - \frac{\lambda_6 v_{\text{SM}}^2 v_u}{2v_d} - \frac{\lambda_7 v_{\text{SM}}^2 v_d}{2v_u}. \quad (2.7)$$

The mass matrix of CP-odd fields also has a zero eigenvalue for the pseudo-Goldstone boson that is absorbed into the neutral Z boson, while the second pseudoscalar boson, A^0 , acquires a mass of

$$M_{A^0}^2 = M_{H^\pm}^2 + \frac{1}{2} (\lambda_4 - \lambda_5) v_{\text{SM}}^2. \quad (2.8)$$

The mass matrix of the CP-even scalar fields has in general no zero eigenvalue. It is given by

$$M_0^2 = \begin{pmatrix} m_{11}^2 + \frac{3\lambda_1 v_u^2}{2} + \frac{\lambda_{345} v_d^2}{2} + 3\lambda_6 v_u v_d & -m_{12}^2 + \frac{3}{2} (\lambda_6 v_u^2 + \lambda_7 v_d^2) + \lambda_{345} v_u v_d \\ -m_{12}^2 + \frac{3}{2} (\lambda_6 v_u^2 + \lambda_7 v_d^2) + \lambda_{345} v_u v_d & m_{22}^2 + \frac{3\lambda_2 v_d^2}{2} + \frac{\lambda_{345} v_u^2}{2} + 3\lambda_7 v_u v_d \end{pmatrix}, \quad (2.9)$$

where we have defined the conventional abbreviation $\lambda_{345} \equiv \lambda_3 + \lambda_4 + \lambda_5$. As a real symmetric matrix it can be diagonalised by an orthogonal 2×2 rotation matrix, whose angle is usually named α . The diagonalisation

$$\begin{pmatrix} h \\ H \end{pmatrix} = \begin{pmatrix} \sin \alpha & -\cos \alpha \\ -\cos \alpha & -\sin \alpha \end{pmatrix} \begin{pmatrix} \text{Re } H_u^0 \\ \text{Re } H_d^0 \end{pmatrix} \quad (2.10)$$

yields two mass eigenstates h and H , the neutral CP-even Higgs bosons. In general, none of the particles h , H , $\text{Re } H_u^0$, or $\text{Re } H_d^0$ coincides with the SM Higgs boson. However, since the 125 GeV mass eigenstate observed at the LHC [1, 2] shows so far no deviations from the postulated SM Higgs boson, it is reasonable to assume at least an approximate alignment between one of the two mass eigenstates and the SM Higgs boson. For definiteness, we show exclusion limits obtained by the CMS collaboration at the LHC in Fig. 2.1 [11]. Such limits were obtained by CMS and ATLAS [12] for several variants of the 2HDM which will be discussed in Section 2.2.1. For the discussions presented within this thesis, the constraints shown in Fig. 2.1 for the so-called 2HDM of type II are expected to be relevant and relatively accurate, given that we are interested in a 2HDM with large down-type quark and charged lepton Yukawa couplings.

2.2. The Yukawa sector of the general two-Higgs-doublet model

In the general two-Higgs-doublet model, both Higgs doublets couple to quarks of all flavours, with the Lagrangian

$$\mathcal{L}_Y = -\bar{Q}'_L [\bar{Y}^d H_d + \bar{\epsilon}^d H_u] d'_R - \bar{Q}'_L [\bar{Y}^u i\sigma_2 H_u^* + \bar{\epsilon}^u i\sigma_2 H_d^*] u'_R + \text{h.c.}, \quad (2.11)$$

where the Higgs doublets are parameterised as

$$H_{u,d} = \begin{pmatrix} H_{u,d}^+ \\ H_{u,d}^0 \end{pmatrix}, \quad i\sigma_2 H_{u,d}^* = \begin{pmatrix} H_{u,d}^{*-} \\ -H_{u,d}^0 \end{pmatrix} \quad (2.12)$$

and the left-handed quark doublets consist of the weak interaction flavour eigenstates

$$Q'_L = \begin{pmatrix} u'_L \\ d'_L \end{pmatrix}. \quad (2.13)$$

Likewise, d'_R (u'_R) denotes the right-handed flavour eigenstates of down-type (up-type) quarks. In Eq. (2.11), the 3×3 complex Yukawa matrices $\bar{Y}^{d,u}$ and $\bar{\epsilon}^{d,u}$ imply a sum on the three fermion generations. We will introduce the leptonic Yukawa Lagrangian below. Both of the Higgs

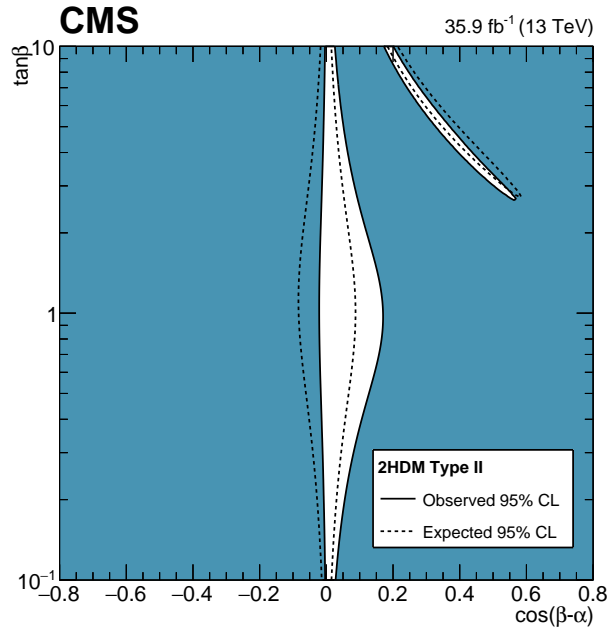


Figure 2.1.: Exclusion limits on the deviation from the alignment limit $\cos(\beta - \alpha) = 0$, in which h_{SM} and $\phi^{0'}$ (defined in Eqs. (2.15) and (2.16)) can be identified with the mass eigenstates h (125 GeV) and H . The constraints are shown in the context of the so-called type-II 2HDM that is discussed below. Taken from an analysis by the CMS collaboration [11]. Similar results were also published by the ATLAS collaboration [12]. The area in blue colours is excluded.

doublets have vacuum expectation values in general, $v_d \equiv v_1 \equiv v \cos \beta$, $v_u \equiv v_2 \equiv v \sin \beta$, where $v \equiv v_{\text{SM}} = 246$ GeV. For flavour physics, it is advantageous to work in the so-called *Higgs basis*, which is related to the basis $\{H_u, H_d\}$ by a rotation in such a way as to eliminate the vacuum expectation value of one doublet, i.e.

$$\begin{pmatrix} \Phi_{\text{SM}} \\ \Phi_{\text{new}} \end{pmatrix} = \begin{pmatrix} \sin \beta & \cos \beta \\ \cos \beta & -\sin \beta \end{pmatrix} \begin{pmatrix} H_u \\ H_d \end{pmatrix}, \quad (2.14)$$

such that $\langle \Phi_{\text{SM}}^0 \rangle = v_{\text{SM}}$ and $\langle \Phi_{\text{new}}^0 \rangle = 0$. The doublet Φ_{SM} corresponds precisely to the SM Higgs doublet,¹

$$\Phi_{\text{SM}} = \begin{pmatrix} G^+ \\ \frac{v+h_{\text{SM}}+iG^0}{\sqrt{2}} \end{pmatrix}. \quad (2.15)$$

In this basis, the second Higgs doublet Φ_{new} can be written as

$$\Phi_{\text{new}} = \begin{pmatrix} H^+ \\ \frac{\phi^{0'}+iA^0}{\sqrt{2}} \end{pmatrix}, \quad (2.16)$$

¹The field h_{SM} has the same couplings as the SM Higgs boson, however it only corresponds to the observed 125 GeV mass eigenstate in the alignment limit $\cos(\beta - \alpha) = 0$.

where H^+ and A^0 are the charged Higgs boson and neutral CP-odd Higgs boson, respectively, and $\phi^{0'}$ and h_{SM} are linear combinations of h and H . In the Higgs basis the quark Yukawa Lagrangian takes the form

$$\begin{aligned} \mathcal{L}_Y = & -\bar{Q}'_L \left[\bar{Y}^d \cos \beta + \bar{\epsilon}^d \sin \beta \right] \Phi_{\text{SM}} d'_R - \bar{Q}'_L \left[-\bar{Y}^d \sin \beta + \bar{\epsilon}^d \cos \beta \right] \Phi_{\text{new}} d'_R \\ & - \bar{Q}'_L \left[\bar{Y}^u \sin \beta + \bar{\epsilon}^u \cos \beta \right] i\sigma_2 \Phi_{\text{SM}}^* u'_R - \bar{Q}'_L \left[\bar{Y}^u \cos \beta - \bar{\epsilon}^u \sin \beta \right] i\sigma_2 \Phi_{\text{new}}^* u'_R + \text{h.c.}, \end{aligned} \quad (2.17)$$

from which we can read off the mass matrices

$$M^u = \bar{Y}^u \frac{v_{\text{SM}}}{\sqrt{2}} \sin \beta + \bar{\epsilon}^u \frac{v_{\text{SM}}}{\sqrt{2}} \cos \beta, \quad (2.18)$$

$$M^d = \bar{Y}^d \frac{v_{\text{SM}}}{\sqrt{2}} \cos \beta + \bar{\epsilon}^d \frac{v_{\text{SM}}}{\sqrt{2}} \sin \beta. \quad (2.19)$$

In general, none of these matrices is diagonal. We diagonalise the mass matrices by the same field redefinitions as in the Standard Model, i.e.

$$u'_{L,R} = U_{L,R}^u u_{L,R}, \quad d'_{L,R} = U_{L,R}^d d_{L,R}, \quad (2.20)$$

where the unprimed fields are the quark mass eigenstates, such that

$$\hat{M}^u = U_L^{u\dagger} M^u U_R^u = \begin{pmatrix} m_u & 0 & 0 \\ 0 & m_c & 0 \\ 0 & 0 & m_t \end{pmatrix}, \quad (2.21)$$

$$\hat{M}^d = U_L^{d\dagger} M^d U_R^d = \begin{pmatrix} m_d & 0 & 0 \\ 0 & m_s & 0 \\ 0 & 0 & m_b \end{pmatrix}. \quad (2.22)$$

For the left-handed doublet, we need to choose any unitary rotation matrix. We take $Q'_L \equiv U_L^d Q_L$, such that the Yukawa Lagrangian is given by

$$\begin{aligned} \mathcal{L}_Y = & -\bar{u}_L U_L^{u\dagger} \left[\bar{Y}^d \cos \beta + \bar{\epsilon}^d \sin \beta \right] G^+ U_R^d d_R + \bar{d}_L U_L^{d\dagger} \left[\bar{Y}^u \sin \beta + \bar{\epsilon}^u \cos \beta \right] G^- U_R^u u_R \\ & -\bar{u}_L U_L^{u\dagger} \left[-\bar{Y}^d \sin \beta + \bar{\epsilon}^d \cos \beta \right] H^+ U_R^d d_R + \bar{d}_L U_L^{d\dagger} \left[\bar{Y}^u \cos \beta - \bar{\epsilon}^u \sin \beta \right] H^- U_R^u u_R \\ & -\bar{d}_L U_L^{d\dagger} \left[\bar{Y}^d \cos \beta + \bar{\epsilon}^d \sin \beta \right] \frac{v_{\text{SM}} + h_{\text{SM}} + iG^0}{\sqrt{2}} U_R^d d_R \\ & -\bar{u}_L U_L^{u\dagger} \left[\bar{Y}^u \sin \beta + \bar{\epsilon}^u \cos \beta \right] \frac{v_{\text{SM}} + h_{\text{SM}} - iG^0}{\sqrt{2}} U_R^u u_R \\ & -\bar{d}_L U_L^{d\dagger} \left[-\bar{Y}^d \sin \beta + \bar{\epsilon}^d \cos \beta \right] \frac{\phi^{0'} + iA^0}{\sqrt{2}} U_R^d d_R \\ & -\bar{u}_L U_L^{u\dagger} \left[\bar{Y}^u \cos \beta - \bar{\epsilon}^u \sin \beta \right] \frac{\phi^{0'} - iA^0}{\sqrt{2}} U_R^u u_R + \text{h.c.} \end{aligned} \quad (2.23)$$

$$\begin{aligned}
 &= -\bar{u}_L V \left[Y^d \cos \beta + \epsilon^d \sin \beta \right] G^+ d_R + \bar{d}_L V^\dagger \left[Y^u \sin \beta + \epsilon^u \cos \beta \right] G^- u_R \\
 &\quad - \bar{u}_L V \left[-Y^d \sin \beta + \epsilon^d \cos \beta \right] H^+ d_R + \bar{d}_L V^\dagger \left[Y^u \cos \beta - \epsilon^u \sin \beta \right] H^- u_R \\
 &\quad - \bar{d}_L \left[Y^d \sin \beta + \epsilon^d \cos \beta \right] \frac{\phi^{0'} + iA^0}{\sqrt{2}} d_R - \bar{u}_L \left[Y^u \cos \beta - \epsilon^u \sin \beta \right] \frac{\phi^{0'} - iA^0}{\sqrt{2}} u_R \\
 &\quad - \bar{d}_L \left[Y^d \cos \beta + \epsilon^d \sin \beta \right] \frac{v_{\text{SM}} + h_{\text{SM}} + iG^0}{\sqrt{2}} d_R \\
 &\quad - \bar{u}_L \left[Y^u \sin \beta + \epsilon^u \cos \beta \right] \frac{v_{\text{SM}} + h_{\text{SM}} - iG^0}{\sqrt{2}} u_R + \text{h.c.}
 \end{aligned} \tag{2.24}$$

In the last equation, we have defined the transformed Yukawa matrices

$$Y^{u,d} = U_L^{d\dagger} \bar{Y}^{u,d} U_R^{u,d}, \quad \epsilon^{u,d} = U_L^{d\dagger} \bar{\epsilon}^{u,d} U_R^{u,d}. \tag{2.25}$$

Furthermore, the Cabibbo-Kobayashi-Maskawa (CKM) matrix is defined as

$$V \equiv V_{\text{CKM}} \equiv U_L^{u\dagger} U_L^d, \tag{2.26}$$

precisely as in the SM. It is worth mentioning that in general neither of the matrices $Y^{u,d}$, $\epsilon^{u,d}$ is diagonal. However, due to Eqs. (2.18) and (2.19), they are not completely independent of each other. We can use these relations to shift the non-diagonal elements into $\epsilon^{u,d}$ and thus get rid of $Y^{u,d}$ by trading them for $\hat{M}^{u,d}$. In its full glory, the quark Yukawa Lagrangian is then given by

$$\begin{aligned}
 \mathcal{L}_Y &= -\bar{d}_L \frac{\sqrt{2}\hat{M}^d}{v} d_R \frac{v + h_{\text{SM}} + iG^0}{\sqrt{2}} - \bar{d}_R \frac{\sqrt{2}\hat{M}^d}{v} d_L \frac{v + h_{\text{SM}} - iG^0}{\sqrt{2}} \\
 &\quad - \bar{u}_L \frac{\sqrt{2}\hat{M}^u}{v} u_R \frac{v + h_{\text{SM}} - iG^0}{\sqrt{2}} - \bar{u}_R \frac{\sqrt{2}\hat{M}^u}{v} u_L \frac{v + h_{\text{SM}} + iG^0}{\sqrt{2}} \\
 &\quad - \bar{u}_L V \frac{\sqrt{2}\hat{M}^d}{v} d_R G^+ - \bar{d}_R \frac{\sqrt{2}\hat{M}^d}{v} V^\dagger u_L G^- \\
 &\quad + \bar{d}_L V^\dagger \frac{\sqrt{2}\hat{M}^u}{v} u_R G^- + \bar{u}_R \frac{\sqrt{2}\hat{M}^u}{v} V d_L G^+ \\
 &\quad + \bar{d}_L \left[\frac{\sqrt{2}\hat{M}^d}{v} \tan \beta + g^d \right] d_R \frac{\phi^{0'} + iA^0}{\sqrt{2}} + \bar{d}_R \left[\frac{\sqrt{2}\hat{M}^d}{v} \tan \beta + g^{d\dagger} \right] d_L \frac{\phi^{0'} - iA^0}{\sqrt{2}} \\
 &\quad - \bar{u}_L \left[\frac{\sqrt{2}\hat{M}^u}{v \tan \beta} + g^u \right] u_R \frac{\phi^{0'} - iA^0}{\sqrt{2}} - \bar{u}_R \left[\frac{\sqrt{2}\hat{M}^u}{v \tan \beta} + g^{u\dagger} \right] u_L \frac{\phi^{0'} + iA^0}{\sqrt{2}} \\
 &\quad + \bar{u}_L V \left[\frac{\sqrt{2}\hat{M}^d}{v} \tan \beta + g^d \right] d_R H^+ + \bar{d}_R \left[\frac{\sqrt{2}\hat{M}^d}{v} \tan \beta + g^{d\dagger} \right] V^\dagger u_L H^- \\
 &\quad + \bar{d}_L V^\dagger \left[\frac{\sqrt{2}\hat{M}^u}{v \tan \beta} + g^u \right] u_R H^- + \bar{u}_R \left[\frac{\sqrt{2}\hat{M}^u}{v \tan \beta} + g^{u\dagger} \right] V d_L H^+.
 \end{aligned} \tag{2.27}$$

Here, we have defined the matrices

$$g^u = -\epsilon^u \cos \beta [\tan \beta + \cot \beta], \quad g^d = -\epsilon^d \sin \beta [\tan \beta + \cot \beta]. \tag{2.28}$$

The parameter $\tan \beta$ corresponds to v_u/v_d and $v \equiv v_{\text{SM}} = 246$ GeV. We will denote the elements of g^d by $g_{d_i d_j} \equiv g_{ij}^d$, where d_i, d_j are the i -th and j -th flavour of down-type quarks, respectively, for example $g_{sb} \equiv g_{23}^d$, and analogously $g_{u_i u_j} \equiv g_{ij}^u$. If we do not specify the indices i, j , we will keep the superscripts u or d in order to make clear which matrix is considered, e.g. g_{ij}^u denotes a generic element of the matrix g^u .

In the lepton sector, without right-handed neutrinos, the most general Yukawa Lagrangian is given by

$$\mathcal{L}_Y^l = -\bar{L}'_L \left[\bar{Y}^l H_d + \bar{\epsilon}^l H_u \right] l'_R + \text{h.c.}, \quad (2.29)$$

with the left-handed lepton doublet

$$\bar{L}'_L = \begin{pmatrix} \bar{\nu}'_L \\ \bar{l}'_L \end{pmatrix}. \quad (2.30)$$

2.2.1. The different classical types of 2HDMs

Depending on the structure of the matrices $\bar{Y}^{u,d}$ and $\bar{\epsilon}^{u,d}$ in Eq. (2.11), the phenomenology of the corresponding 2HDM will be quite different. In the general 2HDM, the matrices $\bar{\epsilon}^{u,d}$ are not diagonalised by the same unitary transformations that diagonalise $\bar{Y}^{u,d}$. Thus, in the basis in which $\bar{Y}^{u,d}$ are diagonal, the matrices $\bar{\epsilon}^{u,d}$ —and correspondingly $g^{u,d}$ —still possess non-diagonal elements that give rise to flavour-changing neutral couplings (FCNCs) to the neutral Higgs bosons. In the down-type quark sector these couplings give rise to tree-level contributions to kaon and B -meson mixing and are heavily constrained by experiment. In the up-type quark sector a tree-level effect would arise in the neutral $D^0-\bar{D}^0$ mixing process, but constraints in the up-type sector are much less severe.

A special case arises if \bar{Y}^d and $\bar{\epsilon}^d$ —and correspondingly \bar{Y}^u and $\bar{\epsilon}^u$ —are simultaneously diagonalisable. In this case the matrices $g^{u,d}$ in Eq. (2.27) are both diagonal, and flavour-changing neutral current processes are mediated only at the loop level.

Furthermore, a number of variants of the 2HDM exists in which up-type quarks, down-type quarks, and charged leptons each couple to one of the Higgs doublets only. These peculiar Yukawa sectors can be realised by imposing a discrete \mathbb{Z}_2 symmetry under which the two Higgs doublets and all right-handed fermion fields transform, while the left-handed fermion doublets are invariant. In all of these cases where each type of fermions (down-type or up-type quarks and charged leptons) couples to one of the Higgs doublets exclusively, the relations in Eqs. (2.18) and (2.19) automatically imply that the non-vanishing Yukawa matrices are diagonal in the same bases as the mass matrices. In this case, all couplings of fermions to the additional Higgs bosons can be expressed in terms of their masses and factors of $\tan \beta$. By convention, in all of these models the Higgs doublets are assigned charges such that up-type quarks always couple to H_u , i.e. all of these models have $\bar{\epsilon}^u = 0$ and the diagonal couplings of right-handed up-type quarks to Φ_{new} are suppressed by $1/\tan \beta$. This leaves four different versions of the 2HDM, depending on which couplings for down-type quarks and leptons vanish.

1. In the 2HDM of *type I* (also called *fermiophobic* 2HDM), $\bar{Y}^d = \bar{Y}^l = 0$, i.e. all charged fermions couple to H_u only. Using Eq. (2.19) with vanishing \bar{Y}^d in Eq. (2.27) one sees that in this case couplings of down-type quarks to the additional Higgs bosons $\phi^{0'}$ and A^0 carry a factor of $\cot \beta = 1/\tan \beta$, and the same holds for charged leptons. Hence, in

Table 2.1.: \mathbb{Z}_2 charge assignments q_i for the Higgs doublets and right-handed fermions in the 2HDMs with discrete \mathbb{Z}_2 symmetry. The fields transform as $\psi_i \rightarrow e^{i\pi q_i} \psi_i$. Left-handed fermion fields transform trivially, $q_{QL} = q_{LL} = 0$.

Yukawa sector	H_d	H_u	u_R	d_R	l_R
type I	0	1	1	1	1
type II	0	1	1	0	0
type X	0	1	1	1	0
type Y	0	1	1	0	1
inert	0	1	0	0	0

the limit of large $\tan \beta$, all flavour processes involving the additional Higgs bosons are heavily suppressed and may thus provide no constraints.

2. In the 2HDM of *type II*, $\bar{\epsilon}^d = \bar{\epsilon}^l = 0$. Consequently, both matrices $g^{u,d}$ vanish. The type-II 2HDM is relevant in super-symmetric theories, whose tree-level Higgs sector has to be of this type [13–15]. In fact, the type-II 2HDM is perhaps the one most studied in the literature, and we have chosen the notation with matrices $g^{u,d}$ with the type-II model in mind. The couplings of the additional Higgs bosons to right-handed down-type quarks and charged leptons carry a factor of $\tan \beta$, while the couplings to right-handed up-type quarks are multiplied by a factor $\cot \beta = 1/\tan \beta$. If $\tan \beta$ is large, processes involving up-type quarks can be severely suppressed, while those involving charged leptons or down-type quarks—e.g. $B_q - \bar{B}_q$ mixing or $B_q \rightarrow l^+ l^-$ decays—can be significantly enhanced.
3. In the 2HDM of *type X* (also called *lepton-specific 2HDM*), $\bar{Y}^d = \bar{\epsilon}^l = 0$. Consequently, couplings of down-type quarks are as in the type-I model, while the couplings of charged leptons carry a factor of $\tan \beta$, as in the type-II model. Hence, for large values of $\tan \beta$ this model becomes *quarkphobic* and branching ratios into leptons dominate over those into quarks.
4. In the 2HDM of *type Y* (also called *flipped 2HDM* with respect to the type-X model), $\bar{\epsilon}^d = \bar{Y}^l = 0$. In this model, the couplings of down-type quarks are the same as in the type-II model, whereas the couplings of charged leptons are as in the type-I model. This model becomes *leptophobic* in the region of large $\tan \beta$ and branching ratios into quarks dominate over those into leptons.

The \mathbb{Z}_2 transformation properties of the Higgs doublets and right-handed fermion fields are shown in Table 2.1 for these four 2HDMs. In Table 2.2 we summarise the Yukawa couplings within these 2HDMs. Usually, the \mathbb{Z}_2 symmetry is softly broken in the Higgs potential by $m_{12}^2 \neq 0$.

As mentioned above, the choice to couple right-handed up-type quarks to H_u is convention, leading to a $\cot \beta$ suppression of up-type quark couplings to the additional neutral Higgs bosons in the case of large $\tan \beta$. In the case of very small $\tan \beta$, the factor $\cot \beta$ can instead become large and possibly enhance the up-type quark couplings, and it seems that “flipped” models

Table 2.2.: Coupling strengths of the different fermion species to the neutral Higgs bosons defined in the Higgs basis, for all four \mathbb{Z}_2 -symmetric 2HDMs with non-trivial Yukawa Lagrangians. These couplings enter the Yukawa Lagrangian as $\mathcal{L}_Y \supset -\bar{f}_L \frac{\hat{M}^f}{v} f_R \xi_\phi^f \phi$, where $f = l, u, d$ and $\phi = h^0, H^0, iA^0$. All couplings are normalised such that couplings to the SM Higgs boson are given by $\xi_{h^0}^f = 1$. The couplings to charged Higgs bosons can be derived from Eq. (2.17).

coupling	type-I	type-II	type-X	type-Y
$\xi_{H^0}^{u}$	$\cot \beta$	$\cot \beta$	$\cot \beta$	$\cot \beta$
$\xi_{H^0}^d$	$\cot \beta$	$-\tan \beta$	$\cot \beta$	$-\tan \beta$
$\xi_{H^0}^l$	$\cot \beta$	$-\tan \beta$	$-\tan \beta$	$\cot \beta$
$\xi_{iA^0}^u$	$-\cot \beta$	$-\cot \beta$	$-\cot \beta$	$-\cot \beta$
$\xi_{iA^0}^d$	$\cot \beta$	$-\tan \beta$	$\cot \beta$	$-\tan \beta$
$\xi_{iA^0}^l$	$\cot \beta$	$-\tan \beta$	$-\tan \beta$	$\cot \beta$

with larger up-type Yukawa couplings can be achieved by considering the limit of small $\tan \beta$. However, there is a lower limit on $\tan \beta$ by the requirement that up-type Yukawa couplings are perturbative, forbidding arbitrarily large values of $\cot \beta$.

As mentioned in the discussion of the type-II 2HDM, we have chosen the notation of Eq. (2.27) with this particular model in mind. The matrices g^u and g^d denote the deviations of the general, sometimes dubbed *type-III*, model from the type-II model. We consider the type-II 2HDM as our “starting point” since in this model down-type quark couplings as well as charged lepton couplings are enhanced by $\tan \beta$, leading to possibly sizeable effects for the process $B_q \rightarrow l^+ l^-$. In what follows we will regard the matrices g^u and g^d as a “perturbation” about the type-II model and will focus on the leading terms in these new couplings, which will add to the 2HDM of type II in the processes considered in this thesis.

Two more variants of the 2HDM are worth mentioning. The *inert* 2HDM [16] contains an unbroken \mathbb{Z}_2 symmetry under which $H_u \rightarrow -H_u$, while H_d and the right-handed fermion fields do not transform at all. In this model H_u does not acquire a vacuum expectation value and the \mathbb{Z}_2 symmetry requires $m_{12}^2 = \lambda_6 = \lambda_7 = 0$. For flavour processes the inert 2HDM is only of little interest since the additional Higgs doublet does not couple to fermions at all. It has however been studied in the context of dark matter since the lightest inert particle is stable due to the unbroken discrete symmetry [17, 18]. The \mathbb{Z}_2 charges of the fields are shown in Table 2.1.

Finally, the *flavour-aligned* 2HDM [19, 20] does not contain a discrete symmetry, but assumes that the Yukawa couplings of Φ_{new} are proportional to the diagonal fermion mass matrices. However, in contrast to the \mathbb{Z}_2 -symmetric models, there is an individual proportionality factor for each type of right-handed fermions, ξ_u , ξ_d , and ξ_l . The Yukawa Lagrangian can be obtained from Eq. (2.27) by $g^u = g^d = 0$ and the replacements

$$\frac{\hat{M}^u}{\tan \beta} \rightarrow \hat{M}^u \xi_u, \quad \hat{M}^d \tan \beta \rightarrow \hat{M}^d \xi_d, \quad \hat{M}^l \tan \beta \rightarrow \hat{M}^l \xi_l. \quad (2.31)$$

Due to the absence of a discrete symmetry forbidding flavour-changing neutral Higgs couplings in all orders of perturbation theory, these couplings are radiatively generated by renormalisation-group effects [21, 22] in the evolution from a high energy scale down to the electroweak scale. However, it was found in Refs. [23, 24] that the flavour-changing neutral currents (FCNCs) induced at the electroweak scale are only moderately sized and not yet excluded by current experiments. The calculation of the leading-order Wilson coefficients for the decays $B_q \rightarrow l^+ l^-$ has been performed in Ref. [25].

2.3. The three-spurion 2HDM of type III

The variants of the two-Higgs-doublet model with a softly broken discrete \mathbb{Z}_2 naturally suppress FCNCs and thus allow for relatively light additional Higgs bosons whilst evading constraints from the flavour physics of down-type mesonic processes such as $B_q - \bar{B}_q$ mixing or rare $B_q \rightarrow l^+ l^-$ decays, where $q = d, s$. These small Higgs masses are within the reach of the LHC, but so far no additional Higgs bosons have been observed, leading to ever increasing lower limits on the masses of these particles. Hence, the restriction to models with discrete symmetry becomes less appealing and the possibility of more general Yukawa sectors should be entertained. However, experimental constraints from the mixing of neutral $K^0 - \bar{K}^0$ and $B_q - \bar{B}_q$ meson pairs as well as rare leptonic or radiative decays of B mesons are quite restrictive, putting severe bounds on the flavour-changing off-diagonal elements of g^d . On the other hand, the off-diagonal elements $g_{it,tj}$ in the up-type sector are almost unconstrained from processes involving D mesons. This motivates our model in which three Yukawa matrices, $Y^{u,d}$ and ϵ^u are arbitrary, while ϵ^d is suppressed. The model with three Yukawa matrices is further motivated by the possibility to incorporate spontaneous CP violation, which requires at least three non-vanishing Yukawa matrices [26]. Realising spontaneous CP violation in the 2HDM would modify the mixing of the charge-neutral mass eigenstates, but for CP-conserving quantities as the ones considered in this thesis the block-diagonal mixing matrix presented in Eq. (2.9) is sufficient. It may be tempting to simply set $\epsilon^d = 0$ in order to evade all constraints from kaon and B -meson experiments. However, such a model would be non-renormalisable since loop corrections involving ϵ^u will be ultraviolet (UV)-divergent, without a parameter yielding a counterterm at hand. This situation is different from \mathbb{Z}_2 -symmetric models in which the discrete symmetry ensures renormalisability, and from the generic 2HDM, in which ϵ^d is present and provides the necessary counterterm. Therefore it is not possible to completely dismiss the flavour-changing couplings ϵ^d , but one has to systematically take these couplings into account by using a so-called *spurion expansion* in which $Y^{u,d}$ and ϵ^u are treated as the three spurions of the model, while ϵ^d is constructed from these spurions. We will discuss the technical aspects of the renormalisation of this particular 2HDM in some detail in Section 5.4. Finally, in the lepton sector we set $\bar{\epsilon}^l = 0$, since we will be concerned with lepton-flavour conserving decays within this thesis, such that the lepton couplings to the additional Higgs bosons are given by

$$\mathcal{L}_Y^l = \bar{l}_L \left[\frac{\sqrt{2}\hat{M}^l}{v} \tan \beta \right] l_R \frac{\phi^{0'} + iA^0}{\sqrt{2}} + \bar{\nu}_L \left[\frac{\sqrt{2}\hat{M}^l}{v} \tan \beta \right] l_R H^+ + \text{h.c.} \quad (2.32)$$

The three-spurion 2HDM under scrutiny in this thesis is a modification of the type-II 2HDM. For the calculation of observables in the relevant observables one therefore has to compute the type-II contributions as well, to which terms proportional to flavour-changing couplings $g_{ij}^{u,d}$ add. Hence, we will dedicate a complete chapter to the computation of the so-called *Wilson coefficients* of interest within the SM and 2HDM of type II, highlighting some general aspects of the calculation, before moving on to the new contributions.

3. The rare decays $B_q \rightarrow l^+l^-$

In this chapter we will introduce the rare leptonic decays of neutral B mesons, $B_q \rightarrow l^+l^-$, where q is a light down-type quark d or s and l are leptons, i.e. electrons, muons, or tau leptons. We will derive an expression for the decay rate and branching ratio.

3.1. The effective Lagrangian

In deriving an expression for the decay rate of $B_q \rightarrow l^+l^-$ one starts with the matrix element \mathcal{M} of the corresponding quark-level transition, i.e. the transition amplitude for the process $\bar{b}q \rightarrow l^+l^-$. This computation can be simplified based on the key observation that in the SM neutral gauge bosons preserve the flavour of quarks, i.e. there is no tree-level Feynman diagram contributing to this decay. In the SM, this process occurs starting at the loop level, with box diagrams involving W^\pm bosons and penguin diagrams with W^\pm bosons in the loop and a Z boson connecting to the leptons. The loop diagrams, see e.g. the left diagram of Fig. 3.1, feature the up-type quarks u , c and t —and in the case of the box diagrams also a neutrino ν_l —, which, with the exception of the top quark, are all much lighter than the heavy W^\pm bosons in the loop. Hence, the effects of non-vanishing masses of up and charm quarks—and potentially non-zero m_{ν_l} —can be safely neglected and occur only as heavily suppressed contributions to the matrix element. Overall, we only have massive W^\pm bosons and top quarks in the loops, while all other particles in the loop can be assumed to be massless. Furthermore, the typical momentum scale of the decay is given by $p^2 \equiv p_\mu p^\mu = M_{B_q}^2 \ll M_W^2$. This allows to use an effective field theory (EFT) to describe the process, in which all heavy particles are *integrated out*. Particles that are integrated out do not appear as propagating degrees of freedom and e.g. cannot be produced on the mass shell. Of course, in integrating particles out of the theory one has to choose a mass scale separating particles that remain as dynamical degrees of freedom—i.e. propagating particles—from particles that are integrated out, see Fig. 3.1. In our case a natural scale for integrating out particles is the mass of heaviest SM particle propagating in the loops, i.e. the top-quark mass $m_t \equiv \bar{m}_t (\bar{m}_t) = 162.464$ GeV, such that the massive electroweak gauge bosons, the Higgs boson, and the top quark are removed as propagating particles. After that, one is left with an *effective Lagrangian* of the form

$$\mathcal{L}_{\text{eff}} = \mathcal{L}_{SU(3)_C \times U(1)_Q}^{(5)} + \left(N \sum_n C_n Q_n + \text{h.c.} \right), \quad (3.1)$$

where $\mathcal{L}_{SU(3)_C \times U(1)_Q}^{(5)}$ contains the strong and electromagnetic interactions of the five light quark flavours u, d, s, c, b as well as the electromagnetic interactions of all charged leptons.

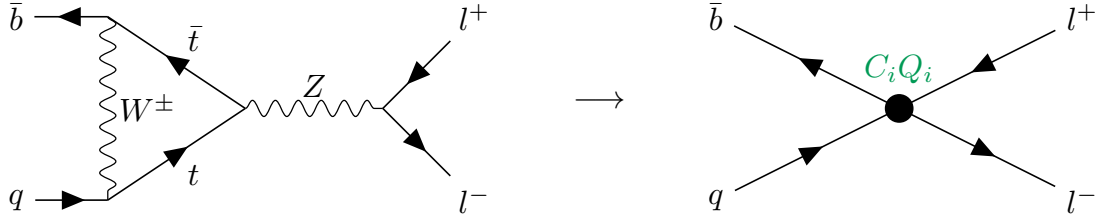


Figure 3.1.: Schematic illustration of the transition from the full SM amplitude to the same amplitude within the EFT. The W^\pm boson and all heavier particles are integrated out, leaving a set of effective operators Q_i that only depend on the external particles involved in the process. The Wilson coefficients C_i act as effective couplings.

In Eq. (3.1) a number of *effective operators* arises, denoted by Q_n .¹ They contain the external particles of the process and can in general be written as

$$Q_n = (\bar{b}\Gamma\Pi q) \otimes (\bar{l}\Gamma'\Pi' l) , \quad (3.2)$$

where $\Gamma^{(\prime)}$ are structures consisting of Dirac γ matrices and $\Pi^{(\prime)}$ are the colour factors. The only general condition here is that all Lorentz indices are contracted between Γ and Γ' and that all colour indices are contracted between Π and Π' , such that Q_n is a Lorentz scalar and colour singlet. In our case, since Π' is contracted between leptons that do not couple to gluons at all, $\Pi' = \mathbb{1}$, implying that $\Pi = \mathbb{1}$ as well.

Considering the Dirac structures $\Gamma^{(\prime)}$ it is clear that the number of possible Dirac structures is finite as longer chains of Dirac matrices can always be reduced to shorter chains in four spacetime dimensions. This leaves only five possible independent options for $\Gamma^{(\prime)}$:

$$\mathbb{1}, \quad \gamma^\mu, \quad \sigma^{\mu\nu}, \quad \gamma^\mu\gamma^5, \quad \gamma^5, \quad (3.3)$$

where $\sigma^{\mu\nu} = i/2 [\gamma^\mu, \gamma^\nu]$ and $\gamma^5 = i\gamma^0\gamma^1\gamma^2\gamma^3$. However, the constraint that all indices must be fully contracted implies that only 9 out of the 25 possible products $\Gamma \otimes \Gamma'$ are allowed. In order to determine which of these operators contribute to the process $B_q \rightarrow l^+l^-$, it is necessary to consider the *hadronic matrix elements* $\langle 0|\bar{b}\Gamma q|B_q\rangle$. Since the ground-state B_q meson is a pseudoscalar particle, only matrix elements where Γ contains a γ^5 matrix are non-vanishing, i.e. Γ can only be $\gamma^\mu\gamma^5$ or γ^5 . Hence, four possible operators are left:

$$\begin{aligned} Q_{AV} &= (\bar{b}\gamma_\mu\gamma_5 q) \otimes (\bar{l}\gamma^\mu l) , & Q_{AA} &= (\bar{b}\gamma_\mu\gamma_5 q) \otimes (\bar{l}\gamma^\mu\gamma_5 l) , \\ Q_{PS} &= (\bar{b}\gamma_5 q) \otimes (\bar{l}l) , & Q_{PP} &= (\bar{b}\gamma_5 q) \otimes (\bar{l}\gamma_5 l) . \end{aligned} \quad (3.4)$$

The two hadronic matrix elements are given in terms of the *leptonic decay constant* f_{B_q} as

$$\begin{aligned} \langle 0|\bar{b}\gamma_\mu\gamma_5 q|B_q(p)\rangle &= if_{B_q}p_\mu , \\ \langle 0|\bar{b}\gamma_5 q|B_q(p)\rangle &= -if_{B_q}\frac{M_{B_q}^2}{m_b + m_q} , \end{aligned} \quad (3.5)$$

¹The symbols C_n and N will be introduced after the discussion of the effective operators Q_n .

where the second equation follows from the first one by the equations of motion. When the momentum $p_\mu = p_\mu^{\bar{b}} + p_\mu^q = p_\mu^{\bar{l}} + p_\mu^l$ of the B_q meson is contracted with the leptonic operator $\bar{l}\gamma^\mu l$ it vanishes by use of the Dirac equation, such that the operator Q_{AV} actually vanishes once the hadronic matrix elements have been taken into account. The remaining three operators are indeed non-vanishing and all of them will occur in the remainder of this thesis. It is, however, customary in flavour physics to define operators to be eigenstates of the chirality operators P_R and P_L , at least for the quark spin lines, and therefore we will use the following basis of operators throughout the rest of this thesis:

$$\begin{aligned} Q_A &= (\bar{b}\gamma_\mu P_L q) \otimes (\bar{l}\gamma^\mu \gamma_5 l) , & Q'_A &= (\bar{b}\gamma_\mu P_R q) \otimes (\bar{l}\gamma^\mu \gamma_5 l) , \\ Q_S &= (\bar{b}P_L q) \otimes (\bar{l}l) , & Q'_S &= (\bar{b}P_R q) \otimes (\bar{l}l) , \\ Q_P &= (\bar{b}P_L q) \otimes (\bar{l}\gamma_5 l) , & Q'_P &= (\bar{b}P_R q) \otimes (\bar{l}\gamma_5 l) . \end{aligned} \quad (3.6)$$

In this notation the subscript refers to the Dirac structure of the lepton line, and chirality projector operators are $P_L = (1 - \gamma^5)/2$ and $P_R = (1 + \gamma^5)/2$.

So far we have ignored the symbols N and C_n in Eq. (3.1), but now it is time to discuss them as well. The factor N is simply an overall prefactor that is convenient to factor out from the symbols C_n . It is given by

$$N = \frac{G_F^2 M_W^2 V_{tb}^* V_{ts}}{\pi^2} = \frac{G_F \alpha_{\text{em}}(\mu) V_{tb}^* V_{ts}}{\sqrt{2} \pi \sin^2 \theta_w} , \quad (3.7)$$

and is motivated by the fact that in the SM the decay $B_q \rightarrow l^+ l^-$ starts at the one-loop level. In Eq. (3.7) the *Fermi constant* is denoted by $G_F = 1.166\,378\,8(6) \text{ GeV}^{-2}$ [3] and $\alpha_{\text{em}}(\mu)$ denotes the running electromagnetic fine-structure constant, evaluated at the scale μ . The weak mixing angle $\sin \theta_w$ defines the rotation between the electrically neutral $SU(2)_L \times U(1)_Y$ gauge bosons and the massive and massless Z boson and photon, respectively. The only elements of the Cabibbo-Kobayashi-Maskawa (CKM) matrix present in Eq. (3.7) are the ones coupling the external quarks to internal top quarks in Eq. (3.7), a feature that we will discuss in more detail later on. We stress that the second equality in Eq. (3.7) only holds to leading order in the electroweak perturbative expansion since higher-order electroweak loop corrections alter, for example, the relation between M_W and $\sin \theta_w$. In the following, we will restrict ourselves to the first definition with $N \propto G_F^2$, for which two-loop electroweak (EW) corrections are smaller [27].

Finally, the symbols C_n denote the so-called *Wilson coefficients* of the effective operators. They can be thought of as an effective coupling of their respective operator, and it is these Wilson coefficients that contain all information about the particles we have integrated out. For example, they typically depend on the masses of the particles integrated out in a non-trivial way. In writing these Wilson coefficients we follow the same notation as for the effective operators, i.e. we will be dealing with the coefficients $C_A^{(\prime)}$, $C_S^{(\prime)}$, and $C_P^{(\prime)}$. The Wilson coefficients can be calculated perturbatively as a series in the small coupling constants

$$C_n = \sum_{i=0}^{\infty} \sum_{j=0}^{\infty} \left(\frac{\alpha_s}{4\pi} \right)^i \left(\frac{\alpha}{4\pi} \right)^j C_n^{(i,j)} , \quad (3.8)$$

where α_s denotes the strong coupling constant of QCD and α the electroweak (EW) coupling. Numerically, $\alpha \sim \alpha_s^2 \ll 1$, so next-to-leading order (NLO) order EW corrections are usually

considered to be of the same size as next-to-next-to-leading order (NNLO) QCD corrections. In this thesis, we will discuss effects arising at leading and next-to-leading order in QCD and at leading order in the electroweak coupling, i.e. $i = 0$ or $i = 1$, while $j = 0$. As discussed above, the typical momentum scale of $B_q \rightarrow l^+l^-$ decays is given by $M_{B_q}^2 \approx (5 \text{ GeV})^2$, but the decay amplitude will typically depend on the masses of heavier particles—for example the W^\pm boson—through logarithms arising from the loop integrals, such that e.g. at $\mathcal{O}(\alpha_s)$ we can schematically write the amplitude as [28]

$$\mathcal{M} = A_1 \left(1 + \alpha_s c \log \left(\frac{M_W^2}{p^2} \right) \right), \quad (3.9)$$

with A_1 and c some coefficients and p^2 the typical momentum transfer squared of the decay. Rewriting the logarithm,

$$\log \left(\frac{M_W^2}{p^2} \right) = \int_{p^2}^{M_W^2} \frac{dk^2}{k^2} = \int_{p^2}^{\mu^2} \frac{dk^2}{k^2} + \int_{\mu^2}^{M_W^2} \frac{dk^2}{k^2} = \log \left(\frac{\mu^2}{p^2} \right) + \log \left(\frac{M_W^2}{\mu^2} \right), \quad (3.10)$$

it becomes clear that, after the splitting, the amplitude can be written at $\mathcal{O}(\alpha_s)$ as

$$\mathcal{M} = A_1 \left(1 + \alpha_s c \log \left(\frac{M_W^2}{\mu^2} \right) \right) \left(1 + \alpha_s c \log \left(\frac{\mu^2}{p^2} \right) \right). \quad (3.11)$$

This is known as the *factorisation* of short-distance and long-distance effects. It is the Wilson coefficients $C_i^{(\prime)}$ that govern the effects from the arbitrary scale μ^2 up to the heavier scales $\sim M_W^2, m_t^2$, while effects at scales smaller than μ^2 are governed by the hadronic matrix elements, or more generally, by the operator matrix elements of the effective operators obtained by integrating out the heavy particles. In particular, both the Wilson coefficients and the operator matrix elements individually depend on the choice of scale μ^2 , and only in the combination will this dependence drop out. At fixed order in perturbation theory, this cancellation is not exact, since higher order terms are neglected, see e.g. the missing $\mathcal{O}(\alpha_s^2)$ term when comparing Eq. (3.9) and Eq. (3.11).

At this point, a short discussion of the infrared behaviour of the effective theory is in order. After integrating out the heavy particles, one obtains a set of effective operators with their respective Wilson coefficients. These coefficients govern the effects of particles that are much heavier than the typical momentum scale. On the other hand, light particles still remain, e.g. the external particles and the massless gauge bosons. The Wilson coefficients are now determined by computing the decay amplitude in the full theory and in the effective theory, requiring them to be equal; this is called *matching*. If the amplitude in the full theory has an infrared singularity due to some massless particle, then so will the amplitude in the effective theory. Hence, in the matching, these infrared singularities will drop out, and the Wilson coefficients are infrared finite. Furthermore, as long as they are computed in a kinematic regime in which the EFT is a reasonable approximation, they do not depend on the precise momentum configuration of the external particles: Since all momenta of external particles are at most of order $p_i^2 = M_{B_q}^2$, the

dependence on this momentum configuration will always drop out in the matching procedure as well. This feature is of great practical use since it allows us to choose a convenient momentum configuration for the external particles, for example we can set all external momenta to zero.

Integrating out the heavy W^\pm , Z , H , and top quark at the scale $\mu_0 \approx m_t$ yields an initial condition for the Wilson coefficients, $C_i(\mu_0 \approx m_t)$. We are however interested in their values at a much smaller scale, $\mu_1 \approx M_{B_q}$. Logarithms appearing in the analytic expressions for the Wilson coefficients or matrix elements cannot be small at both of these scales simultaneously, and thus large logarithms will inevitably arise. These large logarithms can spoil the numerical validity of fixed-order perturbation theory if they become of order $\ln(\mu^2/M^2) \sim 1/\alpha_s$, spoiling the power counting in the coupling constant α_s . The effective theory provides a tool for efficiently performing the sum of all terms with large logarithms,

$$\sum_n (\alpha_s \log(\mu^2/M^2))^n, \quad (3.12)$$

by means of the differential equations governing the renormalisation-group evolution (RGE). The RGE equations relate the Wilson coefficients at different scales,

$$C_i(\mu_1) = U_{ij}(\mu_1, \mu_0) C_j(\mu_0), \quad (3.13)$$

by means of an evolution operator $\hat{U}(\mu_1, \mu_0)$. In general, the matrix \hat{U} is non-diagonal, leading to a mixing between different effective operators (or, equivalently, their Wilson coefficients). Eq. (3.12) sums all leading logarithms; at the next-to-leading order, the logarithms of order $\alpha_s \sum_n (\alpha_s \log(\mu^2/M^2))^n$ need to be summed as well.

3.2. The decay rate

In the effective theory, the matrix element for $B_q \rightarrow l^+ l^-$ can now be written as

$$\begin{aligned} \mathcal{M} &= N \left[(C_A \langle 0 | \bar{b} \gamma_\mu P_L q | B_q \rangle + C'_A \langle 0 | \bar{b} \gamma_\mu P_R q | B_q \rangle) \otimes (\bar{l} \gamma^\mu \gamma^5 l) \right. \\ &\quad + (C_S \langle 0 | \bar{b} P_L q | B_q \rangle + C'_S \langle 0 | \bar{b} P_R q | B_q \rangle) \otimes (\bar{l} l) \\ &\quad \left. + (C_P \langle 0 | \bar{b} P_L q | B_q \rangle + C'_P \langle 0 | \bar{b} P_R q | B_q \rangle) \otimes (\bar{l} \gamma^5 l) \right] \\ &= \frac{iN f_{B_q}}{2} \left\{ \left[-2m_l (C_A - C'_A) + \frac{M_{B_q}^2}{m_b + m_q} (C_P - C'_P) \right] \otimes (\bar{l} \gamma^5 l) \right. \\ &\quad \left. + \frac{M_{B_q}^2}{m_b + m_q} (C_S - C'_S) \otimes (\bar{l} l) \right\}, \quad (3.14) \end{aligned}$$

where m_l denotes the charged-lepton mass and $m_{b,q}$ the masses of the b and q quarks. In the second equality we have used Eq. (3.5) to express the hadronic quark-current matrix elements and the Dirac equation for leptons. When squaring the amplitude, the terms with $(\bar{l} \gamma^5 l)$ and $(\bar{l} l)$ do not interfere since the trace of γ^5 multiplied by at most three γ matrices vanishes. Thus

the two Dirac structures square independently and the squared matrix element is given by

$$|\mathcal{M}|^2 = \frac{|N|^2 f_{B_q}^2}{4} \left[\left| -2m_l (C_A - C'_A) + \frac{M_{B_q}^2}{m_b + m_q} (C_P - C'_P) \right|^2 \cdot 2M_{B_q}^2 + \left(\frac{M_{B_q}^2}{m_b + m_q} \right)^2 |C_S - C'_S|^2 \cdot 2M_{B_q}^2 \left(1 - \frac{4m_l^2}{M_{B_q}^2} \right) \right] \quad (3.15)$$

$$= \frac{|N|^2 f_{B_q}^2 M_{B_q}^4}{2} \left\{ \left| r (C_A - C'_A) - u (C_P - C'_P) \right|^2 + |u\beta (C_S - C'_S)|^2 \right\}, \quad (3.16)$$

where we have introduced the abbreviations

$$r \equiv \frac{2m_l}{M_{B_q}}, \quad \beta \equiv \sqrt{1 - r^2}, \quad u \equiv \frac{M_{B_q}}{m_b + m_q}. \quad (3.17)$$

From Eq. (3.16) we see that the squared matrix element is independent of the momenta of all external particles. Therefore we can integrate over the Lorentz-invariant phase space independently. In particular, the angular integration is trivially done and yields

$$\int d\Omega_l = \int_0^{2\pi} d\varphi \int_0^\pi d\theta \sin \theta = 4\pi. \quad (3.18)$$

Momentum conservation forces the magnitudes $|\vec{p}_l|$ and $|\vec{p}_{\bar{l}}|$ to be equal and fixed, so the integration over one of the three-momenta is trivial and furthermore $E_l = E_{\bar{l}} = M_{B_q}/2$. They are given by

$$|\vec{p}_l| = |\vec{p}_{\bar{l}}| = \frac{M_{B_q}}{2} \sqrt{1 - \frac{4m_l^2}{M_{B_q}^2}}, \quad (3.19)$$

such that

$$\int \frac{d\Omega_l d|\vec{p}_l| |\vec{p}_l|^2}{E_l^2} \delta(M_{B_q} - 2E_l) = \frac{1}{2} \sqrt{1 - \frac{4m_l^2}{M_{B_q}^2}} \int d\Omega_l. \quad (3.20)$$

Putting everything together, the decay rate is given by [3]

$$\begin{aligned} \Gamma &= \frac{(2\pi)^4}{2M_{B_q}} |\mathcal{M}|^2 \int d\Pi_{\text{LIPS}} = \frac{1}{32\pi^2 M_{B_q}} |\mathcal{M}|^2 \int \frac{d^3\vec{p}_l}{E_l^2} \delta(M_{B_q} - 2E_l) \\ &= \frac{1}{64\pi^2 M_{B_q}} \sqrt{1 - \frac{4m_l^2}{M_{B_q}^2}} |\mathcal{M}|^2 \int d\Omega_l \\ &= \frac{|N|^2 f_{B_q}^2 M_{B_q}^3}{32\pi} \beta \left[\left| r (C_A - C'_A) - u (C_P - C'_P) \right|^2 + |u\beta (C_S - C'_S)|^2 \right], \end{aligned} \quad (3.21)$$

where we have inserted the expressions for the squared matrix element (Eq. (3.16)) and the angular integration (Eq. (3.18)) in the last step.

In order to obtain a formula for the branching ratio, we would like to divide by the total decay rate of the B_q meson. However, neutral B mesons mix with their antiparticles, and the mass eigenstates are linear combinations of mesons and their antiparticles. We introduce two factors [29]

$$\begin{aligned} F_P &= 1 - \frac{\Gamma_L^q - \Gamma_H^q}{\Gamma_L^q} \sin^2 \left[\arg (r (C'_A - C_A) - u (C'_P - C_P)) - \frac{\phi_{\text{NP}}^s}{2} \right] \\ F_S &= 1 - \frac{\Gamma_L^q - \Gamma_H^q}{\Gamma_L^q} \cos^2 \left[\arg (C'_S - C_S) - \frac{\phi_{\text{NP}}^s}{2} \right], \end{aligned} \quad (3.22)$$

where ϕ_{NP}^s denotes an additional CP-violating phase from new physics (NP) contributions to the B_s - \bar{B}_s mixing. Unless otherwise stated, we work with $\phi_{\text{NP}}^s = 0$, which is justified because of stringent experimental upper bounds on $|\phi_{\text{NP}}^s|$. In these expressions, Γ_L^q and Γ_H^q denote the decay rates of the lighter and heavier B_q meson mass eigenstates, respectively. With these factors, the *averaged time-integrated branching ratio* can be written as [29]

$$\bar{\mathcal{B}}(B_q \rightarrow l^+ l^-) = \frac{|N|^2 f_{B_q}^2 M_{B_q}^3}{32\pi\Gamma_H^q} \beta \left[|r (C_A - C'_A) - u (C_P - C'_P)|^2 F_P + |u\beta (C_S - C'_S)|^2 F_S \right]. \quad (3.23)$$

3.3. Status of experiment

Rare leptonic decays of neutral B mesons are searched for at current collider experiments, in particular at Belle II and the LHC experiments ATLAS, CMS, and LHCb. In this section, we report on the current experimental status and the future prospects concerning the measurement of these highly suppressed decays.

We begin with the decay $B_s \rightarrow \mu^+ \mu^-$, which is the only decay in this selection that has already been measured. The first observation, exceeding the level of statistical significance of more than six standard deviations, was published by the CMS and LHCb collaborations in 2015 [30]. This joint analysis was performed on the 2011 and 2012 data sets taken at centre-of-mass energies of 7 TeV and 8 TeV, respectively. Whereas LHCb was designed specifically with the sensitivity to study flavour-changing processes such as B -meson decays, CMS has lower reconstruction efficiencies for light particles [30]. However, this disadvantage is to some extent compensated by the higher instantaneous luminosity in the CMS collision point, making CMS a competitive experiment even for some low-energy processes. In the search for $B_s \rightarrow \mu^+ \mu^-$ decays, candidate events were required to have a dimuon invariant mass matching the B_s meson kinematics and a displaced decay vertex. In order to distinguish events from B_s from those stemming from B_d , both experiments need a mass resolution of well below 100 MeV. The measured branching fraction $\bar{\mathcal{B}}(B_s \rightarrow \mu^+ \mu^-) = (2.8_{-0.6}^{+0.7}) \cdot 10^{-9}$ was slightly lower than the SM prediction of $(3.66 \pm 0.23) \cdot 10^{-9}$ [31]. The latter value was obtained using the 2013 inclusive determination [32] of V_{cb} , $|V_{cb}| = 42.42(86) \cdot 10^{-3}$, starting from which the precisely known ratio $|V_{tb}^* V_{ts} / V_{cb}|$ was used in order to determine $|V_{tb}^* V_{ts}|$. The numerical value of V_{ts} , which is related to V_{cb} , is a source of major parametric uncertainty in the determination of the branching ratio, and inclusive and exclusive determinations of $|V_{cb}|$ yield different values, see e.g. Ref. [3]

for a discussion of the present status quo. We will discuss the implications of this uncertainty in Section 4.4.

In 2019, 2020, and 2022, three more analyses including also data taken at 13 TeV by the ATLAS, CMS, and LHCb collaborations were published, reporting² [33–36]

$$\bar{\mathcal{B}}(B_s \rightarrow \mu^+\mu^-)_{\text{ATLAS,2019}} = (2.8_{-0.7}^{+0.8}) \cdot 10^{-9}, \quad (3.24)$$

$$\bar{\mathcal{B}}(B_s \rightarrow \mu^+\mu^-)_{\text{CMS,2020}} = (2.9 \pm 0.7 \pm 0.2) \cdot 10^{-9}, \quad (3.25)$$

$$\bar{\mathcal{B}}(B_s \rightarrow \mu^+\mu^-)_{\text{LHCb,2022}} = (3.09_{-0.43-0.11}^{+0.46+0.15}) \cdot 10^{-9}. \quad (3.26)$$

It is worth noting that all of these measurements consistently fell slightly short of the SM expectation, which was thus also reflected in the world average. However, recently the CMS collaboration reported a new measurement of [37]

$$\bar{\mathcal{B}}(B_s \rightarrow \mu^+\mu^-)_{\text{CMS,2022}} = (3.83_{-0.36-0.21}^{+0.38+0.24}) \cdot 10^{-9}, \quad (3.27)$$

which moved the world average much closer to the SM theory prediction.

For the decay of B_d mesons into muons, due to the smaller CKM matrix element V_{td} entering the normalisation factor N in Eq. (3.7), the SM prediction is smaller by a factor of about 30 [31],

$$\bar{\mathcal{B}}(B_d \rightarrow \mu^+\mu^-)_{\text{SM}} = (1.06 \pm 0.09) \cdot 10^{-10}. \quad (3.28)$$

These decays are currently just beyond the experimental reach and several experiments have reported upper limits on the branching ratio since the begin of data taking at the LHC [30, 33, 38, 39]. The latest LHCb search [35, 36] finds

$$\bar{\mathcal{B}}(B_d \rightarrow \mu^+\mu^-)_{\text{LHCb,2022}} < 2.6 \times 10^{-10} \quad (3.29)$$

at the 95 % confidence level, while the PDG world average quotes an time-averaged branching ratio of $\bar{\mathcal{B}}(B_d \rightarrow \mu^+\mu^-)_{\text{PDG,2022}} = (0.7_{-1.1}^{+1.3}) \cdot 10^{-10}$ [3], still consistent with the background-only hypothesis.

In the high-luminosity phase of the Large Hadron Collider (HL-LHC), a 5σ observation of the decay $B_d \rightarrow \mu^+\mu^-$ is expected with statistically dominated uncertainties, as discussed in the ‘‘Snowmass White Paper’’ contribution ‘‘Physics with the Phase-2 ATLAS and CMS Detectors’’ [40–42]. The increased sensitivity of these analyses profits from an improved mass resolution, crucial in order to distinguish between B_d and B_s mesons, and upgraded trigger systems. For example, the CMS collaboration expects to achieve a total uncertainty on the branching ratio $B_s \rightarrow \mu^+\mu^-$ of about 7 %, in which the systematic uncertainties will begin to play a role. Moreover, further observables such as the decay CP asymmetry will become accessible. These improved measurements, combined with the rather precise SM predictions, will allow for the probing of significant parts of the parameter space of 2HDMs. In Fig. 3.2, we show the projected sensitivity of ATLAS in the HL-LHC phase, assuming an aggregated ‘‘high-yield’’ dataset of 75 times the Run-1 statistics, taken from [41].

²Whenever two sources of uncertainty are given, the first pair of numbers indicates the statistical uncertainty, whereas the second pair of numbers corresponds to the systematic uncertainty.

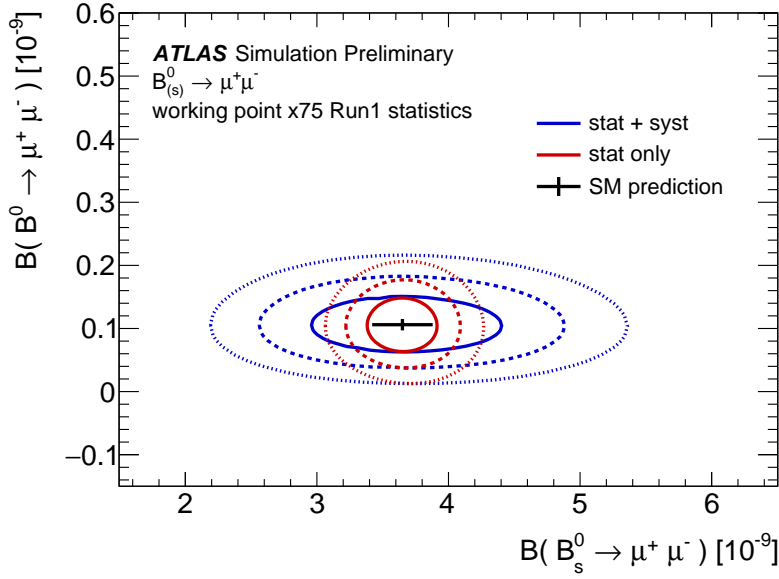


Figure 3.2.: Projected sensitivity of the ATLAS experiment for the decays $B_q \rightarrow \mu^+ \mu^-$ at the HL-LHC. Continuous, dashed, and dotted contours show the projected 68.3 %, 95.5 %, and 99.7 % confidence regions, with (blue) and without (red) including the estimated systematic uncertainties in addition to the statistical ones. For this simulation, an integrated data set of 75 times the Run-1 statistics has been assumed. Furthermore, the lower trigger threshold has been assumed to be $p_T > 6$ GeV for each of the two muons. Taken from Ref. [41].

Concerning decays into τ leptons, the SM predictions for $B_q \rightarrow \tau^+ \tau^-$ [31],

$$\bar{\mathcal{B}}(B_s \rightarrow \tau^+ \tau^-)_{\text{SM}} = (7.73 \pm 0.49) \cdot 10^{-7}, \quad (3.30)$$

$$\bar{\mathcal{B}}(B_d \rightarrow \tau^+ \tau^-)_{\text{SM}} = (2.22 \pm 0.19) \cdot 10^{-8}, \quad (3.31)$$

are roughly 210 times larger than their muonic counterparts, due to the larger helicity factor βr^2 in Eq. (3.23). Unfortunately, on the experimental side the reconstruction of tauonic B_q decays is much more difficult than in $B_q \rightarrow \mu^+ \mu^-$. Since the τ leptons decay almost immediately, the resulting at least two invisible neutrinos make the $\tau^+ \tau^-$ reconstructed invariant mass squared a rather imprecise discriminator between signal and background. Hence, only upper limits can be obtained at present. The LHCb collaboration finds [43]

$$\mathcal{B}(B_s \rightarrow \tau^+ \tau^-)_{\text{LHCb,2017}} < 6.8 \cdot 10^{-3}, \quad (3.32)$$

$$\mathcal{B}(B_d \rightarrow \tau^+ \tau^-)_{\text{LHCb,2017}} < 2.1 \cdot 10^{-3}, \quad (3.33)$$

at the 95 % confidence level.

Decays into electron-positron pairs are negligibly small due to the helicity suppression [31],

$$\bar{\mathcal{B}}(B_s \rightarrow e^+ e^-)_{\text{SM}} = (8.54 \pm 0.55) \cdot 10^{-14}, \quad (3.34)$$

$$\bar{\mathcal{B}}(B_d \rightarrow e^+ e^-)_{\text{SM}} = (2.48 \pm 0.21) \cdot 10^{-15}. \quad (3.35)$$

3. *The rare decays $B_q \rightarrow l^+l^-$*

Due to this extreme suppression, these decays will not be observed by the LHC experiments or Belle II in the foreseeable future.

4. $B_q \rightarrow l^+l^-$ in the two-Higgs-doublet model of type II

In this chapter we describe the perturbative calculation of the Wilson coefficients entering the formula for the branching ratio in Eq. (3.23). Since we have a precise parameterisation of the hadronic matrix elements in Eq. (3.5) in terms of the clean leptonic decay constants, the Wilson coefficients are the last piece required to compute the branching ratio. We highlight the calculation of all Wilson coefficients including NLO corrections of order α_s within the 2HDM of type II, which was discussed in Section 2.2.1. These coefficients have been computed previously,¹ but we will discuss them in some detail nevertheless, mainly for two reasons. Firstly, the Yukawa structure of the Wilson coefficients in the type-II 2HDM is still simple enough that they serve as an ideal ground for the discussion of the cancellation of UV divergences and the electroweak gauge dependence. Indeed, we will present all leading order (LO) coefficients in a general electroweak gauge, thus making the cancellation of the gauge parameter evident. Secondly, as stated in Section 2.2.1, the Wilson coefficients in the three-spurion 2HDM presented in the next chapter can be interpreted as a “perturbation” about the type-II model, so a discussion of the type-II Wilson coefficients is in order by all means.

4.1. Computational setup

We dedicate a short section to the description of the common computational setup used to perform all of the subsequently listed Wilson coefficients. All of the calculations have been carried out using a semi-automated setup consisting of FeynRules [44–46] and its Universal Feynman Output (UFO) format [47, 48],² the relatively recent program `tapir` [49], as well as the programs `qgraf` [50] and `exp` [51–53]. Furthermore, we have extensively used the computer algebra language FORM [54] throughout the calculations.

4.1.1. Feynman rules

The semi-automated setup with `qgraf` and `tapir` requires the Feynman rules to be present in so-called `.lag`, `.prop`, and `.vrtx` files. In the `.lag` file only a list of particle propagators with their spin-statistics as well as a list of all vertices have to be declared, while the `.prop` and `.vrtx` files contain an implementation of the corresponding propagators and vertices, respectively. For calculations involving a small number of vertices, these files can be implemented by hand, but this quickly becomes unfeasible and error-prone if the number and complexity of vertices

¹References to the original publications are provided along with the discussion of the SM and 2HDM calculations, respectively.

²Recently the `Universal FeynRules Output` was renamed to `Universal Feynman Output` [48].

increases, e.g. in electroweak calculations or calculations within the 2HDM. Therefore, in order to reduce the risk of mistakes and the amount of manual labour, we have sought for an automated way of obtaining Feynman rules in a way that is readable to the programs `qgraf` and `tapi` that are tailored towards multi-loop calculations. The result is the `tapi` module `UF0Reader` [49], the use of which we describe in the following, providing some more technical additions in Appendix A.

In order to obtain the Feynman rules for the 2HDM with flavour-changing Yukawa couplings, we have started with the general 2HDM model files [55, 56] from the `FeynRules` database [44–47] and computed the Feynman rules using `Mathematica` version 12.1 [57]. These Feynman rules have then been exported as a Python [58] module using the so-called `Universal Feynman Output (UFO)` format [47]. In order to use them with `tapi`, the `UFO` module containing the Feynman rules had to be converted to version Python 3, for which we used the program `2to3` [59]. The resulting files were then used with the `UF0Reader` module of `tapi` which parsed the `UFO` input into the `.lag`, `.prop`, and `.vrtx` files necessary to perform the automated calculations. Since we wanted to perform several checks involving the automated setup, the set of Feynman rules, and the new `UF0Reader`, a calculation in a general gauge for all gauge bosons was desired, at least at one-loop order. To this end, the `UF0Reader` module restores the gauge-parameter dependence of Feynman rules that was absent in the `UFO` files. We followed the recommendation of `FeynRules` to compute Feynman rules within `Mathematica` in either Feynman gauge ($\xi = 1$) or unitary gauge ($\xi \rightarrow \infty$). Since Goldstone bosons were essential for our calculations and the gauge-dependence checks, we extracted the Feynman rules in Feynman gauge and restored the gauge dependence for the W and Z (and the corresponding Goldstone) bosons using the `UF0Reader`; a more detailed discussion is found in Appendix A.

4.1.2. Feynman graph generation, symbolic expressions, and mapping onto topologies

We use the program `qgraf` [50] to generate Feynman graphs for the process under consideration. The program allows for several filters concerning the type of external and internal particles, and we use these capabilities to split the calculation of Wilson coefficients into several classes of diagrams. Subsequently, `tapi` [49] is used to insert the symbolic Feynman rules obtained in the previous `UF0Reader` step into the diagrams and rewrite them to symbolic expressions. Furthermore, the `tapi` configuration file must contain a specification of all massive particles and all gauge parameters.

Diagrams involving massive gauge bosons feature propagators of the form

$$\mathcal{D}_{\mu\nu}(k, M, \xi) = \frac{-i \left(g_{\mu\nu} - (1 - \xi) \frac{k_\mu k_\nu}{k^2 - \xi M^2} \right)}{k^2 - M^2}. \quad (4.1)$$

The `FORM` routines used to solve the loop integrals perform the integration according to the denominator structure of the amplitudes, which in the case of Eq. (4.1) involves two denominators with different “masses” M^2 and ξM^2 . For reasons of performance it is beneficial to perform a partial fraction decomposition of $\mathcal{D}_{\mu\nu}$, such that each term features only a single mass scale in the dynamic denominator. This splitting into “*transversal*” and “*longitudinal*” particles,

$$\mathcal{D}_{\mu\nu}(k, M, \xi) = \mathcal{D}_{T,\mu\nu}(k, M, \xi) + \mathcal{D}_{L,\mu\nu}(k, M, \xi), \quad (4.2)$$

with the two individual propagators given by

$$\mathcal{D}_{T,\mu\nu}(k, M, \xi) = \frac{-i \left(g_{\mu\nu} - \frac{k_\mu k_\nu}{M^2} \right)}{k^2 - M^2}, \quad (4.3)$$

$$\mathcal{D}_{L,\mu\nu}(k, M, \xi) = -\frac{i}{M^2} \frac{k_\mu k_\nu}{k^2 - \xi M^2}, \quad (4.4)$$

is automatically provided by `tapir` and goes at the expense of generating considerably more diagrams than without decomposition. The terms “transversal” and “longitudinal” refer to the fact that for *on-shell* gauge bosons, with $k_\mu k^\mu = M^2$, one has

$$k^\mu \mathcal{D}_{T,\mu\nu}(k, M, \xi) = 0. \quad (4.5)$$

The new propagators have different masses, which can be specified in the `tapir` configuration file using e.g. for the W -boson (in YAML syntax)

mass:

- **Wtp:** M2
- **Wlp:** M3
- **Gp:** M3

where `Wtp` and `Wlp` are the *transversal* and *longitudinal* propagators, respectively, and `Gp` denotes the charged Goldstone boson G^+ . In the configuration file both masses $M_L^2 \equiv M_3^2 \equiv \xi M^2$ and $M_T^2 \equiv M_2^2 \equiv M^2$ are treated as separate parameters. No further information about the relation between `M2` and `M3` needs to be specified at this point; the relations can be inserted by the user at the very end of the calculation. The assignment of longitudinal propagators to their corresponding transversal counterparts also needs to be provided in the `tapir` configuration file with the option (in YAML syntax)

gaugeprop:

- **Wlp:** Wtp
- **Wlm:** Wtp

in the case of the charged W boson. The `.dia` and `.edia` files produced by `tapir` contain the symbolic FORM code for the diagrams and topology information, respectively. In the next step, the Feynman diagrams are mapped onto integral topologies using `exp` [51–53]. During this step, an expansion in the external momenta is performed, since the Wilson coefficients can be computed in an arbitrary momentum configuration. As a result, only massive tadpole topologies are needed for the calculation. At this step, all Feynman diagrams are expressed in terms of a Dirac tensor product, a colour tensor product, and a number of tensor integrals over the loop momenta.

4.1.3. FORM code, projectors, and integration

We write a general loop integral with tensor structure as

$$I_{\mu_1, \mu_2, \dots, \mu_n} = \int d^d k_1 d^d k_2 \dots d^d k_n \frac{f_{\mu_1, \mu_2, \dots, \mu_n}(\{k_i\}, \{q_i\})}{D_1^{n_1} \dots D_N^{n_N}}. \quad (4.6)$$

Since the loop momenta are integrated out, the only momenta that can appear in the tensor structure of $I_{\mu_1, \mu_2, \dots, \mu_n}$ are the momenta $\{q_i\}$ of the external particles. In addition, products of the metric tensor $g_{\mu\nu}$ may appear as well. We are interested in the Wilson coefficients of the effective operators, $C_A^{(\prime)}$, $C_S^{(\prime)}$, and $C_P^{(\prime)}$, and these Wilson coefficients can be computed with vanishing external momenta, $q_i = 0$. An exception to this are the self-energy contributions that will be discussed in Section 4.2.3, for which the limit $q_i \rightarrow 0$ can only be taken after multiplication with the one-light-particle-irreducible (1LPI) tree-level diagrams.

With $q_i = 0$, the only possible tensor structures appearing in $I_{\mu_1, \mu_2, \dots, \mu_n}$ are products of metric tensors, e.g.

$$I_{\mu_1, \mu_2} = \int d^d k \frac{k_{\mu_1} k_{\mu_2}}{D_1^{n_1} \dots D_N^{n_N}} = A g_{\mu_1 \mu_2} \int d^d k \frac{k \cdot k}{D_1^{n_1} \dots D_N^{n_N}}, \quad (4.7)$$

for which the constant A turns out to be $1/d$. The integrals without tensor structure on the right-hand side of Eq. (4.7) contain only scalar products and are therefore called *scalar integrals*. In practice, any tensor loop integral can be decomposed into a sum of scalar integrals such that calculating the loop integrals becomes equivalent to solving the scalar integrals. This reduction to scalar integrals can be done in two steps. The first step, *integrand tensor reduction* is a generalisation of what we discussed in the preceding lines, i.e. a reduction of the scalar product of momenta—in our case only loop momenta since $q_i = 0$ —into products of metric tensors and (possibly) external momenta which will then be contracted with the Dirac structure of the operators. It has the advantage that it is transparent during all steps of the computation. However, in the calculations presented within this thesis the external particles are fermions with their own Dirac structures $\gamma_{\mu_1} \dots \gamma_{\mu_n}$. Within the custom FORM setup traces of all fermion lines are taken at a certain step, which would result in incorrect results if the external fermion lines are not already taken care of during an earlier step. Therefore, in a second step the Dirac structure of all diagram amplitudes has to be determined as well. The final result of the calculation yields the Wilson coefficients of the effective operators in Eq. (3.6) which determine the relevant Dirac structures. However, the symbolic FORM expressions contain many more structures of Dirac matrices that need to be taken into account in the intermediate steps of the calculation. Furthermore, we regularise the divergences occurring in the Feynman integrals using *dimensional regularisation*, i.e. we compute the integrals in d dimensions rather than 4 dimensions, where $d = 4 - 2\epsilon$. Whereas four-dimensional Dirac bilinears $\bar{\psi} \gamma_{\mu_1} \dots \gamma_{\mu_n} \psi$ can always be reduced to a linear combination of the sixteen four-dimensional bilinears

$$\bar{\psi} \psi, \quad \bar{\psi} \gamma_\mu \psi, \quad \bar{\psi} \sigma_{\mu\nu} \psi, \quad \bar{\psi} \gamma_\mu \gamma_5 \psi, \quad \bar{\psi} \gamma_5 \psi, \quad (4.8)$$

with $\sigma_{\mu\nu} = \frac{i}{2} [\gamma_\mu, \gamma_\nu]$, this is not true in $d \neq 4$ dimensions. For example, in four dimensions a product of three γ matrices can be reduced by use of the Chisholm identity

$$\gamma^\mu \gamma^\nu \gamma^\rho = g^{\mu\nu} \gamma^\rho - g^{\mu\rho} \gamma^\nu + g^{\nu\rho} \gamma^\mu - i \epsilon^{\mu\nu\rho\alpha} \gamma_\alpha \gamma_5. \quad (4.9)$$

In $d \neq 4$ dimensions, $\gamma^\mu \gamma^\nu \gamma^\rho$ is an independent Dirac structure that cannot be completely reduced to simpler structures. As a consequence, also four-fermion Dirac structures such as

$$(\bar{b} \gamma^\mu \gamma^\nu \gamma^\rho P_L q) \otimes (\bar{l} \gamma_\rho \gamma_\nu \gamma_\mu P_L l), \quad (4.10)$$

which arise during the calculation of one-loop box diagrams with W -boson exchanges, cannot be reduced to the physical operators of Eq. (3.6). The fact that the d -dimensional Dirac algebra does not have a finite basis leads to a tower of growing products of γ matrices,

$$\begin{aligned} & \gamma^\mu \otimes \gamma_\mu \\ & \gamma^\mu \gamma^\nu \gamma^\rho \otimes \gamma_\rho \gamma_\nu \gamma_\mu \\ & \gamma^\mu \gamma^\nu \gamma^\rho \gamma^\sigma \gamma^\tau \otimes \gamma_\tau \gamma_\sigma \gamma_\rho \gamma_\nu \gamma_\mu \\ & \dots \end{aligned}$$

that—in principle—must all be taken into account. However, in a practical calculation at fixed order in perturbation theory, the number of propagators and vertices within a Feynman diagram is bounded, putting an upper bound on the number of Dirac matrices that can appear within the calculation to this particular fixed order. Hence, only a finite set of operators $\{O_i = \Gamma^{(i)} \otimes \Gamma'^{(i)}\}$ needs to be considered at a fixed order. It is then possible to define *projectors* $\{P_j\}$ that, when applied to the amplitude

$$\mathcal{A} = \sum_i B_i \left(\bar{b} \Gamma^{(i)} s \right) \otimes \left(\bar{l} \Gamma'^{(i)} l \right), \quad (4.11)$$

“project” onto the Dirac structure O_j after taking the Dirac traces over the external fermion lines, i.e.

$$\text{Tr} [P_j \mathcal{A}] = B_j. \quad (4.12)$$

For our calculation at NLO in QCD, we consider Dirac structures with zero up to five γ matrices, plus optionally γ_5 on either of the two external fermion lines, yielding a total of 24 Dirac structures. The necessary projection “operators” can be composed from the same structures. They were calculated in Ref. [29] and we re-computed them for the calculations presented within this thesis. The complete evaluation of Dirac traces is performed using FORM.

After the application of projection operators the only step left is the actual integration over the loop momenta. For these tadpole integrals we use MATAD [60] procedures implemented in FORM. At one loop, all integrals can be simplified using partial fraction decomposition such that only integrals with a single denominator remain. The two-loop integrals with several massive lines are more complicated, however a procedure for this type of integrals exists as well, and we use a FORM implementation of the algorithm presented by Davydychev and Tausk in Ref. [61], see Ref. [62]. In Fig. 4.1, we summarise the stack of programs used for the semi-automated calculation as a diagram. Red boxes denote the different programs that were used, while blue ellipses indicate the various input and output files used at every step.

4.2. Computation of the Wilson coefficients in the Standard Model

In this section, we describe the computation of the Wilson coefficient C_A in the SM. Contributions from the other Wilson coefficients C'_A , $C_S^{(\prime)}$, and $C_P^{(\prime)}$ are suppressed by mass factors of $\mathcal{O}\left(\frac{M_{B_s}^2}{M_W^2}\right)$ compared to C_A , or even stronger. Throughout the thesis, all Wilson coefficients are

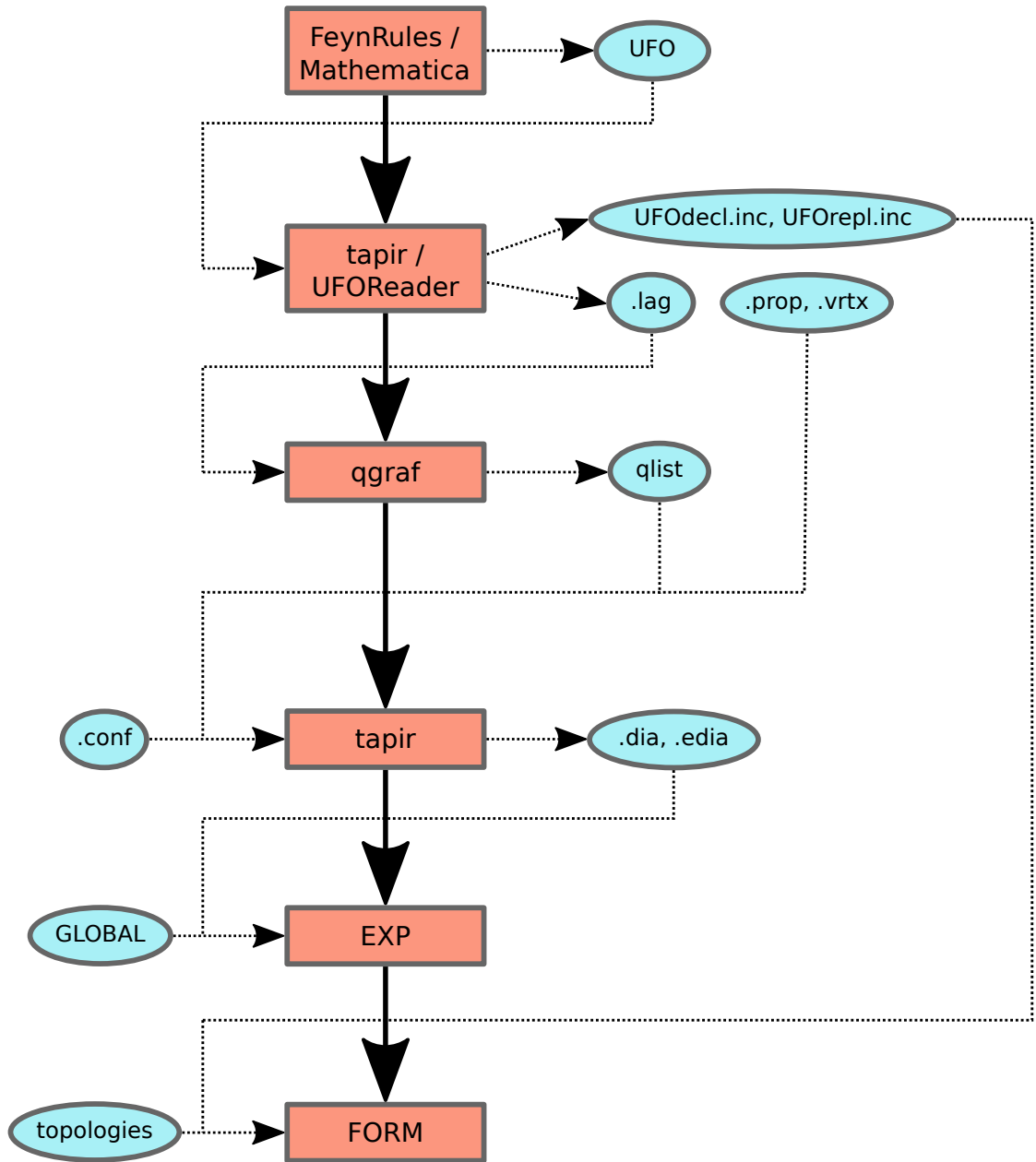


Figure 4.1.: Program chain used for the semi-automated calculation of the Wilson coefficients. The red boxes show the programs that were used, while the blue blobs list the input (left) and output (right) files.

decomposed into powers of α_s (i.e. the number of loops) as

$$C_i = \sum_{n=0}^{\infty} \left(\frac{\alpha_s}{4\pi} \right)^n C_i^{(n)}. \quad (4.13)$$

The SM contributions to C_A are commonly divided into two classes, *box* diagrams with W^\pm exchanges and *penguin* diagrams with a charged W boson in the loop and a neutral Z boson connecting to the lepton line. Technically, there are also diagrams involving a *flavour-changing self-energy* diagram (two-point function) on the quark line connected to a tree-level Z boson exchange, but these diagrams are usually not discussed as a separate class; they are rather implicitly included when Z -penguin diagrams are discussed in the literature. We will, however, always treat the self-energy diagrams as a separate class, since these diagrams play a special role in the variant of the 2HDM considered within this thesis. Some sample Feynman diagrams at LO and NLO in QCD are shown in Fig. 4.2. The Wilson coefficient $C_{A,\text{SM}}$ was first calculated at LO and NLO in QCD in Ref. [63] and Refs. [64–67], respectively. Furthermore, three-loop NNLO QCD corrections have been calculated in 2013 in Ref. [68], while two-loop NLO EW corrections were provided around the same time with Ref. [27]. A combined analysis including NNLO QCD as well as NLO EW corrections was presented in Ref. [31]. Finally, in Refs. [69, 70] enhanced electromagnetic corrections were presented.

4.2.1. Box diagrams

We first discuss the box diagrams. All box diagrams contain an internal muon neutrino and an up-type quark (up, charm, or top) as well as two gauge bosons, either W^\pm or the corresponding charged Goldstone bosons G^\pm . Diagrams with a Goldstone boson coupling to muons are suppressed by factors of m_μ/M_W compared to the leading terms of C_A , and we neglect all of these diagrams within the SM calculation such that only diagrams with two W bosons need to be calculated. Treating the massive W -boson propagators as two separate propagating particles, we are then left with $3 \cdot 2^2 = 12$ diagrams at leading order, where the 3 originates from the sum over internal up-type quarks. In this calculation as well as in all subsequent calculations we will always set $m_u = m_c = 0$, since the up-type quark masses of the first and second generations in the loop are heavily suppressed compared to M_W and m_t . Due to the unitarity of the CKM matrix this implies that after summing all internal up-type quarks, only contributions proportional to powers of m_t and the CKM factor $V_{ts}V_{tb}^*$ remain. Furthermore, the masses m_b , m_q , and m_l are also negligible compared to M_W . Hence, in all calculations presented within this thesis we set the external quark and lepton masses zero in the fermion propagators, such that factors of $m_{b,q,l}$ only appear through Yukawa couplings. This has the practical effect that QCD corrections in the effective vertex are represented by scaleless integrals, which identically vanish.

The contribution of the box diagrams to the Wilson coefficient C_A is finite, but depends on the gauge parameter ξ_W of the W boson. At LO, the box diagrams contribute

$$\begin{aligned} C_{A,\text{SM-box}}^{(0)} &= \frac{x_t (\xi_W^2 (x_t^2 - 8x_t + 4) + 6\xi_W x_t^2 - 3x_t^2) \log(x_t)}{16(x_t - 1)^2 (\xi_W - x_t)^2} \\ &\quad - \frac{\xi_W x_t (\xi_W^2 - 7\xi_W + 6x_t) \log(\xi_W)}{16(\xi_W - 1)(\xi_W - x_t)^2} + \frac{x_t (\xi_W (x_t + 2) - 3x_t)}{16(x_t - 1)(\xi_W - x_t)} \end{aligned} \quad (4.14)$$

4. $B_q \rightarrow l^+l^-$ in the two-Higgs-doublet model of type II

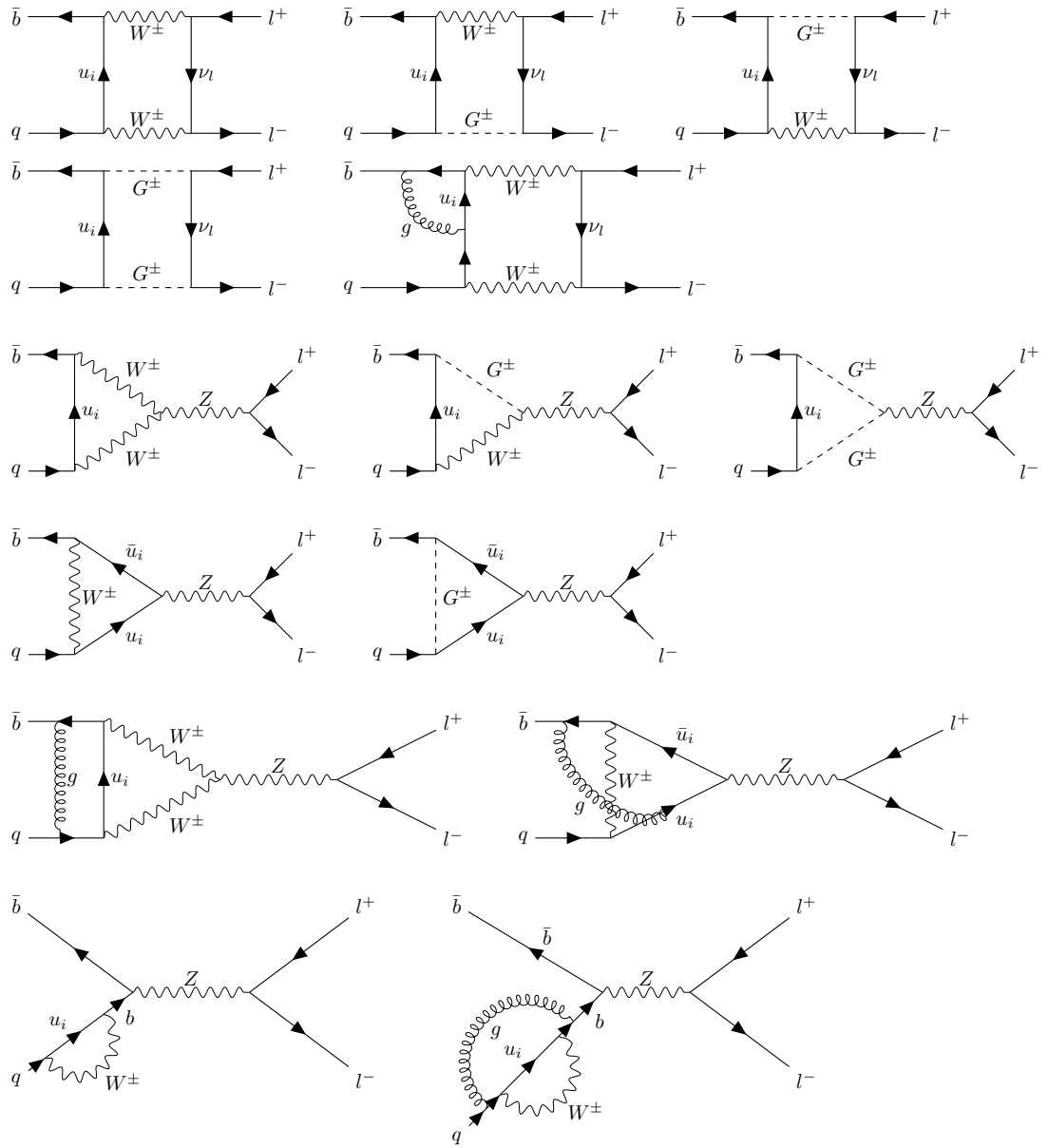


Figure 4.2.: Sample Feynman diagrams contributing in the SM at leading order (LO) and next-to-leading order (NLO) in QCD. The first and second row show box diagrams, the third, fourth, and fifth rows show Z-penguin diagrams, whereas the self-energy diagrams at LO and NLO are depicted in the last row.

to C_A . The dimensionless mass ratio x_t is defined as

$$x_t \equiv \frac{m_t^2}{M_W^2}. \quad (4.15)$$

However, the one-loop amplitude also has terms proportional to the *evanescent operator*

$$E_A = (\bar{b}\gamma_\mu\gamma_\nu\gamma_\sigma P_L s) \otimes (\bar{l}\gamma^\sigma\gamma^\nu\gamma^\mu\gamma_5 l) - 4Q_A. \quad (4.16)$$

This operator identically vanishes in $d = 4$ dimensions, which can be seen using Eq. (4.9). In $d = 4 - 2\epsilon$ dimensions, this operator is proportional to ϵ . It therefore does not contribute to $C_{A,\text{SM-box}}^{(0)}$, but needs to be taken into account during the calculation of the next-to-leading order coefficient, since one-loop gluon corrections to this operator can be proportional to Q_A again. Indeed, they contribute a finite term to $C_{A,\text{SM-box}}^{(1)}$ if the ϵ -proportional operator encounters a $1/\epsilon$ pole from the gluon loop integral. The Wilson coefficient C_{E_A} is given by

$$C_{E_A}^{(0)} = \frac{x_t}{16(x_t - 1)} - \frac{x_t \log(x_t)}{16(x_t - 1)^2}. \quad (4.17)$$

It is independent of ξ_W since it originates from the $g^{\mu\nu}$ terms of the W -boson propagator. In the calculation of QCD corrections to the leptonic $B_q \rightarrow l^+ l^-$ decay, a maximum of three Dirac γ matrices can occur on the leptonic spin line. The quark spin line can have arbitrarily many γ matrices, depending on the number of gluons. However, since at most three Lorentz indices can be left open to be contracted with the lepton line, all structures at higher loop orders can be written as $f(d)\gamma_\mu\gamma_\nu\gamma_\rho P_L \otimes \gamma^\rho\gamma^\nu\gamma^\mu P_L$, where $f(d)$ is some function of the space-time dimension, and thus no further evanescent operators involving more Dirac matrices need to be introduced. At LO in the EW expansion this holds to all orders in QCD.

4.2.2. Z -penguin diagrams

The second class of SM Feynman diagrams contributing to $B_q \rightarrow l^+ l^-$ are the Z -penguin diagrams, some examples of which are shown in the third to fifth rows of Fig. 4.2. In these diagrams, either one up-type quark and two W^\pm or charged Goldstone bosons, or two up-type quarks and one W^\pm or charged Goldstone boson propagate. In principle, since the Z boson couples to both left-handed and right-handed particles, the amplitude could be proportional to some linear combination of $(\bar{b}\gamma_\mu P_L q) \otimes (\bar{l}\gamma^\mu\gamma_5 l)$ and $(\bar{b}\gamma_\mu P_R q) \otimes (\bar{l}\gamma^\mu\gamma_5 l)$. However, since we neglect the external masses m_b and m_q and the corresponding SM Yukawa couplings originating from the interactions of right-handed down-type quarks with the charged Goldstone bosons, the effective $\bar{b}qZ$ vertex is purely left-handed even for the diagrams involving Goldstone bosons and there is no contribution to $(\bar{b}\gamma_\mu P_R q) \otimes (\bar{l}\gamma^\mu\gamma_5 l)$. The contribution of Z -penguin diagrams to the Wilson coefficient C_A can be determined in two slightly different ways. In the first approach one computes the effective $|\Delta B| = 1$ vertex $\bar{b}qZ$, i.e. the 1LPI part of the complete Z -penguin diagrams, by matching between full amplitudes and amplitudes in the effective theory. This effective vertex is then attached to a Z coupled to the leptons. In the second approach one avoids this intermediate step of matching to an effective Z vertex and one rather calculates

the four-particle $\bar{b}ql^+l^-$ vertex directly by computing the complete amplitudes in the full and effective theories. We follow this second approach here.

It is worth noting that technically we again split the massive W^\pm and Z gauge bosons into two components $W_{T/L}^\pm$ and $Z_{T/L}$, respectively, leading to much simpler propagator denominators at the expense of a larger number of diagrams. Diagrams with a ‘‘longitudinal’’ Z boson vanish since the Z -boson carries no momentum in our matching calculation, and so do the terms proportional to $k^\mu k^\nu$ in the ‘‘transversal’’ Z boson. Furthermore, diagrams with a neutral Goldstone boson instead of the Z boson do not contribute to C_A in the SM since they are proportional to $m_l = 0$. Hence, $C_{A,SM-Z}$ is manifestly independent of the Z -boson gauge parameter ξ_Z . The result, however, still depends on the gauge parameter ξ_W of the W boson in the loop. Furthermore, the one-loop LO contribution arising from Z -penguin diagrams is $1/\epsilon$ -divergent, even after the sum over all internal up-type quark flavours has been performed. It is given by

$$\begin{aligned}
 C_{A,SM-Z}^{(0)} = & \frac{(2s_{\theta_w}^2 - 3)x_t}{48\epsilon} + \frac{1}{48} (2s_{\theta_w}^2 - 3)x_t \log\left(\frac{\mu^2}{m_t^2}\right) \\
 & + \frac{x_t \log(x_t)}{48(x_t - 1)^2(\xi_W - x_t)^2} \left[\left(\xi_W^2 (2s_{\theta_w}^2 (4x_t^2 - 8x_t + 1) - 9x_t^2 + 18x_t + 9) \right. \right. \\
 & \quad \left. \left. - 2\xi_W x_t (s_{\theta_w}^2 (4x_t^2 - 8x_t - 2) - 6x_t^2 + 21x_t + 3) + 6x_t^2 (3x_t - s_{\theta_w}^2) \right) \right] \\
 & + \frac{\xi_W x_t \log(\xi_W) \left((9 - 8s_{\theta_w}^2) \xi_W^2 + \xi_W (8s_{\theta_w}^2 (x_t + 1) - 12x_t + 9) - 2(4s_{\theta_w}^2 + 3)x_t \right)}{48(\xi_W - 1)(\xi_W - x_t)^2} \\
 & + \frac{x_t \left(\xi_W (2s_{\theta_w}^2 (x_t + 1) + 3(x_t - 5)) - x_t (2s_{\theta_w}^2 (x_t + 1) + x_t - 13) \right)}{32(x_t - 1)(\xi_W - x_t)} \quad (4.18)
 \end{aligned}$$

where $s_{\theta_w} = \sin \theta_w$ is the weak mixing angle originating from the non-alignment of the Z boson with the neutral W^3 field in the unbroken $SU(2)_L$ symmetry.

4.2.3. Self-energy diagrams

As a leading-order effect, the one-loop electroweak Feynman diagrams contributing to $C_A^{(0)}$ in the SM must conspire to yield a finite and gauge-invariant result. The $1/\epsilon$ divergence from the Z -penguin diagrams can obviously not be cancelled by the W box diagrams since the sum of the latter is finite. Furthermore, the sum of box and penguin diagrams is not independent of ξ_W . The diagrams of the third class, the self-energy diagrams depicted in the last row of Fig. 4.2, cancel both the infinities and the residual gauge dependence. These diagrams arise since the $q \rightarrow \bar{b}$ flavour change can also occur via a two-point function, i.e. a flavour-changing self-energy diagram. Attaching such a self-energy diagram to a $\bar{b}bZ$ or $\bar{q}qZ$ tree-level diagram will yield a contribution to the effective $\bar{b}qZ$ vertex—or correspondingly the Z -mediated $\bar{b}ql^+l^-$ interaction. A generic self-energy amplitude can be decomposed as

$$q \xrightarrow{\quad} \text{[Self-energy loop]} \longrightarrow b = \Sigma_{LL} P_R q + \Sigma_{RR} P_L q + \Sigma_{LR} P_R + \Sigma_{RL} P_L, \quad (4.19)$$

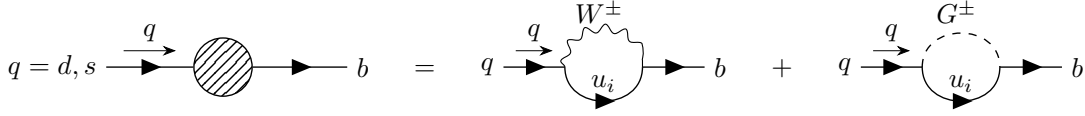


Figure 4.3.: One-loop flavour-changing ‘self-energy’ diagrams in the SM. The index i denotes the three different up-type quarks u, c, t , while the arrow with q shows the direction of the external momentum.

where q above the arrow denotes the external momentum. In the SM, these flavour-changing two-point functions are given by the diagrams shown in Fig. 4.3. Diagrams with W^\pm exchange contribute only to Σ_{LL} due to the left-handedness of the W -boson coupling, whereas the diagrams with G^\pm contribute to all four Dirac structures. The SM contributions are given at LO by

$$\Sigma_{LL,SM}^{(0)} = \frac{G_F M_W^2 V_{tb}^* V_{tq} x_t}{8\pi^2 \sqrt{2}} \left[-\frac{1}{\epsilon} - \log\left(\frac{\mu^2}{m_t^2}\right) - \frac{(4\xi_W x_t^2 - 8\xi_W x_t + \xi_W + 3x_t) \log(x_t)}{(x_t - 1)^2 (\xi_W - x_t)} + \frac{4\xi_W \log(\xi_W)}{\xi_W - x_t} + \frac{3x_t + 3}{2 - 2x_t} \right], \quad (4.20)$$

$$\Sigma_{RR,SM}^{(0)} = \frac{G_F V_{tb}^* V_{tq} m_b m_q x_t}{8\pi^2 \sqrt{2}} \left[\frac{1}{\xi_W - x_t} - \frac{x_t \log(\xi_W)}{(\xi_W - x_t)^2} + \frac{x_t \log(x_t)}{(\xi_W - x_t)^2} \right], \quad (4.21)$$

$$\Sigma_{RL,SM}^{(0)} = \frac{G_F M_W^2 V_{tb}^* V_{tq} m_b x_t}{4\pi^2 \sqrt{2}} \left[-\frac{1}{\epsilon} - \log\left(\frac{\mu^2}{m_t^2}\right) + \frac{\xi_W \log(\xi_W)}{\xi_W - x_t} - \frac{\xi_W \log(x_t)}{\xi_W - x_t} - 1 \right], \quad (4.22)$$

$$\Sigma_{LR,SM}^{(0)} = \frac{m_q}{m_b} \Sigma_{LR,SM}. \quad (4.23)$$

For the calculation of C_A in the SM only Σ_{LL} is needed, since all other Σ_{ij} involve at least one right-handed external quark, and thus are irrelevant for C_A . However, for the calculation of Wilson coefficients involving additional Higgs bosons, self-energy contributions from the structures Σ_{RR} , Σ_{RL} , and Σ_{LR} must also be taken into account. The flavour-changing two-point functions must be attached to tree-level flavour-conserving diagrams with a Z boson in all possible ways, see Fig. 4.4. Due to the internal quark propagator and the Dirac structure of the two-point function involving the external momentum q^μ , this class of diagrams cannot be computed with a priori vanishing external momenta, but we expand them to linear order in the external momentum instead. The internal light-quark propagator can be treated as $\frac{1}{\not{q}}$, neglecting the masses m_q and m_b , but with an additional factor of $\frac{1}{2}$.³ The resulting one-light-particle-reducible (1LPR) diagrams yield a contribution

$$C_{A,SM,2}^{(0)} = -\frac{1}{N} \frac{G_F}{3\sqrt{2}} \left(3 - 2s_{\theta_w}^2 \right) \Sigma_{LL,SM}^{(0)} \quad (4.24)$$

to the SM Wilson coefficient. After connecting the self-energy diagram with the tree-level diagram, the limit $q^\mu \rightarrow 0$ is finite and can be taken. The sum of box, Z -penguin, and self-energy

³The treatment of the propagator as $1/\not{q}$ is somewhat of a ‘shortcut’. In the discussion of self-energy contributions to the diagrams with charged Higgs bosons more attention is paid to the treatment of the external quark momenta. There, no factor of $1/2$ has to be introduced.

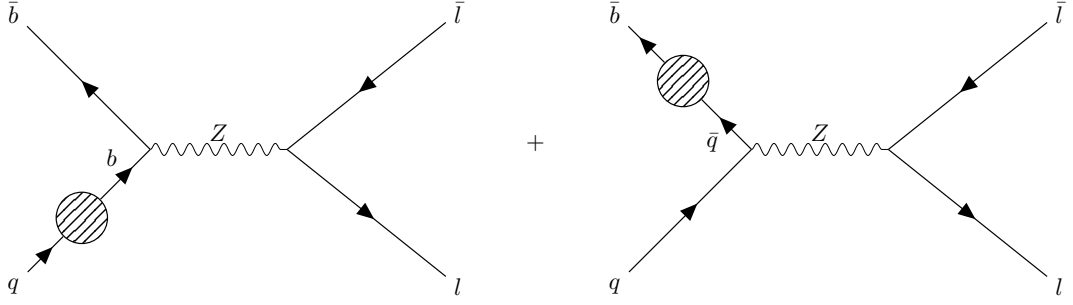


Figure 4.4.: Insertions of the flavour-changing two-point functions into flavour-conserving tree-level diagrams with Z bosons. The blob represents the insertion of $\Sigma_{LL,SM}$, since $\Sigma_{RR,SM}$, $\Sigma_{LR,SM}$, and $\Sigma_{RL,SM}$ can be neglected within the SM.

Wilson coefficients reads

$$C_{A,SM}^{(0)} = \frac{x_t}{8} \left[\frac{x_t - 4}{x_t - 1} + \frac{3x_t \log(x_t)}{(x_t - 1)^2} \right], \quad (4.25)$$

and is manifestly finite and independent of ξ_W . It is also intriguing to observe that s_{θ_w} does not occur in the final Wilson coefficient, despite being present in the 1LPI Z -penguin diagrams.

4.2.4. Next-to-leading order QCD corrections

For the cancellation of the electroweak gauge dependence it is crucial that W -box diagrams, Z -penguin diagrams, and the 1LPR diagrams involving flavour-changing self-energies are taken into account. Only their sum is gauge-independent. However, QCD corrections do not affect this structural behaviour of the electroweak gauge dependence, and hence the calculation of the two-loop $\mathcal{O}(\alpha_s)$ contributions to the Wilson coefficients can be performed in an arbitrary R_{ξ_W} gauge. We use the *Feynman-'t Hooft gauge*, $\xi_W = 1$, in order to obtain the NLO Wilson coefficients. For the gluon propagator a general gauge parameter ξ_g was used, and the cancellation of ξ_g in all physical results was verified.

After summing all W -box diagrams with a gluon exchange, a $1/\epsilon$ UV pole from the region of large loop momenta remains in the bare amplitudes. This pole is removed in the usual way by shifting all bare, i.e. Lagrangian, parameters towards physical *renormalised* parameters in the bare amplitudes of lower order in QCD. The shift, known as the renormalisation procedure, introduces $\frac{\alpha_s}{\epsilon}$ counterterms to the bare parameters, which remove the divergences occurring in the two-loop bare amplitude. Apart from the divergent term there are, however, multiple possible definitions of the counterterm which differ by finite terms. These possible definitions are known as different *renormalisation schemes*. A common choice is the minimal subtraction (MS) scheme, in which only the UV pole is subtracted. This still leaves factors of $(4\pi e^{-\gamma_E})$ from the ϵ -expansion of the loop integrals in the amplitude, where

$$\gamma_E = \lim_{n \rightarrow \infty} \left(-\log(n) + \sum_{k=1}^n \frac{1}{k} \right) \approx 0.57722 \dots \quad (4.26)$$

is the *Euler-Mascheroni constant*. Therefore, we use the more convenient modified minimal subtraction ($\overline{\text{MS}}$) renormalisation scheme in which also the factors $\log(4\pi) \gamma_E$ are subtracted. The LO one-loop bare amplitude contains the parameters m_t and the quark-spinor wave functions \bar{v}_b, u_q , which receive counterterms from the QCD renormalisation constants. Following this procedure, one would find that after renormalising the top-quark mass and the external quark wave functions the full SM amplitude is divergent. The bare amplitude in the effective theory must also be renormalised. Since the top-quark is integrated out, only the wave function renormalisation of the effective one-loop amplitude remains, which leads to identical divergences in the amplitude, and only in the matching process would the divergences cancel, yielding a finite Wilson coefficient. However, since the wave-function renormalisation in the full theory and the effective theory is identical at $\mathcal{O}(\alpha_s)$,

$$Z_\psi^{\text{SM}} - Z_\psi^{\text{eff}} = 0 + \mathcal{O}(\alpha_s^2), \quad (4.27)$$

one can omit it on both sides of the matching equation. Thus, at NLO, only m_t needs to be renormalised in order to compute the Wilson coefficient. At $\mathcal{O}(\alpha_s^2)$ (NNLO), in Z_ψ the difference arises due to corrections to the quark propagators by loops with internal top quarks, which can only appear in the full theory. The quark mass renormalisation constant in the $\overline{\text{MS}}$ scheme is given by

$$Z_{m_q} = 1 - \frac{\alpha_s}{\pi\epsilon} + \mathcal{O}(\alpha_s^2) \equiv Z_m. \quad (4.28)$$

for all different quark flavours. Here, $1/\epsilon$ is to be read as $1/\epsilon - \gamma_E + \log(4\pi)$.

Finally, infrared (IR) divergences are also regularised in dimensional regularisation, and we generally do not distinguish UV from IR divergences. The matching therefore has to be performed in $d \neq 4$ dimensions. As a consequence, the Wilson coefficient of the evanescent operator introduced in Eq. (4.16) yields a finite contribution $-Z_{EQ} C_{EA}^{(0)}$ to the $\mathcal{O}(\alpha_s)$ coefficient of the physical operator Q_A [66, 67]. The renormalisation constant [67]

$$Z_{EQ} = \frac{\alpha_s}{4\pi} \cdot 32 + \mathcal{O}(\alpha_s^2) \quad (4.29)$$

characterises the mixing of the evanescent operator into the physical operator under renormalisation. In general, the operator renormalisation constant Z_{QQ} also contributes to the renormalisation of the two-loop Wilson coefficient. However, since for vanishing quark masses the quark current in Q_A is conserved [67], the renormalisation constant Z_{QQ} of the operator Q_A and its right-handed counterpart Q'_A is given by $Z_{QQ} = 1$ to all orders in QCD and the operator Q_A does not have to be renormalised.

The $\mathcal{O}(\alpha_s)$ Wilson coefficient is given (in the $\xi_W = 1$ gauge) by

$$C_{A,\text{SM-box}}^{(1)} = \left(\frac{2x_t(x_t+1)\log(x_t)}{(x_t-1)^3} - \frac{4x_t}{(x_t-1)^2} \right) \log\left(\frac{\mu^2}{m_t^2}\right) + \frac{2x_t \text{Li}_2\left(1 - \frac{1}{x_t}\right)}{(x_t-1)^2} + \frac{x_t(3x_t-19)}{3(x_t-1)^2} - \frac{(x_t-17)x_t \log(x_t)}{3(x_t-1)^3}, \quad (4.30)$$

with the *dilogarithm*

$$\text{Li}_2(1-z) = \int_1^z \frac{\log t}{1-t} dt. \quad (4.31)$$

In order to determine the two-loop coefficient $C_{A,SM-Z}^{(1)}$, the top-quark mass in the LO coefficient must again be renormalised by $m_t^{(0)} \rightarrow Z_{m_t} m_t^{(r)}$. For the sake of brevity, in the coefficient $C_{A,SM-Z}^{(1)}$ listed below, we do not list the contributions originating from the self-energy 1LPR diagrams separately, but include them already in the discussion of the Z -penguin contribution. The evanescent operator E_A does not contribute to penguin diagrams. At two-loop, the Wilson coefficient is given in electroweak Feynman-'t Hooft gauge by

$$C_{A,SM-Z+2}^{(1)} = \frac{x_t (4x_t^2 + 7x_t + 29)}{3(x_t - 1)^2} - \frac{x_t (3x_t^2 + 14x_t + 23) \log(x_t)}{3(x_t - 1)^3} - \frac{x_t (x_t^2 + 4) \text{Li}_2\left(1 - \frac{1}{x_t}\right)}{(x_t - 1)^2} + \left(\frac{x_t (x_t^2 + x_t + 8)}{(x_t - 1)^2} - \frac{2x_t (4x_t + 1) \log(x_t)}{(x_t - 1)^3} \right) \log\left(\frac{\mu^2}{m_t^2}\right). \quad (4.32)$$

It is worth emphasising that—as in the LO case—neither $C_{A,SM\text{-box}}^{(1)}$ nor $C_{A,SM-Z+2}^{(1)}$ are individually gauge independent, only their sum is. The residual dependence of $C_{A,SM}$ on the renormalisation scale μ of QCD is shown at the end of the chapter in Fig. 4.9 together with the μ -dependence of the additional Wilson coefficients present in the type-II 2HDM, which will be discussed next.

4.3. Wilson coefficients in the Two-Higgs-Doublet Model of type II

In the presence of the additional charged and neutral Higgs bosons, corrections to the SM Wilson coefficient C_A as well as entirely new contributions to the other coefficients C'_A , $C_{S,P}^{(\prime)}$ arise. We will discuss them separately. These coefficients have so far been computed at LO, NLO, and even NNLO QCD in Refs. [29, 71–73].

4.3.1. Contributions to C_A and C'_A

Box diagrams with two charged H^\pm bosons yield a contribution to C_A and C'_A , see Fig. 4.5. In the power counting of $\tan \beta$, the leading contribution to C'_A is parametrically suppressed by $\frac{m_b m_q m_\mu^2 \tan^4 \beta}{m_t^2 M_W^2}$ compared to $C_{A,SM}$. It is given at LO by

$$C_{A,H\text{-box}}^{(\prime,0)} = -\frac{m_b m_\mu^2 m_q r_H^2 (\tan \beta)^4}{16M_W^4 (r_H - 1)^2 x_t} \cdot (r_H - \log(r_H) - 1), \quad (4.33)$$

where we have defined the dimensionless mass ratio

$$r_H \equiv \frac{m_t^2}{M_{H^\pm}^2}. \quad (4.34)$$

Furthermore, if the charged Higgs bosons couple to the internal up-type quarks instead of the external down-type quarks, a contribution to C_A arises from diagrams with two charged Higgs bosons. As a consequence, the $\tan^2 \beta$ enhancement from the muon couplings is cancelled by a factor $\cot^2 \beta$ of the up-type quark couplings, and the resulting contribution to C_A is given by

$$C_{A,H\text{-box}}^{(0)} = \frac{m_\mu^2 r_H}{16M_W^2 (r_H - 1)^2} \cdot (-r_H + r_H \log(r_H) + 1). \quad (4.35)$$

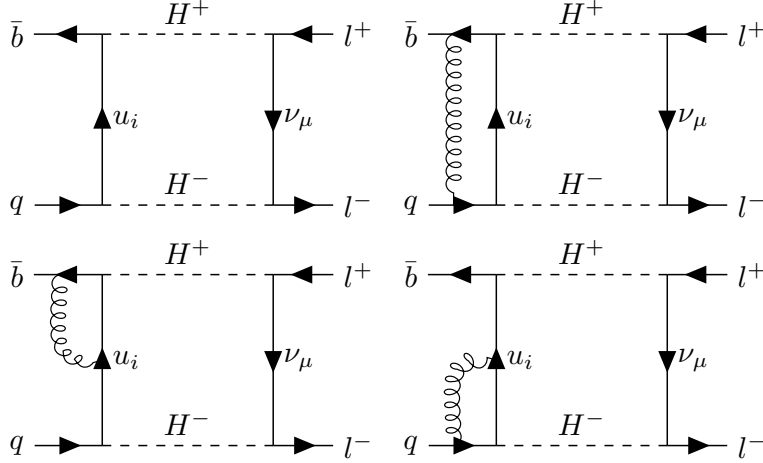


Figure 4.5.: Example box diagrams with two H^\pm bosons contributing to C'_A and C_A at LO and NLO in QCD.

However, it should be noted that contributions proportional to $m_\mu^2 \tan^0 \beta$ can also originate from the neglected $G^\pm - G^\mp$ diagrams in the SM, as well as from the mixed $H^\pm - G^\mp$ diagrams. Furthermore, the mixed box diagrams can also contribute a term of $\mathcal{O}\left(\frac{m_b m_q m_\mu^2 \tan^2 \beta}{M_W^4}\right)$ to C'_A . All of these contributions involving Goldstone bosons are gauge dependent and since all contributions from $H^\pm - H^\mp$, $H^\pm - G^\mp$, and $G^\pm - G^\mp$ box diagrams are proportional to m_μ^2 and therefore strongly suppressed, we neglect all terms of order $\mathcal{O}(\tan^2 \beta)$ or lower, such that only Eq. (4.33) remains.

In order to compute the NLO coefficient $C'_{A,H\text{-box}}{}^{(1)}$, the one-loop coefficient $C'_{A,H\text{-box}}{}^{(0)}$ must be renormalised. In general, the coefficients C'_i receive the same QCD renormalisation as C_i , since QCD is a non-chiral theory. Contrary to the SM Wilson coefficient, $C'_{A,H\text{-box}}$ depends on light-quark masses as well, which also need to be renormalised by $m_b^{(0)} \rightarrow Z_m m_b^{(r)}$, $m_q^{(0)} \rightarrow Z_m m_q^{(r)}$ in addition to the top-quark mass. The renormalised $\mathcal{O}(\alpha_s)$ coefficient is given by

$$C'_{A,H\text{-box}}{}^{(1)} = \frac{m_b m_q m_\mu^2 \tan^4 \beta}{M_W^2 m_t^2} \left[\left(-\frac{(r_H - 3)r_H^2}{2(r_H - 1)^2} - \frac{r_H^2 \log(r_H)}{(r_H - 1)^3} \right) \log\left(\frac{\mu^2}{m_t^2}\right) - \frac{(r_H^2 - 2r_H + 2) r_H^2 \text{Li}_2\left(\frac{r_H - 1}{r_H}\right)}{2(r_H - 1)^2} + \frac{(\pi^2 (r_H - 1)^2 - 11r_H + 27) r_H^2}{12(r_H - 1)^2} - \frac{(12r_H^2 - 33r_H + 37) r_H^2 \log(r_H)}{12(r_H - 1)^3} \right]. \quad (4.36)$$

Due to the suppression by m_μ^2/m_t^2 the coefficient $C'_{A,H\text{-box}}$ is extremely suppressed by a factor of about $10^{-4} - 10^{-3}$ compared to the $\mathcal{O}(1)$ coefficient $C_{A,\text{SM}}$, even for $q = s$ and large values of $\tan \beta$. For example, in order to achieve an $\mathcal{O}(10\%)$ correction to the SM Wilson coefficient, the parameter $\tan \beta$ would be required to be $\gtrsim 240$, which is far outside the domain of perturbative Yukawa couplings.

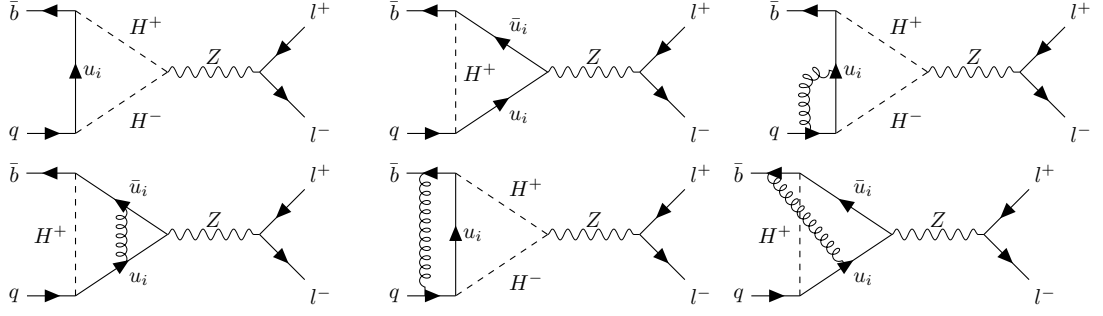


Figure 4.6.: Example Z-penguin diagrams with a charged Higgs bosons in the loop, at LO and NLO. These diagrams contribute to C_A and C'_A .

The second class of diagrams that contribute to C'_A are—as in the SM—the Z-penguin diagrams, but with charged Higgs bosons in the loop. Example diagrams are shown in Fig. 4.6. The 1LPI penguin diagrams can be computed in the same way as in the SM. The amplitude can be written in the form

$$\mathcal{A}_{1\text{PI}} \sim \frac{m_b m_q \tan^2 \beta}{M_W^2} C'_{A,HZ,1\text{PI}} + \frac{m_t^2}{M_W^2 \tan^2 \beta} C_{A,HZ,1\text{PI}}. \quad (4.37)$$

Both parts of the amplitude are trivially independent of ξ_W since the 2HDM does not feature $H^\pm - W^\mp - Z$ or $H^\pm - G^\mp - Z$ vertices. However, $C_{A,HZ,1\text{PI}}^{(0)}$ has a $1/\epsilon$ UV pole which needs to be cancelled by a self-energy diagram involving H^\pm , similar to the SM case. Here, the self-energy diagram is given at one-loop by

$$q \rightarrow \text{loop}(u_i, H^\pm) \rightarrow b = \Sigma_{LL,H} P_R q + \Sigma_{RR,H} P_L q + \Sigma_{LR,H} P_R + \Sigma_{RL,H} P_L, \quad (4.38)$$

with

$$\Sigma_{LL,H}^{(0)} = \frac{G_F M_W^2 V_{tb}^* V_{tq} x_t}{8\sqrt{2}\pi^2 \tan^2 \beta} \left[-\frac{1}{\epsilon} - \log\left(\frac{\mu^2}{m_t^2}\right) + \frac{1-3r_H}{2(r_H-1)} + \frac{(2r_H-1)\log(r_H)}{(r_H-1)^2} \right], \quad (4.39)$$

$$\Sigma_{RR,H}^{(0)} = \frac{G_F V_{tb}^* V_{tq} m_b m_q \tan^2 \beta r_H}{8\sqrt{2}\pi^2} \left[\frac{1}{1-r_H} + \frac{r_H \log(r_H)}{(r_H-1)^2} \right], \quad (4.40)$$

$$\Sigma_{RL,H}^{(0)} = \frac{G_F M_W^2 V_{tb}^* V_{tq} m_b x_t}{4\sqrt{2}\pi^2} \left[\frac{1}{\epsilon} + \log\left(\frac{\mu^2}{m_t^2}\right) + \frac{\log(r_H)}{1-r_H} + 1 \right], \quad (4.41)$$

$$\Sigma_{LR,H}^{(0)} = \frac{m_q}{m_b} \Sigma_{RL,H}. \quad (4.42)$$

Since the Wilson coefficient $C'_{A,HZ,1\text{PI}}$ carries a prefactor proportional to the light external quark masses, we need to keep $\Sigma_{RR,H}$, $\Sigma_{RL,H}$, $\Sigma_{LR,H}$ in addition to $\Sigma_{LL,H}$. As in the SM, the self-energy has to be combined in all possible ways with the tree-level Z-boson diagrams. The same two

diagrams as in Fig. 4.4 arise, where this time in principle all four terms of the H^\pm -self-energy diagram need to be considered. Here, contrary to the shortcut taken in the presentation of the SM self-energy diagrams, one should work with two different external momenta q_q^μ and q_b^μ for the internal quark propagator connecting the self-energy and the tree-level diagram. The insertion of $\Sigma_{LL,H}$ into the two diagrams of Fig. 4.4 gives

$$\begin{aligned} \mathcal{A}_{A,ZH,2}^{(0)} \Big|_{LL} &= -\Sigma_{LL,H} P_R \not{q}_q \frac{i(\not{q}_q + m_q)}{q_q^2 - m_q^2} \frac{ig_2}{c_{\theta_w}} \gamma_\mu \left[\left(-\frac{1}{2} + \frac{1}{3}s_{\theta_w}^2 \right) P_L + \frac{1}{3}s_{\theta_w}^2 P_R \right] \frac{i}{M_Z^2} \\ &\quad \otimes \frac{ig_2}{c_{\theta_w}} \gamma^\mu \left[\frac{1}{4}\gamma_5 + \dots \right] \\ &\quad + \frac{ig_2}{c_{\theta_w}} \gamma_\mu \left[\left(-\frac{1}{2} + \frac{1}{3}s_{\theta_w}^2 \right) P_L + \frac{1}{3}s_{\theta_w}^2 P_R \right] \frac{i(\not{q}_b + m_b)}{q_b^2 - m_b^2} (-1) \Sigma_{LL,H} P_R \not{q}_b \frac{i}{M_Z^2} \\ &\quad \otimes \frac{ig_2}{c_{\theta_w}} \gamma^\mu \left[\frac{1}{4}\gamma_5 + \dots \right]. \end{aligned} \quad (4.43)$$

where $c_{\theta_w} = \sqrt{1 - s_{\theta_w}^2}$. It is important that the external particle of the self-energy diagram, i.e. the particle not connected to the tree-level diagram, is on-shell, that is

$$q_q^2 = m_q^2, \quad \bar{b} \not{q}_q = m_b \bar{b}, \quad q_b^2 = m_b^2, \quad \not{q}_b q = m_b q. \quad (4.44)$$

With this, the insertion of $\Sigma_{LL,H}$ into the two diagrams reduces to

$$\begin{aligned} \mathcal{A}_{A,HZ,2}^{(0)} \Big|_{LL} &= -\frac{g_2^2}{4M_W^2} \frac{\Sigma_{LL,H}}{m_b^2 - m_q^2} \left\{ (m_b^2 P_R + m_q m_b P_L) \gamma_\mu \left[\left(-\frac{1}{2} + \frac{1}{3}s_{\theta_w}^2 \right) P_L + \frac{1}{3}s_{\theta_w}^2 P_R \right] \right. \\ &\quad \left. - \gamma_\mu \left[\left(-\frac{1}{2} + \frac{1}{3}s_{\theta_w}^2 \right) P_L + \frac{1}{3}s_{\theta_w}^2 P_R \right] (m_q^2 P_L + m_b m_q P_R) \right\} \otimes \gamma^\mu \gamma_5 \\ &= \frac{\sqrt{2}G_F}{6} (3 - 2s_{\theta_w}^2) \Sigma_{LL,H} \gamma_\mu P_L \otimes \gamma^\mu \gamma_5, \end{aligned} \quad (4.45)$$

which yields a contribution

$$C_{A,HZ,2}^{(0)} = -\frac{G_F}{3\sqrt{2}} (3 - 2s_{\theta_w}^2) \Sigma_{LL,H}^{(0)}. \quad (4.46)$$

This result is of course the same as in the SM case, with $\Sigma_{LL,SM}$ replaced by $\Sigma_{LL,H}$, but here we have chosen a different momentum configuration. With $q_b^\mu \neq q_q^\mu$ it is evident that each insertion of the self-energies only contributes a factor of $m_b^2/(m_b^2 - m_q^2)$ and $-m_q^2/(m_b^2 - m_q^2)$, respectively, while in the previous calculation they each entered with ‘‘weight’’ 1 instead. This was corrected in Eq. (4.24) by the factor 1/2, but in this section it becomes clear that with distinct $q_b^\mu \neq q_q^\mu$ no ad-hoc factors need to be introduced.

The insertion of $\Sigma_{RR,H}$ can be calculated along the same lines:

$$\begin{aligned} \mathcal{A}_{A,HZ,2}^{(0)} \Big|_{RR} &= -\frac{g_2^2}{4M_W^2} \frac{\Sigma_{RR,H}}{m_b^2 - m_q^2} \gamma_\mu \left\{ (m_b^2 P_R + m_b m_q P_L) \left[\left(-\frac{1}{2} + \frac{1}{3} s_{\theta_w}^2 \right) P_L + \frac{1}{3} s_{\theta_w}^2 P_R \right] \right. \\ &\quad \left. - \left[\left(-\frac{1}{2} + \frac{1}{3} s_{\theta_w}^2 \right) P_L + \frac{1}{3} s_{\theta_w}^2 P_R \right] (m_q^2 P_R + m_b m_q P_L) \right\} \otimes \gamma^\mu \gamma_5 \\ &= -\frac{\sqrt{2} G_F}{3} s_{\theta_w}^2 \Sigma_{RR,H} \gamma_\mu P_R \otimes \gamma^\mu \gamma_5, \end{aligned} \quad (4.47)$$

and therefore

$$C'_{A,HZ,2}{}^{(0)} = \frac{\sqrt{2} G_F s_{\theta_w}^2}{3} \Sigma_{RR,H}^{(0)}. \quad (4.48)$$

Due to the projector structure, $\Sigma_{LL,H}$ contributes only to C_A , while $\Sigma_{RR,H}$ contributes only to C'_A . It is also worth mentioning that the final expressions are independent of the external momenta q_b^μ and q_q^μ , allowing to take the limit $q_b^\mu \rightarrow 0$, $q_q^\mu \rightarrow 0$ at this stage.

Finally, the insertions of $\Sigma_{LR,H}$ and $\Sigma_{RL,H}$ need to be discussed. With the same kinematics as before, one finds

$$\begin{aligned} \mathcal{A}_{A,HZ,2}^{(0)} \Big|_{LR} &= -\frac{g_2^2}{4M_W^2} \frac{\Sigma_{LR,H}}{m_b^2 - m_q^2} \gamma_\mu \left\{ \left[m_b \left(\frac{1}{3} s_{\theta_w}^2 \right) P_R + m_q \left(-\frac{1}{2} + \frac{1}{3} s_{\theta_w}^2 \right) P_L \right] \right. \\ &\quad \left. - \left[m_q \left(-\frac{1}{2} + \frac{1}{3} s_{\theta_w}^2 \right) P_L + m_b \left(\frac{1}{3} s_{\theta_w}^2 \right) P_R \right] \right\} \otimes \gamma^\mu \gamma_5 \\ &= 0, \end{aligned} \quad (4.49)$$

and, analogously, $\mathcal{A}_{A,HZ,2}^{(0)} \Big|_{RL} = 0$. Hence, $\Sigma_{LR,H}$ and $\Sigma_{RL,H}$ do not contribute to the Wilson coefficients of Z -penguin diagrams in general, since no assumptions about the structure of $\Sigma_{ij,H}$ and the second spin line (i.e. leptonic line) were made.

After adding the contributions from the 1LPR diagrams, the Wilson coefficients are given by

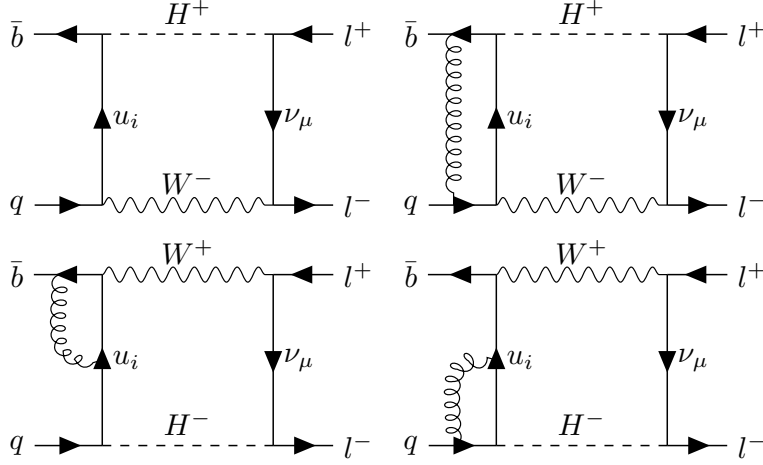
$$C'_{A,HZ}{}^{(0)} \equiv \frac{m_b m_q \tan^2 \beta}{M_W^2} \left(C'_{A,HZ,1PI}{}^{(0)} + C'_{A,HZ,2}{}^{(0)} \right) = \frac{m_b m_q \tan^2 \beta}{M_W^2} \left[\frac{r_H}{8 - 8r_H} + \frac{r_H \log(r_H)}{8(r_H - 1)^2} \right], \quad (4.50)$$

$$C_{A,HZ}{}^{(0)} \equiv \frac{m_t^2}{M_W^2 \tan^2 \beta} \left(C_{A,HZ,1PI}{}^{(0)} + C_{A,HZ,2}{}^{(0)} \right) = -\frac{m_t^2}{m_b m_q \tan^4 \beta} C'_{A,HZ}{}^{(0)}. \quad (4.51)$$

At order $\mathcal{O}(\alpha_s)$, after adding the contribution stemming from the renormalisation of all occurring quark masses in the LO result, the coefficients are given by

$$C'_{A,HZ}{}^{(1)} = \frac{m_b m_q \tan^2 \beta}{M_W^2} \left[\left(-\frac{(r_H - 3)r_H}{(r_H - 1)^2} - \frac{2r_H \log(r_H)}{(r_H - 1)^3} \right) \log \left(\frac{\mu^2}{m_t^2} \right) + \frac{(r_H - 2)r_H \text{Li}_2 \left(\frac{r_H - 1}{r_H} \right)}{(r_H - 1)^2} \right. \\ \left. - \frac{4(r_H - 3)r_H}{3(r_H - 1)^2} + \frac{(3r_H - 11)r_H \log(r_H)}{3(r_H - 1)^3} \right], \quad (4.52)$$

$$C_{A,HZ}{}^{(1)} = -\frac{m_t^2}{m_b m_q \tan^4 \beta} C'_{A,HZ}{}^{(1)}. \quad (4.53)$$


 Figure 4.7.: Mixed H^\pm - W^\mp box diagrams at LO and NLO in QCD.

In contrast to $C'_{A,H\text{-box}}$ the coefficients $C_{A,HZ}^{(\prime)}$ do not have an additional m_μ^2/m_t^2 suppression, and as a consequence can be sizeable. For example, for $\tan\beta = 50$ and $q = s$, $m_b m_s \tan^2\beta/M_W^2 \approx 0.2$. A further suppression is of course provided by the mass ratio r_H from the loop function, but a correction of a few percent is possible.

4.3.2. The Wilson coefficients $C_S^{(\prime)}$ and $C_P^{(\prime)}$

Finally, we discuss the scalar and pseudoscalar Wilson coefficients $C_S^{(\prime)}$ and $C_P^{(\prime)}$. They arise from three different classes of diagrams which we will discuss in the following.

Firstly, mixed H^\pm - W^\mp diagrams, shown in Fig. 4.7 contribute to $C_S^{(\prime)}$ and $C_P^{(\prime)}$. These contributions are finite at one-loop, but depend on ξ_W ; they are given by

$$C_{S,WH\text{-box}}^{(0)} = \frac{m_b m_\mu \tan^2\beta}{M_W^2} \left[\frac{r_H^2 \xi_W \log(r_H)}{4(r_H - 1)(r_H \xi_W - x_t)} - \frac{r_H \xi_W x_t \log(\xi_W)}{4(\xi_W - x_t)(r_H \xi_W - x_t)} + \frac{r_H \xi_W x_t \log(x_t)}{4(\xi_W - x_t)(r_H \xi_W - x_t)} \right] + \mathcal{O}(\tan\beta), \quad (4.54)$$

$$C'_{S,WH\text{-box}}^{(0)} = \frac{m_q}{m_b} C_{S,WH\text{-box}}^{(0)}, \quad (4.55)$$

$$C_{P,WH\text{-box}}^{(0)} = C_{S,WH\text{-box}}^{(0)}, \quad (4.56)$$

$$C'_{P,WH\text{-box}}^{(0)} = -C'_{S,WH\text{-box}}^{(0)}. \quad (4.57)$$

At NLO, the quark masses again need to be renormalised. In addition to their dependence on m_t , the Wilson coefficients $C_{S,P}^{(\prime)}$ are linear in the external quark masses. However, the hadronic matrix element of the current $\langle 0 | \bar{b} \gamma_5 q | B_q(p) \rangle$ is inversely proportional to the quark masses defined in the $n_f = 5$ effective theory, and thus the renormalisation of $m_{b,q}$ cancels in the product of Wilson coefficient and hadronic matrix element. It is then simpler to only renormalise m_t in

4. $B_q \rightarrow l^+ l^-$ in the two-Higgs-doublet model of type II

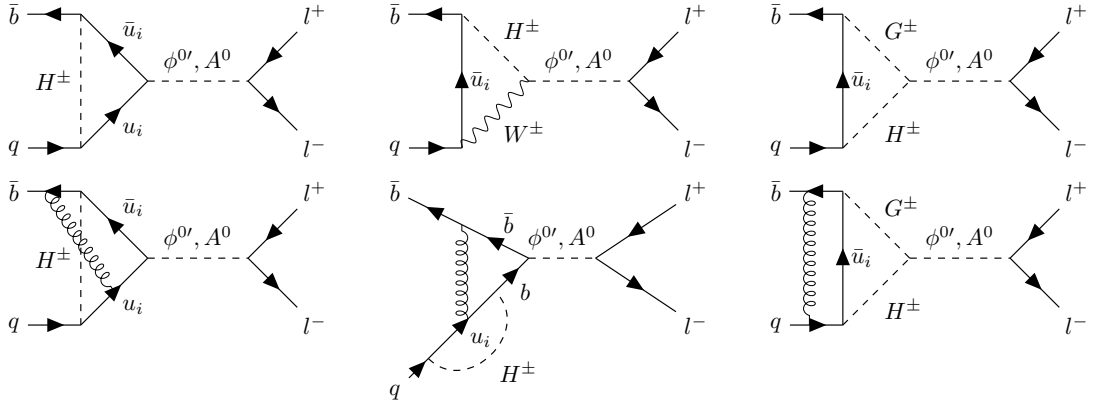


Figure 4.8.: Sample 1LPI Higgs-penguin diagrams at LO and NLO order in the 2HDM of type II.

the Wilson coefficients $C_{S,P}^{(\prime)}$, which yields a finite two-loop result. This statement holds up to $\mathcal{O}(\alpha_s)$, at NNLO an $\mathcal{O}(\alpha_s^2)$ difference arises between the quark mass renormalisation constants in the full theory and the ones in the effective theory, such that in this case it is necessary to renormalise the light quark masses and the effective operator as well. The $\mathcal{O}(\alpha_s)$ coefficients are given (in $\xi_W = 1$ gauge) by

$$C_{S,WH\text{-box}}^{(1)} = \frac{m_b m_\mu \tan^2 \beta r_H}{M_W^2} \left[\frac{\pi^2 (r_H (-x_t) + r_H + x_t - 1) - 8}{3(r_H - 1)(x_t - 1)} + \frac{2r_H(3r_H - 7) \log(r_H)}{3(r_H - 1)^2(r_H - x_t)} \right. \\ \left. + \frac{2x_t(3x_t - 7) \log(x_t)}{3(x_t - 1)^2(x_t - r_H)} + \frac{2r_H \text{Li}_2\left(\frac{r_H - 1}{r_H}\right)}{r_H - x_t} - \frac{2x_t \text{Li}_2\left(\frac{x_t - 1}{x_t}\right)}{r_H - x_t} \right. \\ \left. + \log\left(\frac{\mu^2}{m_t^2}\right) \left(-\frac{2}{(r_H - 1)(x_t - 1)} - \frac{2r_H \log(r_H)}{(r_H - 1)^2(r_H - x_t)} \right. \right. \\ \left. \left. + \frac{2x_t \log(x_t)}{(x_t - 1)^2(r_H - x_t)} \right) \right] + \mathcal{O}(\tan \beta), \quad (4.58)$$

and the remaining coefficients satisfy the same relations as at LO.

The second class of diagrams contributing to $C_{S,P}^{(\prime)}$ are the penguin diagrams mediated by a neutral Higgs boson $\phi^{0'}$ or A^0 . Example diagrams are shown in Fig. 4.8. These diagrams contribute at various orders in $\tan \beta$, the leading ξ_W -dependent contributions are given at order $\tan^2 \beta$ and to linear order in the light Yukawa couplings at LO by

$$C_{S,H\text{-pen,1PI}}^{(0)} = \frac{m_b m_\mu \tan^2 \beta}{M_W^2} \frac{x_t (\log(r_H)(x_t - \xi_W) + (r_H - 1)\xi_W (\log(\xi_W) - \log(x_t)))}{8M_{H_1}^2 M_{H_2}^2 (r_H - 1)(\xi_W - x_t)(r_H \xi_W - x_t)} \\ \cdot \left[\left(M_{H_1}^2 \left(2M_{H_2}^2 r_H + M_W^2 (r_H \xi_W - x_t) \right) + M_{H_2}^2 M_W^2 (r_H \xi_W - x_t) \right) \right. \\ \left. - M_W^2 \cos(2(\beta - \alpha)) \left(M_{H_1}^2 - M_{H_2}^2 \right) (r_H \xi_W - x_t) \right], \quad (4.59)$$

$$C'_{S,H\text{-pen,1PI}}^{(0)} = \frac{m_q}{m_b} C_{S,H\text{-pen,1PI}}^{(0)}, \quad (4.60)$$

$$C_{P,H\text{-pen},1\text{PI}}^{(0)} = \frac{m_b m_\mu \tan^2 \beta}{M_W^2} \frac{x_t (\log(r_H)(x_t - \xi_W) + (r_H - 1)\xi_W (\log(\xi_W) - \log(x_t)))}{4M_{A^0}^2 (r_H - 1)(\xi_W - x_t)(r_H \xi_W - x_t)} \cdot \left(M_{A^0}^2 r_H + M_W^2 (r_H \xi_W - x_t) \right), \quad (4.61)$$

$$C'_{P,H\text{-pen},1\text{PI}}{}^{(0)} = -\frac{m_q}{m_b} C_{P,H\text{-pen},1\text{PI}}^{(0)}. \quad (4.62)$$

In addition to M_{H^\pm} and $\tan \beta$, these 1LPI contributions also depend on the masses of the neutral Higgs bosons. Here, we have expressed the neutral $\phi^{0'}$ boson in terms of the two mass eigenstates $H_{1,2}$, since it is these mass eigenstates that are used within `FeynRules` and `tapir` for the calculations. Furthermore, at lower order $\mathcal{O}(\tan \beta)$, the Wilson coefficients exhibit an additional dependence on the quartic couplings present in the scalar potential of the 2HDM. These contributions arise from $H^+ - H^- - \phi^{0'}(A^0)$ trilinear Higgs vertices, and we will not present them here since they are subleading in $\tan \beta$.⁴

The gauge-parameter dependence does not cancel between $C_{S,P,WH\text{-box}}^{(\prime)}$ and $C_{S,P,H\text{-pen}}^{(\prime)}$. Again, to this end the diagrams involving flavour-changing self-energies need to be added. Since in the 1LPI penguin diagrams not only charged H^\pm bosons but also W^\pm, G^\pm propagate, all self-energy diagrams, $\Sigma \equiv \Sigma_{SM} + \Sigma_H$, are necessary. All four contributions $\Sigma_{LL,RR,LR,RL}$ need to be inserted on both external legs of the $b\bar{b}H(q\bar{q}H)$ vertex, where $H = \phi^{0'}, A^0$. By an argument analogous to the discussion around Eq. (4.43) it can be seen that the insertions of Σ_{LL} and Σ_{RR} do not contribute, since they cancel in the sum over both external legs. This holds again independently of the structure of the leptonic Higgs couplings. On the other hand, for the Higgs-exchange diagrams, the insertions of $\Sigma_{LR,RL}$ are non-zero and contribute with

$$C_{S,H\text{-pen},2} = -\frac{1}{N} \frac{m_\mu \tan^2 \beta}{v_{SM}^2} \left(\frac{\cos^2(\beta - \alpha)}{M_{H_1}^2} + \frac{\sin^2(\beta - \alpha)}{M_{H_2}^2} \right) \Sigma_{RL}, \quad (4.63)$$

$$C'_{S,H\text{-pen},2} = -\frac{1}{N} \frac{m_\mu \tan^2 \beta}{v_{SM}^2} \left(\frac{\cos^2(\beta - \alpha)}{M_{H_1}^2} + \frac{\sin^2(\beta - \alpha)}{M_{H_2}^2} \right) \Sigma_{LR} = \frac{m_q}{m_b} C_{S,H\text{-pen},2}, \quad (4.64)$$

$$C_{P,H\text{-pen},2} = -\frac{1}{N} \frac{m_\mu \tan^2 \beta}{v_{SM}^2 M_{A^0}^2} \Sigma_{RL} = -\frac{m_b}{m_q} C'_{P,H\text{-pen},2}. \quad (4.65)$$

After adding the contributions from the $W^\pm - H^\mp$ box diagrams, the 1LPI Higgs-penguin diagrams, and the associated 1LPR diagrams with a flavour-changing two-point function, the result is ξ_W independent, and we have at LO the simple result

$$C_S^{(0)} = C_P^{(0)} = \frac{m_b}{m_q} C_S^{\prime(0)} = -\frac{m_b}{m_q} C_P^{\prime(0)} = \frac{m_b m_\mu \tan^2 \beta}{M_W^2} \frac{r_H \log(r_H)}{4(r_H - 1)} + \mathcal{O}(\tan \beta). \quad (4.66)$$

The fact that these gauge-invariant Wilson coefficients are independent of the masses of the neutral Higgs bosons is a remarkable result that was first shown in Ref. [71].

⁴In the CP-conserving Higgs potential only the $H^+ - H^- - \phi^{0'}$ coupling is present, while in the general Higgs potential both couplings arise.

At NLO, due to the argument made in the discussion of $C_{S,P,WH\text{-box}}$, it is sufficient to renormalise only m_t , and the sum of 1LPI penguin diagrams and 1LPR self-energy diagrams is given by

$$\begin{aligned}
 C_{S,H}^{(1)} &\equiv C_{S,H\text{-pen},1\text{PI}+2}^{(1)} = C_{P,H\text{-pen},1\text{PI}+2}^{(1)} = \frac{m_b}{m_q} C_{S,H\text{-pen},1\text{PI}+2}^{\prime(1)} = -\frac{m_b}{m_q} C_{P,H\text{-pen},1\text{PI}+2}^{\prime(1)} \\
 &= \frac{m_b m_\mu \tan^2 \beta}{M_W^2} \left[\log\left(\frac{\mu^2}{m_t^2}\right) \left(\frac{2r_H x_t}{(r_H-1)(x_t-1)} + \frac{2r_H x_t \log(r_H)}{(r_H-1)^2(r_H-x_t)} + \frac{2r_H x_t \log(x_t)}{(x_t-1)^2(x_t-r_H)} \right) \right. \\
 &\quad - \frac{2r_H x_t \text{Li}_2\left(1 - \frac{1}{r_H}\right)}{r_H - x_t} + \frac{2r_H x_t \text{Li}_2\left(1 - \frac{1}{x_t}\right)}{r_H - x_t} + \frac{8r_H x_t}{3(r_H-1)(x_t-1)} \\
 &\quad \left. - \frac{2r_H(3r_H-7)x_t \log(r_H)}{3(r_H-1)^2(r_H-x_t)} + \frac{2r_H(3x_t-7)x_t \log(x_t)}{3(x_t-1)^2(r_H-x_t)} \right]. \quad (4.67)
 \end{aligned}$$

As in the one-loop case, only the combination $C_{S,P}^{(\prime)(1)} \equiv C_{S,P,H}^{(\prime)(1)} + C_{S,P,WH\text{-box}}^{(\prime)(1)}$ is independent of ξ_W .

4.4. Scale dependence and branching ratio in the type-II 2HDM

The dependence on the QCD renormalisation scale of the Wilson coefficients is illustrated in Fig. 4.9 at LO and NLO, in arbitrary units. As expected, a significant decrease of the scale uncertainty is observed at NLO. In Fig. 4.10 we show as an example for $q = s, l = \mu$, the dependence of the branching ratio $\overline{\mathcal{B}}(B_s \rightarrow \mu^+ \mu^-)$ on the mass of the charged Higgs boson, M_{H^\pm} , for different values of $\tan \beta$, together with the current SM prediction and recent experimental measurements. Searches for heavy Higgs bosons put $\tan \beta$ -dependent lower bounds on M_{A^0} and the fact that the quartic Higgs couplings in the scalar potential cannot grow arbitrarily large allows to constrain the mass difference $|M_{A^0} - M_{H^\pm}|$, making M_{H^\pm} bounded from below as a function of $\tan \beta$, see the discussion in Section 6.1 and Section 6.2. For each value of $\tan \beta$ depicted in Fig. 4.10, we illustrate the lower limits on M_{H^\pm} by dashed and dotted vertical lines, corresponding to two different upper limits on $|\lambda_i|$ of $|\lambda_i| \leq 4$ (dashed) and $|\lambda_i| \leq 4\pi$ (dotted).⁵ The area left of these vertical lines should not be considered for the value of $\tan \beta$ at hand. Hence, only the curve for $\tan \beta = 50$ has a small range of a few hundred GeV width around $M_{H^\pm} = 2000$ GeV in which the type-II 2HDM allows for a branching ratio outside the uncertainty of the SM prediction. The SM prediction in Ref. [31] was obtained assuming $-V_{ts} \sim |V_{cb}| = 0.0424$, yielding a central value of $10^9 \cdot \overline{\mathcal{B}}(B_s \rightarrow \mu^+ \mu^-) = 3.65$. With the recent PDG average for the inclusive determination [3], $|V_{cb}| = 0.0422 \pm 0.0008$, the central value is shifted to 3.62, while for the exclusive determinations $|V_{cb}| = 0.0408 \pm 0.0014$ [3] and $|V_{cb}| = 0.03910 \pm 0.0005$ [74] it is shifted to 3.38 and 3.10, respectively. Resolving the discrepancy between the different determinations of $|V_{cb}|$ will thus be an integral part of further quantifying the constraints on the 2HDM.

This concludes the rather extensive discussion of $B_q \rightarrow l^+l^-$ decays within the type-II 2HDM. The presentation was in such detail as to make the cancellation of UV divergences and the

⁵These two numbers correspond to one-loop and tree-level studies of perturbative unitarity of longitudinal vector-boson scattering, respectively, and will be discussed in Section 6.2.

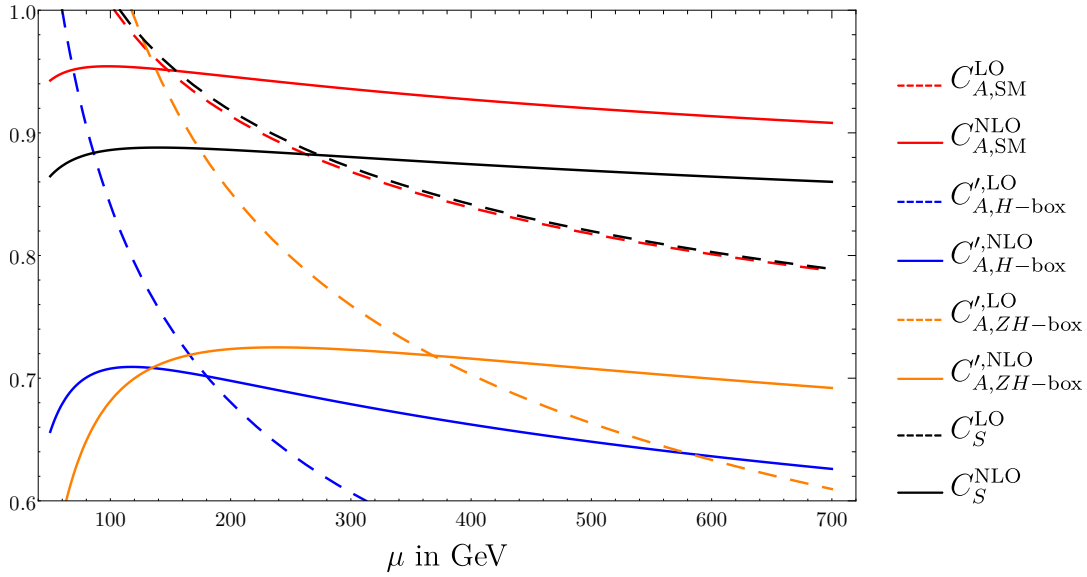


Figure 4.9.: QCD renormalisation-scale dependence of the Wilson coefficients at leading order (LO) and next-to-leading order (NLO). The coefficients absent in the Standard Model (SM) have been rescaled by an appropriate factor in order to fit into the same canvas. The NLO corrections generally lead to a much smaller scale dependence in the interval $M_W/2 \leq \mu \leq 2m_t$. For C_S , the bottom-quark mass has been fixed as $m_b = \bar{m}_b(\bar{m}_t)$, since the running of m_b is compensated for by the running of Eq. (3.5), which is not shown here.

ξ_W gauge-parameter dependence explicit and apparent, an endeavour that would be hardly feasible or instructive in the model with flavour-changing couplings that will be discussed in the next chapter. It is worth stressing that the calculation of the Wilson coefficients within this chapter is valid for $q = d, s$ and all lepton flavours, e, μ, τ . In the next chapter, we will however focus mostly on the decays $B_s \rightarrow \mu^+ \mu^-$ —although the generalisation to other lepton flavours is straightforward—and only discuss B_d decays at the end.

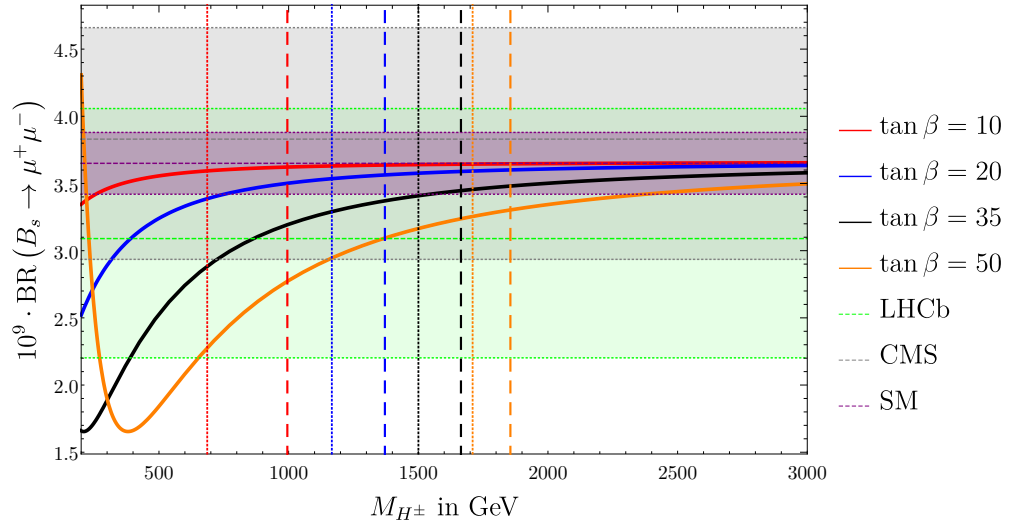


Figure 4.10.: The branching ratio $\overline{\mathcal{B}}(B_s \rightarrow \mu^+ \mu^-)$ (see Eq. (3.23)) as a function of M_{H^\pm} , for different values of $\tan \beta$ in the type-II 2HDM. All running parameters are evaluated at the scale $\mu = \overline{m}_t(\overline{m}_t)$. The purple band denotes the SM prediction obtained in Ref. [31] including also NNLO QCD and NLO EW corrections. The grey and green bands show the recent CMS and LHCb measurements, respectively [35–37]. For each value of $\tan \beta$, the correspondingly coloured vertical dashed and dotted lines illustrate the $\tan \beta$ -dependent lower limits on M_{H^\pm} from collider constraints and the requirement of perturbativity of the scalar Higgs couplings for two different numerical choices of the perturbativity bound for each value of $\tan \beta$, see the discussion in Section 6.2.

5. Additional Wilson coefficients in the three-spurion two-Higgs-doublet model

After the detailed exposition of the type-II Wilson coefficients in the previous chapter, we will now turn to the additional contributions that arise in the considered 2HDM with two non-vanishing Yukawa matrices in the up-type sector. We will discuss the computation of the Wilson coefficients as well as a systematic approach to their renormalisation, which significantly differs from what was illustrated in the previous chapter. The main focus will be on $q = s$ —and $l = \mu$, although the latter is trivially adapted to other lepton generations—, the case $q = d$ will be discussed towards the end of this chapter.

The change from the type-II 2HDM, i.e. the Yukawa Lagrangian with $g^u = g^d = 0$ in Eq. (2.27), to the “three-spurion” 2HDM¹ amounts to evaluating all Feynman diagrams that can arise with the couplings g^u switched on. Phenomenologically, the off-diagonal terms of g^d and thereby ϵ^d are at the same time tightly bounded in magnitude, suggesting to find a rationale for setting $\epsilon^d = 0$. The presence of g^u makes it possible to circumvent the suppression factor $1/\tan\beta$ in the Higgs couplings to right-handed up-type quarks, and can thus lead to terms of higher powers of the large parameter $\tan\beta$. On the other hand, since g^u is a non-diagonal matrix, the CKM matrix is not the only possible source of transitions from one quark family to another family. Therefore, the CKM structure of the individual Feynman diagrams is much more involved, and after summing internal quarks the Wilson coefficients are no longer proportional to $V_{ts}V_{tb}^*$.

5.1. Higgs-boson box diagrams

We begin with a short discussion of the charged-Higgs box diagrams. There are no additional Feynman diagrams arising in the presence of g^u , only the Yukawa couplings change. The Wilson coefficient $C'_{A,H\text{-box}} \sim m_b m_q \tan^4\beta$ remains unaffected since $g^d = 0$ within the loop diagrams. On the other hand, the coefficient $C_{A,H\text{-box}}$ presented in Eq. (4.35) was of order $\tan^0\beta$ since the factor $\tan^2\beta$ from the Higgs-lepton couplings was cancelled by the suppression of the charged-Higgs couplings to the internal up-type quarks. This parametric suppression can be mitigated by g^u couplings, and contributions of order $\mathcal{O}(\tan\beta)$ and $\mathcal{O}(\tan^2\beta)$ arise. Their complete structure is rather involved, but by imposing a power counting on the elements of CKM matrix as

$$\begin{pmatrix} |V_{ud}| & |V_{us}| & |V_{ub}| \\ |V_{cd}| & |V_{cs}| & |V_{cb}| \\ |V_{td}| & |V_{ts}| & |V_{tb}| \end{pmatrix} \sim \begin{pmatrix} 1 & \lambda_w & \lambda_w^3 \\ \lambda_w & 1 & \lambda_w^2 \\ \lambda_w^3 & \lambda_w^2 & 1 \end{pmatrix}, \quad (5.1)$$

¹It will become clear in Section 5.4 what we mean by the “three-spurion” 2HDM.

where λ_w^n denotes the powers of the small *Wolfenstein parameter* [75] $\lambda \approx 0.225$ [3], one can organise the Yukawa structure in powers of λ_w . The Wilson coefficients of the type-II 2HDM are proportional to $V_{ts}V_{tb}^* \sim \lambda_w^2$, and truncating at order λ_w^0 relative to $V_{ts}V_{tb}^*$, we find $C_{A,H\text{-box}}^{(0),\text{III}}$ as a double expansion

$$C_{A,H\text{-box}}^{(0),\text{III}} = \sum_{n_1=1}^2 (\tan \beta)^{n_1} \sum_{n_2=-2}^0 p_{\lambda_w}^{n_2} C_{A,H\text{-box},n_1,n_2}^{(0),\text{III}} \quad (5.2)$$

with

$$C_{A,H\text{-box},1,-2}^{(0),\text{III}} = \frac{g_{ct}^* m_\mu^2 m_t r_H V_{cs} X_H^1}{32 G_F M_W^4 (r_H - 1)^2 v_{\text{SM}} V_{ts} x_t}, \quad (5.3)$$

$$C_{A,H\text{-box},1,-1}^{(0),\text{III}} = \frac{g_{ut}^* m_\mu^2 m_t r_H V_{us} X_H^1}{32 G_F M_W^4 (r_H - 1)^2 v_{\text{SM}} V_{ts} x_t}, \quad (5.4)$$

$$C_{A,H\text{-box},1,0}^{(0),\text{III}} = \frac{m_\mu^2 m_t r_H X_H^1}{32 G_F M_W^4 (r_H - 1)^2 v_{\text{SM}} x_t} \cdot (g_{tt} + g_{tt}^*), \quad (5.5)$$

$$C_{A,H\text{-box},2,-2}^{(0),\text{III}} = \frac{m_\mu^2 r_H V_{cs}}{32 \sqrt{2} G_F M_W^4 (r_H - 1)^2 V_{ts} x_t} \cdot ((r_H - 1)^2 (g_{cc}^* g_{tc} + g_{cu}^* g_{tu}) + g_{ct}^* g_{tt} X_H^1), \quad (5.6)$$

$$C_{A,H\text{-box},2,-1}^{(0),\text{III}} = \frac{m_\mu^2 r_H V_{us}}{32 \sqrt{2} G_F M_W^4 (r_H - 1)^2 V_{ts} x_t} \cdot ((r_H - 1)^2 (g_{tc} g_{uc}^* + g_{tu} g_{uu}^*) + g_{tt} g_{ut}^* X_H^1), \quad (5.7)$$

$$C_{A,H\text{-box},2,0}^{(0),\text{III}} = \frac{m_\mu^2 r_H}{32 \sqrt{2} G_F M_W^4 (r_H - 1)^2 V_{tb}^* V_{ts} x_t} \cdot ((r_H - 1)^2 (V_{cb}^* V_{cs} (g_{cc} g_{cc}^* + g_{cu} g_{cu}^* - g_{uc} g_{uc}^* - g_{uu} g_{uu}^*) + V_{tb}^* V_{ts} (g_{tc} g_{tc}^* + g_{tu} g_{tu}^* - g_{uc} g_{uc}^* - g_{uu} g_{uu}^*) + X_H^1 (g_{ct} g_{ct}^* V_{cb}^* V_{cs} + g_{tt} g_{tt}^* V_{tb}^* V_{ts} - g_{ut} g_{ut}^* (V_{cb}^* V_{cs} + V_{tb}^* V_{ts})))) , \quad (5.8)$$

$$X_H^1 \equiv -(r_H - 1) + r_H \log(r_H). \quad (5.9)$$

In the coefficient $C_{A,H\text{-box},2,0}^{(0),\text{III}}$ we have used the unitarity of the CKM matrix to rewrite the product $V_{ub}^* V_{us} = - (V_{cb}^* V_{cs} + V_{tb}^* V_{ts})$. The parameter $p_{\lambda_w} \equiv 1$ is introduced to facilitate the counting of powers in λ_w , and we have expressed Eq. (5.2) as a double expansion in $\tan \beta$ and powers of the Wolfenstein parameter. The negative powers of p_{λ_w} arise of course only in the Wilson coefficients, since these are multiplied by the prefactor $N \sim \lambda_w^2$, and the branching ratio features only non-negative powers of λ_w . It is worth mentioning that the Wilson coefficients presented in the previous chapter are all proportional to λ_w^0 , and hence the coefficients $C_{A,H\text{-box},i,-2}^{(0),\text{III}}$ are parametrically CKM-enhanced by a factor of $\sim \lambda_w^{-2} \approx 20$.

Here, and henceforth, the superscript III will denote all additional contributions to the Wilson coefficients arising in the three-spurion 2HDM, and it is understood that the complete Wilson coefficient is obtained by summing the type-II contributions discussed in the previous chapter and the additional terms discussed within the present chapter. Despite the fact that these additional contributions come with higher powers of $\tan \beta$ and a smaller CKM suppression factor, they still suffer from the $m_j^2/m_t^2 \approx 4 \cdot 10^{-7}$ (for muons) suppression and are thus

completely negligible, as in the type-II case. Even for $l = \tau$ the suppression factor is about 10^{-4} , and although the factor $\tan^2 \beta$ can lift parts of this suppression, it needs to be accompanied by two $\mathcal{O}(1)$ couplings g_{ij}^u . In this case, the coefficient $C_{A,H\text{-box},2,-2}^{(0),\text{III}}$ can be of order $\mathcal{O}(0.1 - 0.2)$ and indeed alter the branching ratio by $\lesssim 50\%$. However, since the decay into τ leptons has not been observed yet, we will not pursue this possibility any further within this thesis and focus on decays into muons. We will therefore not discuss the NLO corrections to $C_{A,H\text{-box}}^{\text{III}}$. Furthermore, it should be noted that at this order in $\tan \beta$ and in the external light-particle masses, the contributions are again polluted by the gauge-dependent $H^\pm - G^\mp$ diagrams involving the charged Goldstone bosons.

The possible effects of g^u in the mixed $H^\pm - W^\mp$ box diagrams are more interesting, since these diagrams turned out to be sizeable and necessary in order to obtain a gauge-invariant result in the type-II 2HDM. At LO, a sample one-loop Feynman diagram, e.g. the first diagram of Fig. 4.7, is given, in Feynman gauge $\zeta_W = 1$ and with internal top quark, by

$$i\mathcal{M} = \int \frac{d^d k}{(2\pi)^d} \left[\bar{b} i \left(\frac{\sqrt{2}m_b \tan \beta}{v} V_{tb}^* P_L + \left(\frac{\sqrt{2}m_t V_{tb}^*}{v \tan \beta} + (V^\dagger g^u)_{33} \right) P_R \right) \frac{i(k + m_t)}{k^2 - m_t^2} \frac{ig_2}{\sqrt{2}} V_{ts} \gamma_\alpha P_L s \right] \\ \otimes \left[\bar{l} \frac{ig_2}{\sqrt{2}} \gamma_\beta P_L \frac{i\cancel{k}}{k^2} \frac{i\sqrt{2}m_l \tan \beta}{v} P_R l \right] \frac{(-i) g^{\alpha\beta}}{k^2 - M_W^2} \frac{i}{k^2 - M_{H^\pm}^2}. \quad (5.10)$$

The masslessness of the neutrino enforces that only the \cancel{k} term in the top-quark numerator survives, otherwise the complete integrand would be odd under the exchange $k \rightarrow -k$ and the integral would vanish. As a consequence, thanks to the lefthandedness of the W^\pm -boson couplings to fermions, only the P_L term of the $\bar{b}tH^\pm$ vertex will survive and this Feynman diagram does not receive corrections beyond the type-II case. The same holds for the diagram where the charged Higgs boson couples to the external strange quark, except that here $P_L s \rightarrow P_R s$. Furthermore, at NLO, this statement is unaltered since gluonic corrections always add an even number of Dirac matrices to \mathcal{M} . Since QCD is non-chiral, i.e. chirality preserving, QCD cannot modify the chiralities of the external particles or introduce different Dirac structures. In conclusion, due to the masslessness of the neutrino the mixed Higgs- W -box yield the same expressions as in the type-II 2HDM to all order in QCD, and therefore the Wilson coefficients of Eqs. (4.54) to (4.58) do not receive any corrections in the model with g^u .

5.2. Higgs-Z-boson penguin diagrams

The next class of diagrams whose Wilson coefficients are modified by g^u are the Z-boson penguin diagrams with a charged H^\pm boson in the loop. As in the previous section, the Feynman diagrams are the same as in the type-II case, i.e. the ones with examples shown in Fig. 4.6. We discuss the 1LPI penguin diagrams and the 1LPR diagrams obtained from attaching the two-point functions to a tree-level Z-exchange diagram separately, since some interesting cancellations occur in the sum of these. The Wilson coefficient $C'_{A,HZ} \sim m_b m_s$ multiplies the operator in which the external down-type quarks are both right-handed, and thus would receive only corrections from g^d , which we neglect within these loop diagrams. By the same argument it can easily be seen that the $P_L \cancel{q}$ term in the flavour-changing two-point function, $\Sigma_{RR,H}$, does

not receive any beyond-type-II contributions, i.e.

$$\Sigma_{RR,H}^{\text{III}} = 0. \quad (5.11)$$

Therefore only $C_{A,HZ}$, i.e. the coefficient that is suppressed by $\cot^2 \beta$ in the type-II model, receives corrections in our three-spurion 2HDM. At LO, the contribution from the 1LPI penguin diagrams is given by a rather lengthy expression, and we show only the most enhanced $p_{\lambda_w}^{-2}$ and $p_{\lambda_w}^{-1}$ terms here, which are given by

$$C_{A,HZ,1\text{PI}}^{(0),\text{III}} = \sum_{n_1=-1}^0 (\tan \beta)^{n_1} \sum_{n_2=-2}^{-1} p_{\lambda_w}^{n_2} C_{A,HZ,1\text{PI},n_1,n_2}^{(0),\text{III}} + \mathcal{O}(p_{\lambda_w}^0), \quad (5.12)$$

where

$$C_{A,HZ,1\text{PI},-1,-2}^{(0),\text{III}} = \frac{g_{ct}^* m_t V_{cs}}{192 \epsilon G_F M_W^2 (r_H - 1)^2 r_H v_{\text{SM}} V_{ts}} \cdot Y_{H,1}, \quad (5.13)$$

$$C_{A,HZ,1\text{PI},-1,-1}^{(0),\text{III}} = \frac{g_{ut}^* m_t V_{us}}{192 \epsilon G_F M_W^2 (r_H - 1)^2 r_H v_{\text{SM}} V_{ts}} \cdot Y_{H,1}, \quad (5.14)$$

$$\begin{aligned} C_{A,HZ,1\text{PI},0,-2}^{(0),\text{III}} &= \frac{V_{cs}}{192 \sqrt{2} \epsilon G_F M_W^2 (r_H - 1)^2 r_H V_{ts}} \cdot \left[2 \epsilon r_H (r_H - 1)^2 (2s_{\theta_w}^2 - 3) \log\left(\frac{\mu^2}{m_t^2}\right) \right. \\ &\quad \cdot (g_{cc}^* g_{tc} + g_{ct}^* g_{tt} + g_{cu}^* g_{tu}) + g_{cc}^* g_{tc} (r_H - 1)^2 (2s_{\theta_w}^2 - 3) (\epsilon (3r_H + 2X_H^1 - 2) \\ &\quad + 2r_H) + g_{ct}^* g_{tt} \left((r_H - 1)^2 (2s_{\theta_w}^2 (\epsilon (3r_H - 2) + 2r_H) + 3 (\epsilon - 2) r_H + 6 \epsilon) \right. \\ &\quad \left. \left. - 2 \epsilon X_H^1 ((4r_H - 2) s_{\theta_w}^2 + 3) \right) \right. \\ &\quad \left. + g_{cu}^* g_{tu} (r_H - 1)^2 (2s_{\theta_w}^2 - 3) (\epsilon (3r_H + 2X_H^1 - 2) + 2r_H) \right], \quad (5.15) \end{aligned}$$

$$C_{A,HZ,1\text{PI},0,-1}^{(0),\text{III}} = C_{A,HZ,1\text{PI},0,-2}^{(0),\text{III}} \Big|_{\substack{V_{cs} \rightarrow V_{us} \\ g_{ct}^* \rightarrow g_{ui}^*}}, \quad (5.16)$$

$$\begin{aligned} Y_{H,1} &\equiv 2 \epsilon r_H (r_H - 1)^2 (2s_{\theta_w}^2 - 3) \log\left(\frac{\mu^2}{m_t^2}\right) - 2 \epsilon X_H^1 ((4r_H - 2) s_{\theta_w}^2 + 3) \\ &\quad + (r_H - 1)^2 (2s_{\theta_w}^2 (\epsilon (3r_H - 2) + 2r_H) + 3 \epsilon (r_H + 2) - 6r_H). \quad (5.17) \end{aligned}$$

The $1/\epsilon$ UV divergence will be cancelled by the contribution from the 1LPR diagrams, which, when attached to the tree-level Z-boson exchange diagrams in the usual way, yield

$$C_{A,HZ,2}^{(0),\text{III}} = -\frac{G_F}{3\sqrt{2}} (3 - 2s_{\theta_w}^2) \Sigma_{LL,H}^{\text{III}}. \quad (5.18)$$

For this, the additional contributions to the flavour-changing self-energy diagrams $\Sigma_{LL,H}^{\text{III}}$ with the charged Higgs boson in the loop are needed, which are given at LO as

$$\Sigma_{LL,H}^{(0),\text{III}} = \sum_{n_1=-1}^0 (\tan \beta)^{n_1} \sum_{n_2=-2}^{-1} p_{\lambda_w}^{n_2} \Sigma_{LL,H,n_1,n_2}^{(0),\text{III}} + \mathcal{O}(p_{\lambda_w}^0), \quad (5.19)$$

where

$$\Sigma_{LL,H,-1,-2}^{(0),\text{III}} = -\frac{g_{ct}^* m_t V_{cs}}{32\sqrt{2} \epsilon G_F^2 M_W^2 (r_H - 1)^2 r_H v_{\text{SM}} V_{ts}} \cdot Y_{H,2}, \quad (5.20)$$

$$\Sigma_{LL,H,-1,-1}^{(0),\text{III}} = -\frac{g_{ut}^* m_t V_{us}}{32\sqrt{2} \epsilon G_F^2 M_W^2 (r_H - 1)^2 r_H v_{\text{SM}} V_{ts}} \cdot Y_{H,2}, \quad (5.21)$$

$$\begin{aligned} \Sigma_{LL,H,0,-2}^{(0),\text{III}} = & -\frac{V_{cs}}{64 \epsilon G_F^2 M_W^2 (r_H - 1)^2 r_H V_{ts}} \cdot \left[2 \epsilon r_H (r_H - 1)^2 \log\left(\frac{\mu^2}{m_t^2}\right) (g_{cc}^* g_{tc} + g_{ct}^* g_{tt} + g_{cu}^* g_{tu}) \right. \\ & + 2 \epsilon X_H^1 ((g_{cc}^* g_{tc} + g_{cu}^* g_{tu}) (r_H - 1)^2 + g_{ct}^* g_{tt} (1 - 2r_H)) \\ & \left. + (r_H - 1)^2 (\epsilon (3r_H - 2) + 2r_H) (g_{cc}^* g_{tc} + g_{ct}^* g_{tt} + g_{cu}^* g_{tu}) \right], \end{aligned} \quad (5.22)$$

$$\Sigma_{LL,H,0,-1}^{(0),\text{III}} = \Sigma_{LL,H,0,-2}^{(0),\text{III}} \Big|_{\substack{V_{cs} \rightarrow V_{us} \\ g_{ci}^* \rightarrow g_{ui}^*}}, \quad (5.23)$$

$$Y_{H,2} \equiv 2 \epsilon r_H (r_H - 1)^2 \log\left(\frac{\mu^2}{m_t^2}\right) + 2 \epsilon (1 - 2r_H) X_H^1 + (r_H - 1)^2 (\epsilon (3r_H - 2) + 2r_H) \quad (5.24)$$

Many of the flavour-changing couplings g_{ij}^u appear only with a prefactor $3 - 2s_{\theta_w}^2$ in Eq. (5.12). Due to the same factor in the left-handed $Zd_i \bar{d}_i$ coupling most of these couplings are absent from the sum of 1LPI and 1LPR diagrams, and the sum is given at one loop by the remarkably simple expression

$$C_{A,HZ}^{(0),\text{III}} = \sum_{n_1=-1}^0 (\tan \beta)^{n_1} \sum_{n_2=-2}^0 p_{\lambda_w}^{n_2} C_{A,HZ,n_1,n_2}^{(0),\text{III}}, \quad (5.25)$$

with

$$C_{A,HZ,-1,-2}^{(0),\text{III}} = \frac{g_{ct}^* m_t r_H V_{cs} X_{H,2}}{16 G_F M_W^2 (r_H - 1)^2 v_{\text{SM}} V_{ts}}, \quad (5.26)$$

$$C_{A,HZ,-1,-1}^{(0),\text{III}} = C_{A,HZ,-1,-2}^{(0),\text{III}} \Big|_{\substack{V_{cs} \rightarrow V_{us} \\ g_{ct}^* \rightarrow g_{ut}^*}}, \quad (5.27)$$

$$C_{A,HZ,-1,0}^{(0),\text{III}} = \frac{m_t r_H X_{H,2}}{16 G_F M_W^2 (r_H - 1)^2 v_{\text{SM}}} \cdot (g_{tt} + g_{tt}^*), \quad (5.28)$$

$$C_{A,HZ,0,-2}^{(0),\text{III}} = \frac{g_{ct}^* g_{tt} r_H V_{cs} X_{H,2}}{16\sqrt{2} G_F M_W^2 (r_H - 1)^2 V_{ts}}, \quad (5.29)$$

$$C_{A,HZ,0,-1}^{(0),\text{III}} = C_{A,HZ,0,-2}^{(0),\text{III}} \Big|_{\substack{V_{cs} \rightarrow V_{us} \\ g_{ct}^* \rightarrow g_{ut}^*}}, \quad (5.30)$$

$$\begin{aligned} C_{A,HZ,0,0}^{(0),\text{III}} = & \frac{r_H X_{H,2}}{16\sqrt{2} G_F M_W^2 (r_H - 1)^2 V_{tb}^* V_{ts}} \cdot (g_{ct} g_{ct}^* V_{cb}^* V_{cs} + g_{tt} g_{tt}^* V_{tb}^* V_{ts} \\ & - g_{ut} g_{ut}^* (V_{cb}^* V_{cs} + V_{tb}^* V_{ts})), \end{aligned} \quad (5.31)$$

$$X_{H,2} \equiv (r_H - 1) - \log(r_H). \quad (5.32)$$

Note that this result contains terms up to $p_{\lambda_w}^0$, whereas the individual 1LPI and 1LPR contributions to the Wilson coefficients were truncated already at $p_{\lambda_w}^{-1}$. It is noteworthy that indeed the factor $r_H X_{H,2}/(8(r_H - 1)^2)$ is exactly the same as in Eq. (4.51).

5.2.1. Hierarchy between the flavour-changing Yukawa couplings

At this point a discussion about the possible hierarchy between the flavour-changing Yukawa couplings is in order. In writing the Wilson coefficient $C_{A,HZ}^{(0),\text{III}}$ as an expansion in p_{λ_w} we have assumed that the different terms can be ordered in magnitude by employing the hierarchy of the Cabibbo-Kobayashi-Maskawa (CKM) matrix. Put differently, we do not assume a strong hierarchy between the individual elements of the flavour-changing Yukawa matrix, g_{ij}^u , in particular not between the couplings relevant here, g_{it} , where $i = u, c, t$. This can be theoretically motivated by the naturalness assumption, i.e. that in the matrix g^u no elements should be parametrically enhanced compared to others. Of course it is entirely possible that Nature realises a matrix not obeying this assumption. After all, the CKM matrix with its tiny non-diagonal elements and highly suppressed transitions between non-neighbouring generations fails to satisfy this criterion as well and the couplings g_{ij}^u are a priori free parameters. If we do not invoke the hierarchy of the CKM matrix and instead assume that all terms $(g^{u\dagger} V)_{32}$ and $(V^\dagger g^u)_{33}$ could possibly compete in size and need to be taken into account, the expansion in powers of λ_w is of course not permissible anymore. Without the λ_w expansion, the Wilson coefficient $C_{A,HZ}^{(0),\text{III}}$ is given by

$$C_{A,HZ}^{(0),\text{III}} = \sum_{n_1=-1}^0 (\tan \beta)^{n_1} C_{A,HZ,n_1}^{(0),\text{III}}. \quad (5.33)$$

Here, we expand only in the large parameter $\tan \beta$, the coefficients of which are given as

$$C_{A,HZ,-1}^{(0),\text{III}} = \frac{m_t r_H X_{H,2}}{16 G_F M_W^2 (r_H - 1)^2 v_{\text{SM}} V_{tb}^* V_{ts}} \cdot (V_{ts} (g_{ct} V_{cb}^* + V_{tb}^* (g_{tt} + g_{it}^*)) + g_{ut} V_{ub}^* + g_{ct}^* V_{cs} V_{tb}^* + g_{ut}^* V_{tb}^* V_{us}) \quad (5.34)$$

$$\equiv \tilde{C}_{A,HZ,-1}^{(0),\text{III}} \left[\frac{r_H}{8(r_H - 1)} - \frac{r_H \log(r_H)}{8(r_H - 1)^2} \right], \quad (5.35)$$

$$C_{A,HZ,0}^{(0),\text{III}} = \frac{r_H X_{H,2}}{16 \sqrt{2} G_F M_W^2 (r_H - 1)^2 V_{tb}^* V_{ts}} \cdot ((g_{ct} V_{cb}^* + g_{tt} V_{tb}^*) (g_{ct}^* V_{cs} + g_{tt}^* V_{ts} + g_{ut}^* V_{us}) + g_{ut} V_{ub}^* (g_{ct}^* V_{cs} + g_{tt}^* V_{ts}) - g_{ut} g_{ut}^* (V_{cb}^* V_{cs} + V_{tb}^* V_{ts})) \quad (5.36)$$

$$\equiv \tilde{C}_{A,HZ,0}^{(0),\text{III}} \left[\frac{r_H}{8(r_H - 1)} - \frac{r_H \log(r_H)}{8(r_H - 1)^2} \right]. \quad (5.37)$$

In the last lines of both expressions we have explicitly factored out the loop function as in Eq. (4.51). We have also used the unitarity of the CKM matrix to rewrite the product $V_{us} V_{ub}^* = - (V_{cs} V_{cb}^* + V_{ts} V_{tb}^*)$. Ultimately, if this type of 2HDM is realised, the question whether the assumption of expanding in λ_w is justified can only be answered by Nature.

5.2.2. Higgs-Z-boson penguin at next-to-leading order

Returning to the Z-boson penguin diagrams with charged Higgs bosons in the loop, the Feynman diagrams at NLO are again the same diagrams as in the type-II case, and the bare amplitude can be obtained analogously to what was presented in the previous chapter. In order to renormalise the bare amplitudes, renormalisation constants for all QCD parameters of the Lagrangian are needed. The type-II 2HDM had only a small set of these parameters that were relevant for the renormalisation, namely the quark masses, and beyond NLO also the renormalisation of α_s , the wave function renormalisation $Z_\psi^{\text{SM}} - Z_\psi^{\text{eff}}$ and the renormalisation of the effective operators $Q_{S,P}^{(\prime)}$. In the three-spurion model, all Yukawa couplings g_{ij}^u in the Lagrangian are bare QCD quantities as well and thus need to be renormalised. Their renormalisation constants in the $\overline{\text{MS}}$ scheme are precisely the same as the renormalisation constants of quark masses, i.e. they are multiplicatively renormalised by

$$g_{ij}^{u,(0)} \rightarrow Z_m g_{ij}^{u,(r)}. \quad (5.38)$$

In terms of this set of renormalised parameters the amplitude is finite at two loops and the Wilson coefficient is given by

$$C_{A,HZ}^{(1),\text{III}} = \sum_{n_1=-1}^0 (\tan \beta)^{n_1} C_{A,HZ,n_1}^{(1),\text{III}}, \quad (5.39)$$

with

$$C_{A,HZ,n_1}^{(1),\text{III}} = \tilde{C}_{A,HZ,n_1}^{(0),\text{III}} \left[\left(\frac{(r_H - 3) r_H}{(r_H - 1)^2} + \frac{2r_H \log(r_H)}{(r_H - 1)^3} \right) \log\left(\frac{\mu^2}{m_t^2}\right) - \frac{(r_H - 2) r_H \text{Li}_2\left(1 - \frac{1}{r_H}\right)}{(r_H - 1)^2} + \frac{4(r_H - 3) r_H}{3(r_H - 1)^2} - \frac{(3r_H - 11) r_H \log(r_H)}{3(r_H - 1)^3} \right], \quad (5.40)$$

i.e. with the same loop function as $C_{A,HZ}^{(1)}$ in the type-II 2HDM. In Fig. 5.1, we show the renormalisation-scale dependence of $C_{A,HZ}^{\text{III}}$. For this figure, we have set the initial conditions $g_{ij}^u \equiv g_{ij}^{u,(6)}(\bar{m}_t(\bar{m}_t)) = 1$ in order to remove the dependence on the numerical scale of g_{ij}^u . In particular, we assume them all to be real in this figure. An additional imaginary part may enter through the CKM matrix element V_{ub}^* , as can be seen from the *standard parameterisation* [3]

$$V_{\text{CKM}} = \begin{pmatrix} c_{12}c_{13} & s_{12}c_{13} & s_{13}e^{-i\delta} \\ -s_{12}c_{23} - c_{12}s_{23}s_{13}e^{i\delta} & c_{12}c_{23} - s_{12}s_{23}s_{13}e^{i\delta} & s_{23}c_{13} \\ s_{12}s_{23} - c_{12}c_{23}s_{13}e^{i\delta} & -c_{12}s_{23} - s_{12}c_{23}s_{13}e^{i\delta} & c_{23}c_{13} \end{pmatrix}, \quad (5.41)$$

with $c_{ij} = \cos \theta_{ij}$ and $s_{ij} = \sin \theta_{ij}$. We also remove this dependence by setting $g_{ut}^u = 0$ here and choose $M_{H^\pm} = 1000$ GeV, $\tan \beta = 20$ in order to fix the remaining 2HDM parameters, since we are only interested in the QCD running. The *UTfit* collaboration recently determined the angles and complex phase of the standard parameterisation to be [76]

$$\begin{aligned} \sin \theta_{12} &= 0.225\,19(83), & \sin \theta_{13} &= 0.003\,714(92), \\ \sin \theta_{23} &= 0.042\,00(47), & \delta &= 65.15(126)^\circ. \end{aligned} \quad (5.42)$$

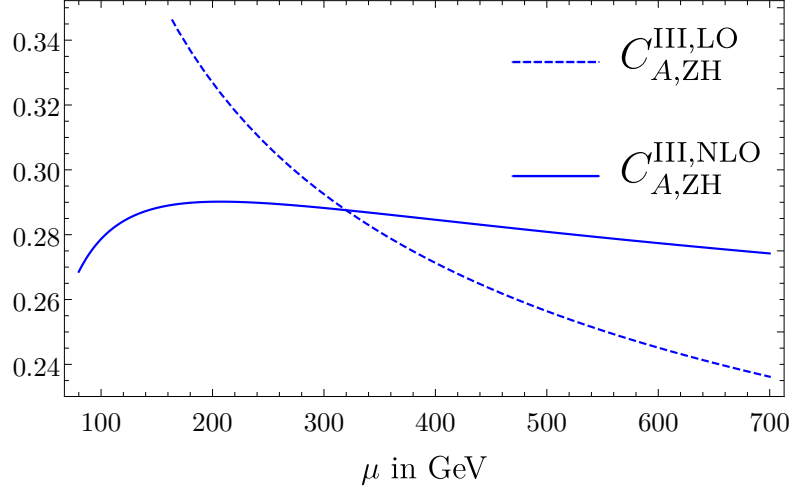


Figure 5.1.: Renormalisation-scale dependence of the Wilson coefficient $C_{A,HZ}^{\text{III}}$, in arbitrary units, see main text. The dashed line shows the LO result, the continuous line the NLO coefficient. The overall scale is arbitrary.

Therefore, the imaginary parts of V_{cs} and V_{ts} are tiny compared to their real parts and can thus be neglected. As a result, the Wilson coefficient is purely real, but given in a somewhat arbitrary scaling in Fig. 5.1. However, since we only focus on the μ dependence $C(\mu) - C(\mu_0)$, this is not a problem.

5.3. Leading terms in $\tan \beta$: self-energy diagrams

So far we have discussed effects of g^u on the Wilson coefficient C_A , which is non-vanishing already in the SM. For the $H^\pm - W^\mp$ mixed box diagrams it turned out that the couplings g_{ij}^u do not enter the Wilson coefficients, cf. Section 5.1. We now turn to the calculation of the Wilson coefficients related to the Higgs-boson penguin diagrams, i.e. the effects arising in the 1LPI penguin diagrams and 1LPR insertions of a flavour-changing self-energy diagram. This time, we will begin with a discussion of the self-energy diagrams, since here a new phenomenon appears. The scalar and pseudoscalar terms of the flavour-changing self-energy diagram shown in Eq. (4.38) also receive contributions proportional to the couplings g_{ij}^u . They are given at leading order by

$$\Sigma_{RL,H}^{(0),\text{III}} = \frac{m_b m_t V_{tb}^* \tan \beta}{8\sqrt{2}\pi^2 v_{\text{SM}}} \cdot (g_{ct}^* V_{cs} + g_{tt}^* V_{ts} + g_{ut}^* V_{us}) \cdot \left(\frac{1}{\epsilon} + \log\left(\frac{\mu^2}{m_t^2}\right) - \frac{\log(r_H)}{r_H - 1} + 1 \right), \quad (5.43)$$

$$\Sigma_{LR,H}^{(0),\text{III}} = \frac{m_s m_t V_{ts} \tan \beta}{8\sqrt{2}\pi^2 v_{\text{SM}}} \cdot (g_{ct} V_{cb}^* + g_{tt} V_{tb}^* + g_{ut} V_{ub}^*) \cdot \left(\frac{1}{\epsilon} + \log\left(\frac{\mu^2}{m_t^2}\right) - \frac{\log(r_H)}{r_H - 1} + 1 \right). \quad (5.44)$$

These results have been first derived in Ref. [77] and we recomputed them within this thesis. Two important features differ from the type-II 2HDM. Firstly, the g_{ij}^u contributions to the self-energy are enhanced by a factor $\tan \beta$. In the type-II case, the factor $\tan \beta$ —e.g. from the $\bar{b}_R t_L H^\pm$

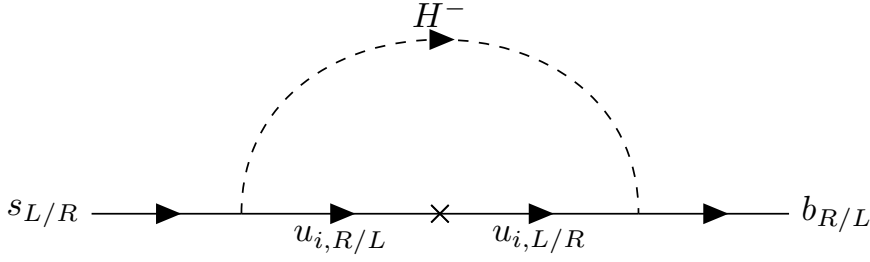


Figure 5.2.: One-loop flavour-changing self-energy with a charged Higgs boson H^\pm . The index i labels the different generations of internal up-type quarks and the cross indicates a chirality flip. This chirality flip is required in order to match onto the spinor field structure $\bar{b}_{R/L}s_{L/R}$. If it occurs on the internal quark line, a $\tan\beta$ enhancement compared to the type-II case and linearity in g_{it}^u are guaranteed.

coupling in Σ_{RL} —is always cancelled by $\cot\beta$ from the $\bar{t}_{RS}H^\mp$ coupling. The modification of the Lagrangian term

$$\bar{u}_R \left[\frac{\sqrt{2}\hat{M}^u V}{v \tan\beta} \right] d_L H^+ \quad \rightarrow \quad \bar{u}_R \left[\frac{\sqrt{2}\hat{M}^u}{v \tan\beta} + g^{u\dagger} \right] V d_L H^+ \quad (5.45)$$

allows the factor $\tan\beta$ to survive. The self-energy diagram is shown in Fig. 5.2 with the chirality flip needed to produce the correct \bar{b}_{RS_L} (or \bar{b}_{LS_R}) chirality structure. This flip ensures that $\Sigma_{LR,RL}$ are only linear in g_{ij}^u . In addition, it introduces a factor of the internal quark mass $m_{u_i} = m_t \delta_{ti}$, and hence only the couplings $g_{it}^{(*)}$ contribute.

Secondly, the leading term in $\tan\beta$ has a $1/\epsilon$ UV pole at one loop. In the type-II 2HDM, both $\Sigma_{RL,LR,SM}$ and $\Sigma_{RL,LR,H}$ had UV poles, but since both self-energy contributions were of order $\tan^0\beta$, these poles cancelled. As a result, the self-energy diagrams yield a finite contribution to the Wilson coefficients $C_{S,P}^{(\prime)}$ in the type-II 2HDM. The additional factor $\tan\beta$ originating from the g_{ij}^u couplings leads to a leftover UV divergence after self-energy diagrams with charged Goldstone bosons and the ones with charged Higgs bosons are summed. Attaching the flavour-changing two-point functions to tree-level $\bar{b}b \rightarrow \phi^{0\prime}(A^0) \rightarrow \mu^+\mu^-$ diagrams then yields a contribution $\sim m_b m_\mu \tan^3\beta g_{ij}^u (1/\epsilon + \text{finite})$ to the bare Wilson coefficients—which we will denote by $C_{S,P,\tan^3\beta}^{(0),\text{III}}$, where g_{ij}^u is a generic element of g^u . For the primed coefficients $C_{S,P,\tan^3\beta}^{\prime(0),\text{III}}$ the same holds with m_s instead of m_b . This would not be a problem if a corresponding contribution to the bare coefficients was given by the 1LPI Higgs-penguin diagrams that cancels the divergence. However, the 1LPI Higgs-penguin diagrams at one loop do not yield a contribution of order $\tan^3\beta$ and linear in the external light quark masses, and thus a proper renormalisation of the Wilson coefficients is necessary. This renormalisation procedure is different from what applied to the type-II 2HDM and the contributions to C_A^{III} discussed so far, and we will discuss it in a systematic way in the following section.

5.4. Renormalisation of the three-spurion 2HDM: spurion expansion

The interaction Lagrangian of the general type-III 2HDM contains terms with mass dimensions of up to four, and is thus renormalisable. It contains four Yukawa matrices in the quark sector, which couple right-handed up-type and down-type quarks to both Higgs doublets, as well as two Yukawa matrices giving masses to the charged leptons in the same way. However, in 2HDMs where an arbitrary subset of the scalar or Yukawa couplings is absent, one usually encounters ultraviolet divergences in the calculation of loops. Depending on which couplings have been removed from the most general type-III 2HDM, there may not be a parameter giving rise to the appropriate counterterm. For example, as seen in Eqs. (5.43) and (5.44), the sum of all one-loop self-energy diagrams yields UV divergences at order $\tan^3 \beta g_{it}^*$, $i = u, c, t$, contributing in total to an $\mathcal{O}(\tan^3 \beta)$ term after combining the self-energy diagrams with the corresponding tree-level Higgs-exchange diagrams. This is explained at the physics level by the fact that these one-loop diagrams generate an effective bs -Higgs coupling, even if we remove flavour-changing neutral down-type Yukawa couplings from the Lagrangian at tree level. For these divergences, no corresponding contribution can be provided by the one-light-particle-irreducible (1LPI) Higgs-penguin diagrams, and they need to be renormalised in a different way.

It should be discussed why this problem does not arise in the popular two-Higgs-doublet models (2HDMs) of type I, II, X, and Y, all of which also feature only a subset of all Yukawa couplings. These models were constructed with the elimination of tree-level flavour-changing neutral currents (FCNCs) in mind, which is achieved by imposing a discrete \mathbb{Z}_2 symmetry on the Higgs doublets and right-handed up-type and down-type quarks, under which these fields transform differently, see Table 2.1. This discrete symmetry ensures that up-type quarks and down-type quarks can only couple to one Higgs doublet each, i.e. that one of the two Yukawa matrices in each sector is absent, and thus all neutral-Higgs Yukawa interactions are flavour-diagonal in the fermion mass eigenbasis. At the same time, the different assignment of \mathbb{Z}_2 charges to up-type and down-type quarks and the Higgs doublets also ensures that loop corrections with additional factors of Yukawa couplings do not mix up-type and down-type Yukawa matrices into one another. For example, in all of the 2HDMs with discrete \mathbb{Z}_2 symmetry, the neutral decay $B_s \rightarrow \mu^+ \mu^-$ proceeds at loop level via charged-current H^\pm diagrams, and no flavour-changing neutral down-type Yukawa couplings are necessary. In the models with exact \mathbb{Z}_2 symmetry the symmetry is preserved at every vertex. The type-II and other 2HDMs with soft \mathbb{Z}_2 breaking feature \mathbb{Z}_2 -violating loops, however these are finite.

In the general type-III 2HDM in the Higgs basis and the basis of fermion mass eigenstates, the flavour-changing neutral Higgs couplings are naturally present in the non-diagonal elements of \hat{g}^d . In this model, there is a tree-level Feynman diagram mediating the rare decays $B_q \rightarrow l^+ l^-$ —and also a tree-level diagram contributing to the $B_q - \bar{B}_q$ mixing—involving the flavour-changing couplings g_{qb} and g_{bq} . This technically constitutes the leading order (LO) contribution to both processes in the perturbative expansion in terms of the Yukawa matrices (i.e. corrections mediated by Higgs bosons), and the class of one-loop Higgs-mediated diagrams that were calculated in the previous chapter become next-to-leading order (NLO) Yukawa corrections to these tree-level processes in the context of the non- \mathbb{Z}_2 -discrete 2HDM. These one-loop diagrams are then UV-divergent, but the one-loop Yukawa counterterms in $g_{qb}^{(0)} = g_{qb}^{(r)} + \delta g_{qb}^{(0)}$

and $g_{bq}^{(0)} = g_{bq}^{(r)} + \delta g_{bq}^{(0)}$ remove these divergences, as required in any renormalisable theory such as the general type-III 2HDM.

Our motivation to consider a model with suppressed flavour-changing couplings of neutral Higgs bosons to down-type quarks has been laid out in Section 2.3 and we do not repeat it here. However, we now need to discuss the technical procedure of renormalising our chosen model. In order to find the minimal renormalisable theory, one can use the flavour symmetries of the gauge sector and systematically expand in the fields breaking this symmetry [78, 79]. Since the gauge interactions of the general 2HDM are flavour-blind, the Lagrangian of the gauge sector possesses an $SU(3)^5$ symmetry—i.e. $[\mathcal{L}_{\text{gauge}}, U] = 0, U \in SU(3)^5$ —under which

$$Q_L \rightarrow U_Q Q_L, \quad u_R \rightarrow U_u u_R, \quad d_R \rightarrow U_d d_R, \quad L_L \rightarrow U_L L_L, \quad l_R \rightarrow U_l l_R, \quad (5.46)$$

and each $U_i \in SU(3)$. The Yukawa matrices couple left-handed to right-handed fields and thus break this $SU(3)^5$ symmetry. However, imposing that the Yukawa matrices transform as

$$Y^{u,d} \rightarrow U_Q Y^{u,d} U_{u,d}^\dagger, \quad \epsilon^{u,d} \rightarrow U_Q \epsilon^{u,d} U_{u,d}^\dagger, \quad (5.47)$$

the $SU(3)^3$ symmetry is formally restored in the quark Yukawa sector. In the lepton sector one can impose

$$Y^l \rightarrow U_L Y^l U_l^\dagger \quad (5.48)$$

in order to restore the flavour $SU(3)^2$ symmetry in the Yukawa Lagrangian. Note that $\bar{\epsilon}^l = 0$ within this thesis.

The renormalisable 2HDMs can be categorised in terms of which Yukawa matrices act as the *spurions* breaking the quark sector $SU(3)^3$. In these models the remaining Yukawa matrices are expressed in terms of the spurion Yukawa matrices. Down-type quark masses require at least one of the matrices \bar{Y}^d or $\bar{\epsilon}^d$ to be non-vanishing, and analogously for up-type quarks. Therefore at least two spurions are necessary, and there are two physically distinct two-spurion 2HDMs. The first possibility is to choose Y^d and Y^u as the spurions, in which case ϵ^d and ϵ^u are expressed as functions $f^{d,u}$ of $Y^{d,u}$. These functions are polynomials with terms involving three Yukawa matrices as the first correction, terms with five Yukawa matrices as the second correction, and so on. We write the series expansion as

$$f^{d,u}(Y^d, Y^u) = \sum_{n=0}^{\infty} f_n^{d,u}(Y^d, Y^u). \quad (5.49)$$

For ϵ^d , that is f^d , invariance under $SU(3)^3$ requires that $f^d \rightarrow U_Q f^d U_d^\dagger$, in accordance with Eq. (5.47), and hence the column index of f^d must transform with U_d^\dagger . For f^u the same holds with $U_d^\dagger \rightarrow U_u^\dagger$. The rest of f_n^d can then only be composed of factors $Y^u Y^{u\dagger}$ and $Y^d Y^{d\dagger}$, both of which transform as $Y^i Y^{i\dagger} \rightarrow U_Q Y^i Y^{i\dagger} U_Q^\dagger$. Note that no factors $Y^d Y^{u\dagger}$ or $Y^u Y^{d\dagger}$ can appear, since they would spoil the transformation properties of $f^{d,u}$. If we truncate Eq. (5.49) at a certain n_{max} , as we will always do in our perturbative calculations within this thesis, the most general form of $f^{d,u}$ is

$$\epsilon^{d,u} = f^{d,u}(Y^d, Y^u) = P_{d,u}(Y^d Y^{d\dagger}, Y^u Y^{u\dagger}) Y^{d,u}, \quad (5.50)$$

with $P_{u,d}$ a polynomial of finite order n_{\max} in the variables $Y^d Y^{d\dagger}$, $Y^u Y^{u\dagger}$. The second possibility contains the spurions Y^d and ϵ^u , such that

$$\epsilon^d = P_d \left(Y^d Y^{d\dagger}, \epsilon^u \epsilon^{u\dagger} \right) Y^d, \quad Y^u = P_u \left(Y^d Y^{d\dagger}, \epsilon^u \epsilon^{u\dagger} \right) \epsilon^u. \quad (5.51)$$

After an appropriate change of basis, the Yukawa matrices can be expressed in terms of the mass matrices of up-type and down-type quarks and all Yukawa matrices can be expressed in terms of the known Yukawa couplings. Therefore the conditions of minimal flavour violation (MFV) [79] are satisfied in both of these scenarios. The first possibility represents a generalisation of the type-II 2HDM, whereas the second possibility is a generalisation of the type-I 2HDM, cf. the discussion in Section 2.2.1. It is worth noting that the two remaining possibilities of choosing spurions, ϵ^d , Y^u and ϵ^d , ϵ^u , amount to the same renormalisable 2HDMs upon relabelling $H_u \leftrightarrow H_d$ and $\epsilon^i \leftrightarrow Y^i$. Concerning 2HDMs with three spurions, there are again two physically distinct possibilities. The first possible choice are three spurions, Y^u , Y^d , and ϵ^d , in which case the minimal renormalisable theory would be constructed by expressing ϵ^u in terms of these three matrices, with the requirement of formal $SU(3)^3$ invariance of the Yukawa Lagrangian. In this scenario it would be possible to suppress ϵ^u , but without a compelling symmetry argument for its smallness ϵ^d would be sizeable and in conflict with experimental constraints. The second scenario is the one of phenomenological interest for us, containing the three spurions Y^u , Y^d , and ϵ^u as a priori arbitrary Yukawa matrices. All calculations presented in this chapter apply in the context of this particular 2HDM, which we call the *three-spurion* 2HDM. In the cases with three spurions there are more possible products having the correct transformation behaviour, namely $Y^d Y^{d\dagger}$, $Y^u Y^{u\dagger}$, $Y^u \epsilon^{u\dagger}$, $\epsilon^u Y^{u\dagger}$, and $\epsilon^u \epsilon^{u\dagger}$. The fourth matrix, ϵ^d is then given in expanded form as

$$\epsilon^d = c Y^d + c_{11} Y^d Y^{d\dagger} Y^d + b_{11} \epsilon^u \epsilon^{u\dagger} Y^d + b_{12} \epsilon^u Y^{u\dagger} Y^d + b_{21} Y^u \epsilon^{u\dagger} Y^d + b_{22} Y^u Y^{u\dagger} Y^d + \dots, \quad (5.52)$$

where \dots indicates terms with five or more spurions. The coefficients c , c_{11} , b_{ij} are in general complex numbers. Equation (5.52) is the so-called *spurion expansion* of ϵ^d since the function f^d is expanded in a power series of the non-vanishing matrices $Y^{d,u}$, ϵ^u . Of course, this expansion is only useful if higher-order corrections that add terms with higher powers of the spurions are small enough to be insignificant. In particular, for the expansion at hand, Eq. (5.52), this implies that terms with at least five spurions should be negligible. This condition is satisfied in our calculation where the one-loop penguin diagrams can induce coefficients up to third order in the spurions, while higher terms are generated at higher loop order in the Yukawa couplings. QCD corrections are independent of the Yukawa couplings and hence do not affect this discussion [80].

The coefficient c can be eliminated by a suitable rotation of (H_u, H_d) , but in general it will be re-generated beyond LO in the Yukawa expansion [80]. We therefore keep c and require $c = 0$ at tree level rather than perturbatively eliminating it order by order through rotations. Once $Y^{u,d}$ are expressed in terms of the quark masses the minimal renormalisable model therefore contains 14 additional complex parameters, namely the five coefficients of the spurion expansion, c_{11} , b_{11} , \dots , b_{22} , as well as the a priori arbitrary elements of the 3×3 matrix ϵ^u . In the practical case at hand, Eqs. (5.43) and (5.44) show that the leptonic $|\Delta B| = |\Delta S| = 1$ decay involves the couplings g_{it} , and we will work with the g_{ij}^u rather than ϵ_{ij}^u . In particular, setting up the

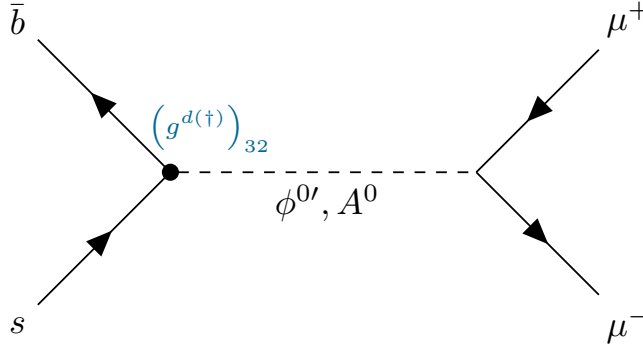


Figure 5.3.: Tree-level diagram contributing to $B_s \rightarrow \mu^+ \mu^-$ via $C_{S,P}^{(\prime)}$. The dot denotes a coupling g_{ij}^d resulting from the spurion expansion.

renormalisation in terms of g_{ij}^u is far more convenient. We work in the $\overline{\text{MS}}$ renormalisation scheme for g_{ij}^u and add counterterms in such a way that Eq. (5.52) is obeyed at tree level. Hence, the renormalisation of $C_{S,P}$ requires a counterterm to the ϵ^d coupling g_{sb} , whereas the renormalisation of the primed coefficients $C'_{S,P}$ requires a counterterm to g_{bs} , as will be demonstrated in the next section.

In conclusion, the 2HDM in which $\epsilon^d = 0$ exactly, while $\epsilon^u \neq 0$, is not renormalisable. A minimal renormalisable theory can be constructed using the spurion expansion, which “re-introduces” off-diagonal flavour-changing neutral couplings in the down-type sector, ϵ^d . However, the important conceptual difference compared to the general 2HDM is that ϵ^d is not completely arbitrary, but rather given as an expansion in powers of the spurions $Y^{d,u}$, ϵ^u . With this mechanism, the potentially dangerous off-diagonal terms in ϵ^d can be brought under control.

5.5. Renormalisation of $C_{S,P,\tan^3\beta}^{(\prime),(0),\text{III}}$

With the expansion of ϵ^d in terms of the spurions $Y^{d,u}$, ϵ^u it is clear why the one-loop bare coefficients in Eqs. (5.43) and (5.44) are not finite: in the presence of ϵ^d they are not LO coefficients, but strictly speaking become NLO in the EW/Yukawa expansion. In order to renormalise them, all true LO—i.e. tree level—diagrams contributing to $B_s \rightarrow \mu^+ \mu^-$ must be computed and the bare quantities appearing therein need to be shifted towards their renormalised counterparts. There are two tree-level diagrams, shown in Fig. 5.3, which contribute to the Wilson coefficients at $\mathcal{O}(\tan\beta)$ as

$$\begin{aligned}
 C_{S,\text{tree}}^{(0),\text{III}} &= -\frac{1}{N} \frac{m_\mu \tan\beta \left(c_{\beta-\alpha}^2 M_{H_2}^2 + M_{H_1}^2 s_{\beta-\alpha}^2 \right)}{\sqrt{2} M_{H_1}^2 M_{H_2}^2 v_{\text{SM}}} g_{sb}^* = \frac{g_{sb}^*}{g_{bs}} C'_{S,\text{tree}}{}^{(0),\text{III}}, \\
 C_{P,\text{tree}}^{(0)} &= \frac{1}{R_M M_{A^0}^2} C_{S,\text{tree}}^{(0),\text{III}} = -\frac{g_{sb}^*}{g_{bs}} C'_{P,\text{tree}}{}^{(0),\text{III}},
 \end{aligned} \tag{5.53}$$

where we have defined the “mass” of the neutral scalar² $\phi^{0'}$

$$\frac{1}{M_{\phi^{0'}}^2} \equiv R_M \equiv \frac{M_{H_1}^2 s_{\beta-\alpha}^2 + M_{H_2}^2 c_{\beta-\alpha}^2}{M_{H_1}^2 M_{H_2}^2}. \quad (5.54)$$

As claimed in the previous section, the process $B_s \rightarrow \mu^+ \mu^-$ involves the two flavour-violating Yukawa couplings, g_{sb} and g_{bs} . It should be noted that $g_{sb,bs}^{(0)}$ in Eq. (5.53) are bare couplings. We express these bare couplings in terms of renormalised quantities as

$$g_{sb}^{(0)} = g_{sb} + \delta^{(0)} g_{sb} + \left(\frac{\alpha_s}{4\pi}\right) \delta^{(1)} g_{sb} + \dots, \quad g_{bs}^{(0)} = g_{bs} + \delta^{(0)} g_{bs} + \left(\frac{\alpha_s}{4\pi}\right) \delta^{(1)} g_{bs} + \dots, \quad (5.55)$$

where $\delta^{(i)} g_{sb,bs}$, $i = 0, 1$, are EW/Yukawa and QCD-Yukawa counterterms of order $\mathcal{O}(G_F \alpha_s^i)$ and the \dots indicate terms of order $\mathcal{O}(G_F^2; G_F \alpha_s^2)$. These counterterms are required in order to renormalise the coefficients in Eqs. (5.43) and (5.44) and we determine them such that they satisfy this requirement. In the $\overline{\text{MS}}$ renormalisation scheme, the one-loop Yukawa counterterms are given by

$$\begin{aligned} \delta^{(0)} g_{sb} &= -\frac{1}{\epsilon} \frac{\sqrt{2} G_F m_t m_b \tan^2 \beta}{8\pi^2} (g_{ut} V_{us}^* + g_{ct} V_{cs}^* + g_{tt} V_{ts}^*) V_{tb} + \mathcal{O}(\tan \beta), \\ \delta^{(0)} g_{bs} &= -\frac{1}{\epsilon} \frac{\sqrt{2} G_F m_t m_s \tan^2 \beta}{8\pi^2} (g_{ut} V_{ub}^* + g_{ct} V_{cb}^* + g_{tt} V_{tb}^*) V_{ts} + \mathcal{O}(\tan \beta). \end{aligned} \quad (5.56)$$

It is an important consistency check for our calculation that these counterterms are *local*, i.e. do not contain logarithms.³ With the counterterms added, the renormalised one-loop Wilson coefficients $C_{S,P,\tan^3 \beta}^{(0),(\prime),\text{III}}$ read

$$\begin{aligned} C_{S,\tan^3 \beta}^{(0),\text{III}} &= -\frac{m_b m_\mu m_t \tan^3 \beta}{8 G_F M_W^2 v_{\text{SM}} V_{ts}} R_M (g_{ct}^* V_{cs} + g_{tt}^* V_{ts} + g_{ut}^* V_{us}) \\ &\quad \cdot \left[\log\left(\frac{\mu^2}{m_t^2}\right) - \frac{\log(r_H)}{r_H - 1} + 1 \right], \end{aligned} \quad (5.57)$$

$$\begin{aligned} C_{S,\tan^3 \beta}^{\prime(0),\text{III}} &= -\frac{m_\mu m_s m_t \tan^3 \beta}{8 G_F M_W^2 v_{\text{SM}} V_{tb}^*} R_M (g_{ct} V_{cb}^* + g_{tt} V_{tb}^* + g_{ut} V_{ub}^*) \\ &\quad \cdot \left[\log\left(\frac{\mu^2}{m_t^2}\right) - \frac{\log(r_H)}{r_H - 1} + 1 \right], \end{aligned} \quad (5.58)$$

$$C_{P,\tan^3 \beta}^{(0),\text{III}} = \frac{1}{R_M M_{A^0}^2} C_{S,\tan^3 \beta}^{(0),\text{III}}, \quad (5.59)$$

$$C_{P,\tan^3 \beta}^{\prime(0),\text{III}} = -\frac{1}{R_M M_{A^0}^2} C_{S,\tan^3 \beta}^{\prime(0),\text{III}}. \quad (5.60)$$

²The scalar $\phi^{0'}$ is in general not a mass eigenstate, hence the right-hand side is a non-trivial function of the two physical masses and the mixing angle $\beta - \alpha$.

³At one loop, locality of the counterterms is trivially achieved per construction, but at NLO this serves as a check.

The explicit $\log(\mu^2)$ dependence in the $\overline{\text{MS}}$ scheme indicates that in introducing g^d via the spurion expansion the one-loop coefficients are of NLO in the perturbative Yukawa expansion.

At NLO in QCD, we need to renormalise the quark masses as well as the flavour-changing Yukawa couplings in the $\overline{\text{MS}}$ scheme. We observe that the leading $\mathcal{O}(\tan^3\beta)$ Wilson coefficients in the three-spurion 2HDM depend on the masses and mixing of the neutral Higgs bosons, in contrast to the leading contributions in the type-II 2HDM. One can omit the renormalisation of the linear prefactors $m_{b,s}$ in Eqs. (5.57) to (5.60) at NLO if the quark masses in Eq. (3.5) are kept unrenormalised as well, as before, since the product of quark mass and (pseudo)scalar quark current does not renormalise. However, the QCD renormalisation constants for quark masses and Yukawa couplings are not sufficient to make the two-loop contributions stemming from the self-energy diagrams finite. In addition, the coupling g_{sb} must also be renormalised. The $\mathcal{O}(\alpha_s)$ local counterterms $\delta^{(1)}g_{sb,bs}$ are given by

$$\begin{aligned}\delta^{(1)}g_{sb} &= -\left[\frac{1}{\epsilon^2} + \frac{4}{3\epsilon}\right] \frac{G_F m_t m_b \tan^2\beta}{\sqrt{2}\pi^2} (g_{ut}V_{us}^* + g_{ct}V_{cs}^* + g_{tt}V_{ts}^*) V_{tb} + \mathcal{O}(\tan\beta), \\ \delta^{(1)}g_{bs} &= -\left[\frac{1}{\epsilon^2} + \frac{4}{3\epsilon}\right] \frac{G_F m_t m_s \tan^2\beta}{\sqrt{2}\pi^2} (g_{ut}V_{ub}^* + g_{ct}V_{cb}^* + g_{tt}V_{tb}^*) V_{ts} + \mathcal{O}(\tan\beta).\end{aligned}\quad (5.61)$$

It should be noted that the Yukawa structure of these counterterms agrees with the one at LO QCD, in agreement with the statement made in Eq. (5.52). The renormalised two-loop (NLO) Wilson coefficients at order $\tan^3\beta$ are given by

$$\begin{aligned}C_{S,\tan^3\beta}^{(1),\text{III}} &= -\frac{m_b m_\mu m_t \tan^3\beta}{6G_F M_W^2 v_{\text{SM}} V_{ts}} R_M (g_{ct}^* V_{cs} + g_{tt}^* V_{ts} + g_{ut}^* V_{us}) \\ &\quad \cdot \left[\left(\frac{2(4r_H - 7)}{r_H - 1} + \frac{6 \log(r_H)}{(r_H - 1)^2} \right) \log\left(\frac{\mu^2}{m_t^2}\right) + 3 \log^2\left(\frac{\mu^2}{m_t^2}\right) - 6 \text{Li}_2\left(\frac{r_H - 1}{r_H}\right) \right. \\ &\quad \left. + \frac{8(r_H - 2)}{r_H - 1} + \frac{(14 - 6r_H) \log(r_H)}{(r_H - 1)^2} \right].\end{aligned}\quad (5.62)$$

The coefficient C_P and the primed coefficients can be obtained from $C_{S,\tan^3\beta}^{(1),\text{III}}$ by

$$C_{S,\tan^3\beta}^{\prime,(1),\text{III}} = C_{S,\tan^3\beta}^{(1),\text{III}} \Big|_{\substack{m_b \rightarrow m_s \\ g_{it}^* \rightarrow g_{it} \\ V_{is} \rightarrow V_{ib}^*}}, \quad C_{P,\tan^3\beta}^{(1),\text{III}} = \frac{1}{R_M M_{A^0}^2} C_{S,\tan^3\beta}^{(1),\text{III}}, \quad C_{P,\tan^3\beta}^{\prime,(1),\text{III}} = -\frac{1}{R_M M_{A^0}^2} C_{S,\tan^3\beta}^{\prime,(1),\text{III}}. \quad (5.63)$$

These coefficients were previously unknown and have been published in Ref. [80]. We show the renormalisation-scale dependence of the $\mathcal{O}(\tan^3\beta)$ Wilson coefficients at LO and NLO in QCD in Fig. 5.7. However, the discussion of the scale dependence will be deferred to the end of Section 5.6, after the presentation of the subleading $\tan^2\beta$ contributions arising from the 1LPI penguin diagrams.

The Wilson coefficients $C_{S,P,\tan^3\beta}^{(\prime),\text{III}}$ arise from flavour-changing self-energy diagrams that are attached to tree-level diagrams, i.e. from 1LPR Feynman diagrams. Power counting in $\tan\beta$ suggests that at two loops additional $\mathcal{O}(\tan^3\beta)$ contributions can arise from Feynman diagrams in which a gluon connects the flavour-changing two-point function with the other

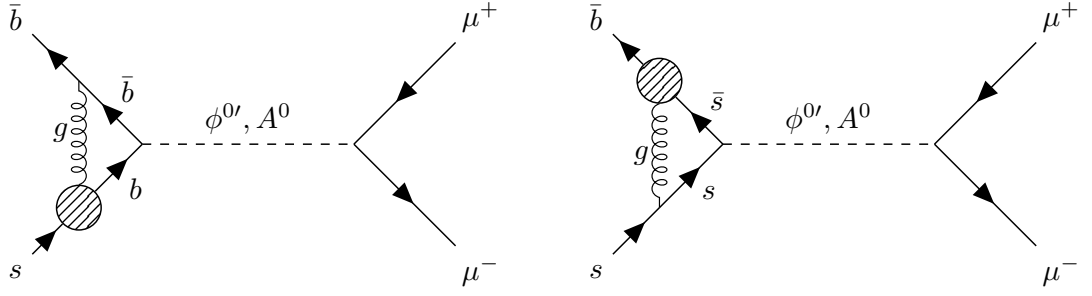


Figure 5.4.: Two-loop QCD corrected one-light-particle-irreducible (1LPI) diagrams resulting from gluon exchange between one external quark line and the internal self-energy loop on the second quark line. These diagrams are also of order $O(\tan^3 \beta)$, but, as discussed in the main text, are further suppressed by another power of the external light quark Yukawa couplings.

quark leg (QCD-corrected 1LPI diagrams), see Fig. 5.4. However, these contributions are strongly suppressed by at least one additional power of $m_{b,s}/v_{\text{SM}}$. To demonstrate this, we consider the left diagram of Fig. 5.4 with the pseudoscalar A^0 boson and the H^\pm and top quark in the loop. As in all other 1LPI diagrams, the masses $m_{b,s}$ within propagators are taken to be zero and we keep only the Yukawa couplings. The diagram is then given by

$$\begin{aligned}
 &\propto \int d^d k d^d l \left[\bar{b} \gamma_\mu \frac{l}{l^2} \frac{m_b \tan \beta}{v_{\text{SM}}} \gamma_5 \frac{l}{l^2} \left(\frac{m_b \tan \beta V_{tb}^*}{v_{\text{SM}}} P_L + \frac{m_t V_{tb}^*}{v_{\text{SM}} \tan \beta} P_R \right) \frac{k+l+m_t}{(k+l)^2 - m_t^2} \gamma^\mu \frac{k+m_t}{k^2 - m_t^2} \right. \\
 &\quad \cdot \left. \left(\frac{m_s \tan \beta V_{ts}}{v_{\text{SM}}} P_R + \left(\frac{m_t V_{ts}}{v_{\text{SM}} \tan \beta} + \frac{1}{\sqrt{2}} (g^{u\dagger} V)_{32} \right) P_L \right) s \right] \otimes \left[\bar{\mu} \frac{m_\mu \tan \beta}{v_{\text{SM}}} \gamma_5 \mu \right] \frac{1}{M_{A^0}^2}. \quad (5.64)
 \end{aligned}$$

We are interested in effects proportional to $g^{u\dagger}$ at order $O(\tan^3 \beta)$, which implies that all factors $\tan \beta$ in the above expression carry an additional factor of $m_{b,s}$. The contribution of this type of diagrams is therefore suppressed by a factor $m_{b,s}/v_{\text{SM}}$ relative to the contribution from the 1LPR diagrams. In other words, the appearance of the fermion bridge $1/(\not{q}_s - m_b)$ in attaching the self-energy diagrams to a tree-level diagram is crucial in order to obtain contributions linear in $m_{b,s}$.

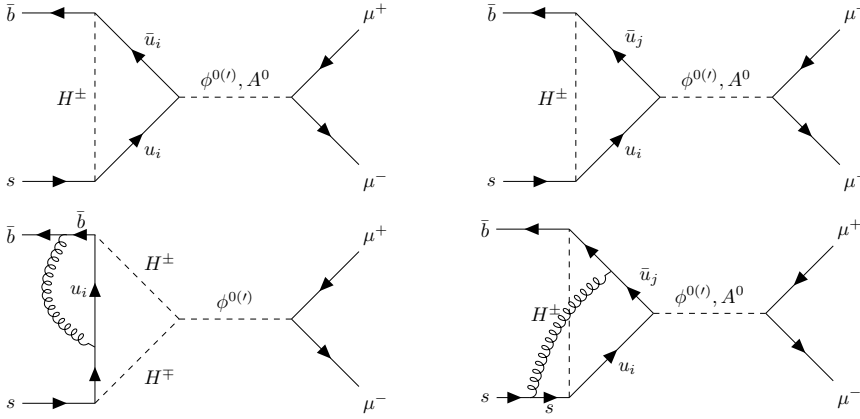


Figure 5.5.: Sample 1LPI Higgs-penguin diagrams at LO and NLO in QCD. The diagrams on the left-hand side arise also in the type-II 2HDM, whereas the diagrams on the right-hand side only appear in the presence of g_{ij}^u for $i \neq j$. The diagram in the lower left with A^0 instead of $\phi^{0(\prime)}$ is absent if the 2HDM potential is CP conserving with $\lambda_7 \in \mathbb{R}$.

An analogous argument holds for the diagrams with the other up-type quarks and $\phi^{0\prime}$ as well as with the exchange of the b and s line in the above argument. Hence, the 1LPI diagrams of order $\mathcal{O}(\tan^3\beta)$ are generally suppressed by an additional power of a light-quark mass $m_{b,s}/v_{\text{SM}}$.

5.6. The Wilson coefficients $C_{S,P}^{(\prime),\text{III}}$: subleading $\tan\beta$ orders

With the renormalisation of the three-spurion model presented in Section 5.4 all prerequisites are met for the discussion of the contributions to $C_{S,P}^{(\prime),\text{III}}$ from the 1LPI penguin diagrams with a neutral $\phi^{0\prime}$ or A^0 boson connecting the lepton line. This is the only class of diagrams for $B_s \rightarrow \mu^+\mu^-$ in which truly new Feynman diagrams arise. Some example LO and NLO Feynman diagrams are shown in Fig. 5.5. The right-hand side of Fig. 5.5 shows sample Feynman diagrams that, if $i \neq j$, are only present in the three-spurion model, whereas the diagrams on the left-hand side also appear in the type-II 2HDM, see Fig. 4.8. However, it should be noted that, due to the diagonal elements of g^u , for example the diagram in the top left corner of Fig. 5.5 also contributes to the coefficients C_i^{III} . In total there are 252 Higgs-penguin diagrams at one loop in a general ξ_W gauge with “transversal” and “longitudinal” W propagators and 1080 two-loop Feynman diagrams in $\xi_W = 1$ gauge.

We are interested in the contributions to $C_{S,P}^{(\prime),\text{III}}$ at subleading orders in $\tan\beta$, i.e. at order $\mathcal{O}(\tan^2\beta)$. By inspecting e.g. the top-right Feynman diagram of Fig. 5.5 for $u_i = c, \bar{u}_j = \bar{t}$ it becomes clear that at least one of the $\bar{b}\bar{t}H^\pm$ or sH^\pm couplings must contribute with a factor of $\tan\beta$ in order to obtain terms of $\mathcal{O}(\tan^2\beta)$. However, if both contribute with $\tan\beta$, the contributions to the Wilson coefficients would be quadratic in the light-quark masses $m_{b,s}$, and we neglect these suppressed effects here, as discussed in the context of Fig. 5.4. Instead,

at order $\mathcal{O}(\tan^2 \beta)$ the previous argument makes clear that all contributions from diagrams with two internal quark lines are quadratic in g_{ij}^u . In addition, diagrams such as the lower left one of Fig. 5.5 also contribute at $\mathcal{O}(\tan^2 \beta)$ if one of the Higgs-quark couplings is enhanced by $\tan \beta$, while the second one features g^u . The contributions from these diagrams are only linear in g^u . On the other hand, it is easy to see that the insertions of flavour-changing self-energy diagrams cannot give contributions quadratic in g_{ij}^u . The only term of Σ_H that is quadratic is the $P_R \not{q}$ term $\Sigma_{LL,H}^{\text{III}}$. However, it has been shown in Section 4.3.2 that only Σ_{LR} and Σ_{RL} enter the calculation of the Wilson coefficients $C_{S,P}^{(\prime)}$ on general grounds, and thus the two-point diagrams are irrelevant for $C_{S,P}^{(\prime)}$ at order $\tan^2 \beta$ (g^u)².

We begin with the discussion of $C_{P,\tan^2 \beta}^{(\prime),\text{III}}$. The sum of all one-loop diagrams contributing to C_P is UV-divergent at order $\mathcal{O}(\tan^2 \beta)$, similar to the $\mathcal{O}(\tan \beta)$ terms of the self-energy diagrams. This divergence again needs to be cancelled by a counterterm to $g_{sb,bs}$. Inspecting Eq. (5.53), it is clear that the counterterm must be $\mathcal{O}(\tan \beta)$, in contrast to the $\mathcal{O}(\tan^2 \beta)$ counterterm presented in Eq. (5.56). At one loop, the $\mathcal{O}(\tan \beta)$ contributions to the counterterms to $g_{sb,bs}$ are given by

$$\begin{aligned} \delta^{(0)} g_{sb}^* &= \frac{1}{\epsilon} \frac{G_F v_{\text{SM}} m_b \tan \beta}{8\pi^2} Y_1, \\ \delta^{(0)} g_{bs} &= \frac{1}{\epsilon} \frac{G_F v_{\text{SM}} m_s \tan \beta}{8\pi^2} Y_1, \end{aligned} \quad (5.65)$$

where we have defined the combination Y_1 of Yukawa couplings for future use as

$$Y_1 \equiv \sum_{i,j,k=1}^3 V_{is} V_{jb}^* g_{ik}^* g_{jk}. \quad (5.66)$$

It is intriguing to observe that the UV pole can be written in this concise form after the sum of all diagrams has been taken. Consequently, one expects the explicit $\log\left(\frac{\mu^2}{m_t^2}\right)$ term to be proportional precisely to Y_1 . Indeed, with the insertion of the counterterm, the renormalised one-loop Wilson coefficients $C_{P,\tan^2 \beta}^{(0)\prime,\text{III}}$ read

$$\begin{aligned} C_{P,\tan^2 \beta}^{(0),\text{III}} &= -\frac{m_b m_\mu \tan^2 \beta}{8\sqrt{2} G_F M_{A^0}^2 M_W^2 V_{tb}^* V_{ts}} \cdot \left[\log(r_H) \left(Y_1 + \frac{r_H (Y_3 (-r_H) + Y_3 + Y_4 Y_-)}{(r_H - 1)^2} \right) \right. \\ &\quad \left. + Y_1 \log\left(\frac{\mu^2}{m_t^2}\right) + Y_1 - \frac{Y_4 Y_- r_H}{r_H - 1} \right], \end{aligned} \quad (5.67)$$

$$\begin{aligned} C_{P,\tan^2 \beta}^{(0)\prime,\text{III}} &= \frac{m_s m_\mu \tan^2 \beta}{8\sqrt{2} G_F M_{A^0}^2 M_W^2 V_{tb}^* V_{ts}} \cdot \left[\log(r_H) \left(Y_1 + \frac{r_H (Y_3' (-r_H) + Y_3' + Y_4' Y_-)}{(r_H - 1)^2} \right) \right. \\ &\quad \left. + Y_1 \log\left(\frac{\mu^2}{m_t^2}\right) + Y_1 - \frac{Y_4' Y_- r_H}{r_H - 1} \right], \end{aligned} \quad (5.68)$$

with the abbreviations

$$\begin{aligned}
 Y_3 &= \sum_{i=1}^3 \left[\sum_{j=1}^3 V_{is} V_{jb}^* g_{jt} g_{it}^* + V_{tb}^* \sum_{j=1}^2 V_{is} g_{tj} g_{ij}^* \right], \\
 Y_3' &= \sum_{j=1}^3 \left[\sum_{i=1}^3 V_{is} V_{jb}^* g_{it}^* g_{jt} + V_{ts} \sum_{i=1}^2 V_{jb}^* g_{ji} g_{ti}^* \right], \\
 Y_4 &= V_{tb}^* \sum_{i=1}^3 V_{is} g_{it}^*, \\
 Y_4' &= -V_{ts} \sum_{j=1}^3 V_{jb}^* g_{jt}, \\
 Y_{\pm} &= g_{tt} \pm g_{tt}^* = \begin{cases} 2 \operatorname{Re}(g_{tt}) \\ 2i \operatorname{Im}(g_{tt}) \end{cases}.
 \end{aligned} \tag{5.69}$$

At NLO QCD, the renormalisation procedure is again analogous to what was presented in Section 5.5. The two-loop counterterms in the $\overline{\text{MS}}$ renormalisation schemes are given by

$$\begin{aligned}
 \delta^{(1)} g_{sb}^* &= \left[\frac{4}{\epsilon^2} + \frac{10}{3\epsilon} \right] \frac{G_F v_{\text{SM}} m_b \tan\beta}{8\pi^2} Y_1, \\
 \delta^{(1)} g_{bs} &= \left[\frac{4}{\epsilon^2} + \frac{10}{3\epsilon} \right] \frac{G_F v_{\text{SM}} m_s \tan\beta}{8\pi^2} Y_1.
 \end{aligned} \tag{5.70}$$

With the ordinary QCD renormalisation of m_t and g_{ij} —again, $m_{b,s}$ do not need to be renormalised at NLO—the resulting finite counterterm-inserted two-loop Wilson coefficients are given by

$$\begin{aligned}
 C_{P,\tan^2\beta}^{(1),\text{III}} &= \frac{m_b m_\mu \tan^2\beta}{12\sqrt{2} G_F M_{A^0}^2 M_W^2 V_{tb}^* V_{ts}} \cdot \left[-12 Y_1 \log^2 \left(\frac{\mu^2}{m_t^2} \right) - (40 + 3\pi^2) Y_1 + \frac{6 Y_2 r_H}{r_H - 1} \right. \\
 &\quad + \log(r_H) \left(\frac{2r_H (3Y_2 (r_H^2 - 3r_H + 2) + Y_3 (17r_H^2 - 45r_H + 28) + 28Y_4 Y_-)}{(r_H - 1)^3} - 34Y_1 \right) \\
 &\quad + \log \left(\frac{\mu^2}{m_t^2} \right) \left(\log(r_H) \left(\frac{24r_H (Y_3 (r_H^2 - 3r_H + 2) + 2Y_4 Y_-)}{(r_H - 1)^3} - 24Y_1 \right) - 34Y_1 \right. \\
 &\quad \left. + \frac{24r_H (Y_3 (r_H - 1) + Y_4 Y_- (r_H - 3))}{(r_H - 1)^2} \right) + 12 Y_3 \operatorname{Li}_2 \left(\frac{r_H - 1}{r_H} \right) \\
 &\quad \left. - \frac{6 \log^2(r_H) (2Y_1 (r_H - 1)^3 + Y_3 (-2r_H^3 + 6r_H^2 - 5r_H + 1) - 2Y_4 Y_- r_H)}{(r_H - 1)^3} \right. \\
 &\quad \left. + \frac{22 Y_3 r_H}{r_H - 1} + 2\pi^2 Y_3 + \frac{8 Y_4 Y_- r_H (2r_H - 9)}{(r_H - 1)^2} \right],
 \end{aligned} \tag{5.71}$$

$$C_{P,\tan^2\beta}^{(1),\prime,\text{III}} = -\frac{m_s}{m_b} C_{P,\tan^2\beta}^{(1),\text{III}} \Big|_{Y_{2,3,4} \rightarrow Y_{2,3,4}'}. \tag{5.72}$$

In Eq. (5.71) we have introduced another combination of Yukawa couplings,

$$\begin{aligned} Y_2 &= V_{tb}^* \sum_{i=1}^3 V_{is} \sum_{j=1}^2 g_{tj} g_{ij}^*, \\ Y_2' &= V_{ts} \sum_{j=1}^3 V_{jb}^* \sum_{i=1}^2 g_{ji} g_{ti}^*. \end{aligned} \quad (5.73)$$

Comparing the one-loop and two-loop Wilson coefficients with the calculation in the type-II 2HDM or the contributions discussed previously in the present chapter it is striking that here the Yukawa couplings and loop functions cannot be separated into two factors. Previously all Wilson coefficients were proportional to powers of the top-quark mass m_t , which was due to the fact that the underlying Feynman diagrams are exactly the same set as in the type-II case. The Higgs-penguin diagrams are the only class to feature fundamentally new Feynman diagrams, namely the diagrams in the right of Fig. 5.5 with $u_i \neq \bar{u}_j$. As a result, contributions that are not proportional to m_t can arise and the Yukawa structure of the complete Wilson coefficients is much richer.

In the 2HDM with general scalar potential, diagrams with trilinear $H^\pm - H^\mp - A^0$ couplings also contribute to $C_P^{(\prime)}$. However, since we are restricting ourselves to the case of a CP-conserving scalar potential in which the neutral mass matrix is block-diagonal and $\lambda_7 \in \mathbb{R}$, those Feynman diagrams are absent, since this trilinear coupling vanishes. Hence, $C_P^{(\prime)}$ is independent of the parameters of the neutral Higgs sector, apart from the trivial dependence on $M_{A^0}^2$.

The scalar Wilson coefficients $C_{S,\tan^2\beta}^{(\prime),\text{III}}$ are more complex, but they can be decomposed into two contributions of different origin. We express the decomposition as

$$C_{S,\tan^2\beta}^{(\prime),\text{III}} = C_{S,\tan^2\beta,R_M}^{(\prime),\text{III}} + C_{S,\tan^2\beta,R_M'}^{(\prime),\text{III}}, \quad (5.74)$$

where R_M was defined in Eq. (5.54) and we will define R_M' when discussing the second term. The first term is analogous to the previous discussion of $C_{P,\tan^2\beta}^{(\prime),\text{III}}$ and it arises from the diagrams with a $\phi^{0'}$ propagating between the loop and the lepton line. One important conceptual difference is the presence of trilinear $\phi^{0'} - H^\pm - H^\mp$ couplings which introduce a non-trivial dependence on the parameters of the scalar potential. It is an important check that the counterterms derived in the context of $C_P^{(\prime)}$ in Eq. (5.65) also yield a finite result for the scalar coefficients $C_{S,R_M}^{(\prime)}$. Indeed, with these counterterms, we find the one-loop coefficient

$$\begin{aligned} C_{S,\tan^2\beta,R_M}^{(0),\text{III}} &= -\frac{m_b m_\mu R_M \tan^2\beta}{8\sqrt{2}G_F M_W^2 V_{tb}^* V_{ts}} \cdot \left[\log(r_H) \left(Y_1 + \frac{r_H \left(Y_3(-r_H) + Y_3 + Y_4 \left(Y_+ + r_H \text{Re}(\tilde{\lambda}_7) \right) \right)}{(r_H - 1)^2} \right) \right. \\ &\quad \left. + Y_1 \log\left(\frac{\mu^2}{m_t^2}\right) + Y_1 - \frac{Y_4 r_H \left(Y_+ + \text{Re}(\tilde{\lambda}_7) \right)}{r_H - 1} \right], \end{aligned} \quad (5.75)$$

$$C_{S,\tan^2\beta,R_M}^{(0),\text{III}} = -\frac{m_s m_\mu R_M \tan^2\beta}{8\sqrt{2}G_F M_W^2 V_{tb}^* V_{ts}} \cdot \left[\log(r_H) \left(Y_1 - \frac{r_H \left(Y_3' (r_H - 1) + Y_4' \left(Y_+ + r_H \text{Re}(\tilde{\lambda}_7) \right) \right)}{(r_H - 1)^2} \right) \right. \\ \left. + Y_1 \log\left(\frac{\mu^2}{m_t^2}\right) + Y_1 + \frac{Y_4' r_H \left(Y_+ + \text{Re}(\tilde{\lambda}_7) \right)}{r_H - 1} \right], \quad (5.76)$$

where we have introduced the dimensionless rescaled couplings

$$\tilde{\lambda}_i \equiv \frac{\lambda_i}{G_F m_t v_{\text{SM}}} \approx 2.15 \lambda_i. \quad (5.77)$$

By inspection of Eqs. (5.67), (5.75) and (5.76) it becomes evident that the one-loop coefficients satisfy the relatively simple relations

$$C_{S,\tan^2\beta,R_M}^{(0),\text{III}} \Big|_{\tilde{\lambda}_7 \rightarrow 0} = M_{A^0}^2 R_M C_{P,\tan^2\beta}^{(0),\text{III}} \Big|_{Y_- \rightarrow Y_+}, \quad \frac{m_s}{m_b} C_{S,\tan^2\beta,R_M}^{(0),\text{III}} = C_{S,\tan^2\beta,R_M}^{(0),\text{III}} \Big|_{\substack{Y_{3,4}' \rightarrow -Y_{3,4} \\ Y_2' \rightarrow Y_2}}. \quad (5.78)$$

Although Y_2' is not present in the one-loop coefficients, we make the replacement of Y_2' in the second relation, in anticipation of the two-loop results.

Proceeding to the $O(\alpha_s)$ coefficients, with the help of Eq. (5.70) we obtain a finite two-loop result, given by

$$C_{S,\tan^2\beta,R_M}^{(1),\text{III}} = \frac{m_b m_\mu R_M \tan^2\beta}{12\sqrt{2}G_F M_W^2 V_{tb}^* V_{ts}} \cdot \left[-12Y_1 \log^2\left(\frac{\mu^2}{m_t^2}\right) - (40 + 3\pi^2) Y_1 + \frac{6Y_2 r_H}{r_H - 1} \right. \\ \left. + \log(r_H) \left(\frac{2r_H (3Y_2 (r_H^2 - 3r_H + 2) + Y_3 (17r_H^2 - 45r_H + 28))}{(r_H - 1)^3} \right. \right. \\ \left. \left. + \frac{8r_H Y_4 (7Y_+ + 4r_H \text{Re}(\tilde{\lambda}_7) + 3\text{Re}(\tilde{\lambda}_7))}{(r_H - 1)^3} - 34Y_1 \right) + 12Y_3 \text{Li}_2\left(\frac{r_H - 1}{r_H}\right) \right. \\ \left. + \log\left(\frac{\mu^2}{m_t^2}\right) \left(\log(r_H) \left(\frac{24r_H (Y_3 (r_H^2 - 3r_H + 2) + 2Y_4 (Y_+ + r_H \text{Re}(\tilde{\lambda}_7)))}{(r_H - 1)^3} \right. \right. \right. \\ \left. \left. - 24Y_1 \right) - 34Y_1 + \frac{24r_H (Y_3 (r_H - 1) + Y_4 Y_+ (r_H - 3) - Y_4 (r_H + 1) \text{Re}(\tilde{\lambda}_7))}{(r_H - 1)^2} \right) \right. \\ \left. - \frac{6 \log^2(r_H)}{(r_H - 1)^3} \left(2Y_1 (r_H - 1)^3 + Y_3 (-2r_H^3 + 6r_H^2 - 5r_H + 1) - 2Y_4 r_H \left(Y_+ \right. \right. \right. \\ \left. \left. \left. + r_H \text{Re}(\tilde{\lambda}_7) \right) \right) + 2Y_3 \left(\frac{11r_H}{r_H - 1} + \pi^2 \right) \right]$$

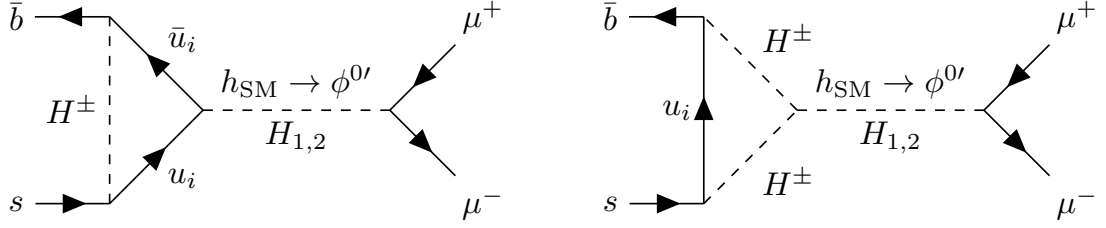


Figure 5.6.: Sample one-loop Feynman diagrams contributing to $C_{S, \tan^2 \beta, R'_M}^{(\prime), \text{III}}$. In the left diagram, the up-type quark couples to the SM-like Higgs boson $\phi^0 \equiv h_{\text{SM}}$, whereas the leptons couple to $\phi^{0'}$. The trilinear Higgs coupling in the right diagram also involves the SM Higgs boson. The fields $H_{1,2}$ denote the propagating (mass) eigenstates.

$$+ \left. \frac{8Y_4 r_H \left(Y_+ (2r_H - 9) - (2r_H + 5) \text{Re}(\tilde{\lambda}_7) \right)}{(r_H - 1)^2} \right], \quad (5.79)$$

$$C_{S, \tan^2 \beta, R'_M}^{(1)\prime, \text{III}} = \frac{m_s}{m_b} C_{S, \tan^2 \beta, R'_M}^{(1), \text{III}} \Big|_{\substack{Y_{3,4} \rightarrow -Y'_{3,4} \\ Y_2 \rightarrow Y'_2}}. \quad (5.80)$$

We now turn to the second term introduced in Eq. (5.74). An additional contribution of order $\mathcal{O}(\tan^2 \beta)$, proportional to

$$\frac{1}{M_{h^0 \phi^{0'}}^2} \equiv \frac{1}{M_{h_{\text{SM}} \phi^{0'}}^2} \equiv R'_M \equiv \frac{c_{\beta - \alpha} s_{\beta - \alpha} (M_{H_1}^2 - M_{H_2}^2)}{M_{H_1}^2 M_{H_2}^2}, \quad (5.81)$$

arises from Feynman diagrams such as the examples shown in Fig. 5.6, in which the lepton couples to the field $\phi^{0'}$, whereas the up-type internal quark in the loop of the left diagram couples to the SM-like Higgs boson $h^0 \equiv h_{\text{SM}}$. Since h_{SM} and $\phi^{0'}$ are in general not mass eigenstates, there is a non-vanishing transition probability for $h_{\text{SM}} \leftrightarrow \phi^{0'}$. This peculiar structure makes it possible for the lepton coupling to be enhanced with a factor $\tan \beta$, while the SM-like up-type quark coupling guarantees the absence of the cancelling factor $\cot \beta$ and instead provides an $\mathcal{O}(\tan^0 \beta)$ coupling. A second factor $\tan \beta$ originates from the $\bar{b} \bar{u}_i H^\pm$ coupling—for the primed coefficients the $su_i H^\pm$ coupling—and the remaining charged-Higgs coupling contributes with a single insertion of g^u . In the right diagram of Fig. 5.6, the trilinear $H^\pm - H^\mp - h_{\text{SM}}$ coupling is automatically of order $\mathcal{O}(\tan^0 \beta)$, and for the quark-Higgs couplings the same argument as above applies. As a result, the coefficients $C_{S, \tan^2 \beta, R'_M}^{(\prime), \text{III}}$ provide contributions exclusively linear in g^u at order $\mathcal{O}(\tan^2 \beta)$. This is in contrast to the previous discussions of $C_{S, \tan^2 \beta, R'_M}^{(\prime), \text{III}}$, in which all contributions but the ones proportional to $\tilde{\lambda}_7$ were quadratic in g_{ij}^u , and $C_{P, \tan^2 \beta}^{(\prime), \text{III}}$, in which all contributions were quadratic.

Upon calculation of the one-loop contributions proportional to $R'_M \tan^2 \beta$ one again encounters the recurring problem of UV divergences in the sum of all diagrams. The divergences must be cancelled by an appropriate counterterm inserted into the tree-level $g_{sb, bs}$ diagrams, of which

the R'_M part must be considered, which can be obtained from Eq. (5.53) by the replacement $R_M \tan \beta \rightarrow R'_M$ in the $C_S^{(\prime)}$ terms. The resulting tree-level diagram with the bare $g_{sb,bs}$ couplings is of order $\mathcal{O}(\tan^0 \beta)$, and hence an $\mathcal{O}(\tan^2 \beta)$ counterterm linear in g_{ij}^u is needed. However, such a counterterm was already calculated in the context of the $\mathcal{O}(\tan^3 \beta)$ contributions originating from the flavour-changing two-point functions in Section 5.5. Once we fix the renormalisation scheme to $\overline{\text{MS}}$, these counterterms have to be unique, and thus it is vital that the counterterms presented in Eqs. (5.56) and (5.61) are sufficient to cancel all UV divergences. Indeed, we find that this is the case and the renormalised Wilson coefficients at one loop are given by

$$C_{S,\tan^2 \beta,R'_M}^{(0),\text{III}} = \frac{Y_4 m_b m_\mu R'_M \tan^2 \beta}{16 G_F M_W^2 v_{\text{SM}} V_{tb}^* V_{ts}} \cdot \left[2m_t \log\left(\frac{\mu^2}{m_t^2}\right) + \frac{\log(r_H) \left(2m_t (r_H + 1) - \sqrt{2} r_H^2 \tilde{\lambda}_3 v_{\text{SM}}\right)}{(r_H - 1)^2} + \frac{\sqrt{2} r_H \tilde{\lambda}_3 v_{\text{SM}} - 2m_t (r_H + 1)}{r_H - 1} \right], \quad (5.82)$$

$$C_{S,\tan^2 \beta,R'_M}^{(0)\prime,\text{III}} = \frac{m_s}{m_b} C_{S,\tan^2 \beta,R'_M}^{(0),\text{III}} \Big|_{Y_4 \rightarrow -Y'_4}. \quad (5.83)$$

At NLO QCD the procedure is now straightforward, and we simply present the Wilson coefficients that are obtained after insertion of the two-loop counterterm and QCD renormalisation of all relevant parameters. They are given by

$$C_{S,\tan^2 \beta,R'_M}^{(1),\text{III}} = -\frac{Y_4 m_b m_\mu R'_M \tan^2 \beta}{12 G_F M_W^2 v_{\text{SM}} V_{tb}^* V_{ts}} \cdot \left[\log\left(\frac{\mu^2}{m_t^2}\right) \left(\frac{8m_t (4r_H^2 - 11r_H - 5) + 12\sqrt{2} r_H (r_H + 1) \tilde{\lambda}_3 v_{\text{SM}}}{(r_H - 1)^2} + \frac{24 \log(r_H) \left(3m_t r_H + m_t - \sqrt{2} r_H^2 \tilde{\lambda}_3 v_{\text{SM}}\right)}{(r_H - 1)^3} \right) - 12m_t \log^2\left(\frac{\mu^2}{m_t^2}\right) + 12m_t \text{Li}_2\left(\frac{r_H - 1}{r_H}\right) + \frac{6 \log^2(r_H) \left(3m_t r_H + m_t - \sqrt{2} r_H^2 \tilde{\lambda}_3 v_{\text{SM}}\right)}{(r_H - 1)^3} + \frac{4\sqrt{2} r_H (2r_H + 5) \tilde{\lambda}_3 v_{\text{SM}} - m_t (-16r_H^2 + \pi^2 (r_H - 1)^2 + 84r_H + 44)}{(r_H - 1)^2} + \frac{\log(r_H) \left(4m_t (3r_H^2 + 15r_H + 10) - 4\sqrt{2} r_H (4r_H + 3) \tilde{\lambda}_3 v_{\text{SM}}\right)}{(r_H - 1)^3} \right], \quad (5.84)$$

$$C_{S,\tan^2 \beta,R'_M}^{(1)\prime,\text{III}} = \frac{m_s}{m_b} C_{S,\tan^2 \beta,R'_M}^{(1),\text{III}} \Big|_{Y_4 \rightarrow -Y'_4}. \quad (5.85)$$

It is worth mentioning that the coefficients $C_{S,\tan^2 \beta,R'_M}^{(\prime),\text{III}}$ are proportional to powers of the top-quark mass, in contrast to $C_{S,\tan^2 \beta,R_M}^{(\prime),\text{III}}$ and $C_{P,\tan^2 \beta}^{(\prime),\text{III}}$. In the left diagram of Fig. 5.6, the SM-Higgs

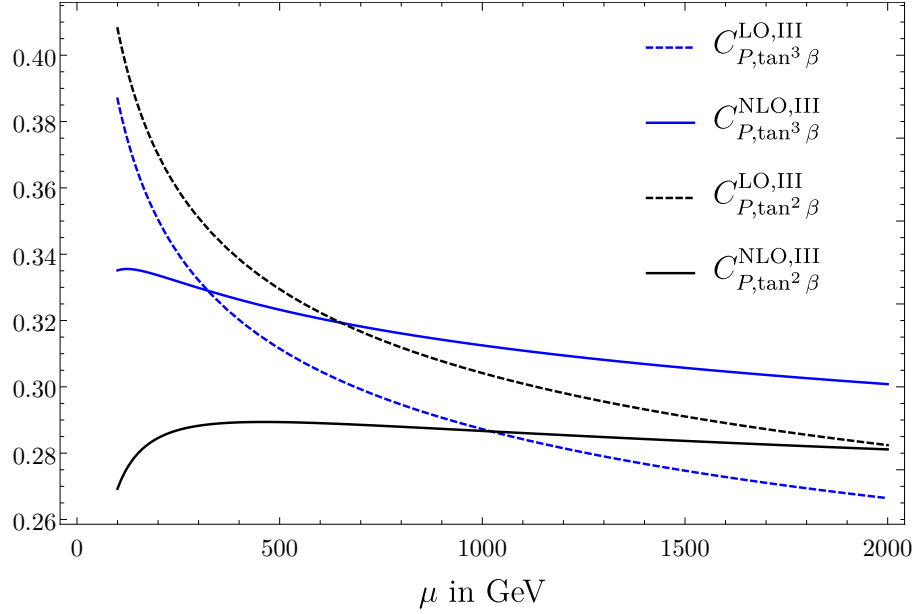


Figure 5.7.: Dependence of the Wilson coefficients $C_{P,\tan^{2,3}\beta}^{\text{III}}$ on the QCD renormalisation scale μ in leading order (LO) and next-to-leading order (NLO). These Wilson coefficients are given in arbitrary units, with an irrelevant choice of couplings $g_{ij}^u = g_{ij}^u(\bar{m}_t, \bar{m}_t)$. The relevant—i.e. non-factorising—parameters of the 2HDM were chosen as $\tan\beta = 50$ and $M_{H^\pm} = 1500$ GeV, the scale μ_{Yuk} of the Yukawa-type logarithms (see main text) was taken to be $\bar{m}_t(\bar{m}_t)$.

coupling to the internal up-type quark ensures at least one power of m_t , while in the right diagram the numerator of the top-quark propagator must contribute with m_t to guarantee an even power of slashed loop momenta. To our knowledge all Wilson coefficients shown within this section have been presented for the first time in this thesis.

Finally, we show the QCD renormalisation-scale dependence of the Wilson coefficients $C_{S,P,\tan^{2,3}\beta}^{\text{III}}$, i.e. of the Wilson coefficients that were renormalised using the counterterms from the spurion expansion, in Fig. 5.7. These coefficients explicitly depend on μ^2 already at LO through logarithms. However, it is clear that this μ dependence cannot be of QCD origin since no gluons are involved in the one-loop diagrams. Instead, they should be classified as *Yukawa-type logarithms*. In order to correctly illustrate the QCD scale dependence it is therefore necessary to carefully disentangle logarithms of different origin. Furthermore, it is necessary to choose a scale for the Yukawa-type logarithms, which we take to be $\bar{m}_t(\bar{m}_t)$. The resulting QCD scale dependence for some arbitrary initial values $g_{ij}^u(\bar{m}_t, \bar{m}_t)$ is shown in arbitrary units in Fig. 5.7.

5.7. Leading terms of Y_i

The general structure of the combinations of Yukawa couplings $Y_{1,\pm}, Y_{2,3,4}^{(\prime)}$ is quite involved, with Y_1 being a triple sum over flavour indices. However, assuming that all g_{ij}^u are of the same order

of magnitude, we can expand the $Y_i^{(\prime)}$ in terms of the Wolfenstein parameter, which should yield a sensible approximation to the exact results. Keeping only terms of order $O(\lambda_w^0)$, we can rewrite the combinations $Y_i^{(\prime)}$ as

$$\begin{aligned}
 Y_1 &= V_{cs} V_{tb}^* \sum_{k=1}^3 g_{ck}^* g_{tk} + O(\lambda_w) , \\
 Y_2 &= V_{cs} V_{tb}^* (g_{tu} g_{cu}^* + g_{tc} g_{cc}^*) + O(\lambda_w) , \\
 Y_3 &= V_{cs} V_{tb}^* \sum_{k=1}^3 g_{ck}^* g_{tk} + O(\lambda_w) = Y_1 + O(\lambda_w) , \\
 Y_3' &= V_{cs} V_{tb}^* g_{ct}^* g_{tt} + O(\lambda_w) , \\
 Y_4 &= V_{cs} V_{tb}^* g_{ct}^* + O(\lambda_w) , \\
 Y_2' &= Y_4' = O(\lambda_w) .
 \end{aligned} \tag{5.86}$$

The combinations Y_{\pm} are independent of the CKM matrix and therefore unaffected by the expansion.

5.8. A general observation on the structure of the counterterms in the three-spurion 2HDM

In Ref. [77] the structure of the counterterms $\delta g_{sb,bs}$ was discussed and a relation to the pole structure of the flavour-changing self-energy diagrams was presented. The presence of flavour-changing self-energy diagrams spoils the canonical normalisation of the quark kinetic terms in the Lagrangian, and in order to properly normalise these terms again, a field redefinition

$$q_i^{L,R} \rightarrow \left(\delta_{ij} + \frac{\Sigma_{ij}^{LL,RR}}{2} \right) q_j^{L,R} , \tag{5.87}$$

is necessary, where the flavour-changing two-point function Σ_{ji} describes a transition $q_i \rightarrow q_j$. The quark mass matrices are affected by this procedure as well: the mass terms $\sim \bar{q}_L q_R$ receive a contribution from the Σ^{LR} part of the self-energy, as well as from the “re-normalisation” of the kinetic terms [77, 81, 82]. It was argued by the authors of Ref. [77] that the divergent parts of these self-energy terms are sufficient in order to construct counterterms to the couplings $g_{sb,bs}$ that remove all divergences occurring for $b \rightarrow sl^+ l^-$ transitions.

We confirm the finding of Ref. [77] with the calculation presented within this thesis. Indeed, the counterterms $\delta^{(0)} g_{sb,bs}$ can be written as

$$\begin{aligned}
 \delta^{(0)} g_{sb}^* &= -\frac{1}{\epsilon} 4G_F v_{SM} m_b \tan \beta \left(\Sigma_{bs}^{LL} + \frac{\Sigma_{bs}^{RL}}{2m_b} \right) \Big|_{\text{div.}} , \\
 \delta^{(0)} g_{bs} &= -\frac{1}{\epsilon} 4G_F v_{SM} m_s \tan \beta \left(\Sigma_{bs}^{LL} + \frac{\Sigma_{bs}^{LR}}{2m_s} \right) \Big|_{\text{div.}} ,
 \end{aligned} \tag{5.88}$$

where div. denotes the coefficient of the UV poles. In particular, the divergent part of Σ_{bs}^{LL} is proportional to Y_1 and does not feature any other of the abbreviations $Y_{2,\dots,4}$, Y_{\pm} introduced above, which is exactly the pattern observed in the UV divergences left over after summing all 1LPI penguin diagrams. Our calculation including $\mathcal{O}(\alpha_s)$ QCD corrections provides explicit confirmation of the statements made in Ref. [77].

5.9. The decay $B_d \rightarrow \mu^+ \mu^-$

We add a short discussion of the decays $B_d \rightarrow \mu^+ \mu^-$. In the SM and 2HDM of type II, it is obvious that the Wilson coefficients for this decay can be obtained simply by the replacements $V_{ts} \rightarrow V_{td}$ and $m_s \rightarrow m_d$. Compared to $B_s \rightarrow \mu^+ \mu^-$, in which we considered also small effects proportional to $m_s \neq 0$, the down-quark mass m_d is yet much smaller and all contributions proportional to m_d are truly negligible. Furthermore, $V_{tb}^* V_{td} \sim \lambda^3$, and hence contributions from g_{ij}^u proportional to $V_{ud} V_{tb}^*$ could be potentially enhanced by $\lambda^{-3} \approx 90$, depending on the size of the relevant flavour-changing Yukawa couplings. Constraints regarding these couplings will be discussed in the following chapter. The Wilson coefficients for the case $B_d \rightarrow \mu^+ \mu^-$ can be obtained from the ones presented in this chapter by the simple replacements

$$m_s \rightarrow m_d \approx 0, \quad V_{is} \rightarrow V_{id}, \quad g_{sb} \rightarrow g_{db}, \quad g_{bs} \rightarrow g_{bd}, \quad (5.89)$$

with no further replacements of the sums of flavour-changing Yukawa couplings necessary. The lepton flavour only enters through the factor $(m_l \tan \beta)^n$, and hence within a type-II-like lepton sector the replacement $\mu \rightarrow e, \tau$ is trivially implemented.

Similarly to Section 5.7, we expand the combinations Y_i in terms of the Wolfenstein parameter and find

$$\begin{aligned} Y_1 &= V_{ud} V_{tb}^* \sum_{k=0}^3 g_{tk} g_{uk}^* + \mathcal{O}(\lambda_w), \\ Y_2 &= V_{ud} V_{tb}^* (g_{tu} g_{uu}^* + g_{tc} g_{uc}^*) + \mathcal{O}(\lambda_w), \\ Y_3 &= Y_1 + \mathcal{O}(\lambda_w), \\ Y_4 &= V_{ud} V_{tb}^* g_{ut}^* + \mathcal{O}(\lambda_w), \\ Y_3' &= V_{ud} V_{tb}^* g_{ut}^* g_{tt} + \mathcal{O}(\lambda_w), \\ Y_2' &= Y_4' = \mathcal{O}(\lambda_w). \end{aligned} \quad (5.90)$$

This concludes the discussion of the Wilson coefficients in 2HDMs with flavour-changing up-type Yukawa couplings. In addition to the computation of the bare coefficients we have discussed the renormalisation of the minimal three-spurion 2HDM in some detail. The next chapter will host a survey of some of the most relevant constraints experiments with B mesons can put on the couplings g_{ij}^u .

6. Phenomenology of g^u

In the previous chapter we presented the leading contributions of the flavour-changing couplings g^u to the Wilson coefficients, where “leading” refers to the counting of powers of $\tan\beta$ and the light-quark Yukawa masses $m_{b,s}$. Now we discuss a list of phenomenological constraints for these couplings.

6.1. Collider Higgs searches

The large experiments at the LHC carry out a diverse program of searches for additional spin-0 particles and decays of (pseudo)scalar particles. Experimental evidence has by now become quite convincing that the mass eigenstate H_{125} observed by ATLAS [1] and CMS [2] with a mass of 125.38(14) GeV (CMS [83]) or 125.17(14) GeV (ATLAS [84]) fulfills the properties of the Higgs boson of the Standard Model. For example, a search for CP violation in the decay kinematics and vector-boson fusion production of the Higgs boson with decay chain $H_{125} \rightarrow ZZ^* \rightarrow 4l$ ($l = e$ or μ) was conducted by the ATLAS collaboration on the Run-2 data of 139 fb^{-1} taken at $\sqrt{s} = 13 \text{ TeV}$ [85], where CP-odd couplings were expressed within an EFT setup. This analysis found no signs for CP violation and thus full compatibility with the SM. Higgs-fermion Yukawa couplings to top quarks and τ leptons were also probed and found to be consistent with the SM expectation of CP-even couplings in [86–89], although sizeable CP-odd components are not fully excluded yet due to rather large uncertainties. For example, CMS measured the mixing angle between CP-even and CP-odd Higgs- τ Yukawa couplings to be $-1 \pm 19 \text{ deg}$, with the statistical uncertainty dominating the total one, excluding a purely CP-odd Yukawa coupling at around 3σ [88]. Furthermore, searches for flavour-violating decays of the 125 GeV boson, mainly in the lepton sector, i.e. decays into $e\mu, e\tau, \mu\tau$ pairs, were presented in Refs. [90–93]. All of these analyses found no significant excess above the background-only hypothesis, in agreement with SM expectations. In Ref. [90], Higgs-boson decays into e^+e^- pairs were also searched for, with no excess found. Contrasting the decays into $l_i^+l_j^-$, $i \neq j$, the decay into electron-positron pairs is predicted by the SM, however with an extremely tiny branching fraction $\sim 5 \cdot 10^{-9}$ [90], due to the small electron Yukawa coupling, and hence is expected to be unobservable by LHC. Thus, in this aspect, the decay into electron-positron can be regarded similarly to the lepton-flavour violating decays, i.e. any observation of this decay mode would be an immediate proof of new physics. The couplings to third-generation fermions and massive vector bosons have shown remarkable agreement with the SM predictions, see Fig. 6.1 [94, 95], while evidence has been reported for Higgs-boson decays into muons at CMS [96]. In summary, the 125 GeV scalar mass eigenstate satisfies all requirements of the SM Higgs boson and in the following phenomenological analysis we will therefore identify one of the two mass eigenstate, H_1 , of the 2HDM with the SM Higgs $h^0 \equiv \phi^0 \equiv h_{\text{SM}}$ boson and assign a mass of $\approx 125 \text{ GeV}$ to it, see e.g.

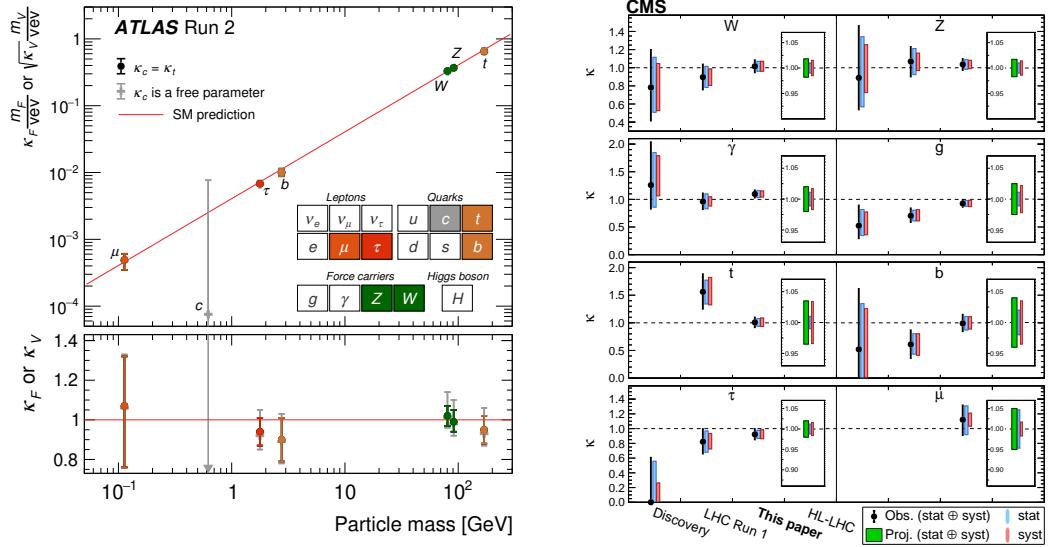


Figure 6.1.: (Left) ATLAS combined measurements of Higgs couplings to fermions and massive gauge bosons in the so-called κ framework [97], taken from Ref. [94]. The values $\kappa_i = 1$ correspond to the SM prediction. (Right) CMS projections for future measurements of the Higgs couplings at the HL-LHC. The black dots and error bars show the observed values, where applicable, whereas the green rectangles illustrate the projected sensitivity; taken from Ref. [95].

also Fig. 2.1 for the constraint on the mixing angles between mass eigenstates and $h_{SM}, \phi^{0'}$. This identification amounts to $\sin(\beta - \alpha) = 1 \Rightarrow \cos(\beta - \alpha) = 0$ and eliminates the contribution to $B_s \rightarrow \mu^+ \mu^-$ from $C_{S, \tan^2 \beta, R'_M}^{(\prime), III}$.

Turning to Higgs bosons beyond the SM, for our model featuring large Yukawa couplings and large $\tan \beta$ discussed within this thesis, searches for heavy additional scalar bosons are more important than searches for light resonances, although there is also an active program in the lighter sector, e.g. searches for sub-125 GeV diphoton or dilepton resonances [98, 99]. These lighter resonances are, however, typically interpreted in the context of dark photons or axion-like particles, rather than within the 2HDM. Within the 2HDM, we will limit our attention to searches for additional Higgs bosons heavier than 125 GeV, some examples of which we will mention in the following. All of these searches have in common that to date no significant excess in any of the production and decay channels considered has been observed. Consequently, in most cases an upper limit on the product of production cross section and subsequent decay is derived, the detailed interpretation of which in terms of model parameters of course depends on the model at hand then. Many analyses search for resonances in an invariant mass spectrum of a certain final state containing SM particles. If a decay chain of a heavy boson into this particular final state exists, the invariant mass spectrum can have a narrow peak, depending on the mass resolution for the reconstruction of the invariant mass.

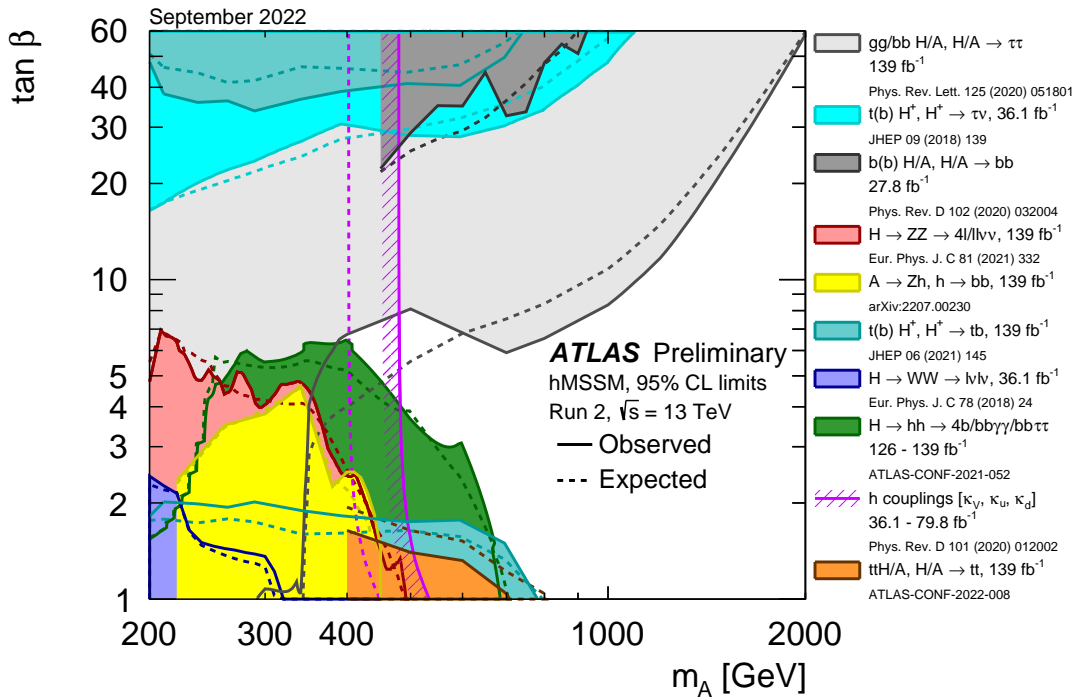


Figure 6.2.: Exclusion limits for the pair of parameters $\tan\beta, M_{A^0}$ in the so-called “habemus MSSM? (hMSSM)” (see main text). All coloured regions are excluded. Taken from Ref. [124].

An excellent mass resolution is offered e.g. by diphoton final states, and several searches have been performed for heavy resonances X decaying either directly into two photons [100] or via e.g. two SM Higgs bosons into $\bar{b}b\gamma\gamma$ [101]. In the latter case, the second Higgs boson is required to decay into a pair of bottom quarks since the branching ratio is still large enough to be sensitive to effects of heavy resonances, see e.g. also the search for decays into two $\bar{b}b$ pairs [102]. Further analyses include the decays chains $X \rightarrow ZZ^*(WW^*) \rightarrow$ quarks or leptons [103–107], associated Higgs- $Z(W)$ production [108–110], decays of charged Higgs bosons into third-generation fermions [111–114], as well as decays of neutral Higgs bosons into $t\bar{t}$, $b\bar{b}$, or $\tau^+\tau^-$ pairs [115–121], and many more [12, 122, 123].

The plethora of searches for additional Higgs bosons culminates in summary plots such as the one by the ATLAS collaboration [124] shown in Fig. 6.2. Constraints in terms of certain parameters of a model are certainly valid in the strict sense only within the model they were derived for. The exclusion limits in Fig. 6.2 were derived for the so-called *habemus MSSM?* (hMSSM) [125–127], a variant of the minimal supersymmetric standard model (MSSM) that takes into account the existence of the 125 GeV boson. It was shown in Refs. [125, 128, 129] that in the hMSSM many parameters of the MSSM can be traded in approximately for the measured mass of the observed Higgs boson, such that the resulting simplified model depends only on $\tan\beta$ and M_{A^0} , even to higher loop orders. This simplified model approximately corresponds

to the type-II 2HDM at tree level, and is therefore rather close to our three-spurion 2HDM. In supersymmetric models $\epsilon^d \neq 0$ and $\epsilon^u \neq 0$ are induced by loop corrections and one can arrange for $|\epsilon^d| \ll |\epsilon^u|$. The presence of the flavour-changing Yukawa couplings generally modifies the exclusion bounds. However, since all relevant collider constraints shown in Fig. 6.2 stem from processes involving neutral Higgs bosons, which—in contrast to the charged Higgs bosons—do not feature CKM enhancement factors in their couplings to fermions, we consider the exclusion limits largely valid. Corrections of $\mathcal{O}(10 - 20\%)$ are still feasible, depending on the size and structure of the couplings g_{ij}^u , and we thus do not take these bounds as literal limits, but we will follow the general picture, e.g. that large values $\tan\beta \gtrsim 30$ require heavy Higgs bosons $M_{A^0} \gtrsim 1.5$ TeV. In particular, constraints from the decay of heavy Higgs bosons into τ lepton pairs give the most stringent constraints for large values of $\tan\beta$.

6.2. Perturbativity of the quartic couplings and the Higgs-boson mass spectrum

At large values of $\tan\beta$, the collider constraints discussed in the previous section require a heavy A^0 Higgs boson. It becomes clear from Eq. (2.8) and Eq. (2.9) that the splittings between the masses squared of the Higgs bosons are of order $\lambda_i v_{\text{SM}}$, where λ_i are the various quartic couplings in the Higgs scalar potential. The quartic couplings should be of order $|\lambda_i| \lesssim 4$ in order for the theory to be perturbative, and a multitude of studies of perturbativity and unitarity of the 2HDM have been performed in the past [130–143].¹ Regardless of their precise values, at large A^0 masses the differences between the Higgs-boson masses become rather small, e.g. for $M_{A^0} = 1.5$ TeV and $\lambda_4 - \lambda_5 = 10$ one finds with Eq. (2.8) that $M_{A^0} - M_{H^\pm} \approx 100$ GeV. A more detailed analysis of the mass differences can be found e.g. in Fig. 6 of Ref. [130], where a global fit including also experimental constraints was performed. In the following analysis, we will adhere rather closely to the bounds derived in that reference, although the detailed numerical values of the perturbativity bounds differ between different studies. For very large values of $\tan\beta$, implying large values of the Higgs-boson masses $M_{H_i} \gtrsim 1.5$ TeV, these bounds will inevitably entail small relative mass differences of $\lesssim 5\%$.

6.3. Perturbativity of Yukawa couplings

Analogously to the scalar couplings, the Yukawa couplings are also bounded by the requirement of perturbativity. Typical upper limits imposed in the literature are in the region $|g_{ij}^{u,d}| \leq \sqrt{4\pi}$ [130], or somewhat smaller. These constraints are motivated by the practical requirement that perturbation theory should still hold, i.e. that $(n+1)$ -loop amplitudes do not exceed the n -loop amplitudes in magnitude, and in particular, that tree-level amplitudes should be the dominant contribution to amplitudes that do not vanish at tree-level. However, in the processes discussed within this thesis, large effects typically occur even with rather small numerical

¹The omission of one-loop bounds from $2 \rightarrow 2$ scattering processes weakens the constraints to $|\lambda_i| \lesssim 4\pi$. For our purpose the constraint $|\lambda_i| \lesssim 4$ is the relevant one, although we also show the more relaxed 4π contours in some figures, for example in Fig. 4.10.

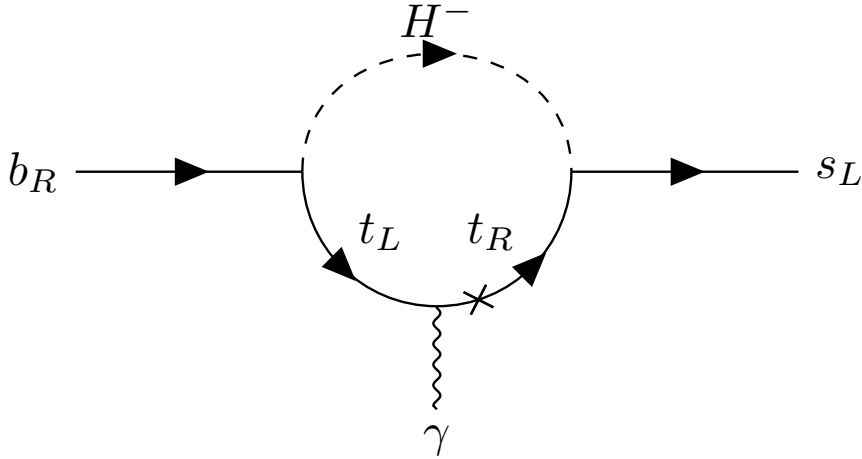


Figure 6.3.: Sample one-loop Feynman diagram for the rare decay $b \rightarrow s\gamma$ in the 2HDM. The cross indicates a chirality flip $t_L \rightarrow t_R$.

values of $|g_{ij}^u|$, due to the large enhancement factors by $\tan\beta \gg 1$ and $\frac{V_{cs,us}}{V_{ts}} \gg 1$. For example, large values of the coupling g_{ct} are therefore excluded by experimental constraints, well before the perturbativity bounds become relevant. The notable exception discussed in Section 6.5 are the tree-level contributions to the $B_s-\bar{B}_s$ mixing arising from two insertions of the tree-level couplings $g_{sb,bs}$ introduced in the context of the spurion expansion, which are neither CKM-enhanced nor carry additional factors of $\tan\beta$, as well as the constraints on the $\tan\beta$ - and CKM-suppressed coupling g_{tc} discussed in Section 6.6.2. Still, as shown in Section 6.5, also for the constraints on $g_{sb,bs}$ experimental bounds are much stronger than the upper limits from perturbativity.

6.4. $b \rightarrow s\gamma$

The rare decays $B \rightarrow X_s\gamma$, where X_s denotes an inclusive sum over all hadrons containing a strange quark, are mediated at the quark level through a top-quark loop with a W^\pm boson in the SM. In the 2HDM, these processes receive further contributions through diagrams involving a charged Higgs boson instead of W^\pm , see Fig. 6.3. Hence, they can provide an important constraint on the magnitude of some of the flavour-changing Yukawa couplings g_{ij}^u [144]. Instead of using the branching ratio $\mathcal{B}(b \rightarrow s\gamma)$ it is tradition to work with the ratio

$$R_\gamma \equiv \frac{\mathcal{B}(b \rightarrow s\gamma) + \mathcal{B}(b \rightarrow d\gamma)}{\mathcal{B}(b \rightarrow cl\nu)}, \quad (6.1)$$

in order to reduce the parametric uncertainty, where $\mathcal{B}(b \rightarrow cl\nu)$ is the CP- and isospin-averaged inclusive semi-leptonic branching ratio [145, 146]. This procedure is equivalent to using $|V_{cb}|$ from inclusive decays in the prediction of $|V_{ts}|$ entering $\mathcal{B}(B \rightarrow X_s\gamma)$. In the early days of $b \rightarrow s\gamma$ phenomenology also m_b was poorly known and R_γ reduces the m_b dependence

compared to $\mathcal{B}(B \rightarrow X_s \gamma)$. Nowadays, this is not an issue anymore. Within the SM and the type-II 2HDM, the branching ratio of $b \rightarrow d \gamma$ is much smaller than that of $b \rightarrow s \gamma$, due to the smaller CKM factor entering the top-down-quark vertex. The three-spurion 2HDM considered within this thesis does not have CKM suppression in this vertex, and thus both $\mathcal{B}(b \rightarrow s \gamma)$ and $\mathcal{B}(b \rightarrow d \gamma)$ can be comparable in size. In the following we will discuss the cases $q = s$ and $q = d$ separately. For the discussion of $q = s$, we will assume that R_γ is given by the decay into a strange quark exclusively, while for $q = d$ we will assume that the 2HDM contribution is entirely given by the decay into a down quark, while the SM contribution remains dominated by the decay $b \rightarrow s \gamma$. The bounds derived in this fashion are then rather conservative and will become even stronger if both $\mathcal{B}(b \rightarrow s \gamma)$ and $\mathcal{B}(b \rightarrow d \gamma)$ contribute to R_γ .

In Ref. [146], an experimental average value of R_γ was determined as

$$R_{\gamma,\text{exp.}} = (3.22 \pm 0.15) \cdot 10^{-3}, \quad (6.2)$$

where a minimum photon energy of $E^0 \geq 1.6$ GeV was imposed. On the theory side, NNLO calculations for the branching ratio in terms of Wilson coefficients are available both in the SM [145, 147–152] as well as in the 2HDM [146, 153–159]. We use the theory prediction of [146]

$$R_{\gamma,\text{SM}} = (3.31 \pm 0.22) \cdot 10^{-3}, \quad (6.3)$$

with the same lower photon energy cutoff $E_0 \geq 1.6$ GeV, for our analysis.² In the type-II 2HDM the charged-Higgs diagrams constructively interfere with the SM amplitude, enhancing the branching ratio and moving it away from the experimental average of Eq. (6.2), see Fig. 6.4. Furthermore, in the type-II 2HDM the amplitude for $b \rightarrow s \gamma$ can be written as

$$\mathcal{A} \sim a_1 m_b m_t + a_2 m_t^2 \cot^2 \beta + a_3 m_s m_b \tan^2 \beta + a_4 m_s m_t. \quad (6.4)$$

Dropping the terms proportional to m_s arising from the right-handed strange quark, as is commonly done [159], the amplitude starts at $\mathcal{O}(\tan^0 \beta)$ and becomes practically independent of $\tan \beta$ already for moderately large values $\tan \beta \gtrsim 3$, see e.g. Fig. 5 of Ref. [159]. In the context of the type-II model, this independence of $\tan \beta$ effectively reduces the number of undetermined parameters of the 2HDM relevant for $b \rightarrow s \gamma$ to a single one, M_{H^\pm} , which could then be constrained with the help of precise SM predictions and the experimental value. A lower 95 % confidence limit of

$$M_{H^\pm} \geq 570 \text{ GeV} - 800 \text{ GeV} \quad (6.5)$$

was then found in Ref. [146], the exact value depending on whether the confidence interval is being placed centrally or shifted towards one of the sides.

In the general 2HDM, the factor $\tan \beta$ from the btH^- vertex is not necessarily cancelled by a corresponding factor $\cot \beta$ from the tsH^- vertex, and consequently the quantity R_γ depends

²A more recent value of $R_\gamma = (3.35 \pm 0.16) \cdot 10^{-3}$ was presented in Ref. [160]. However, using this value implies a change of the approximate relation of Ref. [145] that is used later. Since the central values of both references are in good agreement, we will use the value quoted in the main text. The larger uncertainty of the value used in this analysis makes the constraints slightly more conservative.

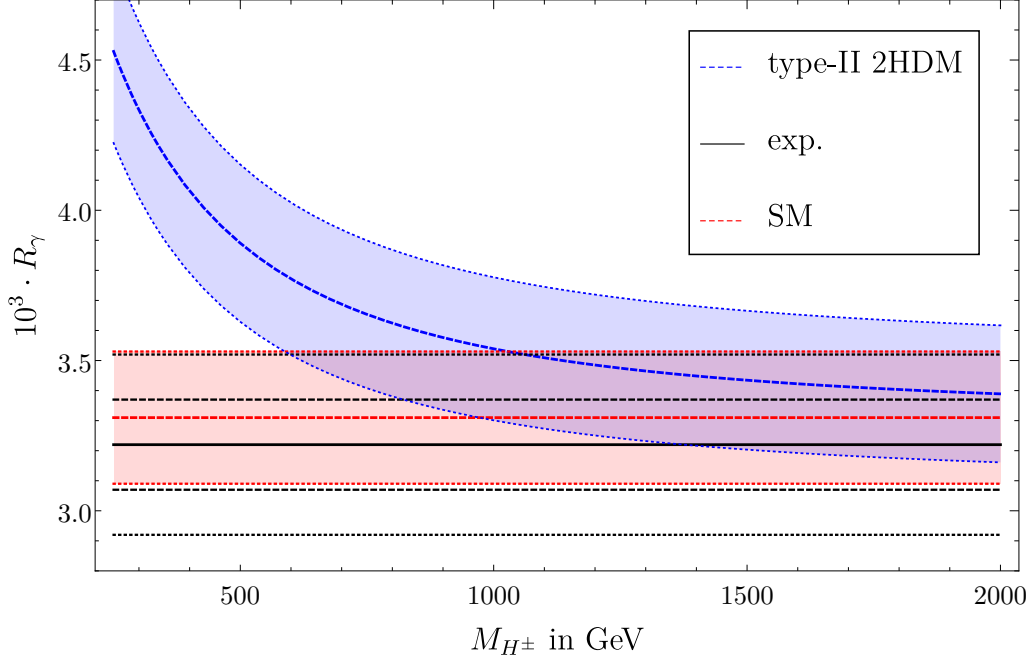


Figure 6.4.: The branching ratio R_γ as a function of M_{H^\pm} . The red lines and band show the SM prediction including the relative uncertainty of 6.7% [146], the black lines depict the experimental central value and the $\pm 1\sigma$ and $\pm 2\sigma$ deviations [146]. The blue lines and band correspond to the prediction in the type-II 2HDM with 6.7% uncertainty bands [145, 146]. This prediction has been obtained for $\tan\beta = 20$, but as discussed in the main text, the dependence on $\tan\beta$ is negligible for $\tan\beta \gtrsim 3$.

on $\tan\beta$. The relevant combination of the $\bar{t}_L b_R H^\pm$ and $\bar{s}_L t_R H^\mp$ Yukawa couplings arising in the decay $b \rightarrow s\gamma$ is then

$$\left(\frac{\sqrt{2}m_b \tan\beta V_{tb}}{v_{\text{SM}}} \right) \left(\frac{\sqrt{2}m_t V_{ts}^*}{v_{\text{SM}} \tan\beta} + V_{ts}^* g_{tt} + V_{cs}^* g_{ct} + V_{us}^* g_{ut} \right) \equiv \frac{2m_b m_t V_{tb} V_{ts}^*}{v_{\text{SM}}^2} (1 + g_{st}^{\text{eff}}), \quad (6.6)$$

where we have defined the short-hand notation

$$g_{st}^{\text{eff}} \equiv \frac{v_{\text{SM}} \tan\beta}{\sqrt{2}m_t} \left(g_{ut} \frac{V_{us}^*}{V_{ts}^*} + g_{ct} \frac{V_{cs}^*}{V_{ts}^*} + g_{tt} \right). \quad (6.7)$$

The different factors $\sqrt{2}$ of Eqs. (6.6) and (6.7) compared to the definitions in Ref. [80] are due to different choices for the normalisation of the VEV. However, the numerical values of g_{st}^{eff} are unaffected by the freedom to redefine the VEV and thus comparable between this thesis and Ref. [80]. Furthermore, in Ref. [80], effects of g_{ut} were not considered. They are only enhanced by one power of the Wolfenstein parameter λ instead of the λ^2 enhancement of the g_{ct} terms. The effective g_{st}^{eff} coupling is chosen such that the limit $g_{st}^{\text{eff}} = 0$ corresponds to the type-II 2HDM, while the SM limit of the $b \rightarrow s\gamma$ amplitude is obtained with $g_{st}^{\text{eff}} = -1$. Comparing with e.g.

Eq. (5.57) one notices that $g_{st}^{\text{eff}*}$ is proportional to exactly the combination of Yukawa couplings arising in the $\tan^3 \beta$ Wilson coefficients; the reason is of course the presence of the same $s_L t_R H^\pm$ vertex. It should also be noted that g_{st}^{eff} carries an explicit factor of $\tan \beta$. With the appropriate rescaling of the Yukawa couplings as shown in Eq. (6.6) we can directly adopt the approximate formula presented in Ref. [145] for R_Y in the presence of new physics (NP) contributions ΔC_i to the Wilson coefficients C_7 and C_8 of the operators [151]

$$Q_7 = \frac{em_b}{16\pi^2} (\bar{s}_L \sigma_{\mu\nu} b_R) F^{\mu\nu}, \quad Q_8 = \frac{g_s m_b}{16\pi^2} (\bar{s}_L \sigma_{\mu\nu} T^a b_R) G^{a,\mu\nu}, \quad (6.8)$$

together with the Wilson coefficients presented in Ref. [159]. The approximate formula in Ref. [145] was derived assuming that only the interference between the NP and SM contributions is relevant, i.e. that terms quadratic in the NP contributions can be discarded. In particular, since the SM Wilson coefficients are real (up to possibly a global CKM prefactor), the approximate formula allows to constrain the real part of g_{st}^{eff} only. Since the full three-loop NNLO results [159] are rather long, we derive an approximate relation,

$$\begin{aligned} R_Y \approx 10^{-4} \cdot \left\{ 33.10|_{\text{SM}} + \left(1 + \text{Re } g_{st}^{\text{eff}}\right) \left[\right. \right. \\ \left. \left. \begin{aligned} & \left(-0.15 \log^3(r_H) - 1.00 \log^2(r_H) - 47.63 \log(r_H) + 4.72 \text{Li}_2\left(1 - \frac{1}{r_H}\right) - 48.96\right) r_H \\ & + \left(-0.10 \log^3(r_H) - 2.07 \log^2(r_H) - 98.25 \log(r_H) + 4.80 \text{Li}_2\left(1 - \frac{1}{r_H}\right) - 53.88\right) r_H^2 \\ & + \left(0.06 \log^3(r_H) - 2.37 \log^2(r_H) - 150.57 \log(r_H) + 3.18 \text{Li}_2\left(1 - \frac{1}{r_H}\right) - 56.11\right) r_H^3 \\ & \left. - 0.13 \text{Li}_2\left(1 - \frac{1}{r_H}\right) r_H^4 \right] \right\}, \end{aligned} \quad (6.9)$$

for faster numerical evaluation, by expanding in the small ratio $r_H = m_t^2/M_{H^\pm}^2 \ll 1$. We will comment on the quality of this numerical approximation below. In deriving Eq. (6.9) the renormalisation scale μ was fixed as $\mu = \bar{m}_t$ (\bar{m}_t). The assessment of theoretical uncertainties of Ref. [146] yields a total uncertainty of about 6.7%, being shared between individual non-perturbative uncertainties (5%), parametric uncertainties (1.5%), uncertainties from missing higher-order corrections (3%), and an uncertainty (3%) from interpolation in the charm-quark mass m_c . For the 2HDM value of R_Y , we employ the same relative estimate of uncertainties, i.e. we take them to be given by 6.7% of the respective M_{H^\pm} -dependent value.

In Fig. 6.5 we illustrate the variation of the ratio R_Y for different numerical parameters in the $(M_{H^\pm}, \text{Re } g_{st}^{\text{eff}})$ plane. Different background colours indicate the different values of R_Y obtained for a fixed combination of M_{H^\pm} and $\text{Re } g_{st}^{\text{eff}}$. The thick dashed blue (“isobaric”) line shows the central experimental value given in Eq. (6.2), whereas the thinner blue lines show the quantity $R_{Y,\text{exp.}} \pm \Delta_{\text{exp.+th.}}$, where

$$\Delta_{\text{exp.+th.}} = 2\sigma_{\text{exp.}} + \delta_{\text{th.}} \quad (6.10)$$

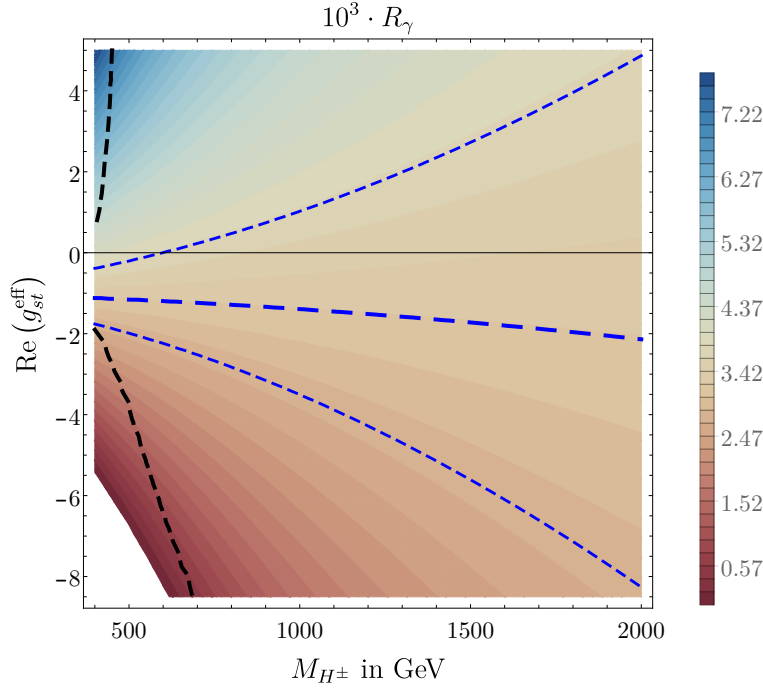


Figure 6.5.: Coloured bands show the regions of equal values of R_γ (“isobaric lines”) depending on M_{H^\pm} and $\text{Re } g_{st}^{\text{eff}}$. The region that is theoretically and experimentally feasible is delimited by the blue dashed lines, where the thick dashed line shows the experimental central value and the thinner dashed lines are obtained by adding the sum of experimental 2σ and theoretical uncertainties to the experimental central value. The region left of the dashed black lines illustrates the region in which the relative error of the approximate formula in Eq. (6.9) is larger than 1%. The bounds from perturbativity of the Yukawa couplings are not shown as they lie well outside the intervals shown here.

is the sum of the experimental 2σ uncertainties and the relative theoretical uncertainty of 6.7% discussed above. At rather small values of M_{H^\pm} , the excellent agreement between the SM prediction and the central experimental value as well as the rather large corrections of the type-II 2HDM force $\text{Re } g_{st}^{\text{eff}}$ to be rather close to -1 , i.e. to approximately cancel the complete type-II correction. For example, if $M_{H^\pm} = 400$ GeV, the allowed range for $\text{Re } g_{st}^{\text{eff}}$ is only $\approx [-1.7, -0.3]$. Roughly half of the allowed interval is due to the 6.7% theoretical uncertainty for $M_{H^\pm} = 400$ GeV. The dashed black line is the contour line where the approximate formula in Eq. (6.9) deviates by more than 1% from the exact expression. In this region the expansion parameter m_t/M_{H^\pm} is rather large and the few terms presented above are not sufficient for a good approximation, such that in the region left of this line Eq. (6.9) should not be used. However, we find that Eq. (6.9) is an excellent approximation in the complete relevant region delimited by the dashed blue lines representing the current uncertainties.

Due to the perturbativity bounds discussed in Section 6.3 $|g_{st}^{\text{eff}}| \geq |\text{Re } g_{st}^{\text{eff}}|$ cannot be arbitrarily large. However, restricting all Yukawa couplings on the right-hand side of Eq. (6.7) to be absolutely bounded by $\sqrt{4\pi}$ one finds an upper bound on g_{st}^{eff} of approximately

$$|g_{st}^{\text{eff}}| \lesssim \tan \beta \left| \frac{V_{us}^* + V_{cs}^* + V_{ts}^*}{V_{ts}^*} \right| \sqrt{4\pi} \approx 30 \tan \beta \sqrt{4\pi}. \quad (6.11)$$

Even for very low values of $\tan \beta \approx 1$ the perturbativity bound on $|g_{st}^{\text{eff}}|$ is very large, $\mathcal{O}(100)$. In the absence of a quite high lower limit on $|\text{Im } g_{st}^{\text{eff}}|$ we interpret the upper limit on $|g_{st}^{\text{eff}}|$ as an upper limit on $|\text{Re } g_{st}^{\text{eff}}|$. This rather large limit is of course due to the fact that in the SM and the 2HDM of type II the decay $b \rightarrow sy$ is severely CKM-suppressed and that experimental precision matches the accuracy of the theory prediction. Thus, the perturbativity bound never has the chance of competing with the exclusion constraints stemming from the disagreement between theory and experiment, and we do not show them in the figure.

Figure 6.5 allows to derive M_{H^\pm} -dependent upper and lower limits on the real part of $g_{st}^{\text{eff}} \equiv g_{st}^{\text{eff}}(\bar{m}_t, \bar{m}_t)$ by requiring R_Y to be between the two thin dashed lines. These constraints are independent of $\tan \beta$, but by Eq. (6.7) it is clear that the recasting into constraints on g_{ij}^u makes the latter $\tan \beta$ -dependent, as expected once R_Y becomes $\tan \beta$ -dependent itself.

6.5. B_s - \bar{B}_s mixing

The neutral B_q and \bar{B}_q mesons, where $q = d, s$, are not identical to the mass eigenstates, and can therefore mix. Their oscillations are characterised by two quantities, the decay width difference and the mass difference of the heavy (H) and light (L) mass eigenstates

$$\Delta\Gamma_q = \Gamma_L^q - \Gamma_H^q, \quad (6.12)$$

$$\Delta M_q = M_H^q - M_L^q. \quad (6.13)$$

The total decay rates $\Gamma_{L,H}^q$ can only involve particles that can be produced on-shell, i.e. that are lighter than the B_q meson. In particular, no Feynman diagrams with top quarks contribute. By the optical theorem, it can be obtained by computing the absorptive part of the $B_q \rightarrow \bar{B}_q$ transition amplitude, which is found from the full amplitude by replacing the loop integral by its imaginary part. The calculation of $\Delta\Gamma_q$ involves the matching of the SM to an effective $|\Delta B| = 1$ Hamiltonian [161–164] and a subsequent operator product expansion (OPE) in terms of local $|\Delta B| = 2$ four-quark operators [165–172], and has been performed at NNLO accuracy in QCD recently [173]. On the other hand, the mass difference ΔM_q is obtained from the real part of the transition amplitude and is sensitive to effects of heavy particles, including the top quark and possible additional Higgs bosons. In the SM the only effective four-quark operator relevant for ΔM_s is

$$Q_{VLL} = (\bar{b}_L \gamma_\mu s_L) \otimes (\bar{b}_L \gamma^\mu s_L), \quad (6.14)$$

the Wilson coefficient of which is known including NLO QCD corrections [162]. Similarly to $B_s \rightarrow l^+ l^-$, the decay proceeds in the SM through loop diagrams—in the case of mixing only W -box diagrams—and is therefore heavily suppressed with a Wilson coefficient $\sim G_F^2 (V_{tb}^* V_{ts})^2$.

In extensions of the SM in which e.g. a discrete symmetry forbids flavour-changing neutral currents at tree level, such as the 2HDM of type II, this property is preserved. However, once flavour-changing Yukawa couplings are introduced in the down-type sector, tree-level Feynman diagrams contributing to the $B_s-\bar{B}_s$ mixing are possible. In light of the three-spurion 2HDM considered within this thesis, in which the couplings $g_{sb,bs}$ and their Yukawa-type counterterms need to be introduced in the context of the spurion expansion, a discussion of the constraints from $B_s-\bar{B}_s$ mixing is necessary.

In order to assess the possible constraints from $B_s-\bar{B}_s$ mixing, we use the effective $|\Delta B| = |\Delta S| = 1$ Hamiltonian

$$\begin{aligned} \mathcal{H}_{\text{eff},2\text{HDM}}^{|\Delta B|=|\Delta S|=1} = & \Gamma_{bsZ}^L \bar{b}_L \gamma_\mu s_L Z^\mu + \Gamma_{bsZ}^R \bar{b}_R \gamma_\mu s_R Z^\mu + \Gamma_{bsA^0}^L \bar{b}_R s_L A^0 + \Gamma_{bsA^0}^R \bar{b}_L s_R A^0 \\ & + \Gamma_{bs\phi^{0'}}^L \bar{b}_R s_L \phi^{0'} + \Gamma_{bs\phi^{0'}}^R \bar{b}_L s_R \phi^{0'} + \Gamma_{bsh^0}^L \bar{b}_R s_L h^0 + \Gamma_{bsh^0}^R \bar{b}_L s_R h^0 + \text{h.c.} . \end{aligned} \quad (6.15)$$

The effective couplings $\Gamma_{bsX}^{L/R}$, $X = Z, A^0, \phi^{0'}, h^0 \equiv h_{\text{SM}}$, can be obtained straightforwardly from the Wilson coefficients of $B_s \rightarrow \mu^+ \mu^-$ by removing the leptonic fermion line and the internal boson propagator. Their structure is thus analogous to the Wilson coefficients presented in the preceding chapter; we list the effective couplings in Appendix B. It should be noted that in Eq. (6.15) the pseudoscalar A^0 does not carry a prefactor of i , in contrast to e.g. the Lagrangian density in Eq. (2.27). The Feynman rule for the insertion of any of the effective $\bar{b}sX$ vertices is therefore given by $-i\Gamma_{bsX}^{L/R}$. In the presence of $g_{sb,bs}$, tree-level contributions to $\Gamma_{bs\phi^{0'}}^{L/R}$ and $\Gamma_{bsA^0}^{L/R}$ arise, while the couplings $\Gamma_{bsZ}^{L/R}$ and $\Gamma_{bsh^0}^{L/R}$ are purely loop-induced due to the flavour-diagonal couplings of the Z -boson and $h^0 \equiv h_{\text{SM}}$ -Yukawa couplings. While the contributions involving h_{SM} to $B_s \rightarrow \mu^+ \mu^-$ vanish in the alignment limit at order $\mathcal{O}(\tan^2 \beta)$, they still arise in the B_s mixing via a double insertion of the effective $\bar{b}s h^0$ vertex. The coupling Γ_{bsZ}^R is purely of type-II origin, since we consistently neglected effects of g^d within loops in the calculation of the Wilson coefficients. In the left-handed Γ_{bsZ}^L coupling type-II contributions as well as contributions involving g^u arise. Both effective couplings are gauge-independent. On the other hand, the type-II-like contributions to $\Gamma_{bs\phi^{0'}}^{L/R}$ ($\Gamma_{bsA^0}^{L/R}$) are extracted from the Wilson coefficients presented in Eqs. (4.59) to (4.65) and (4.67). In Section 4.3 we explicitly discussed the gauge dependence of the individual classes of Feynman diagrams, and we showed that only with the addition of the contributions from the mixed $W^\pm-H^\mp$ box diagrams the corresponding Wilson coefficients are gauge-independent. Since the contributions from box diagrams are one-particle-irreducible (1PI), it is not possible to separate an effective $|\Delta B| = |\Delta S| = 1$ vertex without reference to the second fermion line. If we included the type-II-like contributions to $\Gamma_{bs\phi^{0'}}^{L/R}$ ($\Gamma_{bsA^0}^{L/R}$) they would therefore be gauge-dependent. Hence, we only show the terms involving flavour-changing Yukawa couplings in the effective couplings to the Higgs bosons $A^0, \phi^{0'}$, and h^0 . With the effective couplings, we can construct contributions to the effective Hamiltonian for $\Delta M_s^{2\text{HDM}}$ by double insertions,³ see Fig. 6.6. In the 2HDM, the effective Hamiltonian for $\Delta M_s^{2\text{HDM}}$ can be written as

$$\begin{aligned} \mathcal{H}_{\text{eff},2\text{HDM}}^{\Delta M_s} = & C_{VLL} (\bar{b}_L \gamma_\mu s_L) \otimes (\bar{b}_L \gamma^\mu s_L) + C_{VRR} (\bar{b}_R \gamma_\mu s_R) \otimes (\bar{b}_R \gamma^\mu s_R) + C_{VLR} (\bar{b}_L \gamma_\mu s_L) \otimes (\bar{b}_R \gamma^\mu s_R) \\ & + C_{SLL} (\bar{b}_R s_L) \otimes (\bar{b}_R s_L) + C_{SRR} (\bar{b}_L s_R) \otimes (\bar{b}_L s_R) + C_{SLR} (\bar{b}_R s_L) \otimes (\bar{b}_L s_R) . \end{aligned} \quad (6.16)$$

³The superscript “2HDM” denotes the additional contributions to ΔM_s within the 2HDM.

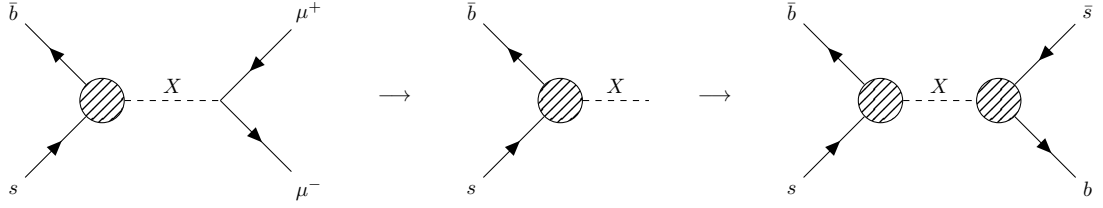


Figure 6.6.: Construction of the contributions to $B_s - \bar{B}_s$ mixing from the effective vertices extracted from $B_s \rightarrow \mu^+ \mu^-$. The particle X denotes $Z, A^0, \phi^{0'}, h^0 \equiv \phi^0 \equiv h_{\text{SM}}$.

The effective operators are named Q_i , where i is the subscript of the Wilson coefficient. The coefficients can be obtained by matching $\mathcal{H}_{\text{eff},2\text{HDM}}^{\Delta M_s}$ to the double insertion of $\mathcal{H}_{\text{eff},2\text{HDM}}^{|\Delta B|=|\Delta S|=1}$,

$$\begin{aligned}
 \mathcal{M}_{2\text{HDM}}^{\Delta M_s} &= - \left\langle \mathcal{H}_{\text{eff},2\text{HDM}}^{\Delta M_s} \right\rangle \\
 &= \left[\frac{\left(\Gamma_{bs\phi^{0'}}^L \right)^2}{M_{\phi^{0'}}^2} + \frac{\left(\Gamma_{bsA^0}^L \right)^2}{M_{A^0}^2} + \frac{\left(\Gamma_{bsh^0}^L \right)^2}{M_{h^0}^2} \right] \langle P_L \otimes P_L \rangle \\
 &\quad + \left[\frac{\left(\Gamma_{bs\phi^{0'}}^R \right)^2}{M_{\phi^{0'}}^2} + \frac{\left(\Gamma_{bsA^0}^R \right)^2}{M_{A^0}^2} + \frac{\left(\Gamma_{bsh^0}^R \right)^2}{M_{h^0}^2} \right] \langle P_R \otimes P_R \rangle \\
 &\quad + \left[\frac{\Gamma_{bs\phi^{0'}}^L \Gamma_{bs\phi^{0'}}^R}{M_{\phi^{0'}}^2} + \frac{\Gamma_{bsA^0}^L \Gamma_{bsA^0}^R}{M_{A^0}^2} + \frac{\Gamma_{bsh^0}^L \Gamma_{bsh^0}^R}{M_{h^0}^2} \right] \langle (P_L \otimes P_R + P_R \otimes P_L) \rangle \\
 &\quad - \frac{1}{M_Z^2} \left[\left(\Gamma_{bsZ}^L \right)^2 \langle \gamma_\mu P_L \otimes \gamma^\mu P_L \rangle + \left(\Gamma_{bsZ}^R \right)^2 \langle \gamma_\mu P_R \otimes \gamma^\mu P_R \rangle \right. \\
 &\quad \left. + \Gamma_{bsZ}^L \Gamma_{bsZ}^R \langle (\gamma_\mu P_L \otimes \gamma^\mu P_R + \gamma_\mu P_R \otimes \gamma^\mu P_L) \rangle \right]. \tag{6.17}
 \end{aligned}$$

As mentioned above we restrict ourselves to the alignment limit in which h_{SM} and $\phi^{0'}$ propagate independently. In Eq. (6.16) colour indices are contracted within the parentheses. Gluon corrections connecting the two external quark lines also lead to the introduction of operators of the form $(\bar{b}^i \Gamma^j s^j) \otimes (\bar{b}^k \Gamma'^l s_l)$ in Eq. (6.16). However, since we do not compute these additional 1PI Feynman diagrams within this thesis, we neglect the additional operators. Consequently, we also restrict ourselves to the LO effective couplings $\Gamma_{bsX}^{L/R}$.

From the effective couplings listed in Appendix B it can be seen that the Wilson coefficient C_{SLL} is proportional to m_b^2 , while C_{SLR} and C_{SLL} are parametrically suppressed by factors of m_s/m_b and m_s^2/m_b^2 , respectively. However, at order $\mathcal{O}(\tan^2 \beta)$ the effective left-handed A^0 and $\phi^{0'}$ couplings are related by $\Gamma_{bsA^0,2,k}^L = i \Gamma_{bs\phi^{0'},2,k}^L$. In the limit $M_{A^0} \rightarrow M_{\phi^{0'}}$, the contributions from $\Gamma_{bsA^0}^L$ and $\Gamma_{bs\phi^{0'}}^L$ therefore cancel at this order, and the Wilson coefficient C_{SLL} is suppressed, since $\Gamma_{bsh^0}^{L/R}$ is of order $\mathcal{O}(\tan \beta)$ only. At order $\mathcal{O}(\tan \beta)$ the couplings $\Gamma_{bsA^0}^L$ and $\Gamma_{bs\phi^{0'}}^L$ differ as well, due to the scalar couplings and $Y_- \neq Y_+$. Thus, for large $\tan \beta$ and close values of

Table 6.1.: Hadronic matrix elements of the four-quark operators for $B_s - \bar{B}_s$ and $B_d - \bar{B}_d$ mixing in GeV^3 , taken from Table 13.1 of Ref. [178], see also Ref. [179].

	$\langle \bar{B}_q Q_{VLR}(\bar{m}_t(\bar{m}_t)) B_q \rangle$	$\langle \bar{B}_q Q_{SLL}(\bar{m}_t(\bar{m}_t)) B_q \rangle$	$\langle \bar{B}_q Q_{SLR}(\bar{m}_t(\bar{m}_t)) B_q \rangle$
B_s	-0.30	-0.14	0.40
B_d	-0.21	-0.095	0.27

$M_{A^0} \approx M_{\phi^0}$, C_{SLL} becomes rather small and the $\mathcal{O}(m_b m_s)$ coefficient C_{SLR} becomes important. This behaviour is due to the fact that the operator Q_{SLL} (and Q_{SRR}) is a $|\Delta Y| = 2$ operator, where $Y = 1$ is the hypercharge of the Higgs bosons, and is thus suppressed by $v_{SM}^2/M_{A^0}^2$ compared to the hypercharge-conserving operator Q_{SLR} , a phenomenon studied in Refs. [81, 174–176]. On the other hand, the coefficient $C_{SRR} \sim m_s^2$ can always be neglected. An additional contribution to C_{VLL} is given by H^\pm -box diagrams with g_{ij}^μ couplings, for which we use the LO one-loop Wilson coefficient presented in Ref. [177].

The mass difference $\Delta M_s^{2\text{HDM}}$ is given by

$$\Delta M_s^{2\text{HDM}} \approx 2\text{Re} \left(\langle \bar{B}_s | \mathcal{H}_{\text{eff},2\text{HDM}}^{\Delta M_s} | B_s \rangle \right) = 2 \sum_i \text{Re}(C_i) \langle \bar{B}_s | Q_i | B_s \rangle, \quad (6.18)$$

with the hadronic matrix element expressed in terms of the leptonic decay constant f_{B_s} and a *bag parameter* $B_{B_s}(\mu_b)$ evaluated at $\mu_b \approx \bar{m}_b(\bar{m}_b)$ [28, 180, 181],

$$\langle \bar{B}_s | Q_{VLL}(\mu_b) | B_s \rangle \equiv \frac{1}{3} B_{B_s}(\mu_b) f_{B_s}^2 M_{B_s} \approx \frac{1}{3} (0.2561 \text{ GeV})^2 M_{B_s}. \quad (6.19)$$

The Wilson coefficients in Eq. (6.16) are however taken at the matching scale of the $B_s \rightarrow \mu^+ \mu^-$ calculation, $\mu \approx \bar{m}_t$. In order to evaluate Wilson coefficients and matrix elements at the same scale, we choose to evolve $\langle Q_{VLL} \rangle$ from $\bar{m}_b(\bar{m}_b)$ to $\bar{m}_t(\bar{m}_t)$ using the LO RGE for $n_f = 5$ active quark flavours

$$\frac{\langle \bar{B}_s | Q_{VLL}(\mu_1) | B_s \rangle}{\langle \bar{B}_s | Q_{VLL}(\mu_0) | B_s \rangle} = \left(\frac{\alpha_s^{(5)}(\mu_1)}{\alpha_s^{(5)}(\mu_0)} \right)^{-\frac{6}{23}}, \quad (6.20)$$

leading to an increase by about 20 % at \bar{m}_t . For the operators $Q_{VLR,SLL,SLR}$ we use the matrix elements shown in Tab. 13.1 of Ref. [178], which were obtained in Ref. [179] and are shown for completeness in Table 6.1. These matrix elements are already given at the scale \bar{m}_t , and hence no RGE evolution is necessary. The matrix elements of $Q_{VRR,SRR}$ are the same as of their *LL* counterparts since QCD does not distinguish between left-handed and right-handed quark fields.

With the full formula Eq. (6.17) for $\Delta M_s^{2\text{HDM}}$ and the full effective couplings shown in Appendix B it is clear that in its most generic form $\Delta M_s^{2\text{HDM}}$ depends on all of the flavour-changing up-type Yukawa couplings, and therefore the $B_s - \bar{B}_s$ mixing is insufficient to constrain all of these couplings individually. However, since the bulk of the g_{ij}^μ enter through vertices with a charged Higgs boson, the hierarchy of the CKM matrix can be employed in order to retain only the couplings with the largest numerical impact, assuming that the g_{ij}^μ in Eq. (2.27) are roughly of

the same magnitude. In this approximation the rare decay $b \rightarrow sy$ presented in Section 6.4 yields an M_{H^\pm} -dependent upper bound on $\tan \beta \cdot |\operatorname{Re}(g_{ct})|$, which receives $\operatorname{Re}(g_{ut})/\operatorname{Re}(g_{ct}) \cdot \mathcal{O}(20\%)$ CKM-suppressed corrections depending on the size of g_{ut} . Thus, assuming that $|\operatorname{Im}(g_{ct})|$ is of the same order of magnitude as the real part, we obtain an upper limit on $|g_{ct}|$. Finally, considering only the leading term in the expansion in terms of the Wolfenstein parameter, see Section 5.7, the number of elements g_{ij}^u can be significantly reduced. For the remaining flavour-changing couplings we again assume $\mathcal{O}(g_{ij}^u) = \mathcal{O}(g_{ct})$, such that the effective couplings of Appendix B are functions of a single flavour-changing parameter $g_{ct} \equiv g_{ct}(\tan \beta, M_{H^\pm})$. Both these approximations are of course somewhat ad hoc and should be supplemented with correction factors to allow for deviations from $|\operatorname{Im}(g_{ct})| = |\operatorname{Re}(g_{ct})|$ and $|g_{ij}^u| = |g_{ct}|$. From the practical point of view it is easiest to use these two relations exactly and replace all g_{ij}^u by $|g_{ct}|_{\max}$, and then rescale $|g_{ct}|_{\max}$ in order to account for deviations.

The first question that should be addressed concerns the impact of the tree-level flavour-changing down-type Yukawa couplings $g_{sb,bs}$. In order to estimate their maximal size we consider only the tree-level contributions to $\Gamma_{bsA^0(\phi^{0'})}$. The mass difference ΔM_s is then given by

$$\begin{aligned} \Delta M_s^{2\text{HDM}} = & \left[-2.13 \cdot 10^5 \operatorname{Re}(g_{sb}^{*2}) \left[\left(\frac{1 \text{ TeV}}{M_{A^0}} \right)^2 - \left(\frac{1 \text{ TeV}}{M_{\phi^{0'}}} \right)^2 \right] \right. \\ & \left. - 6.08 \cdot 10^5 \operatorname{Re}(g_{sb}^* g_{bs}) \left[\left(\frac{1 \text{ TeV}}{M_{A^0}} \right)^2 + \left(\frac{1 \text{ TeV}}{M_{\phi^{0'}}} \right)^2 \right] \right] \text{ps}^{-1}. \end{aligned} \quad (6.21)$$

The maximal difference between the squared masses,

$$M_{\phi^{0'}}^2 - M_{A^0}^2 \lesssim 4v_{\text{SM}}^2, \quad (6.22)$$

is bounded by the requirement of perturbativity of the scalar couplings $|\lambda_i|$ [130]. However, this bound needs not be saturated. In order to account for non-saturation of the bound, we define a parameter γ through the relation

$$M_{\phi^{0'}}^2 - M_{A^0}^2 \equiv -4\gamma v_{\text{SM}}^2, \quad (6.23)$$

with $\gamma \in [-1, 1]$, thus fixing $M_{\phi^{0'}}$ in terms of M_{A^0} for fixed γ .⁴ Furthermore, the spurion expansion Eq. (5.52) implies that after diagonalising the Yukawa matrices $Y^{u,d}$ the couplings $g_{sb,bs}$ are proportional to

$$g_{sb} \sim m_b, \quad (6.24)$$

$$g_{bs} \sim m_s \sim \frac{m_s}{m_b} g_{sb}. \quad (6.25)$$

⁴In general, $M_{\phi^{0'}}^2 - M_{A^0}^2$ is a much more complicated function than $M_{H^\pm}^2 - M_{A^0}^2$ that depends on several parameters of the Higgs potential simultaneously, see e.g. Refs. [138, 182]. However, the mass difference is still bounded, and for the purposes of this thesis the numerical values of the Higgs masses are more relevant than the parameters of the potential, and hence we estimate the mass difference directly.

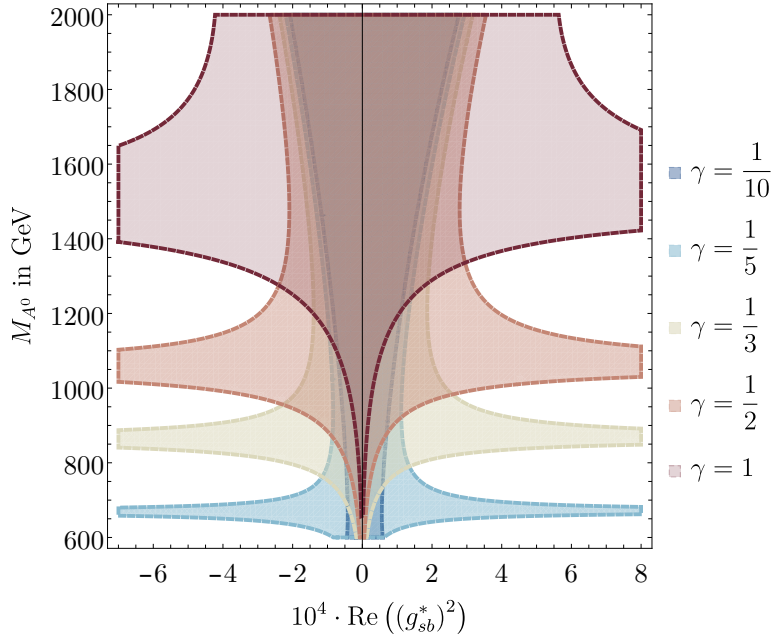


Figure 6.7.: Allowed regions (in different colours) in the $(\text{Re}(g_{sb}^{*2}), M_{A^0})$ plane, for different values γ of the splitting between the squared masses. The parameter α (see main text) is chosen to be $\frac{1}{50}$.

Hence, g_{bs} is suppressed by $\sim m_s/m_b$ compared to g_{sb} , very much in the same way as the right-handed effective Γ_{bsX} couplings at higher powers of $\tan\beta$ are explicitly m_s/m_b -suppressed compared to the left-handed ones. We thus also fix $\text{Re}(g_{sb}^*g_{bs}) = \alpha \text{Re}(g_{sb}^{*2})$, with α of order $\mathcal{O}\left(\frac{\bar{m}_s(\bar{m}_t)}{\bar{m}_b(\bar{m}_t)}\right) \sim \frac{1}{50}$ and real.⁵ The numerical parameter α should not be larger than a few percent. With this, the tree-level effects to $\Delta M_s^{2\text{HDM}}$ depend on $\text{Re}(g_{sb}^{*2})$ and M_{A^0} only, and we show the allowed regions in Fig. 6.7 for $\alpha = \frac{1}{50}$ and different values of γ . In order to obtain the boundaries of these regions, we required that the 2HDM contribution to ΔM_s , with only the insertion of the $g_{sb,bs}$ couplings, does not exceed the current SM uncertainty⁶ of still $\mathcal{O}(8\%)$ [183],

$$\Delta M_s = (20.1_{-1.6}^{+1.2}) \text{ps}^{-1}. \quad (6.26)$$

For other values of α we show analogous exclusion plots in Fig. C.1 in Appendix C. Depending on the separation between M_{ϕ^0} and M_{A^0} there is a small window in which $\mathcal{O}(5\%)$ couplings

⁵For complex $\alpha \in \mathbb{C}$, the approximate formula for $2\text{Re} M_{12,s}^{2\text{HDM}} = 2\text{Re}\left(\langle \bar{B}_s | \mathcal{H}_{\text{eff},2\text{HDM}}^{\Delta M_s} | B_s \rangle\right)$ is shown in Eq. (C.2). Note that with a generic value of α any complex g_{bs} can be expressed in terms of g_{sb} and the couplings g_{sb} and g_{bs} can be arbitrary. The relation between the two couplings is encoded in $|\alpha| \sim \frac{1}{50}$, which suppresses the contributions proportional to g_{bs} . In leading approximation it is therefore irrelevant whether α is real or complex.

⁶We do not take into account the fact that the most recent SM central value lies outside the experimentally measured interval. This difference would be reflected in a slight horizontal shift in Fig. 6.7.

g_{sb} are allowed, in the remaining region the bounds are stronger, $\sqrt{|\operatorname{Re}(g_{sb}^{*2})|} \lesssim 2.5 \cdot 10^{-2}$. In the following we will not consider these small regions in which “fine-tuning” between $M_{\phi^{0r}}$ and M_{A^0} occurs. The constraints from $B_s - \bar{B}_s$ mixing were also discussed in Ref. [184], where bounds on the product $\operatorname{Re}(g_{sb}^* g_{bs})$ were derived. In that reference it was argued that if the Peccei-Quinn $U(1)_{\text{PQ}}$ symmetry of the 2HDM is conserved only the mixed term C_{SLR} survives, and the bounds were derived under this assumption. Here, we consider also the deviation from the symmetry limit ($M_{\phi^{0r}} = M_{A^0}$), and obtain bounds on C_{SLL} through $\operatorname{Re}(g_{sb}^{*2})$, at the expense of having to make assumptions on the ratio α . While a direct comparison with the findings of Ref. [184] is therefore difficult, we still find constraints of the same order of magnitude.

The phase of

$$M_{12,s}^{2\text{HDM}} \equiv \langle \bar{B}_s | \mathcal{H}_{\text{eff},2\text{HDM}}^{\Delta M_s} | B_s \rangle \quad (6.27)$$

can be used in order to constrain the imaginary part of g_{sb}^2 . In the SM, $\arg M_{12,s} = -2\beta_s$, with $-2\beta_s = -0.03686_{-0.0009}^{+0.0007}$ [185–187].⁷ NP modifies the phase of $M_{12,s}$ according to

$$\begin{aligned} \arg M_{12,s} &= \arctan \left(\frac{\operatorname{Im} M_{12,s}}{\operatorname{Re} M_{12,s}} \right) = \arctan \left(\frac{\operatorname{Im} M_{12,s}^{\text{SM}} + \operatorname{Im} M_{12,s}^{2\text{HDM}}}{\operatorname{Re} M_{12,s}^{\text{SM}} + \operatorname{Re} M_{12,s}^{2\text{HDM}}} \right) \\ &\approx \arctan \left(\sin(2\beta_s) + \frac{2\operatorname{Im} M_{12,s}^{2\text{HDM}}}{\Delta M_s^{\text{exp}}} \right), \end{aligned} \quad (6.28)$$

where we have neglected the 2HDM contributions to $\operatorname{Re} M_{12,s}$ in the denominator and used the experimental value $\Delta M_s^{\text{exp}} = 17.765(6) \text{ ps}^{-1}$ [3, 188–194] for the mass difference. Thus,

$$\operatorname{Im} M_{12,s}^{2\text{HDM}} = \frac{\Delta M_s^{\text{exp}}}{2} [\tan(\phi_s) - \sin(-2\beta_s)], \quad (6.29)$$

which can be used together with the recent measurement $\phi_s = -0.039 \pm 0.023$ [185] in order to constrain $\operatorname{Im} M_{12,s}^{2\text{HDM}}$. Taking into account the 2σ uncertainties of ϕ_s and $-2\beta_s$ and setting $g_{bs} = \alpha g_{sb}^*$ with $\alpha \in \mathbb{C}$, $|\alpha| \sim \frac{1}{50}$, we therefore find the constraint

$$\begin{aligned} -0.45 \text{ ps}^{-1} &\leq \frac{1 \text{ ps}^{-1}}{2} \left\{ 2.13 \cdot 10^5 \left[\left(\frac{1 \text{ TeV}}{M_{\phi^{0r}}} \right)^2 - \left(\frac{1 \text{ TeV}}{M_{A^0}} \right)^2 \right] [\operatorname{Im}(\alpha^2) \operatorname{Re}(g_{sb}^2) \right. \\ &\quad \left. - \operatorname{Im}(g_{sb}^2) (1 - \operatorname{Im}^2(\alpha) + \operatorname{Re}^2(\alpha))] \right. \\ &\quad \left. + 6.08 \cdot 10^5 \left[\left(\frac{1 \text{ TeV}}{M_{\phi^{0r}}} \right)^2 + \left(\frac{1 \text{ TeV}}{M_{A^0}} \right)^2 \right] [\operatorname{Re}(\alpha) \operatorname{Im}(g_{sb}^2) - \operatorname{Im}(\alpha) \operatorname{Re}(g_{sb}^2)] \right\} \\ &\leq 0.40 \text{ ps}^{-1}. \end{aligned} \quad (6.30)$$

Another question that naturally poses itself concerns the possible size of the $\mathcal{O}(\tan\beta)$ terms of the effective $\bar{b}sA^0$ (ϕ^{0r}) couplings with respect to their $\mathcal{O}(\tan^2\beta)$ counterparts. With the approximation described above, it is possible to evaluate the ratio $\Gamma_{bsX,1}^L / \Gamma_{bsX,2}^L$ numerically. In

⁷The updated results on the CKMfitter home page have been used.

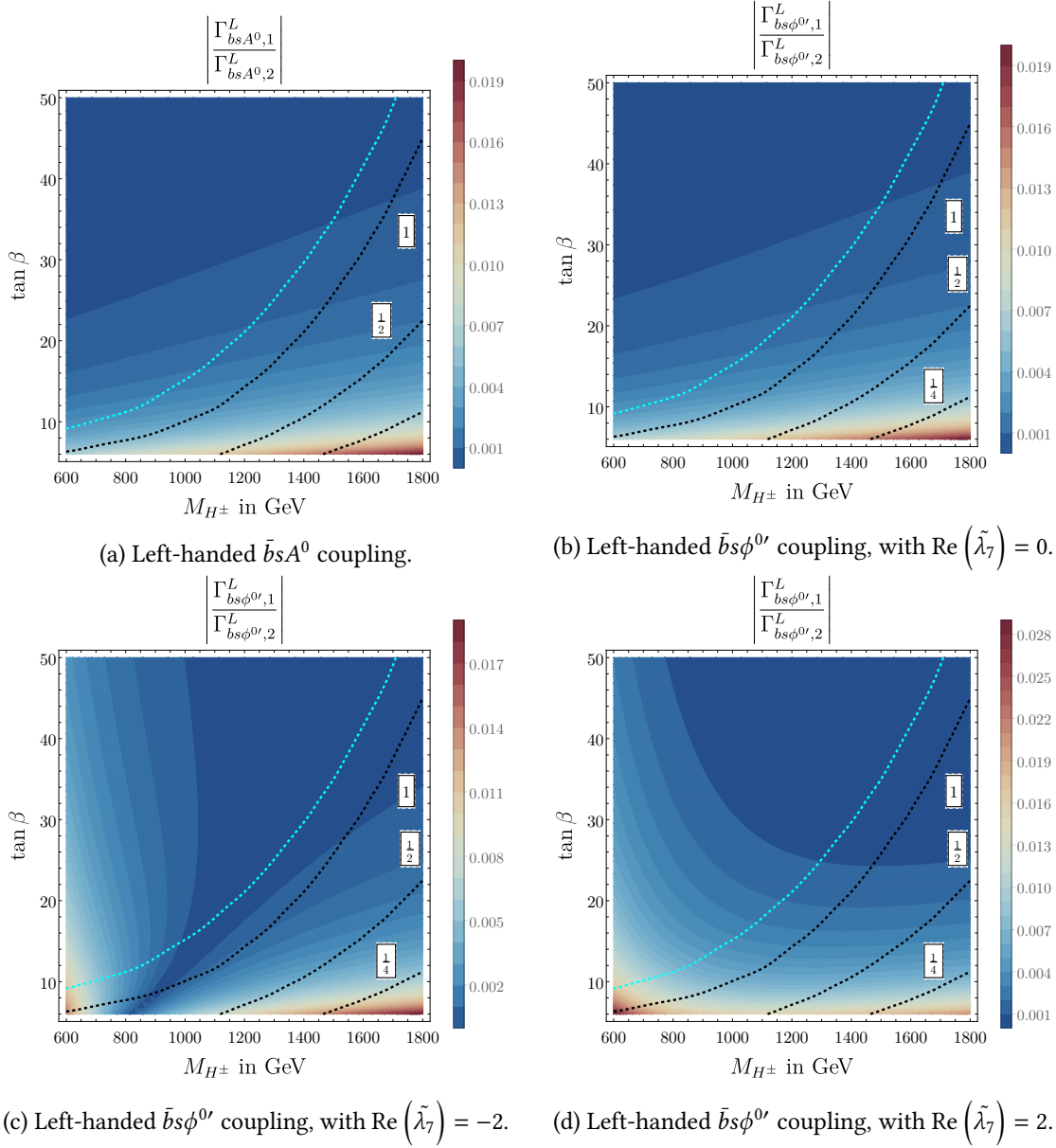


Figure 6.8.: Ratio of the $\mathcal{O}(\tan\beta)$ coefficients of the effective couplings to their respective $\mathcal{O}(\tan^2\beta)$ counterparts. The dashed black contours denote the value of $\tan\beta$ in units of the maximal value of $\tan\beta$ for given M_{H^\pm} . The cyan contour illustrates the maximum value of $\tan\beta$ with more relaxed bounds on the scalar couplings, see main text for additional details. All running parameters were evaluated at the matching scale $\mu = \bar{m}_t$.

Fig. 6.8 we show the ratio of subleading $\tan \beta$ terms to the leading $\tan^2 \beta$ for the effective left-handed $\bar{b}sA^0$ (Fig. 6.8a) and $\bar{b}s\phi^{0'}$ couplings (Figs. 6.8b to 6.8d). All of these plots were obtained with a rescaling factor of 1, i.e. with $|g_{ij}^u| = |g_{ct}| = \sqrt{2}|\text{Re}(g_{ct})|$. For different rescaling factors in the regime 0.2–5 the ratios scale linearly with the rescaling factor in a good approximation. The upper limits on $|g_{ct}|$ depend on the value of $\tan \beta$. While collider searches put upper bounds on $\tan \beta$ in dependence of M_{A^0} and thus of M_{H^\pm} by means of e.g. Fig. 6.2, these bounds need not be saturated. The black dashed contour lines show the values of $\tan \beta$ at a fraction X of its maximal allowed value, where $X = 1/4, 1/2, 1$. In order to obtain these bounds, Eq. (2.8) was used in order to relate the given value of M_{H^\pm} to a maximal value of M_{A^0} under the assumption $|\lambda_i| \leq 4$ and subsequently derive an upper limit on $\tan \beta = \tan \beta(M_{H^\pm})$. With the more relaxed bound $|\lambda_i| \leq 4\pi$ the mass difference $M_{A^0} - M_{H^\pm}$ may increase, and thus the maximal value of $\tan \beta$, such that the dashed cyan contour is obtained at saturation. In conclusion, even with a rescaling factor of 4 for the Yukawa couplings, the ratios $\Gamma_{bsA^0(\phi^{0'})_1}^L / \Gamma_{bsA^0(\phi^{0'})_2}^L$ reach a maximum of only approximately 11 % in the lower left and right corners, respectively. We will therefore neglect the subleading $\mathcal{O}(\tan \beta)$ contributions of the effective couplings in the following.

Finally, we discuss whether the $B_s - \bar{B}_s$ mixing provide more stringent constraints on g_{ct} than the decays $b \rightarrow s\gamma$. For this, following the previous discussion we consider only the highest contributions of order $\mathcal{O}(\tan^4 \beta)$ to the Wilson coefficients $C_{SLL,SLR}$. In particular, the down-type couplings $g_{sb,bs}$ and all CKM-subleading terms are also neglected. The mass difference $\Delta M_s^{2\text{HDM}}$ then depends only on $\tan \beta$, the Higgs masses M_{H^\pm} , $M_{\phi^{0'}}$, and M_{A^0} as well as on

$$\text{Re}(g_{ct}^2) = (\text{Re}(g_{ct}))^2 - (\text{Im}(g_{ct}))^2 \leq (\text{Re}(g_{ct}))^2. \quad (6.31)$$

Since $|\text{Re}(g_{ct})|$ is constrained by $b \rightarrow s\gamma$, an upper limit for $\text{Re}(g_{ct}^2)$ can be derived as well. This upper limit is much more restrictive than the one obtained from the requirement that the uncertainty of the SM prediction of ΔM_s is not exceeded by the 2HDM contributions for all reasonable values of the heavy Higgs masses. On the other hand, a lower limit on $\text{Re}(g_{ct}^2)$ cannot be obtained from $b \rightarrow s\gamma$ and we have to take the $B_s - \bar{B}_s$ constraint in this case. Since the SM uncertainty is only slightly asymmetric, this lower bound is of the same order as the upper bound derived from $\Delta M_s^{2\text{HDM}}$ and therefore much weaker than the $b \rightarrow s\gamma$ constraint on $|\text{Re}(g_{ct})|$. As a consequence, these bounds still allow $|\text{Im}(g_{ct})| \gg |\text{Re}(g_{ct})|$, and thus the complex argument $\arctan\left(\frac{\text{Im}(g_{ct})}{\text{Re}(g_{ct})}\right)$ remains essentially unconstrained. Caution is advised if $|\text{Im}(g_{ct})|$ is much larger than the magnitude of the real part, since in the derivation of the bound from $b \rightarrow s\gamma$ we assumed the NP contribution to be approximated by the interference between the SM and the 2HDM amplitudes, neglecting the imaginary parts of g_{ct} . If $|\text{Im}(g_{ct})| \gg |\text{Re}(g_{ct})|$ by a large factor, this assumption becomes dubitable at the least. Therefore, we do not consider the bounds on $|\text{Im}(g_{ct})|$ obtained from $B_s - \bar{B}_s$ mixing in the following.

6.6. The branching ratio $\mathcal{B}(B_s \rightarrow \mu^+ \mu^-)$

With the known constraints from collider searches, $b \rightarrow s\gamma$ and $B_s - \bar{B}_s$ mixing we can finally discuss the impact from $\bar{\mathcal{B}}(B_s \rightarrow \mu^+ \mu^-)$. In Fig. 4.10 we showed the branching ratio for the type-II limit in which the only relevant parameters at leading powers of $\tan \beta$ were $\tan \beta$ and

M_{H^\pm} . Beyond type II, the branching ratio generally depends on all Higgs-boson masses, the scalar couplings λ_3 and λ_7 , as well as on all the flavour-changing couplings $g_{ij}^{u,d}$ entering the effective vertices in Appendix B. It is therefore not possible to present figures of the branching ratio in the general form, but we will restrict ourselves to some well-motivated limiting cases. However, our starting point are the full Wilson coefficients of the type-II 2HDM together with all contributions in the three-spurion 2HDM, presented in Chapters 4 and 5. All of the following figures were obtained under the assumption of *alignment* of the Higgs doublets, i.e. $\sin(\beta - \alpha) = 1$, in which case one of the Higgs bosons, $\phi^0 = h^0 = h_{\text{SM}}$ is the 125 GeV mass eigenstate, while $\phi^{0'}$ is promoted to a mass eigenstate with mass $M_{\phi^{0'}} = M_{H_2}$ as well. In particular $R_M = M_{\phi^{0'}}^{-2}$ and $R'_M = 0$ and the Wilson coefficients in Eqs. (5.82) to (5.85) vanish. This alignment limit is well motivated experimentally by constraints such as the one shown in Fig. 2.1 which constrain $|\cos(\beta - \alpha)| \ll 1$ for large values of $\tan\beta$, except for a tiny region that we do not consider in the following. Even if in the alignment limit the coefficients proportional to R'_M do not contribute to $B_s \rightarrow \mu^+ \mu^-$, they still play a role in $B_s - \bar{B}_s$ mixing, as discussed in the previous section.

6.6.1. The coupling g_{ct}

We begin by discussing the constraints on the coupling g_{ct} in the absence of other couplings $g_{ij}^u = 0$, $(ij) \neq (ct)$. These contributions can be obtained by neglecting all terms of order $\mathcal{O}\left((\tan\beta)^{\alpha \leq 2} \left(g_{ij}^u\right)^{n \geq 1}\right)$ in the Wilson coefficients as well as the renormalised⁸ down-type couplings $g_{sb,bs}$ and keeping only the SM and type-II coefficients together with the $\mathcal{O}(\tan^3\beta)$ Wilson coefficients $C_{S,P,\tan^3\beta}^{(\prime),\text{III}}$, which are proportional to $g_{st}^{\text{eff}*}$. The restriction to the CKM-leading term $\sim V_{cs}/V_{ts}$ then allows to derive bounds on g_{ct} itself. We show an example of these constraints for a specific “large- $\tan\beta$ ” choice of parameters of the Higgs sector in Fig. 6.9. The axis range of $\text{Re}(g_{ct})$ is determined by the M_{H^\pm} -dependent constraint from $b \rightarrow sy$, which was again converted from a bound on $\text{Re}(g_{st}^{\text{eff}})$ to a bound on $\text{Re}(g_{ct})$ by neglecting all subleading CKM factors. It is worth emphasising that even tiny flavour-changing Yukawa couplings smaller than 0.01 in magnitude do significantly impact and can even dominate the branching ratio in the regime of large $\tan\beta$, even though large values of $\tan\beta$ imply heavy additional Higgs bosons per the experimental collider constraints. This is due to the fact that the leading three-spurion contributions to the branching ratio are enhanced by a factor $\frac{\tan^2\beta |V_{cs}|^2 |g_{ct}|^2}{|V_{ts}|^2}$ compared to the leading type-II terms. In tree-level neutral processes such as the decay $\phi^{0'} \rightarrow \bar{t}c$ the CKM enhancement factors as well as $\tan\beta$ are absent, and thus in those processes the effects of tiny g_{ct} couplings remain tiny, allowing these processes to still evade detection at present experiments. We show further exclusion plots in the complex g_{ct} plane in Fig. C.2. For lower values of $\tan\beta \sim 5 - 10$, the bounds from $b \rightarrow sy$ on $\text{Re}(g_{st}^{\text{eff}})$ become more constraining if M_{H^\pm} is chosen close to the minimal value allowed by the collider constraints from Section 6.1 for any given $\tan\beta$. However, the constraints on $\text{Re}(g_{ct}) \sim \text{Re}(g_{st}^{\text{eff}})/\tan\beta$ become weaker at the same time, allowing a slightly larger range of values than in the large- $\tan\beta$

⁸The bare couplings $g_{sb,bs}^{(0)}$ must still be present in order to provide the necessary counterterms to renormalise the UV-divergences of the self-energy Wilson coefficients, as discussed Section 5.4.

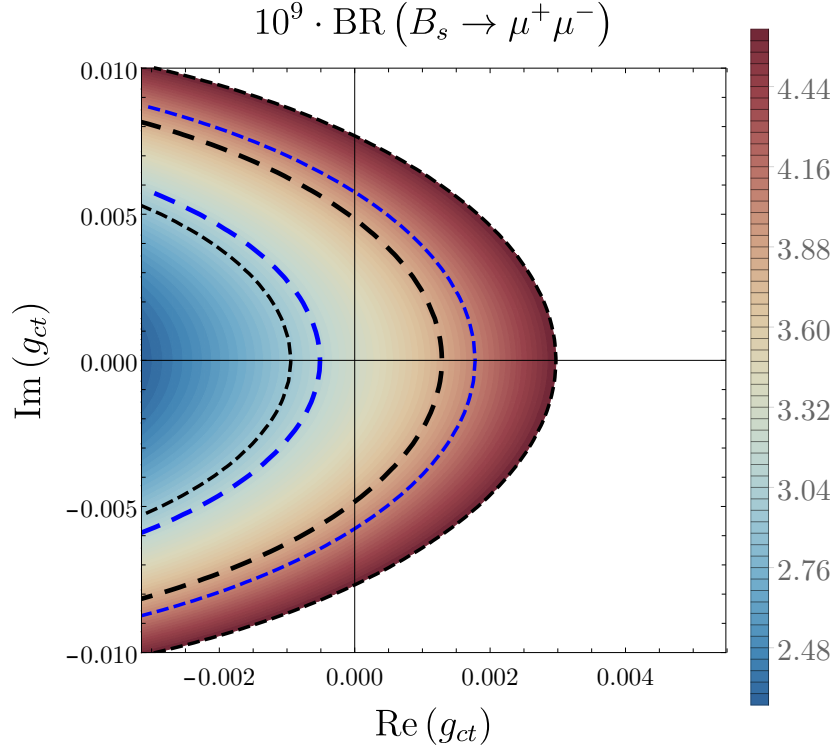


Figure 6.9.: Constraints in the complex plane of g_{ct} for $\tan\beta = 55$, $M_{H^\pm} = 1950$ GeV, $M_{A^0} = 2000$ GeV, $M_{\phi^0} = 2050$ GeV. All running QCD parameters were evaluated at $\mu = \bar{m}_t$ (\bar{m}_t). The axis range for $\text{Re}(g_{ct})$ was obtained from the $b \rightarrow sy$ constraint. The plot colours show the value of $\overline{\mathcal{B}}(B_s \rightarrow \mu^+\mu^-)$ obtained for a given complex value of g_{ct} . The uncoloured area is excluded. Dashed black and blue lines denote the central experimental values and $\pm 2\sigma$ uncertainties of the recent CMS [37] and LHCb [35, 36] measurements.

scenario, but still in the $|\text{Re}(g_{ct})| \lesssim \mathcal{O}(3\%)$ regime. At the same time, the impact of g_{ct} on $\overline{\mathcal{B}}(B_s \rightarrow \mu^+\mu^-)$ is much smaller in this regime due to the strong dependence on $\tan\beta$, allowing large values of $|g_{ct}|$. Together with the $b \rightarrow sy$ constraint on the real part, this implies that $\mathcal{O}(1)$ values of $|\text{Im}(g_{ct})|$ are not excluded by $B_s \rightarrow \mu^+\mu^-$ decays. As explained already in the discussion of B_s - \bar{B}_s mixing constraints, such large imaginary parts should be considered with caution, since in this case the approximation used for $b \rightarrow sy$ loses its validity. If we restrict $|\text{Im}(g_{ct})| \leq \mathcal{O}(1-10) \max|\text{Re}(g_{ct})|$, the branching ratio is essentially constant as a function of $g_{ct} \in \mathbb{C}$ or shows only minor variation, see e.g. the areas $|\text{Im}(g_{ct})| \leq 10 \cdot 0.014$ in Figs. C.2a and C.2b. Thus, for values of $\tan\beta$ of $\mathcal{O}(\lesssim 10)$ the exclusion figures show only the bounds from $B_s \rightarrow \mu^+\mu^-$, and possible further restrictions of $|\text{Im}(g_{ct})|$ —the precise numerical values of which are somewhat arbitrary—need to be taken into account additionally. This situation improves already for medium-sized values $\tan\beta \gtrsim \mathcal{O}(25)$, for which $|\text{Im}(g_{ct})| \lesssim \mathcal{O}(1)$, as can

be seen in Figs. C.2c and C.2d. Finally, for large values of $\tan \beta$, $|\text{Im}(g_{ct})| \sim |\text{Re}(g_{ct})|$, as shown in Figs. 6.9, C.2e and C.2f.

The scalar Wilson coefficients at order $\mathcal{O}(\tan^2 \beta)$ depend also on $\text{Re}(\lambda_7)$. In Fig. C.2e we show the exclusions for the same numerical values as in Fig. 6.9 except for $\text{Re}(\lambda_7) = 1$. As before, we have only kept the coupling g_{ct} , but taken into account the effect of λ_7 at $\mathcal{O}(\tan^2 \beta)$. Figure C.2e confirms that the effect of the $\mathcal{O}(\tan^2 \beta)$ contributions to the Wilson coefficients is rather small, cf. the difference between Figs. 6.9 and C.2e.

Finally, so far the effects of the CP angle ϕ_{NP}^s introduced in Eq. (3.22) have been neglected by setting $\phi_{\text{NP}}^s = 0$. In Fig. C.2f we show the exclusions for the same numerical values as in Fig. 6.9 except that we use the maximal choice $\phi_{\text{NP}}^s = \pi$. This choice results in a noticeable shift of the allowed range to the right, in particular it makes the lower experimental limits accessible. However, this shift does not drastically alter the statements of the previous discussion. In particular, the overall scale of g_{ct} remains approximately identical. Experimental constraints require the NP contribution ϕ_{NP}^s to the phase ϕ^s to be much smaller than the maximal choice, see the discussion around Eq. (6.29), such that the actual shift has to be much smaller than in Fig. C.2f.

6.6.2. The coupling g_{tc}

In Ref. [195] a 2HDM with exactly one flavour-changing coupling in the up-type quark sector, $\rho_{tc} \equiv g_{tc}$, was introduced in order to address several current discrepancies between measured flavour observables and their predicted SM counterterms, such as

$$R_{D^{(*)}} \equiv \frac{\mathcal{B}(B \rightarrow D^{(*)} \tau \bar{\nu}_\tau)}{\mathcal{B}(B \rightarrow D^{(*)} l \bar{\nu}_l)}, \quad l = e, \mu. \quad (6.32)$$

the current experimental world average of which reads [74, 196–203]

$$\begin{aligned} R_D &= 0.357 \pm 0.029, \\ R_{D^*} &= 0.284 \pm 0.012, \end{aligned} \quad (6.33)$$

Compared to the SM predictions that average to [74, 204–210]

$$\begin{aligned} R_D^{\text{SM}} &= 0.298 \pm 0.004, \\ R_{D^*}^{\text{SM}} &= 0.254 \pm 0.005, \end{aligned} \quad (6.34)$$

a combined tension of about 3.3σ between the SM prediction and the experimental world average is observed. In a 2HDM with g_{tc} an additional charged-Higgs mediated tree-level contribution arises (see also Refs. [177, 211]), proportional to $g_{tc}^* g_{\tau\tau}^*$, where $g_{\tau\tau}$ is the $\tau\tau$ component of the lepton Yukawa matrix, which in our model would correspond to $-\sqrt{2}m_\tau \tan \beta / v_{\text{SM}}$. Focusing on light charged Higgs bosons of order $M_{H^\pm} \sim 200 - 250 \text{ GeV}$, the author of Ref. [195] derived best-fit values for g_{tc} , which were of order $0.6 - 0.8$. It is therefore worthwhile dedicating a short discussion to this particular coupling.

In the decay $B_s \rightarrow \mu^+ \mu^-$, the coupling g_{tc} enters the Wilson coefficients only at order $\mathcal{O}(\tan^2 \beta)$ and all terms proportional to g_{tc}^2 are furthermore CKM-suppressed. If we consider

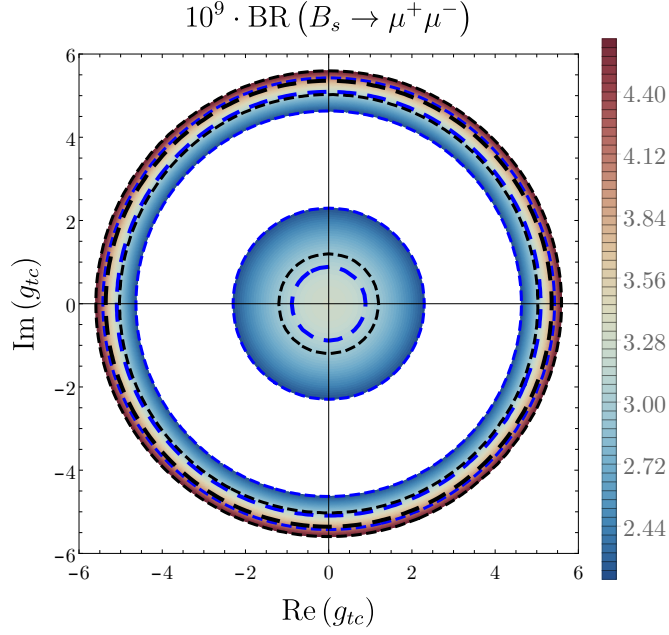


Figure 6.10.: Exclusions in the complex g_{tc} plane, neglecting all other up-type couplings g_{ij}^u and $g_{sb,bs}$, for parameters chosen as $\tan \beta = 55$, $M_{H^\pm} = 1950$ GeV, $M_{\phi^{0\prime}} = 2050$ GeV, $M_{A^0} = 2000$ GeV, $\text{Re}(\lambda_7) = 0$. All running parameters have been evaluated at $\mu = \bar{m}_t(\bar{m}_t)$. Dashed black and blue lines denote the central experimental values and $\pm 2\sigma$ uncertainties of the recent CMS [37] and LHCb [35, 36] measurements. Uncoloured areas are excluded. The perturbativity bound is not shown.

only the coupling g_{tc} and neglect—as in Ref. [195]—all other couplings g_{ij}^u , $(ij) \neq (tc)$, and $g_{sb,bs}$, we therefore expect rather weak constraints. Indeed, this is observed for example in Fig. 6.10 for a specific choice of parameters. Since we are generally interested in effects occurring at large $\tan \beta$, implying large Higgs masses, we chose $\tan \beta = 55$, $M_{H^\pm} = 1950$ GeV, $M_{\phi^{0\prime}} = 2050$ GeV, $M_{A^0} = 2000$ GeV for Fig. 6.10. Figure 6.10 shows that two regions are allowed by $B_s \rightarrow \mu^+ \mu^-$. Between these regions, the branching ratio drops too far below the lower experimental bounds and the corresponding values of g_{tc} are therefore excluded. However, the outer ring of allowed values is outside the perturbativity bounds of $|g_{tc}| \lesssim \sqrt{4\pi}$ (or $|g_{tc}| \lesssim 2$), and therefore should not be considered. For lower values of $\tan \beta$ and lighter Higgs bosons, the region between the center disk and the ring is not necessarily excluded since the falloff of the branching ratio can be much weaker in this case. The region allowed by $B_s \rightarrow \mu^+ \mu^-$ is therefore a full disk, however even larger than at large $\tan \beta$. The perturbativity bound removes the vast bulk of the allowed region again. In conclusion, if only the coupling g_{tc} is kept, the decay $B_s \rightarrow \mu^+ \mu^-$ does not constrain the coupling g_{tc} any further than the fit results of Ref. [195].

The shape of the allowed regions changes if in addition to g_{tc} we also keep the “CKM- and $\tan \beta$ ”-leading coupling g_{ct} . In this case, for given non-Yukawa parameters $\tan \beta$, M_{H^\pm} , $M_{\phi^{0\prime}}$, M_{A^0} , two of the four real parameters ($\text{Re}(g_{ct})$, $\text{Im}(g_{ct})$, $\text{Re}(g_{tc})$, $\text{Im}(g_{tc})$) need to be eliminated in order to draw exclusion plots. We show two such figures in Fig. 6.11. With the constraint from

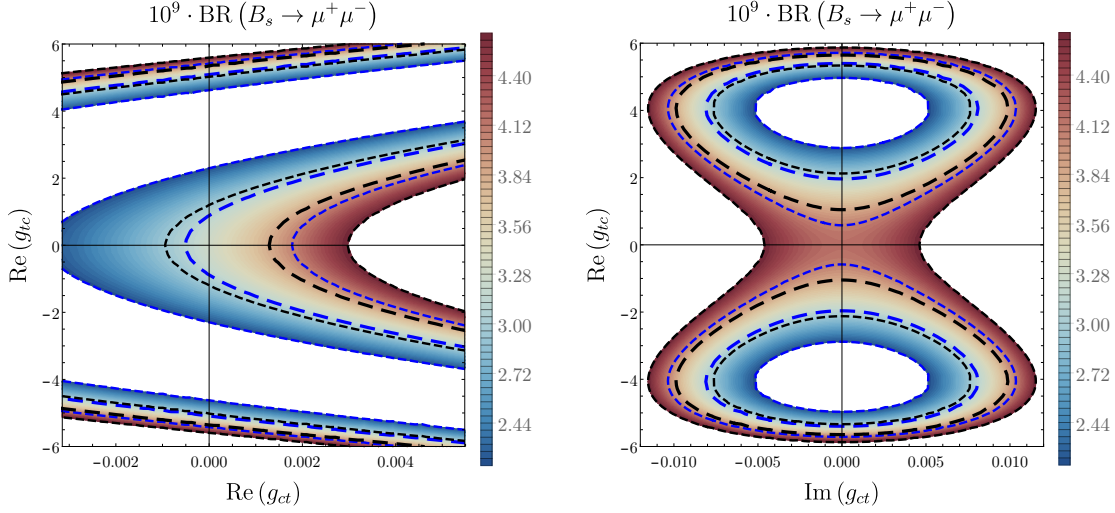


Figure 6.11.: Exclusions for $\tan \beta = 55$, $M_{H^\pm} = 1950$ GeV, $M_{\phi^{0\prime}} = 2050$ GeV, $M_{A^0} = 2000$ GeV, $\lambda_3 = \text{Re}(\lambda_7) = 0$. In the left figure $\text{Im}(g_{ct}) = \text{Im}(g_{tc}) = 0$, while $\text{Re}(g_{ct})$ is varied over its range allowed by $b \rightarrow s\gamma$. In the right figure we have fixed $\text{Re}(g_{ct}) = 2 \cdot 10^{-3}$, which is already relatively close to the upper limit set by $b \rightarrow s\gamma$, while $\text{Im}(g_{tc}) = 0$. All running parameters have been evaluated at $\mu = \bar{m}_t$ (\bar{m}_t). Dashed black and blue lines denote the central experimental values and $\pm 2\sigma$ uncertainties of the recent CMS [37] and LHCb [35, 36] measurements. Uncoloured areas are excluded. The perturbativity bound for $\text{Re}(g_{tc})$ is not shown.

$B_s \rightarrow \mu^+ \mu^-$ alone, both of these figures show an interesting set of allowed regions. However, the perturbativity bound again needs to be taken into account for g_{tc} , removing a significant part of the parameter space.

We conclude that with the incorporation of g_{ct} rather large values of g_{tc} are still possible, up to the perturbativity bounds. While some small patches of the g_{tc} parameter space may be excluded for specific values of g_{ct} , we will not make general statements about g_{tc} here except that the values obtained in Ref. [195] are generally consistent with $B_s \rightarrow \mu^+ \mu^-$.

6.6.3. The coupling g_{sb}

Finally, we discuss constraints on the down-type couplings $g_{sb,bs}$. Throughout the discussion, we will set $g_{bs} = \frac{1}{50}g_{sb}$, in accordance with the spurion expansion yielding $g_{bs} \sim \frac{m_s}{m_b}g_{sb}$. For definiteness we will also begin by neglecting all flavour-changing up-type couplings, $g_{ij}^u = 0$. The decay $B_s \rightarrow \mu^+ \mu^-$ then depends on $|g_{sb}|$, while the $B_s - \bar{B}_s$ mixing constrains $\text{Re}(g_{sb}^{*2}) = (\text{Re}(g_{sb}))^2 - (\text{Im}(g_{sb}))^2$ and $\text{Im}(g_{sb}^{*2}) = 2\text{Re}(g_{sb}^*)\text{Im}(g_{sb}^*)$, and thus the two processes complement each other. The constraint on $\text{Re}(g_{sb}^{*2})$ takes an x -like shape in the complex g_{sb} plane, whereas the bound on the imaginary part takes the form of a compass rose with hyperbolic needles. For the parameters $\tan \beta = 55$, $M_{H^\pm} = 1950$ GeV, $M_{\phi^{0\prime}} = 2050$ GeV,

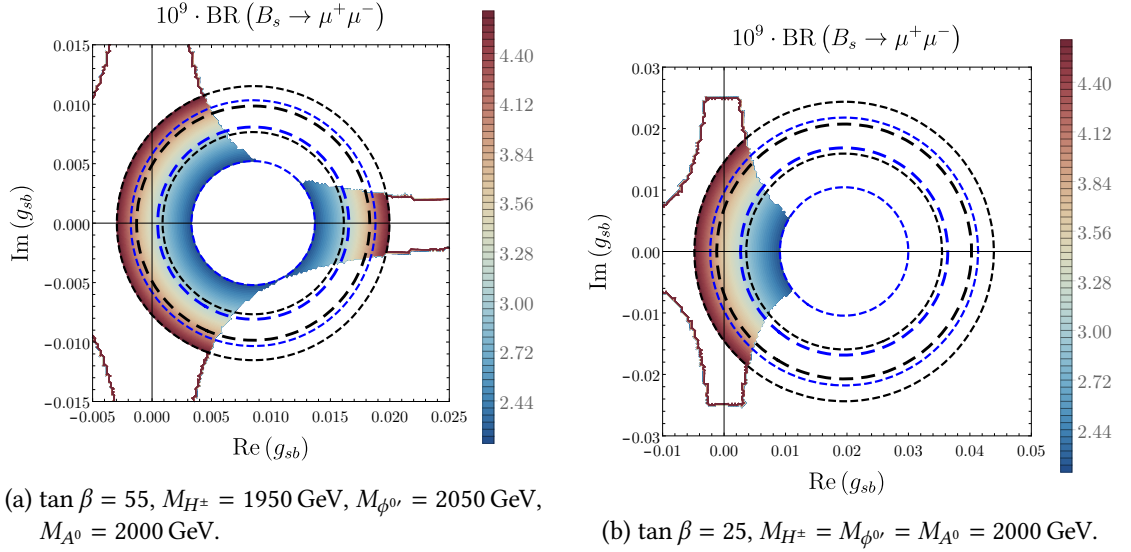


Figure 6.12.: Exclusions in the complex g_{sb} plane, neglecting all up-type flavour-changing couplings g_{ij}^u . All running parameters have been evaluated at $\mu = \bar{m}_t$ (\bar{m}_t). Dashed black and blue lines denote the central experimental values and $\pm 2\sigma$ uncertainties of the recent CMS [37] and LHCb [35, 36] measurements. Bounds from $B_s \rightarrow \mu^+ \mu^-$ and $B_s - \bar{B}_s$ mixing are incorporated. Uncoloured areas are excluded.

$M_{A^0} = 2000$ GeV the allowed region in the complex g_{sb} plane is illustrated in Fig. 6.12a. With this choice of Higgs masses we have nearly exhausted the differences $|M_{A^0}^2 - M_{\phi^{0r}}^2|$ and $|M_{A^0}^2 - M_{H^\pm}^2|$ to their maximal values allowed by perturbativity of the scalar Higgs couplings, corresponding to $\gamma = 1$ in Fig. 6.7. We therefore require $\left| \sqrt{\text{Re}(g_{sb}^{*2})} \right| \leq 0.025$, in agreement with Fig. 6.7. For the given parameters, the ring-shaped constraints from $B_s \rightarrow \mu^+ \mu^-$ force g_{sb} to be completely within by the x -like shape resulting from the B_s mixing bound on $\text{Re}(g_{sb}^{*2})$, and $B_s \rightarrow \mu^+ \mu^-$ does in fact provide stronger constraints on g_{sb} than ΔM_s . A significant portion of the parameter space is then only removed by the constraint on $\text{Im}(g_{sb}^{*2})$. If we do not choose the maximal value of $\tan \beta$ for given M_{A^0} the decay $B_s \rightarrow \mu^+ \mu^-$ allows a larger range for $|g_{sb}|$ due to the $\tan \beta$ in the Higgs-lepton coupling, while the constraint from $B_s - \bar{B}_s$ mixing is independent of $\tan \beta$. In this case the B_s mixing constraint on $\text{Re}(g_{sb}^{*2})$ becomes relevant as well, see e.g. Fig. 6.12b for the exclusions taking into account all constraints and Fig. C.3, which is taken with the same numerical input, but without the constraint on $\text{Im}(g_{sb}^{*2})$.

At lower Higgs masses, if we assume the Higgs-boson mass splitting to be sizeable, $\gamma \gtrsim \frac{1}{3}$, the mass difference $\Delta M_s^{2\text{HDM}}$ requires much smaller values $\left| \sqrt{\text{Re}(g_{sb}^{*2})} \right| \leq 5 \cdot 10^{-3}$, again by virtue of Fig. 6.7. In this case the x -shape exclusion from mixing becomes much narrower and

$B_s - \bar{B}_s$ mixing can exclude a significant portion of the donut-like or disk-like regions allowed by $B_s \rightarrow \mu^+ \mu^-$, see Fig. C.4 for an exemplary figure.

In conclusion, if we neglect g_{ij}^u and consider only g_{sb} , the decay $B_s \rightarrow \mu^+ \mu^-$ and B_s -meson mixing can give independent constraints. While at large Higgs masses and large $\tan \beta$ the bound from $B_s \rightarrow \mu^+ \mu^-$ completely overrules the mixing constraint on $\text{Re}(g_{sb}^{*2})$, if one of the two conditions is relaxed, they will in general give complementary information. On the other hand, the B_s mixing constraint on $\text{Im}(g_{sb}^{*2})$ excludes a significant part of the parameter space in all cases discussed.

6.6.4. The couplings g_{ct} and g_{sb}

Finally we discuss effects of the simultaneous presence of g_{ct} and g_{sb} . This case incorporates the coupling g_{ct} that carries the highest CKM enhancement as well as the highest powers of the large parameter $\tan \beta$ and the coupling g_{sb} that is already present at tree-level. In Fig. 6.13 we show the exclusions obtained in the $(\text{Re}(g_{ct}), \text{Re}(g_{sb}))$ plane, obtained for $\text{Im}(g_{sb}) = \text{Im}(g_{ct}) = 0$ with the usual parameters $\tan \beta = 55$, $M_{H^\pm} = 1950$ GeV, $M_{\phi^0} = 2050$ GeV, $M_{A^0} = 2000$ GeV. As in the previous subsection we have also used $g_{bs} = \frac{1}{50}g_{sb}$ again and have varied $\text{Re}(g_{ct})$ over the range allowed by $b \rightarrow s\gamma$. The decay $B_s \rightarrow \mu^+ \mu^-$ leaves two possible bands in the parameter plane, between which the branching ratio again drops off below the experimentally measured values. It is thus possible to compensate larger values of $\text{Re}(g_{ct})$ by larger values of $\text{Re}(g_{sb})$. However, it should be noted that in the upper right corner of the figure $\text{Re}(g_{sb})$ approaches its limit set by B_s mixing.

6.7. $B_d \rightarrow \mu^+ \mu^-$

Finally, we discuss the case of $B_d \rightarrow \mu^+ \mu^-$ decays. It has been illustrated in Section 5.9 how the Wilson coefficients for $B_d \rightarrow \mu^+ \mu^-$ can be obtained from the coefficients by simple replacements of $m_s \rightarrow m_d$ and $V_{is} \rightarrow V_{id}$.

Beginning with the constraint from R_γ , we introduce an effective coupling g_{dt}^{eff} analogously to g_{st}^{eff} (see Eq. (6.7)),

$$g_{dt}^{\text{eff}} \equiv \frac{v_{\text{SM}} \tan \beta}{\sqrt{2}m_t} \left(g_{ut} \frac{V_{ud}^*}{V_{td}^*} + g_{ct} \frac{V_{cd}^*}{V_{td}^*} + g_{tt} \right). \quad (6.35)$$

It should be emphasised that the coupling g_{ut} is enhanced by a factor $V_{ud}/V_{td} \sim \lambda^{-3}$, compared to the type-II and SM case, even stronger than for $b \rightarrow s\gamma$ by one additional factor λ^{-1} . In order to use the approximate relation given in Ref. [145],

$$R_\gamma \cdot 10^3 = (3.31 \pm 0.22)|_{\text{SM}} - 8.05\Delta C_7 - 1.94\Delta C_8, \quad (6.36)$$

we need to adjust it in order to account for $b \rightarrow d\gamma$. The SM part of the ratio is still dominated by $b \rightarrow s\gamma$. However, the interference terms $\text{Re}\left(\left(C_{7,q}^{\text{SM}}\right)^* C_{7,q}^{2\text{HDM}}\right)$, and analogously for C_8 , are now assumed to be dominated by $b \rightarrow d\gamma$, where the SM Wilson coefficients satisfy

$$\left(C_{7,d}^{\text{SM}}\right)^* = \frac{V_{td}}{V_{ts}} \left(C_{7,s}^{\text{SM}}\right)^*, \quad \left(C_{8,d}^{\text{SM}}\right)^* = \frac{V_{td}}{V_{ts}} \left(C_{8,s}^{\text{SM}}\right)^*. \quad (6.37)$$

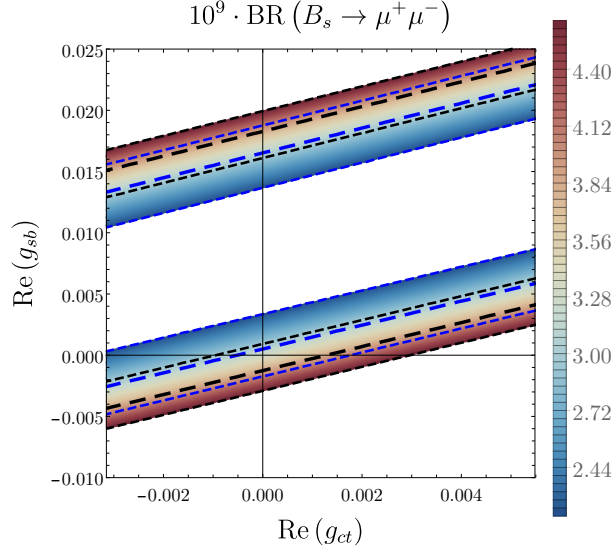


Figure 6.13.: Exclusions for $\text{Re}(g_{sb})$ versus $\text{Re}(g_{ct})$, neglecting all other flavour-changing Yukawa couplings (except $g_{bs} = \frac{1}{50}g_{sb}$). All running parameters have been evaluated at $\mu = \bar{m}_t$ (\bar{m}_t). Dashed black and blue lines denote the central experimental values and $\pm 2\sigma$ uncertainties of the recent CMS [37] and LHCb [35, 36] measurements. Uncoloured areas are excluded.

The approximate relation for R_Y is therefore modified and reads

$$R_Y = (3.31 \pm 0.22)|_{\text{SM}} - \frac{8.05}{V_{ts}} \text{Re}\left(V_{td} C_{7,d}^{2\text{HDM}}\right) - \frac{1.94}{V_{ts}} \text{Re}\left(V_{td} C_{8,d}^{2\text{HDM}}\right), \quad (6.38)$$

where we have explicitly denoted the pure 2HDM parts of the Wilson coefficients as such. The CKM matrix element V_{td} has a sizeable imaginary part and can therefore not simply be pulled out in front of the real part. This yields an approximate relation similar to Eq. (6.9), which we show in Eq. (C.1) in Appendix C,⁹ where in this case the type-II case can be safely neglected, and hence the 2HDM contribution to R_Y will be proportional to $\text{Re}(V_{td} g_{ut}) \propto \text{Re}\left(|V_{td}|^2 g_{dt}^{\text{eff}}\right) \propto \text{Re}\left(g_{dt}^{\text{eff}}\right)$. The constraint on $\text{Re}\left(g_{dt}^{\text{eff}}\right)$ is therefore independent of the phase of V_{td} . Neglecting the CKM-subleading terms in the definition of g_{dt}^{eff} , a constraint on g_{ut} can be derived, which however depends on the imaginary part of V_{td} . For $b \rightarrow d\gamma$, we will therefore not present a constraint on g_{ut} , but rather on $\text{Re}\left(g_{dt}^{\text{eff}}\right)$.

We show the bounds on $\text{Re}\left(g_{dt}^{\text{eff}}\right)$ in Fig. 6.14. Due to the $|V_{td}|^2/V_{ts}$ suppression of the interference term with respect to the case $b \rightarrow s\gamma$, the allowed range for $\text{Re}\left(g_{dt}^{\text{eff}}\right)$ is much larger, allowing even values of $\mathcal{O}(1000)$, and a discussion of the perturbativity bounds is in order. Since g_{dt}^{eff} is not a fundamental coupling of the Lagrangian and does not appear in the

⁹When expressed in terms of $\text{Re}\left(g_{dt}^{\text{eff}}\right)$, all prefactors are effectively divided by $|V_{td}|^2/V_{ts} \approx -560$.

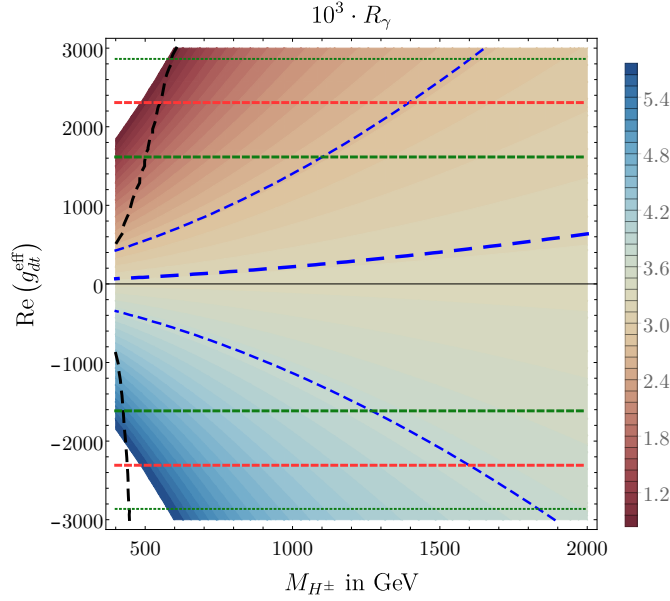


Figure 6.14.: Coloured bands show the regions of equal values of R_γ (“isobaric lines”) depending on M_{H^\pm} and $\text{Re } g_{dt}^{\text{eff}}$. The region allowed by experiment is delimited by the blue dashed lines, where the thick dashed line shows the experimental central value and the thinner dashed lines are obtained by adding the sum of experimental and theoretical uncertainties to the experimental central value. The region left of the dashed black lines illustrates the region in which the relative error of the approximate formula in Eq. (6.9) is larger than 1%. Horizontal dashed and dotted lines mark the upper and lower perturbativity bounds for $\tan \beta = 7$ (green) and $\tan \beta = 10$ (red), derived from the perturbativity bounds on g_{ut} by the replacement $V_{td} \rightarrow |V_{td}|$ and neglecting CKM-subleading terms under the assumptions $|g_{ut}| \leq 2$ (dashed) and $|g_{ut}| \leq \sqrt{4\pi}$ (dotted).

Feynman rules as such,¹⁰ the perturbativity bound is derived from the fundamental g_{ut} coupling, which is dominant if all non-leading CKM matrix elements are neglected. The $\tan \beta$ -dependent perturbativity bounds for $|g_{ut}| \leq 2$ (dashed) and $|g_{ut}| \leq \sqrt{4\pi}$ (dotted) are shown as horizontal lines for two relatively low values of $\tan \beta = 7$ (green) and $\tan \beta = 10$ (red). For large values of M_{H^\pm} and $\mathcal{O}(10)$ values of $\tan \beta$, it can be seen that the perturbativity bounds restrict $\text{Re } (g_{dt}^{\text{eff}})$ in addition to the pure R_γ constraint, making some values within the experimental and theoretical uncertainty unreachable with perturbative values of $\text{Re } (g_{dt}^{\text{eff}})$. On the other hand, since the perturbativity bounds are proportional to $\tan \beta$, they do not impose an additional constraint in the region of large $\tan \beta$ that is our main focus within this thesis. In the end, the large possible values of $\text{Re } (g_{dt}^{\text{eff}})$ still result in $|g_{ut}| \lesssim \mathcal{O}(1)$.

¹⁰It is possible to express the $\bar{d}_L t_R H^\pm$ Feynman rule in terms of g_{dt}^{eff} , but then it is multiplied by a strong CKM suppression factor and an additional power of $1/\tan \beta$.

Finally, since the interference contribution to R_γ is suppressed by the smallness of the SM (and type-II 2HDM) contributions, it is debatable whether the approximation in Eq. (6.36), see Ref. [145], is still appropriate for $b \rightarrow d\gamma$. This approximation may well receive sizeable corrections from the squared—i.e. non-interference— terms, resulting from squaring the pure 2HDM Wilson coefficients. Including such terms would likely lead to more stringent bounds on g_{dt}^{eff} . However, with the full 2HDM Wilson coefficients R_γ would also become dependent on $\text{Im}(g_{dt}^{\text{eff}})$, and deriving an individual bound on the real part would be difficult. We will therefore not abandon the approximation, but emphasise that the bounds on $\text{Re}(g_{ut})$ presented here are rather conservative.

Next, we discuss the neutral $B_d-\bar{B}_d$ meson mixing. The effective couplings $\Gamma_{bdX}^{L/R}$ can be obtained from their bsX counterparts by the replacements in Eq. (5.89). As outlined there, the down-quark mass is even further suppressed compared to m_b than the strange-quark mass, and here we will set $m_d = 0$, which also implies $g_{bd} = 0$ by the spurion expansion in Eq. (5.52). As a consequence, all Wilson coefficients (and effective Γ_{bsX}^R couplings with a right-handed down quark) vanish, and $\Delta M_d^{2\text{HDM}}$ is given by

$$\Delta M_d^{2\text{HDM}} \approx 2 \text{Re}(C_{VLL}) \langle \bar{B}_d | (\bar{b}_L \gamma_\mu d_L) (\bar{b}_L \gamma^\mu d_L) | B_d \rangle + 2 \text{Re}(C_{SLL}) \langle \bar{B}_d | (\bar{b}_R d_L) (\bar{b}_R d_L) | B_d \rangle, \quad (6.39)$$

where only C_{SLL} depends on the down-type coupling g_{db} . In particular, in the limit of equal masses, $M_{\phi^{0'}} = M_{A^0}$, the coefficient C_{SLL} vanishes and g_{db} is not bounded by $\Delta M_d^{2\text{HDM}}$ at all. An estimate for g_{db} can be obtained by setting $g_{ij}^u = 0$ and keeping only the down-type tree-level flavour-changing couplings. In absence of g_{ij}^u , the coefficient C_{VLL} is only determined by the type-II $C_{A,HZ}$ (see Eq. (4.51)) contribution to Γ_{bdZ}^L , and can safely be neglected due to its strong suppression for any medium-sized values of $\tan\beta$ and the Higgs masses. The 2HDM contribution to $\Delta M_d^{2\text{HDM}}$ is then given by the simple relation

$$\Delta M_d^{2\text{HDM}} = \left[-1.44 \cdot 10^5 \cdot \beta \cdot \left(\frac{1 \text{ TeV}}{M_{A^0}} \right)^2 \text{Re}(g_{db}^2) \right] \text{ps}^{-1}, \quad (6.40)$$

where we have introduced the parameter

$$\beta \equiv \frac{M_{\phi^{0'}}^2 - M_{A^0}^2}{M_{\phi^{0'}}^2} \quad (6.41)$$

in order to account for the relative difference between the squared masses of the heavy neutral Higgs bosons. The allowed range for β depends on the overall mass scale of the additional Higgs bosons. For example, with the perturbativity bound for the scalar couplings, $|\beta| \lesssim \frac{1}{4}$ for $M_{\phi^{0'}} = 1000 \text{ TeV}$, while for $M_{\phi^{0'}} = 2 \text{ TeV}$ it is already constrained to $|\beta| \lesssim \frac{1}{16}$. Requiring the 2HDM contribution to ΔM_d to not exceed the SM uncertainty [183],

$$\Delta M_d = (0.582_{-0.056}^{+0.049}) \text{ps}^{-1}, \quad (6.42)$$

one finds that for given β and M_{A^0} the bounds on $\text{Re}(g_{db}^2)$ are weaker by a factor of around 25 – 30 compared to the bounds from $B_s-\bar{B}_s$ mixing, since the absolute SM uncertainties in ΔM_d are smaller by approximately the same factor.

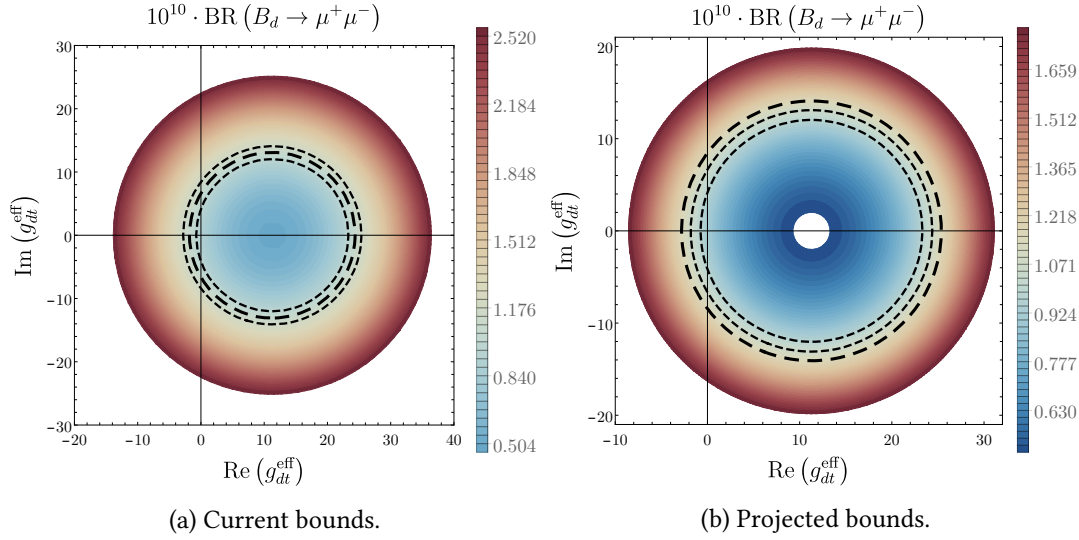


Figure 6.15.: Exclusions for g_{dt}^{eff} , for $\tan \beta = 55$, $M_{H^\pm} = 1950$ GeV, M_{ϕ^0} , $M_{A^0} = 2000$ GeV. The left figure shows the constraints obtained from the current experimental upper limit, whereas the right figure assumes the projected ATLAS sensitivity [41] shown in Fig. 3.2. Dashed black lines show the SM prediction including the uncertainty, see Eq. (3.28). The coloured region shows the allowed parameter space in which $\mathcal{B}(B_d \rightarrow \mu^+ \mu^-) < 2.6 \cdot 10^{-10}$ [35, 36].

Finally, we discuss the constraint from $B_d \rightarrow \mu^+ \mu^-$ on g_{ut} . Focusing on the coupling g_{ut} , or rather the equivalent coupling g_{dt}^{eff} , neglecting non-diagonal CKM matrix elements and the tree-level g_{db} coupling, exclusions can be derived based on the current experimental upper limit. In order to be conservative, we use the 95 % confidence limit upper experimental limit of $\mathcal{B}(B_d \rightarrow \mu^+ \mu^-) < 2.6 \cdot 10^{-10}$ from the recent LHCb analysis [35, 36] and require that the branching ratio¹¹ with the addition of 2HDM contributions does not exceed this upper limit. We show the current experimental bounds in Fig. 6.15a for a large value of $\tan \beta$ and the lightest corresponding masses of Higgs bosons, taking into account the collider constraints. Comparing these bounds to the ones from Fig. 6.14 one finds that $B_d \rightarrow \mu^+ \mu^-$ provides much more stringent constraints. This highlights that the interference contribution considered in the discussion of $b \rightarrow d\gamma$ should not be used, and we will not take that bound into account.

Since the decay $B_d \rightarrow \mu^+ \mu^-$ has not yet been observed, it is interesting to also discuss the future projections. In Fig. 6.15b we show the projected exclusion limits, assuming the 2σ ATLAS projections [41] for the measurement of $\mathcal{B}(B_d \rightarrow \mu^+ \mu^-)$ shown in Fig. 3.2. These projections reduce the parameter space of the current constraints slightly further, e.g. removing the central part of the disk, see Fig. 6.15. However, since the current upper limit on the branching ratio is only a factor 2.5 larger than the SM prediction and only about 45 % larger than the projected upper 2σ uncertainty, the shrinking of the allowed region with the projected sensitivity is not

¹¹For B_d the lifetime difference between the mass eigenstates is negligible, and we will therefore use \mathcal{B} rather than $\overline{\mathcal{B}}$.

drastic. It should be noted that the projected sensitivity assumes that ATLAS will measure the branching ratio to be equal to the SM prediction. Hence, any deviations from this assumption are not shown in Fig. 6.15b and the allowed region for g_{dt}^{eff} only compensates for the type-II contribution within the projected uncertainties.

In the scenario with non-vanishing g_{db} in addition to g_{dt}^{eff} , the exclusion figures take a different shape, as shown e.g. in Fig. C.5. If both couplings are present, the branching ratio also depends on the phase of V_{td} .

6.8. Summary

In this chapter, we have discussed several constraints on the flavour-changing up-type Yukawa couplings relevant for decays $B_q \rightarrow \mu^+ \mu^-$, as well as on the down-type Yukawa couplings entering through the renormalisation of the three-spurion 2HDM. We have shown the impact of collider searches, which give lower limits for the masses of the heavy Higgs bosons as a function of $\tan \beta$. Furthermore, collider searches point towards the so-called *alignment* limit in the Higgs sector, implying that the scalar CP-even bosons are mass eigenstates. The perturbativity of the scalar Higgs potential requires that its couplings are bounded, and therefore the difference between the Higgs masses cannot become arbitrarily large. In particular, for heavy Higgs bosons, the relative mass difference becomes quite small. This has profound consequences for the constraints from $B_q - \bar{B}_q$ mixing. For $q = s$, the mixed left-right Wilson coefficient C_{SLR} becomes important due to this phenomenon, and thus in particular points of the parameter space the constraint from $B_s - \bar{B}_s$ mixing can become weak. For $q = d$, the vanishing of the coefficient C_{SLR} implies that in the limit of equal A^0 and ϕ^{0r} masses there is no constraint from $B_d - \bar{B}_d$ mixing at all. While we have used the bounds from meson mixing in order to constrain the down-type flavour-changing couplings, a constraint on the most important coupling g_{ct} comes from the decay $b \rightarrow s\gamma$. We found that the rare decays $b \rightarrow s\gamma$ and $B_s \rightarrow \mu^+ \mu^-$ give complementary constraints on this coupling, thus leading to stringent bounds. In the case of $b \rightarrow d\gamma$, the approximation used for the observable R_γ is not useful anymore, and the decay $B_d \rightarrow \mu^+ \mu^-$ serves much better in order to constrain the relevant CKM-enhanced and $\tan \beta$ -leading coupling $g_{ut} \sim g_{dt}^{\text{eff}}$.

Overall, we have shown in this chapter that even tiny couplings $g_{ct} \lesssim 5 \cdot 10^{-3}$ (and slightly smaller for g_{ut}) can have a drastic impact on the branching ratio of the decays $B_q \rightarrow \mu^+ \mu^-$, due to the enormous enhancement by small CKM matrix elements in the denominator and large powers of $\tan \beta$, which were shown to arise in the self-energy diagrams computed in the previous chapter. In addition, down-type couplings of the same order of magnitude are still possible, due to the sizeable SM uncertainties for the mass difference in the neutral meson mixing and the suppression of the leading Wilson coefficient in the case of similar Higgs-boson masses.

7. Conclusion and outlook

We have presented a two-Higgs-doublet model (2HDM) incorporating flavour-changing couplings of neutral Higgs bosons in the up-type quark sector, while suppressing down-type flavour-changing couplings. The presented model is less generic than the general 2HDM, but has a much larger diversity in the Yukawa sector compared to the popular 2HDMs with a discrete \mathbb{Z}_2 symmetry, such as the model of type II. A detailed discussion has been devoted to the calculation of the partial decay $B_s \rightarrow \mu^+ \mu^-$, which is particularly sensitive to some of the additional non-diagonal couplings, and the related $B_d \rightarrow \mu^+ \mu^-$. Working in the framework of an effective field theory, we computed the Wilson coefficients entering the formula for the branching ratio, including next-to-leading order two-loop QCD corrections. We have used the discussion of the type-II 2HDM as an opportunity to emphasise the most important aspects of the general computation, in particular related to the issue of gauge independence and the treatment of diagrams with flavour-changing self-energies.

In the three-spurion 2HDM we have paid special attention to the flavour-changing self-energy diagrams again. These diagrams contribute at order $O(\tan^3 \beta)$ to the scalar and pseudoscalar $C_S^{(\prime)}$ and $C_P^{(\prime)}$. Furthermore, the contributions proportional to the flavour-changing coupling g_{ct} (for B_s) and g_{ut} (B_d) do not suffer from the CKM suppression V_{ts} (V_{td}) that is present both in the Standard Model and the type-II 2HDM. Therefore, even tiny couplings g_{ct} and g_{ut} can have a drastic impact on the branching ratios. The main focus of this thesis was the scenario of large $\tan \beta$, since in this regime the decays $B_q \rightarrow l^+ l^-$ are among the observables most sensitive to the flavour-changing couplings. For large $\tan \beta$, we discussed that collider searches for heavy Higgs bosons put stringent lower limits on the mass of the additional particles, with $M_{A^0} \sim 2 \text{ TeV}$ if $\tan \beta = 55$. With these values for the Higgs masses, the combined constraints from $b \rightarrow s\gamma$ and $B_s \rightarrow \mu^+ \mu^-$ allowed to restrict the viable parameter space to a subset of the interval $(\text{Re}(g_{ct}), \text{Im}(g_{ct})) \in [-3 \cdot 10^{-3}, 3 \cdot 10^{-3}] \times [-0.01, 0.01]$, excluding couplings of more than $O(1\%)$. These constraints assume the minimum value of M_{A^0} for $\tan \beta = 55$. For fixed $\tan \beta$, the bounds are relaxed by a factor $\sim M_{A^0}^2 / (2 \text{ TeV})^2$ if the Higgs masses are not taken at their minimal possible values. At lower values of $\tan \beta$, the $O(\tan^3 \beta)$ terms become much less dominant, and in this case the bounds on g_{ct} become much weaker than in the high- $\tan \beta$ scenario. For values $\tan \beta \lesssim 25$, the constraint from $b \rightarrow s\gamma$ makes it impossible to reach the current central value of the LHCb measurement [35, 36] at all. The lower uncertainty limits of this measurement can only be reached in the case of large $\tan \beta$.

For $B_d \rightarrow \mu^+ \mu^-$, since the decay has not been observed yet in experiment, we derived upper limits on the coupling g_{ut} based on the current experimental upper limits on the branching ratio. In this case, rather than deriving a direct upper limit on g_{ut} we chose to derive bounds on the “effective” down-top coupling $g_{dt}^{\text{eff}} \equiv v_{\text{SM}} \tan \beta g_{ut} V_{ud}^* / (\sqrt{2} m_t V_{td}^*) + \text{CKM-suppressed}$, due to the complex phase of V_{td} . However, the allowed parameter region for g_{ut} can be estimated to be

given by the disk bounded by $g_{ut} \in (1.9 + 3.8 \cdot e^{i\theta}) \cdot 10^{-3}$, where θ sweeps the full circle. This bound corresponds again to the minimal choice of $M_{A^0} = 2 \text{ TeV}$ at $\tan \beta = 55$. The scaling for non-minimal values of the heavy Higgs mass is analogous to the case of g_{ct} .

Without flavour-changing couplings in the down-type sector, one-loop Feynman diagrams involving the up-type couplings g_{ij}^u are in general not finite, even after summing over the internal up-type quarks. A renormalisable theory requires the presence of the down-type couplings as well. These couplings are suppressed by experimental constraints, in the case at hand mainly by the neutral $B_q - \bar{B}_q$ mixing. The spurion expansion discussed in this thesis offers a possibility to introduce these couplings in a systematic way, while keeping them suppressed at the same time. This is achieved by allowing three out of the four Yukawa matrices to be arbitrary, while the fourth matrix is a function of the other three. A rather detailed section was dedicated to the discussion of the renormalisation procedure within this three-spurion 2HDM and the corresponding spurion expansion. We used the mass difference and its phase in the B_q meson systems in order to constrain the down-type flavour-changing Yukawa couplings g_{sb} (for B_s) and g_{db} (B_d). At rather large masses of the Higgs bosons, as required by large values of $\tan \beta$, the near-degeneracy of the heavy Higgs mass spectrum weakens the otherwise leading constraints, allowing the couplings g_{sb} (g_{db}) to become as large as $\sim \mathcal{O}(2.5\%)$ (around a factor $\sqrt{30}$ stronger for g_{db}).

Summarising the constraints on the flavour-changing coupling, we showed how even tiny couplings can have a significant impact on the branching ratios $B_q \rightarrow \mu^+ \mu^-$, due to the missing CKM suppression and additional enhancement by powers of $\tan \beta$.

The two-Higgs-doublet model remains an interesting candidate for the extension of the Standard Model in many aspects, not only in the context of rare B -meson decays. For example, the type-II 2HDM constitutes the tree-level Higgs sector of the minimal supersymmetric standard model [13–15]. We also discussed briefly a recent analysis of the flavour-changing coupling g_{tc} as a solution to the $R_{D^{(*)}}$ anomalies. Furthermore, the 2HDM has been invoked to address the discrepancy between the theory prediction and measurement of the current muon anomalous magnetic moment $(g - 2)_\mu$, see e.g. Ref. [212] and references therein for a recent review. In the latter two scenarios, lighter Higgs bosons are typically preferred in contrast to the mass range favoured within this thesis.

Ultimately, it is up to experiments to determine which theory beyond the Standard Model is realised, possibly through direct observation of a new particle. An observation of such particles may be achieved during the lifetime of the LHC or with the HL-LHC programme. Alternatively, if some of the anomalies in flavour physics happen to persist in the future, indirect evidence for a certain model of new physics may become overwhelming, and it is well possible that flavour observables provide the first hints towards physics beyond the Standard Model.

A. The UFOReader module for `tapir`

Here, we describe the module `UFOReader` that was written to interface the `tapir` [49] package with the Universal Feynman Output (UFO) [47, 48] format¹ provided by the `FeynRules` [44–46] package.²

The Lagrangian of the Standard Model (SM) already gives rise to a plethora of Feynman rules, and this number increases even more in larger theories, e.g. two-Higgs-doublet models (2HDMs). Deriving the enormous set of Feynman rules for these models by hand is unreasonable and error-prone and therefore better left as a task for dedicated software packages such as `FeynRules`. `FeynRules` provides the Feynman rules in terms of a Python module if the UFO output is selected.

On the other hand, multi-loop calculations typically heavily rely on extremely efficient computer algebra languages such as FORM [54] due to the complexity of the expressions involved and number of diagrams at higher loop orders. Originally conceived as an interface between the Feynman diagram generator `qgraf` [50] and the topology identifier/mapper `exp` [51–53] by Marvin Gerlach and Florian Herren, the Python program `tapir` soon grew to incorporate additional features, amongst them partial fraction decomposition and Cutkosky cut filters [213]. For the calculations presented in this thesis, an additional module, the `UFOReader`, was developed and integrated into `tapir` in order to facilitate automated FORM-based calculations even with rather large, automatically produced sets of Feynman rules.

The workflow is depicted in Fig. 4.1.³ First, `FeynRules` must be provided with a number of files corresponding to a physics model.⁴ The `UFOReader` is designed to produce Feynman rules in an arbitrary gauge, including the massive gauge bosons in a theory with spontaneously broken symmetry, e.g. the electroweak theory. To this end, the user should use the Feynman-’t Hooft gauge ($\xi = 1$) during the generation of Feynman rules with `FeynRules`, in order to not eliminate the Goldstone bosons from the list of particles. After the generation of Feynman rules, they should be exported using the `WriteUFO[]` command of `FeynRules`, which produces a Python 2 module. Since `tapir` is entirely written in Python 3, the module needs to be converted between the two versions. During all tests, the program `2to3` [59] performed well:

```
#!/bin/bash
for f in `ls <FR_output_dir>`
do
  2to3 -w $f
```

¹Originally named `Universal FeynRules Output`.

²In Section 4.1, we have presented the features relevant to the calculation presented in this thesis. Here, we also mention some more general aspects of the `UFOReader` that may be useful for higher-order calculations in general.

³All of the following statements refer to the version of `FeynRules` used during this thesis, 2.3.36, but most of them should hold with other `FeynRules` version numbers as well.

⁴It is recommended to start with an existing file from the `FeynRules` model database and to expand on that rather than producing such files from scratch.

done

The Python 3 module can then be used with *tapir*. It is recommended to first use *tapir* to convert the model into *qgraf* and *tapir* notation. This will produce a `.lag` file in which all propagators and vertices are declared in terms of their field content. In addition, two further files, `.prop` and `.vrtx`, are produced with the definitions of the propagators and vertices, respectively, in terms of structures compatible with *tapir* and FORM. Finally, the UF0Reader also provides two auxiliary files containing the declarations (`UF0decl.inc`) and definitions (`UF0repl.inc`) of all couplings in the Lagrangian in FORM code. The philosophy behind this splitting is that in FORM-based calculations the declaration of symbols and functions needs to be given at several stages, but it is usually advantageous to not insert the coupling constants themselves in order to keep the size of intermediate expressions at the minimum possible size. The actual insertion of the definitions of these couplings can then be reserved until the final steps of the calculation, where all (sub-)diagrams are added and the last manipulations are made. That being said, it is mandatory to emphasise that all structures that may have to be manipulated during the intermediate steps – colour factors, Lorentz and Dirac structures – are not absorbed into these couplings, and can therefore be treated in a proper way during all stages of the calculation. It should be mentioned that a small subset of coupling rules is not automatically defined by the two files introduced above, consisting of a number of couplings of fermions to Goldstone bosons or Higgs bosons (in theories with several Higgs bosons). These could in principle also be automatically produced by using the `parameters.py` file produced by *FeynRules*, but they involve CKM matrix elements which would then be set to $V_{ij} = 0$ (if i or $j = 3$ and $i \neq j$), i.e. restricted to the single Cabibbo angle, in the default SM file provided on the *FeynRules* web page, and therefore the automated substitution of the mentioned couplings could produce incorrect results. Hence, we refrain from making any automated replacements involving the `parameters.py` file, which means that the user will have to manually include a small number of replacement rules (which can be looked up in `parameters.py`), in order to maintain compatibility with the default SM and 2HDM files provided in the *FeynRules* model database.⁵ These replacements have to be implemented only once for each model.

After the `.lag` file has been produced, it can be used with *qgraf* to generate all desired Feynman diagrams for the process at hand. The output of *qgraf*, together with the additional `.prop` and `.vrtx` files are then given to *tapir* again, which produces `.dia` and `.edia` files, containing symbolic FORM code for each diagram and per-diagram topological information, respectively.⁶ In the `.dia` file, all propagators and vertices have been replaced by their respective symbolic FORM expressions, as defined in the `.prop` and `.vrtx` files. It should be noted that *FeynRules* and the UF0Reader use spinor indices to express quantities such as $\gamma^\mu \gamma^5$, i.e. they are represented as $(\gamma^\mu \gamma^5)_{ik} = \gamma_{ij}^\mu \gamma_{jk}^5$, with explicit indices, in the symbolic expressions. The `.dia` and `.edia` files can then be used in the usual way by applying projectors or integral tensor reduction, mapping to integral topologies with `exp`, and finally performing the integrations themselves using FORM or other means to solve master integrals.

⁵Future work on the UF0Reader may address this aspect.

⁶A certain number of further files can be produced in addition, such as a file containing `topsel` entries, or files with FORM code for partial fraction decomposition.

A few peculiarities of the `.prop` and `.vrtx` files deserve a discussion and documentation, which we provide in the following two subsections.

A.1. Propagators

As mentioned earlier, the `UF0Reader` is designed to provide Feynman rules in a general R_ξ gauge. Since the `FeynRules` model is given in the Feynman-'t Hooft gauge, no particles are missing, and it is easy to restore the propagator of massive gauge bosons in the R_ξ gauge. The identification of massive gauge bosons is achieved using the spin quantum number and mass parameter of particles.⁷ The association of the Goldstone bosons and ghosts with the gauge boson is also achieved by use of the mass parameter. The propagator of massive gauge bosons in R_ξ gauge,

$$D_{\mu\nu}(k, M, \xi) = \frac{-i \left(g^{\mu\nu} - (1 - \xi) \frac{k^\mu k^\nu}{k^2 - \xi M^2} \right)}{k^2 - M^2}, \quad (\text{A.1})$$

introduces an additional, albeit purely practical difficulty, which is resolved by decomposing these propagators into “transversal” and “longitudinal” components with the help of Eqs. (4.2) to (4.4), where the two components each feature only a single mass in the momentum-dependent part of the denominator and are therefore much easier to treat in automated calculations. At the technical level, this is achieved by the introduction of two particle components X_T and X_L for each massive vector boson, where the subscripts T and L refer to “transversal” and “longitudinal”. For example, the Z boson is decomposed into two fields Z_T and Z_L , which have the propagators of Eqs. (4.3) and (4.4), respectively.

In all other aspects concerning particle propagators, the `UF0Reader` acts as a parser between Python and `tapir`, i.e. it makes some notational changes to the objects and fields.

A.2. Vertices

The action on vertices of the model is also mainly limited to parsing, with two notable exceptions.

Firstly, the restoration of the correct gauge dependence implies that a few vertices have to carry an overall factor of the relevant gauge parameter ξ , for example the three-particle vertex involving the Z -boson ghost, the W^+ -boson ghost and the G^- Goldstone boson, see e.g. Ref. [214]. This factor is simply prefixed to the “Lorentz” section of the corresponding vertex in the `.vrtx` file:

```
{cghZ,CghWp,Gp: *<gauge_parameter_xiZ> *( ufoGC95 * ( 1 ) ) | *(1) | | }
```

The remaining numerical factors expressed in terms of the fundamental parameters of the Lagrangian are contained in `ufoGC95`, and similarly for all other vertices. Furthermore, since the massive gauge bosons are represented by two fields according to Eq. (4.2), for each possible

⁷For this reason, it is not recommended to use the `UF0Reader` with theories incorporating massive vector bosons that are not gauge bosons.

combination of “transversal” and “longitudinal” propagator components entering the vertex an identical copy of the Feynman rule is generated.

Secondly, the four-gluon vertex of QCD does not allow for a trivial factorisation of the colour and non-colour terms of the Feynman rule. This technical difficulty can be solved by the introduction of a so-called *sigma* particle whose propagator is a static contraction of Lorentz and colour indices. While this approach works well for QCD, it would be necessary to introduce a new *sigma* particle for each additional non-factorisable vertex in theories beyond the SM, and we therefore follow a less QCD-tailored approach that was used e.g. in Ref. [215]. For the Feynman rules of non-factorising vertices an auxiliary function `nonfactag()` is introduced with three arguments. The rule for the four-gluon vertex is then given by `(ufocomplex(0,1) = i)`

```
{g,g,g,g:*( ufoGC12 * (
  d_(<lorentz_index_particle_1>,<lorentz_index_particle_4>)
  *d_(<lorentz_index_particle_2>,<lorentz_index_particle_3>)
  -d_(<lorentz_index_particle_1>,<lorentz_index_particle_2>)
  *d_(<lorentz_index_particle_3>,<lorentz_index_particle_4>)
  )*nonfactag(0,1,<local_index_F>)
+ ufoGC12 * (
  d_(<lorentz_index_particle_1>,<lorentz_index_particle_4>)
  *d_(<lorentz_index_particle_2>,<lorentz_index_particle_3>)
  -d_(<lorentz_index_particle_1>,<lorentz_index_particle_3>)
  *d_(<lorentz_index_particle_2>,<lorentz_index_particle_4>)
  ) *nonfactag(0,0,<local_index_F>)
+ ufoGC12 * (
  d_(<lorentz_index_particle_1>,<lorentz_index_particle_3>)
  *d_(<lorentz_index_particle_2>,<lorentz_index_particle_4>)
  -d_(<lorentz_index_particle_1>,<lorentz_index_particle_2>)
  *d_(<lorentz_index_particle_3>,<lorentz_index_particle_4>)
  ) *nonfactag(0,2,<local_index_F>))
|*( ufocomplex(0,1)
  *V3g(<colour_index_particle_-1>,<colour_index_particle_1>,
  <colour_index_particle_2>)*ufocomplex(0,1)
  *V3g(<colour_index_particle_3>,<colour_index_particle_4>,
  <colour_index_particle_-1>)*nonfactag(0,0,<local_index_F>)
+ ufocomplex(0,1)
  *V3g(<colour_index_particle_-1>,<colour_index_particle_1>,
  <colour_index_particle_3>)*ufocomplex(0,1)
  *V3g(<colour_index_particle_2>,<colour_index_particle_4>,
  <colour_index_particle_-1>)*nonfactag(0,1,<local_index_F>)
+ ufocomplex(0,1)
  *V3g(<colour_index_particle_-1>,<colour_index_particle_1>,
  <colour_index_particle_4>)*ufocomplex(0,1)
  *V3g(<colour_index_particle_2>,<colour_index_particle_3>,
  <colour_index_particle_-1>)*nonfactag(0,2,<local_index_F>))
```


|}]

While this rule is rather long it generalises to models with several non-factorisable vertices much better. The three terms in the “Lorentz” section (between the “:” and the first “|”) of the vertex rule differ in the second argument of `nonfactag()`, which labels the term inside the Feynman rule. The third argument, which is the same for all three terms, will be replaced with an index by `tapi r` and corresponds to the position of the vertex in a given Feynman diagram.⁸ The structure of the colour section (between the first and second “|”) is analogous. Finally, the first argument of `nonfactag()` denotes the different non-factorising vertices of the Lagrangian, starting from zero. With this construction, the colour factor and the remaining structure of the Feynman diagram can be computed separately. The correct contraction properties are obtained by setting `nonfactag(x1,y1,z1) * nonfactag(x1,y1,z1) = 1`, and removing all combinations with differing arguments.

⁸For example, the four-gluon vertex may appear twice in a Feynman diagram.

B. The effective $|\Delta B| = |\Delta S| = 1$ vertices

In this chapter we list the effective $\bar{b}_{R/L}S_{L/R}X$ vertices that can be extracted from the Wilson coefficients of the X -penguin diagrams for $B_s \rightarrow \mu^+\mu^-$, where $X = Z, A^0, \phi^{0'}, h^0$ are the Z boson, the pseudoscalar neutral A^0 boson, the additional scalar $\phi^{0'}$ boson and the SM Higgs boson h^0 . In the presence of flavour-changing neutral Yukawa couplings g_{ij}^u these vertices are part of the effective $|\Delta B| = |\Delta S| = 1$ effective Hamiltonian defined in Section 6.5. Written as a double expansion in $\tan \beta$ and $\alpha_s/4\pi$ they read

$$\Gamma_{bsZ}^L = \sum_{n_1=-2}^0 (\tan \beta)^{n_1} \sum_{n_2=0}^1 \left(\frac{\alpha_s}{4\pi}\right)^{n_2} \Gamma_{bsZ, n_1, n_2}^L \quad (\text{B.1})$$

$$\Gamma_{bsZ, -2, 0}^L = -\frac{G_F^2 M_W^4 V_{tb}^* V_{ts} x_t}{2\pi^2 c_{\theta_w} g_w} \cdot \left[\frac{r_H}{r_H - 1} - \frac{r_H \log(r_H)}{(r_H - 1)^2} \right] \equiv -\frac{G_F^2 M_W^4 V_{tb}^* V_{ts} x_t}{2\pi^2 c_{\theta_w} g_w} Z_{H,1}, \quad (\text{B.2})$$

$$\Gamma_{bsZ, -2, 1}^L = -\frac{4G_F^2 M_W^4 V_{tb}^* V_{ts} x_t}{3\pi^2 c_{\theta_w} g_w} \cdot Z_{H,2}, \quad (\text{B.3})$$

$$Z_{H,2} \equiv (r_H) \cdot \left[\left(\frac{3(r_H - 3)}{(r_H - 1)^2} + \frac{6 \log(r_H)}{(r_H - 1)^3} \right) \log\left(\frac{\mu^2}{m_t^2}\right) + \frac{(3 - 3(r_H - 1)) \text{Li}_2\left(\frac{r_H - 1}{r_H}\right)}{(r_H - 1)^2} \right. \\ \left. + \frac{4(r_H - 3)}{(r_H - 1)^2} + \frac{(8 - 3(r_H - 1)) \log(r_H)}{(r_H - 1)^3} \right], \quad (\text{B.4})$$

$$\Gamma_{bsZ, -1, 0}^L = \left(-\frac{G_F m_t M_W^2}{4\pi^2 c_{\theta_w} g_w v_{\text{SM}}} \right) \cdot (Y_4 - Y'_4) \cdot Z_{H,1}, \quad (\text{B.5})$$

$$\Gamma_{bsZ, -1, 1}^L = \left(-\frac{2G_F m_t M_W^2}{3\pi^2 c_{\theta_w} g_w v_{\text{SM}}} \right) \cdot (Y_4 - Y'_4) \cdot Z_{H,2}, \quad (\text{B.6})$$

$$\Gamma_{bsZ, 0, 0}^L = \left(\frac{Y_4 Y'_4 G_F M_W^2}{4\sqrt{2}\pi^2 c_{\theta_w} g_w V_{tb}^* V_{ts}} \right) \cdot Z_{H,1}, \quad (\text{B.7})$$

$$\Gamma_{bsZ, 0, 1}^L = \left(\frac{\sqrt{2} Y_4 Y'_4 G_F M_W^2}{3\pi^2 c_{\theta_w} g_w V_{tb}^* V_{ts}} \right) \cdot Z_{H,2}, \quad (\text{B.8})$$

The coefficients $\Gamma_{bsZ, -2, k}^L$ appear already in the type-II 2HDM, while $\Gamma_{bsZ, i=-1, 0, k}^L$ only exist in the presence of g^u . The right-handed effective $\bar{b}_{RSR}Z$ coupling is purely type-II-like, but we list it here nevertheless:

$$\Gamma_{bsZ}^R = \tan^2 \beta \sum_{n_2=0}^1 \left(\frac{\alpha_s}{4\pi}\right)^{n_2} \Gamma_{bsZ, 2, n_2}^R \quad (\text{B.9})$$

with

$$\Gamma_{bsZ,2,0}^R = \frac{G_F^2 m_b m_s M_W^2 V_{tb}^* V_{ts}}{2\pi^2 c_{\theta_w} g_w} \cdot Z_{H,1}, \quad (\text{B.10})$$

$$\Gamma_{bsZ,2,1}^R = \frac{4G_F^2 m_b m_s M_W^2 V_{tb}^* V_{ts}}{3\pi^2 c_{\theta_w} g_w} \cdot Z_{H,2}. \quad (\text{B.11})$$

The lefthanded A^0 coupling can be expanded as

$$\Gamma_{bsA^0}^L = \sum_{n_1=0}^2 (\tan \beta)^{n_1} \sum_{n_2=0}^1 \left(\frac{\alpha_s}{4\pi}\right)^{n_2} \Gamma_{bsA^0, n_1, n_2}^L, \quad (\text{B.12})$$

with expansion coefficients given by

$$\Gamma_{bsA^0,0,0}^L = \frac{ig_{sb}^*}{\sqrt{2}}, \quad (\text{B.13})$$

$$\Gamma_{bsA^0,0,1}^L = 0, \quad (\text{B.14})$$

$$\Gamma_{bsA^0,1,0}^L = \frac{iG_F m_b v_{SM}}{8\sqrt{2}\pi^2} \cdot \left[\frac{\log(r_H) (Y_4 Y_- r_H - (r_H - 1) (-Y_1 (r_H - 1) + Y_3 (r_H - 1) + Y_3))}{(r_H - 1)^2} + Y_1 \log\left(\frac{\mu^2}{m_t^2}\right) + Y_1 - \frac{Y_4 Y_- r_H}{r_H - 1} \right], \quad (\text{B.15})$$

$$\begin{aligned} \Gamma_{bsA^0,1,1}^L = & -\frac{iG_F m_b v_{SM}}{12\sqrt{2}\pi^2} \cdot \left[-12Y_1 \log^2\left(\frac{\mu^2}{m_t^2}\right) + 12Y_3 \text{Li}_2\left(\frac{r_H - 1}{r_H}\right) \right. \\ & + \frac{1}{(r_H - 1)^2} \{ (r_H - 1) (-(40 + 3\pi^2) Y_1 (r_H - 1) + 6Y_2 r_H \\ & \quad + 2Y_3 ((11 + \pi^2) (r_H - 1) + 11)) + 8Y_4 Y_- (2(r_H - 1)^2 - 5(r_H - 1) - 7) \} \\ & + \frac{\log^2(r_H) (12Y_4 Y_- r_H - 6(r_H - 1) (2Y_1 (r_H - 1)^2 - 2Y_3 (r_H - 1)^2 + Y_3))}{(r_H - 1)^3} \\ & + \log\left(\frac{\mu^2}{m_t^2}\right) \left(-34Y_1 + \frac{24r_H (Y_3 (r_H - 1) + Y_4 Y_- (r_H - 3))}{(r_H - 1)^2} \right. \\ & \quad \left. \left. + \frac{24 \log(r_H) (-Y_1 (r_H - 1)^3 + Y_3 ((r_H - 1)^2 - 1) (r_H - 1) + 2Y_4 Y_- r_H)}{(r_H - 1)^3} \right) \right. \\ & \left. + \frac{\log(r_H)}{(r_H - 1)^3} \{ -34Y_1 (r_H - 1)^3 + 6Y_2 ((r_H - 1)^2 - 1) (r_H - 1) \right. \\ & \quad \left. + 2Y_3 (17(r_H - 1)^2 + 6(r_H - 1) - 11) (r_H - 1) + 56Y_4 Y_- r_H \} \right], \quad (\text{B.16}) \end{aligned}$$

$$\Gamma_{bsA^0,2,0}^L = \frac{iY_4 G_F m_b m_t}{8\pi^2} \cdot \left[\log\left(\frac{\mu^2}{m_t^2}\right) - \frac{\log(r_H)}{r_H - 1} + 1 \right], \quad (\text{B.17})$$

$$\begin{aligned} \Gamma_{bsA^0,2,1}^L = & \frac{iY_4 G_F m_b m_t}{6\pi^2} \cdot \left[\left(-\frac{6}{r_H - 1} + \frac{6 \log(r_H)}{(r_H - 1)^2} + 8 \right) \log\left(\frac{\mu^2}{m_t^2}\right) + 3 \log^2\left(\frac{\mu^2}{m_t^2}\right) - 6 \text{Li}_2\left(\frac{r_H - 1}{r_H}\right) \right. \\ & \left. - \frac{8}{r_H - 1} + \frac{(8 - 6(r_H - 1)) \log(r_H)}{(r_H - 1)^2} + 8 \right]. \quad (\text{B.18}) \end{aligned}$$

For the right-handed $\bar{b}sA^0$ coupling, we write the same expansion

$$\Gamma_{bsA^0}^R = \sum_{n_1=0}^2 (\tan \beta)^{n_1} \sum_{n_2=0}^1 \left(\frac{\alpha_s}{4\pi}\right)^{n_2} \Gamma_{bsA^0, n_1, n_2}^R. \quad (\text{B.19})$$

The individual coefficients of the expansion can be obtained from the left-handed effective vertex by use of the replacements

$$\Gamma_{bsA^0, k, l}^R = \Gamma_{bsA^0, k, l}^L (m_b \rightarrow -m_s, g_{sb}^* \rightarrow -g_{bs}, Y_{2,3} \rightarrow Y'_{2,3}, Y_4 \rightarrow -Y'_4, Y_- \rightarrow -Y_-). \quad (\text{B.20})$$

Comparing with Eq. (5.71) the more complicated set of replacements is due to the $\mathcal{O}(\tan^2 \beta)$ term stemming from the diagrams with a flavour-changing self-energy, in which the replacement of Eq. (5.71) would lead to incorrect coefficients $\Gamma_{bsA^0, 2, l}^R$.

We emphasise that for the effective $\bar{b}sA^0$ couplings we have only shown terms involving the flavour-changing couplings g_{ij}^μ . In Section 4.3.2 we have discussed the computation of contributions to $C_{S,P}^{(\prime)}$ within the 2HDM of type-II. There it was shown that a gauge-invariant result is only obtained after summing contributions from box diagrams and Higgs-penguin diagrams. However, since the box diagrams are 1PI it is not possible to extract from them an effective $|\Delta B| = |\Delta S| = 1$ vertex without reference to the second fermion line, the lepton line in our case. If we only included the type-II-like contributions to the effective $\bar{b}sA^0$ couplings, the result would be gauge-dependent and the addition of box diagrams would be required by all means in order to use the results. We have therefore not included the type-II-like contributions to $\bar{b}sA^0$, but restricted ourselves to the terms involving g_{ij}^μ , which are gauge-invariant. The same holds for the couplings to the $\phi^{0'}$ and h^0 bosons discussed below.

The couplings of the neutral additional Higgs boson $\phi^{0'}$ can be written as

$$\Gamma_{bs\phi^{0'}}^L = \sum_{n_1=0}^2 (\tan \beta)^{n_1} \sum_{n_2=0}^1 \left(\frac{\alpha_s}{4\pi}\right)^{n_2} \Gamma_{bs\phi^{0'}, n_1, n_2}^L, \quad (\text{B.21})$$

with

$$\Gamma_{bs\phi^{0'}, 0, 0}^L = -\frac{g_{sb}^*}{\sqrt{2}}, \quad (\text{B.22})$$

$$\Gamma_{bs\phi^{0'}, 0, 1}^L = 0, \quad (\text{B.23})$$

$$\Gamma_{bs\phi^{0'}, 1, 0}^L = -\frac{G_F m_b v_{\text{SM}}}{8\sqrt{2}\pi^2} \cdot \left[\frac{\log(r_H)}{(r_H - 1)^2} \left\{ Y_4 r_H \left(Y_+ + (r_H - 1) \text{Re}(\tilde{\lambda}_7) + \text{Re}(\tilde{\lambda}_7) \right) \right. \right. \\ \left. \left. - (r_H - 1) (-Y_1 (r_H - 1) + Y_3 (r_H - 1) + Y_3) \right\} \right. \\ \left. + Y_1 \log\left(\frac{\mu^2}{m_t^2}\right) + Y_1 - \frac{Y_4 r_H \left(Y_+ + \text{Re}(\tilde{\lambda}_7) \right)}{r_H - 1} \right], \quad (\text{B.24})$$

$$(\text{B.25})$$

$$\begin{aligned}
 \Gamma_{bs\phi^{0r},1,1}^L &= \frac{G_F m_b v_{\text{SM}}}{12\sqrt{2}\pi^2} \cdot \left[\frac{1}{(r_H - 1)^2} \left\{ (r_H - 1) \left(- (40 + 3\pi^2) Y_1 (r_H - 1) + 6Y_2 r_H \right. \right. \right. \\
 &\quad \left. \left. \left. + 2Y_3 \left((11 + \pi^2) (r_H - 1) + 11 \right) \right) \right. \right. \\
 &\quad \left. \left. \left. + 8Y_4 r_H \left(Y_+ \left(2(r_H - 1) - 7 \right) - \left(2(r_H - 1) + 7 \right) \text{Re} \left(\tilde{\lambda}_7 \right) \right) \right\} \right. \\
 &\quad \left. + \frac{\log(r_H)}{(r_H - 1)^3} \left\{ 2(r_H - 1) \left(-17Y_1 (r_H - 1)^2 + 3Y_2 \left((r_H - 1)^2 - 1 \right) \right. \right. \right. \\
 &\quad \left. \left. \left. + Y_3 \left(17(r_H - 1)^2 + 6(r_H - 1) - 11 \right) \right) \right. \right. \\
 &\quad \left. \left. \left. + 8Y_4 r_H \left(7Y_+ + \left(4(r_H - 1) + 7 \right) \text{Re} \left(\tilde{\lambda}_7 \right) \right) \right\} \right. \\
 &\quad \left. + \log\left(\frac{\mu^2}{m_t^2}\right) \left(\frac{24 \log(r_H)}{(r_H - 1)^3} \left\{ -Y_1 (r_H - 1)^3 + Y_3 \left((r_H - 1)^2 - 1 \right) (r_H - 1) \right. \right. \right. \\
 &\quad \left. \left. \left. + 2Y_4 r_H \left(Y_+ + (r_H - 1) \text{Re} \left(\tilde{\lambda}_7 \right) + \text{Re} \left(\tilde{\lambda}_7 \right) \right) \right\} - 34Y_1 \right. \right. \\
 &\quad \left. \left. \left. + \frac{24r_H \left(Y_3 (r_H - 1) + Y_4 Y_+ (r_H - 3) - Y_4 (r_H + 1) \text{Re} \left(\tilde{\lambda}_7 \right) \right)}{(r_H - 1)^2} \right) \right. \\
 &\quad \left. + \frac{\log^2(r_H)}{(r_H - 1)^3} \left\{ 12Y_4 r_H \left(Y_+ + (r_H - 1) \text{Re} \left(\tilde{\lambda}_7 \right) + \text{Re} \left(\tilde{\lambda}_7 \right) \right) \right. \right. \\
 &\quad \left. \left. \left. - 6(r_H - 1) \left(2Y_1 (r_H - 1)^2 - 2Y_3 (r_H - 1)^2 + Y_3 \right) \right. \right. \\
 &\quad \left. \left. \left. - 12Y_1 \log^2\left(\frac{\mu^2}{m_t^2}\right) + 12Y_3 \text{Li}_2\left(\frac{r_H - 1}{r_H}\right) \right\} \right], \tag{B.26}
 \end{aligned}$$

$$\Gamma_{bs\phi^{0r},2,0}^L = -\frac{Y_4 G_F m_b m_t}{8\pi^2} \cdot \left[\log\left(\frac{\mu^2}{m_t^2}\right) - \frac{\log(r_H)}{r_H - 1} + 1 \right], \tag{B.27}$$

$$\begin{aligned}
 \Gamma_{bs\phi^{0r},2,1}^L &= \frac{Y_4 G_F m_b m_t}{6\pi^2} \cdot \left[\left(\frac{6}{r_H - 1} - \frac{6 \log(r_H)}{(r_H - 1)^2} - 8 \right) \log\left(\frac{\mu^2}{m_t^2}\right) - 3 \log^2\left(\frac{\mu^2}{m_t^2}\right) \right. \\
 &\quad \left. + 6 \text{Li}_2\left(\frac{r_H - 1}{r_H}\right) + \frac{8}{r_H - 1} + \frac{(6(r_H - 1) - 8) \log(r_H)}{(r_H - 1)^2} - 8 \right]. \tag{B.28}
 \end{aligned}$$

In order to obtain the right-handed effective couplings, one can expand $\Gamma_{bs\phi^{0r}}^R$ in the same way,

$$\Gamma_{bs\phi^{0r}}^R = \sum_{n_1=0}^2 (\tan \beta)^{n_1} \sum_{n_2=0}^1 \left(\frac{\alpha_s}{4\pi} \right)^{n_2} \Gamma_{bs\phi^{0r},n_1,n_2}^R, \tag{B.29}$$

and make the replacements

$$\Gamma_{bs\phi^{0r},k,l}^R = \Gamma_{bs\phi^{0r},k,l}^L (m_b \rightarrow m_s, g_{sb}^* \rightarrow g_{bs}, Y_{2,3} \rightarrow Y'_{2,3}, Y_4 \rightarrow -Y'_4). \tag{B.30}$$

Finally, the effective $\bar{b}sh^0$ couplings to the SM Higgs boson can be expanded as

$$\Gamma_{bsh^0}^L = \sum_{n_1=0}^1 (\tan \beta)^{n_1} \sum_{n_2=0}^1 \left(\frac{\alpha_s}{4\pi} \right)^{n_2} \Gamma_{bsh^0,n_1,n_2}^L, \tag{B.31}$$

with expansion coefficients

$$\Gamma_{bsh^0,0,0}^L = 0, \quad (\text{B.32})$$

$$\Gamma_{bsh^0,0,1}^L = 0, \quad (\text{B.33})$$

$$\Gamma_{bsh^0,1,0}^L = \frac{Y_4 G_F m_b}{16\pi^2} \cdot \left[2m_t \log\left(\frac{\mu^2}{m_t^2}\right) + \frac{\log(r_H) \left(2m_t (r_H + 1) - \sqrt{2}r_H^2 \tilde{\lambda}_3 v_{\text{SM}}\right)}{(r_H - 1)^2} + \frac{\sqrt{2}r_H \tilde{\lambda}_3 v_{\text{SM}} - 2m_t (r_H + 1)}{r_H - 1} \right], \quad (\text{B.34})$$

$$\begin{aligned} \Gamma_{bsh^0,1,1}^L = \frac{Y_4 G_F m_b}{12\pi^2} \cdot & \left[\log\left(\frac{\mu^2}{m_t^2}\right) \left(\frac{24 \log(r_H) \left(\sqrt{2}r_H^2 \tilde{\lambda}_3 v_{\text{SM}} - m_t (3(r_H - 1) + 4)\right)}{(r_H - 1)^3} \right. \right. \\ & \left. \left. - \frac{4 \left(m_t (8(r_H - 1)^2 - 6(r_H - 1) - 24) + 3\sqrt{2}((r_H - 1)^2 + 3(r_H - 1) + 2) \tilde{\lambda}_3 v_{\text{SM}}\right)}{(r_H - 1)^2} \right) \right. \\ & + 12m_t \log^2\left(\frac{\mu^2}{m_t^2}\right) - 12m_t \text{Li}_2\left(\frac{r_H - 1}{r_H}\right) \\ & + \frac{\log^2(r_H) \left(6\sqrt{2}r_H^2 \tilde{\lambda}_3 v_{\text{SM}} - 6m_t (3(r_H - 1) + 4)\right)}{(r_H - 1)^3} \\ & + \frac{m_t \left((\pi^2 - 16)(r_H - 1)^2 + 52(r_H - 1) + 112\right)}{(r_H - 1)^2} \\ & + \frac{4\sqrt{2} \left(2(r_H - 1)^2 + 9(r_H - 1) + 7\right) \tilde{\lambda}_3 v_{\text{SM}}}{(r_H - 1)^2} \\ & \left. + \frac{\log(r_H)}{(r_H - 1)^3} \left\{ 4\sqrt{2} \left(4(r_H - 1)^2 + 11(r_H - 1) + 7\right) \tilde{\lambda}_3 v_{\text{SM}} \right. \right. \\ & \left. \left. - 4m_t \left(3(r_H - 1)^2 + 21(r_H - 1) + 28\right) \right\} \right]. \quad (\text{B.35}) \end{aligned}$$

In order to obtain the right-handed effective couplings, one can expand $\Gamma_{bsh^0}^R$ in the same way,

$$\Gamma_{bsh^0}^R = \sum_{n_1=0}^1 (\tan \beta)^{n_1} \sum_{n_2=0}^1 \left(\frac{\alpha_s}{4\pi}\right)^{n_2} \Gamma_{bsh^0,n_1,n_2}^R \quad (\text{B.36})$$

and express right-handed couplings in terms of left-handed couplings with the replacements

$$\Gamma_{bsh^0,k,l}^R = \Gamma_{bsh^0,k,l}^L (m_b \rightarrow m_s, g_{sb}^* \rightarrow g_{bs}, Y_{2,3} \rightarrow Y'_{2,3}, Y_4 \rightarrow -Y'_4). \quad (\text{B.37})$$

C. Supplementary figures and equations

The approximate formula for R_γ in the case of $b \rightarrow d\gamma$ is given, with the SM value given by $b \rightarrow s\gamma$, while assuming the 2HDM arise in the interference between the SM and 2HDM Wilson coefficients for $b \rightarrow d\gamma$, by

$$\begin{aligned}
 R_\gamma \approx 10^{-4} \cdot \left\{ 33.10|_{\text{SM}} + 10^{-3} \text{Re } g_{dt}^{\text{eff}} \right. & \\
 + \left(0.28 \log^3 (r_H) + 1.78 \log^2 (r_H) + 85.03 \log (r_H) - 8.42 \text{Li}_2 \left(1 - \frac{1}{r_H} \right) + 87.41 \right) r_H & \\
 + \left(0.18 \log^3 (r_H) + 3.69 \log^2 (r_H) + 175.41 \log (r_H) - 8.56 \text{Li}_2 \left(1 - \frac{1}{r_H} \right) + 96.19 \right) r_H^2 & \\
 + \left(-0.11 \log^3 (r_H) + 4.23 \log^2 (r_H) + 268.82 \log (r_H) - 5.68 \text{Li}_2 \left(1 - \frac{1}{r_H} \right) + 100.18 \right) r_H^3 & \\
 + \left. 0.23 r_H^4 \text{Li}_2 \left(1 - \frac{1}{r_H} \right) \right\}. & \tag{C.1}
 \end{aligned}$$

The approximate relation for $\text{Re } M_{12,s}^{2\text{HDM}}$ for complex $\alpha \in \mathbb{C}$ is given by

$$\begin{aligned}
 \frac{2\text{Re } M_{12,s}^{2\text{HDM}}}{1 \text{ ps}^{-1}} = 2.13 \cdot 10^5 \left[\left(\frac{1 \text{ TeV}}{M_{\phi^{0'}}} \right)^2 - \left(\frac{1 \text{ TeV}}{M_{A^0}} \right)^2 \right] & \left[\text{Re } (g_{sb}^2) (1 + \text{Re}^2 (\alpha) - \text{Im}^2 (\alpha)) \right. \\
 & \left. - \text{Im} (\alpha^2) \text{Im } (g_{sb}^2) \right] \\
 - 6.08 \cdot 10^5 \left[\left(\frac{1 \text{ TeV}}{M_{\phi^{0'}}} \right)^2 + \left(\frac{1 \text{ TeV}}{M_{A^0}} \right)^2 \right] & \left[\text{Re } (\alpha) \text{Re } (g_{sb}^2) + \text{Im } (\alpha) \text{Im } (g_{sb}^2) \right]. & \tag{C.2}
 \end{aligned}$$

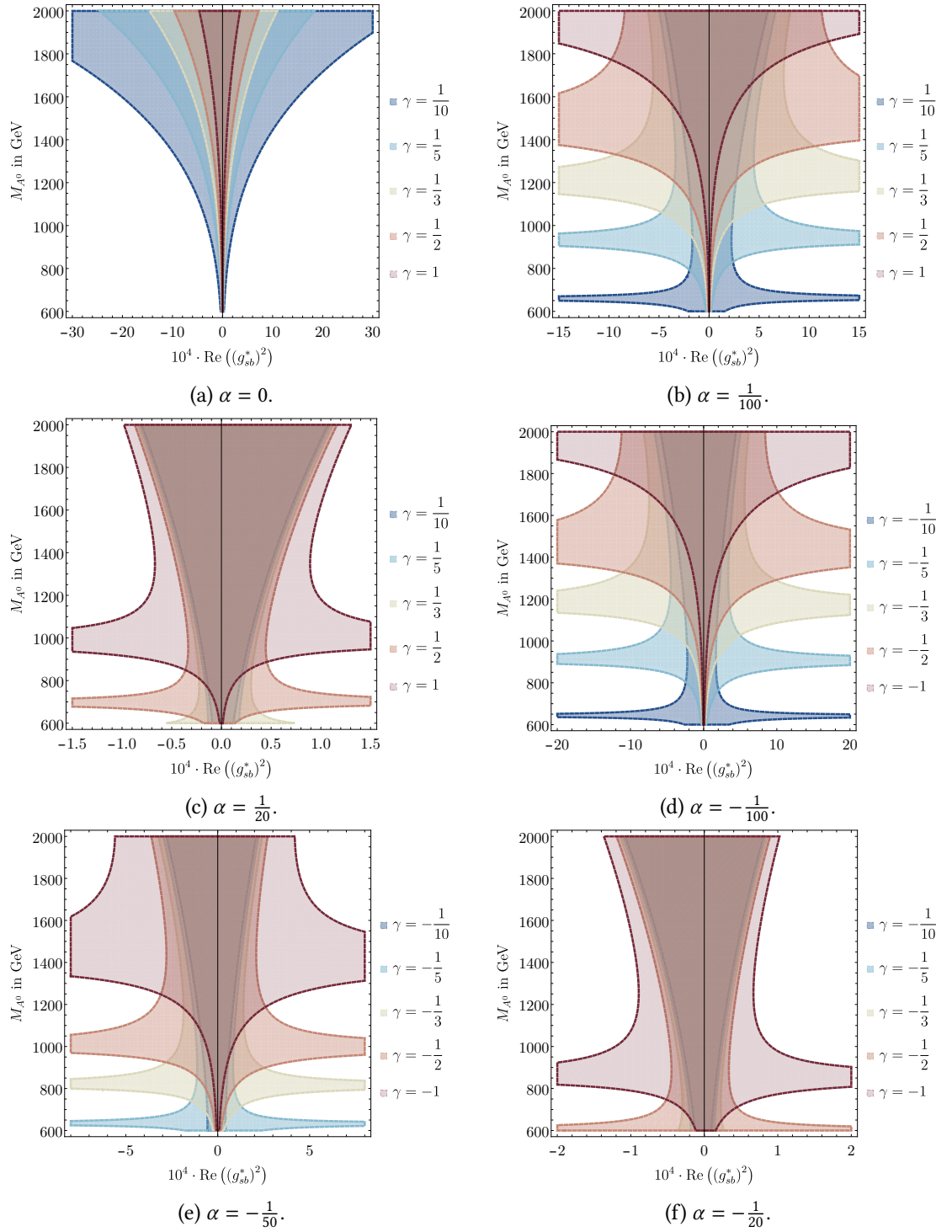
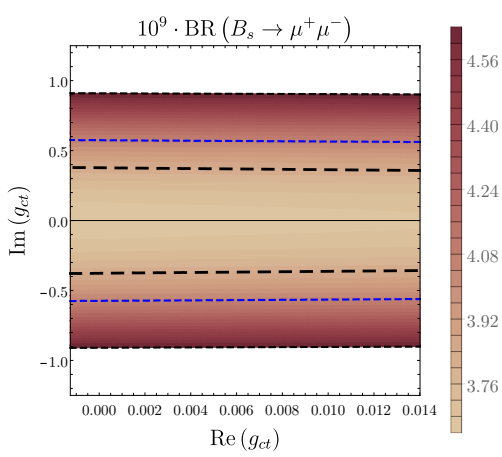
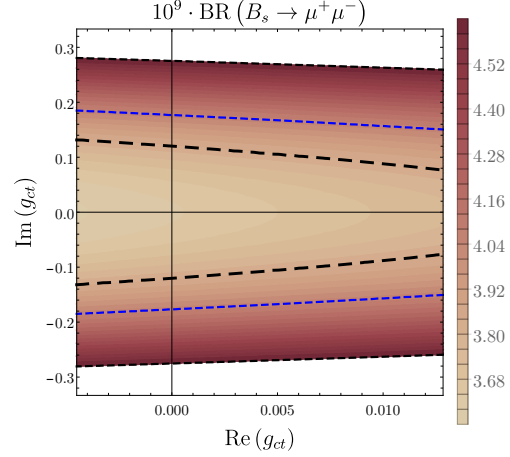


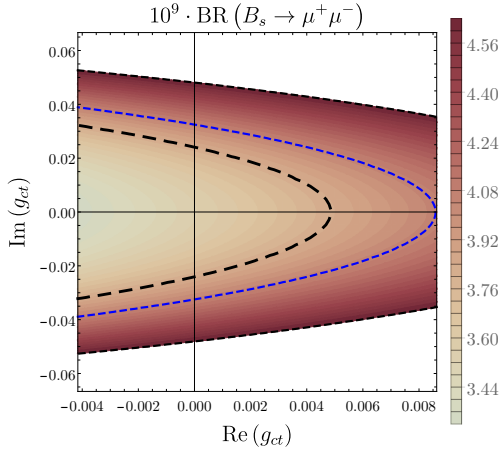
Figure C.1.: Caption identical to Fig. 6.7, except for different values of α .



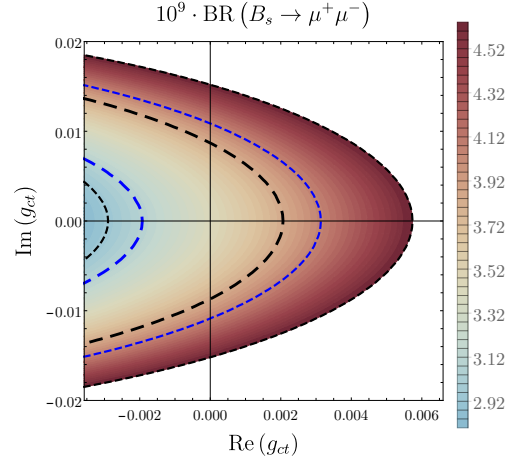
(a) $\tan \beta = 7$, $M_{H^\pm} = M_{\phi^{0\prime}} = 700$ GeV, $M_{A^0} = 850$ GeV.



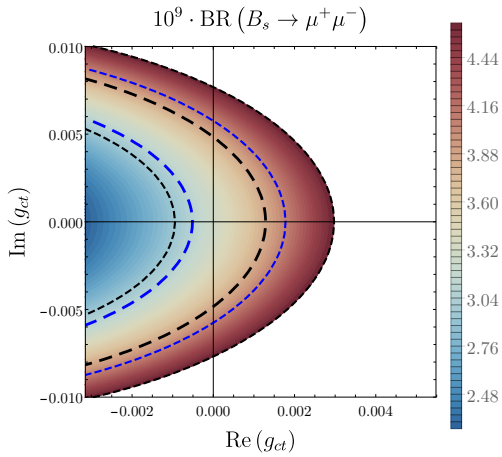
(b) $\tan \beta = 12$, $M_{H^\pm} = M_{\phi^{0\prime}} = 1100$ GeV, $M_{A^0} = 1200$ GeV.



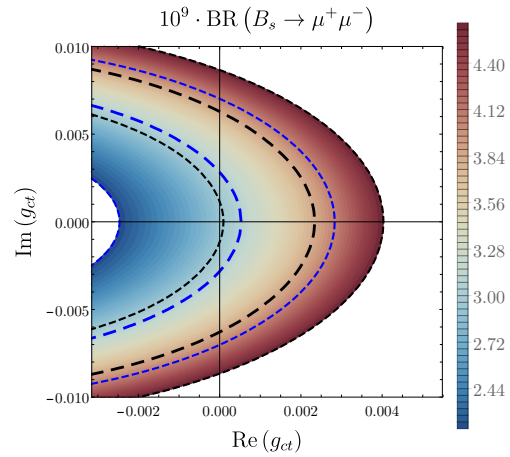
(c) $\tan \beta = 25$, $M_{H^\pm} = M_{\phi^{0\prime}} = 1500$ GeV, $M_{A^0} = 1600$ GeV.



(d) $\tan \beta = 40$, $M_{H^\pm} = M_{\phi^{0\prime}} = 1750$ GeV, $M_{A^0} = 1800$ GeV.



(e) $\tan \beta = 55$, $M_{H^\pm} = 1950$ GeV, $M_{\phi^{0\prime}} = 2050$ GeV, $M_{A^0} = 2000$ GeV, $\text{Re}(\lambda_7) = 1$.



(f) $\tan \beta = 55$, $M_{H^\pm} = 1950$ GeV, $M_{\phi^{0\prime}} = 2050$ GeV, $M_{A^0} = 2000$ GeV, $\phi_{\text{NP}}^s = \pi$.

Figure C.2.: Caption identical to Fig. 6.9, except for different input parameters.

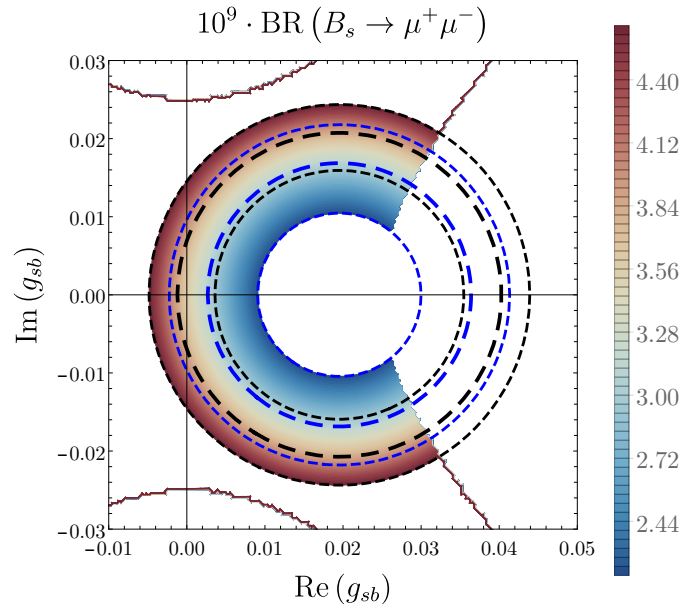


Figure C.3.: Figure analogous to Fig. 6.12b with the same numerical input, but without the constraint on $\text{Im}(g_{sb}^*{}^2)$.

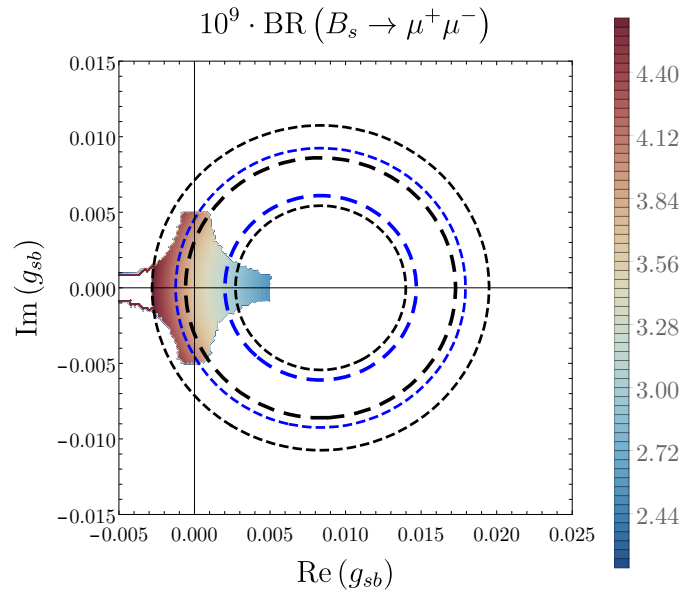


Figure C.4.: Figure analogous to Fig. 6.12b, but with different numerical input $\tan \beta = 7$, $M_{H^\pm} = 700$ GeV, $M_{\phi^{0,\prime}} = 700$ GeV, $M_{A^0} = 850$ GeV.

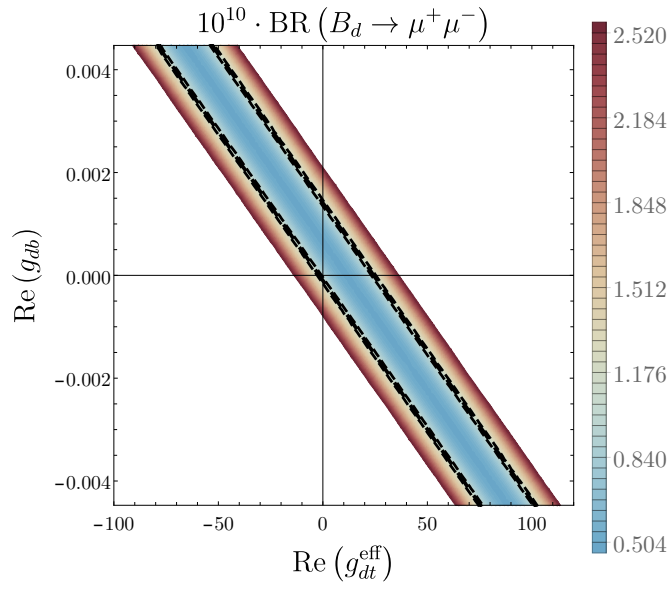


Figure C.5.: Exclusions for $\text{Im}(g_{dt}^{\text{eff}}) = \text{Im}(g_{db}) = 0$, $\tan\beta = 55$, $M_{H^\pm} = 1950$ GeV, $M_{\phi^{0,\prime}} = 2050$ GeV, $M_{A^0} = 2000$ GeV. Dashed black lines show the SM prediction including its uncertainties, the coloured area shows the region in which $\mathcal{B}(B_d \rightarrow \mu^+ \mu^-) < 2.6 \cdot 10^{-10}$.

D. Numerical input

Table D.1.: Numerical input used for the phenomenological analysis. For the QCD running of the quark masses and the renormalisation scale we have used RunDec [216, 217]. The numerical values of the CKM matrix elements have been taken from the recent updates on the CKMfitter [186] web page. Since the constraints discussed in Chapter 6 are affected with significant uncertainties, mainly due to the various approximations made in order to reduce the complexity and dimensionality of the parameter space, we do not show the (generally much smaller) uncertainties of the numerical input parameters here.

parameter	value	reference
m_μ	0.105 66 GeV	PDG [3]
V_{tb}	0.999142	CKMfitter
V_{ts}	-0.04065	CKMfitter
G_F	$1.166\,378\,8 \times 10^{-5} \text{ GeV}^{-2}$	PDG [3]
V_{cs}	0.973521	CKMfitter
V_{cb}	0.04145	CKMfitter
V_{us}	0.225	CKMfitter
V_{td}	$0.008519 \cdot e^{-i\frac{2.456}{2\pi}}$	CKMfitter
V_{ud}	0.974353	CKMfitter
$\bar{m}_t (\bar{m}_t)$	162.464 GeV	PDG [3] (converted from $m_t^{\text{pole}} = 172.69 \text{ GeV}$)
$\bar{m}_b (\bar{m}_b)$	4.18 GeV	PDG [3]
$\bar{m}_s (2 \text{ GeV})$	0.0934 GeV	PDG [3]
M_W	80.379 GeV	PDG [3]
M_Z	91.1876 GeV	PDG [3]
$\alpha_s (M_Z)$	0.1179	PDG [3]
M_{B_s}	5.366 92 GeV	PDG [3]
M_{B_d}	5.279 66 GeV	PDG [3]
f_{B_s}	0.2303 GeV	FLAG [180, 218–221]
Γ_H^s	1.624 ps^{-1}	PDG [3]
Γ_L^s	1.431 ps^{-1}	PDG [3]
f_{B_d}	0.1900 GeV	FLAG [180, 218–221]
$\Gamma_H^d = \Gamma_L^d$	1.519 ps^{-1}	PDG [3]

Bibliography

- [1] ATLAS Collaboration, G. Aad et al. “Observation of a new particle in the search for the Standard Model Higgs boson with the ATLAS detector at the LHC”. *Phys. Lett. B* 716 (2012), pp. 1–29. DOI: 10.1016/j.physletb.2012.08.020. arXiv: 1207.7214 [hep-ex].
- [2] CMS Collaboration, S. Chatrchyan et al. “Observation of a New Boson at a Mass of 125 GeV with the CMS Experiment at the LHC”. *Phys. Lett. B* 716 (2012), pp. 30–61. DOI: 10.1016/j.physletb.2012.08.021. arXiv: 1207.7235 [hep-ex].
- [3] Particle Data Group, R. L. Workman et al. “Review of Particle Physics”. *PTEP* 2022 (2022), p. 083C01. DOI: 10.1093/ptep/ptac097.
- [4] G. C. Branco et al. “Theory and phenomenology of two-Higgs-doublet models”. *Phys. Rept.* 516 (2012), pp. 1–102. DOI: 10.1016/j.physrep.2012.02.002. arXiv: 1106.0034 [hep-ph].
- [5] F. Englert and R. Brout. “Broken Symmetry and the Mass of Gauge Vector Mesons”. *Phys. Rev. Lett.* 13 (1964), pp. 321–323. DOI: 10.1103/PhysRevLett.13.321.
- [6] P. W. Higgs. “Broken symmetries, massless particles and gauge fields”. *Phys. Lett.* 12 (1964), pp. 132–133. DOI: 10.1016/0031-9163(64)91136-9.
- [7] P. W. Higgs. “Broken Symmetries and the Masses of Gauge Bosons”. *Phys. Rev. Lett.* 13 (1964), pp. 508–509. DOI: 10.1103/PhysRevLett.13.508.
- [8] G. S. Guralnik, C. R. Hagen, and T. W. B. Kibble. “Global Conservation Laws and Massless Particles”. *Phys. Rev. Lett.* 13 (1964), pp. 585–587. DOI: 10.1103/PhysRevLett.13.585.
- [9] P. W. Higgs. “Spontaneous Symmetry Breakdown without Massless Bosons”. *Phys. Rev.* 145 (1966), pp. 1156–1163. DOI: 10.1103/PhysRev.145.1156.
- [10] T. W. B. Kibble. “Symmetry breaking in non-Abelian gauge theories”. *Phys. Rev.* 155 (1967), pp. 1554–1561. DOI: 10.1103/PhysRev.155.1554.
- [11] CMS Collaboration, A. M. Sirunyan et al. “Combined measurements of Higgs boson couplings in proton–proton collisions at $\sqrt{s} = 13$ TeV”. *Eur. Phys. J. C* 79.5 (2019), p. 421. DOI: 10.1140/epjc/s10052-019-6909-y. arXiv: 1809.10733 [hep-ex].
- [12] ATLAS Collaboration, G. Aad et al. “Combined measurements of Higgs boson production and decay using up to 80 fb⁻¹ of proton-proton collision data at $\sqrt{s} = 13$ TeV collected with the ATLAS experiment”. *Phys. Rev. D* 101.1 (2020), p. 012002. DOI: 10.1103/PhysRevD.101.012002. arXiv: 1909.02845 [hep-ex].
- [13] T. Banks. “Supersymmetry and the Quark Mass Matrix”. *Nucl. Phys. B* 303 (1988), pp. 172–188. DOI: 10.1016/0550-3213(88)90222-2.

- [14] L. J. Hall, R. Rattazzi, and U. Sarid. “The Top quark mass in supersymmetric SO(10) unification”. *Phys. Rev. D* 50 (1994), pp. 7048–7065. DOI: 10.1103/PhysRevD.50.7048. arXiv: hep-ph/9306309.
- [15] M. Carena, M. Olechowski, S. Pokorski, and C. E. M. Wagner. “Electroweak symmetry breaking and bottom - top Yukawa unification”. *Nucl. Phys. B* 426 (1994), pp. 269–300. DOI: 10.1016/0550-3213(94)90313-1. arXiv: hep-ph/9402253.
- [16] N. G. Deshpande and E. Ma. “Pattern of Symmetry Breaking with Two Higgs Doublets”. *Phys. Rev. D* 18 (1978), p. 2574. DOI: 10.1103/PhysRevD.18.2574.
- [17] E. Ma. “Verifiable radiative seesaw mechanism of neutrino mass and dark matter”. *Phys. Rev. D* 73 (2006), p. 077301. DOI: 10.1103/PhysRevD.73.077301. arXiv: hep-ph/0601225.
- [18] R. Barbieri, L. J. Hall, and V. S. Rychkov. “Improved naturalness with a heavy Higgs: An Alternative road to LHC physics”. *Phys. Rev. D* 74 (2006), p. 015007. DOI: 10.1103/PhysRevD.74.015007. arXiv: hep-ph/0603188.
- [19] A. Pich and P. Tuzon. “Yukawa Alignment in the Two-Higgs-Doublet Model”. *Phys. Rev. D* 80 (2009), p. 091702. DOI: 10.1103/PhysRevD.80.091702. arXiv: 0908.1554 [hep-ph].
- [20] P. Tuzon and A. Pich. “The Aligned two-Higgs Doublet model”. *Acta Phys. Polon. Supp.* 3 (2010), pp. 215–220. arXiv: 1001.0293 [hep-ph].
- [21] P. M. Ferreira, L. Lavoura, and J. P. Silva. “Renormalization-group constraints on Yukawa alignment in multi-Higgs-doublet models”. *Phys. Lett. B* 688 (2010), pp. 341–344. DOI: 10.1016/j.physletb.2010.04.033. arXiv: 1001.2561 [hep-ph].
- [22] J. Bijnens, J. Lu, and J. Rathsman. “Constraining General Two Higgs Doublet Models by the Evolution of Yukawa Couplings”. *JHEP* 05 (2012), p. 118. DOI: 10.1007/JHEP05(2012)118. arXiv: 1111.5760 [hep-ph].
- [23] C. B. Braeuninger, A. Ibarra, and C. Simonetto. “Radiatively induced flavour violation in the general two-Higgs doublet model with Yukawa alignment”. *Phys. Lett. B* 692 (2010), pp. 189–195. DOI: 10.1016/j.physletb.2010.07.039. arXiv: 1005.5706 [hep-ph].
- [24] S. Gori, H. E. Haber, and E. Santos. “High scale flavor alignment in two-Higgs doublet models and its phenomenology”. *JHEP* 06 (2017), p. 110. DOI: 10.1007/JHEP06(2017)110. arXiv: 1703.05873 [hep-ph].
- [25] X.-Q. Li, J. Lu, and A. Pich. “ $B_{s,d}^0 \rightarrow \ell^+ \ell^-$ Decays in the Aligned Two-Higgs-Doublet Model”. *JHEP* 06 (2014), p. 022. DOI: 10.1007/JHEP06(2014)022. arXiv: 1404.5865 [hep-ph].
- [26] U. Nierste, M. Tabet, and R. Ziegler. “Cornering Spontaneous CP Violation with Charged-Higgs-Boson Searches”. *Phys. Rev. Lett.* 125.3 (2020), p. 031801. DOI: 10.1103/PhysRevLett.125.031801. arXiv: 1912.11501 [hep-ph].
- [27] C. Bobeth, M. Gorbahn, and E. Stamou. “Electroweak Corrections to $B_{s,d} \rightarrow \ell^+ \ell^-$ ”. *Phys. Rev. D* 89.3 (2014), p. 034023. DOI: 10.1103/PhysRevD.89.034023. arXiv: 1311.1348 [hep-ph].

- [28] A. J. Buras. “Weak Hamiltonian, CP violation and rare decays”. *Les Houches Summer School in Theoretical Physics, Session 68: Probing the Standard Model of Particle Interactions*. 1998, pp. 281–539. arXiv: hep-ph/9806471.
- [29] T. Hermann. “Seltene B-Meson-Zerfälle innerhalb und jenseits des Standardmodells”. PhD thesis. KIT, Karlsruhe, 2014. DOI: 10.5445/IR/1000041138.
- [30] CMS, LHCb Collaborations, V. Khachatryan et al. “Observation of the rare $B_s^0 \rightarrow \mu^+ \mu^-$ decay from the combined analysis of CMS and LHCb data”. *Nature* 522 (2015), pp. 68–72. DOI: 10.1038/nature14474. arXiv: 1411.4413 [hep-ex].
- [31] C. Bobeth et al. “ $B_{s,d} \rightarrow l^+ l^-$ in the Standard Model with Reduced Theoretical Uncertainty”. *Phys. Rev. Lett.* 112 (2014), p. 101801. DOI: 10.1103/PhysRevLett.112.101801. arXiv: 1311.0903 [hep-ph].
- [32] P. Gambino and C. Schwanda. “Inclusive semileptonic fits, heavy quark masses, and V_{cb} ”. *Phys. Rev. D* 89.1 (2014), p. 014022. DOI: 10.1103/PhysRevD.89.014022. arXiv: 1307.4551 [hep-ph].
- [33] ATLAS Collaboration, M. Aaboud et al. “Study of the rare decays of B_s^0 and B^0 mesons into muon pairs using data collected during 2015 and 2016 with the ATLAS detector”. *JHEP* 04 (2019), p. 098. DOI: 10.1007/JHEP04(2019)098. arXiv: 1812.03017 [hep-ex].
- [34] CMS Collaboration, A. M. Sirunyan et al. “Measurement of properties of $B_s^0 \rightarrow \mu^+ \mu^-$ decays and search for $B^0 \rightarrow \mu^+ \mu^-$ with the CMS experiment”. *JHEP* 04 (2020), p. 188. DOI: 10.1007/JHEP04(2020)188. arXiv: 1910.12127 [hep-ex].
- [35] LHCb Collaboration, R. Aaij et al. “Measurement of the $B_s^0 \rightarrow \mu^+ \mu^-$ decay properties and search for the $B^0 \rightarrow \mu^+ \mu^-$ and $B_s^0 \rightarrow \mu^+ \mu^- \gamma$ decays”. *Phys. Rev. D* 105.1 (2022), p. 012010. DOI: 10.1103/PhysRevD.105.012010. arXiv: 2108.09283 [hep-ex].
- [36] LHCb Collaboration, R. Aaij et al. “Analysis of Neutral B-Meson Decays into Two Muons”. *Phys. Rev. Lett.* 128.4 (2022), p. 041801. DOI: 10.1103/PhysRevLett.128.041801. arXiv: 2108.09284 [hep-ex].
- [37] CMS Collaboration, A. Tumasyan et al. “Measurement of the $B_s^0 \rightarrow \mu^+ \mu^-$ decay properties and search for the $B^0 \rightarrow \mu^+ \mu^-$ decay in proton-proton collisions at $\sqrt{s} = 13$ TeV”. *Phys. Lett. B* 842 (2023), p. 137955. DOI: 10.1016/j.physletb.2023.137955. arXiv: 2212.10311 [hep-ex].
- [38] CMS Collaboration, S. Chatrchyan et al. “Measurement of the $B_s^0 \rightarrow \mu^+ \mu^-$ Branching Fraction and Search for $B^0 \rightarrow \mu^+ \mu^-$ with the CMS Experiment”. *Phys. Rev. Lett.* 111 (2013), p. 101804. DOI: 10.1103/PhysRevLett.111.101804. arXiv: 1307.5025 [hep-ex].
- [39] LHCb Collaboration, R. Aaij et al. “Measurement of the $B_s^0 \rightarrow \mu^+ \mu^-$ branching fraction and effective lifetime and search for $B^0 \rightarrow \mu^+ \mu^-$ decays”. *Phys. Rev. Lett.* 118.19 (2017), p. 191801. DOI: 10.1103/PhysRevLett.118.191801. arXiv: 1703.05747 [hep-ex].
- [40] ATLAS Collaboration, *Snowmass White Paper Contribution: Physics with the Phase-2 ATLAS and CMS Detectors*. Tech. rep. Geneva: CERN, 2022. URL: <https://cds.cern.ch/record/2805993>.

- [41] ATLAS Collaboration, *Prospects for the $\mathcal{B}(B_{(s)}^0 \rightarrow \mu^+ \mu^-)$ measurements with the ATLAS detector in the Run 2 and HL-LHC data campaigns*. Tech. rep. Geneva: CERN, 2018. URL: <https://cds.cern.ch/record/2317211>.
- [42] CMS Collaboration, *Measurement of rare $B \rightarrow \mu^+ \mu^-$ decays with the Phase-2 upgraded CMS detector at the HL-LHC*. Tech. rep. Geneva: CERN, 2018. URL: <https://cds.cern.ch/record/2650545>.
- [43] LHCb Collaboration, R. Aaij et al. “Search for the decays $B_s^0 \rightarrow \tau^+ \tau^-$ and $B^0 \rightarrow \tau^+ \tau^-$ ”. *Phys. Rev. Lett.* 118.25 (2017), p. 251802. DOI: 10.1103/PhysRevLett.118.251802. arXiv: 1703.02508 [hep-ex].
- [44] A. Alloul et al. “FeynRules 2.0 - A complete toolbox for tree-level phenomenology”. *Comput. Phys. Commun.* 185 (2014), pp. 2250–2300. DOI: 10.1016/j.cpc.2014.04.012. arXiv: 1310.1921 [hep-ph].
- [45] N. D. Christensen et al. “A Comprehensive approach to new physics simulations”. *Eur. Phys. J. C* 71 (2011), p. 1541. DOI: 10.1140/epjc/s10052-011-1541-5. arXiv: 0906.2474 [hep-ph].
- [46] A. Alloul et al. “New developments in FeynRules”. *J. Phys. Conf. Ser.* 523 (2014), p. 01. DOI: 10.1088/1742-6596/523/1/012044. arXiv: 1309.7806 [hep-ph].
- [47] C. Degrande et al. “UFO - The Universal FeynRules Output”. *Comput. Phys. Commun.* 183 (2012), pp. 1201–1214. DOI: 10.1016/j.cpc.2012.01.022. arXiv: 1108.2040 [hep-ph].
- [48] L. Darmé et al. “UFO 2.0: the ‘Universal Feynman Output’ format”. *Eur. Phys. J. C* 83.7 (2023), p. 631. DOI: 10.1140/epjc/s10052-023-11780-9. arXiv: 2304.09883 [hep-ph].
- [49] M. Gerlach, F. Herren, and M. Lang. “tapir: A tool for topologies, amplitudes, partial fraction decomposition and input for reductions”. *Comput. Phys. Commun.* 282 (2023), p. 108544. DOI: 10.1016/j.cpc.2022.108544. arXiv: 2201.05618 [hep-ph].
- [50] P. Nogueira. “Automatic Feynman graph generation”. *J. Comput. Phys.* 105 (1993), pp. 279–289. DOI: 10.1006/jcph.1993.1074.
- [51] R. Harlander, T. Seidensticker, and M. Steinhauser. “Complete corrections of Order α_s^2 to the decay of the Z boson into bottom quarks”. *Phys. Lett. B* 426 (1998), pp. 125–132. DOI: 10.1016/S0370-2693(98)00220-2. arXiv: hep-ph/9712228.
- [52] T. Seidensticker. “Automatic application of successive asymptotic expansions of Feynman diagrams”. *6th International Workshop on New Computing Techniques in Physics Research: Software Engineering, Artificial Intelligence Neural Nets, Genetic Algorithms, Symbolic Algebra, Automatic Calculation*. 1999. arXiv: hep-ph/9905298.
- [53] R. Harlander, T. Seidensticker, and M. Steinhauser. *q2e/exp*. 1997. URL: <http://sfb-tr9.ttp.kit.edu/software/html/q2eexp.html>.
- [54] B. Ruijl, T. Ueda, and J. Vermaseren. “FORM version 4.2” (2017). arXiv: 1707.06453 [hep-ph].
- [55] C. Degrande. “Automated Two Higgs Doublet Model at NLO”. *PoS Charged2014* (2015), p. 024. DOI: 10.22323/1.209.0024. arXiv: 1412.6955 [hep-ph].

- [56] C. Degrande. “Automatic evaluation of UV and R2 terms for beyond the Standard Model Lagrangians: a proof-of-principle”. *Comput. Phys. Commun.* 197 (2015), pp. 239–262. DOI: 10.1016/j.cpc.2015.08.015. arXiv: 1406.3030 [hep-ph].
- [57] W. R. Inc. *Mathematica, Version 12.1*. Champaign, IL. 2020.
- [58] G. Van Rossum and F. L. Drake Jr. *Python tutorial*. Centrum voor Wiskunde en Informatica Amsterdam, The Netherlands, 1995.
- [59] *2to3 - Automated Python 2 to 3 code translation*. <https://docs.python.org/3/library/2to3.html>.
- [60] M. Steinhauser. “MATAD: A Program package for the computation of MASSive TAD-poles”. *Comput. Phys. Commun.* 134 (2001), pp. 335–364. DOI: 10.1016/S0010-4655(00)00204-6. arXiv: hep-ph/0009029.
- [61] A. I. Davydychev and J. B. Tausk. “Two loop selfenergy diagrams with different masses and the momentum expansion”. *Nucl. Phys. B* 397 (1993), pp. 123–142. DOI: 10.1016/0550-3213(93)90338-P.
- [62] J. E. Salomon. “Das Laufen und die Vereinigung der Eichkopplungen des Standardmodells zur Drei-Schleifen-Ordnung”. PhD thesis. KIT, Karlsruhe, 2012. DOI: 10.5445/IR/1000030116.
- [63] T. Inami and C. S. Lim. “Effects of Superheavy Quarks and Leptons in Low-Energy Weak Processes $K_L \rightarrow \mu\bar{\mu}$, $K^+ \rightarrow \pi + \nu\bar{\nu}$ and $K^0 \leftrightarrow \bar{K}^0$ ”. *Progress of Theoretical Physics* 65.1 (1981), pp. 297–314. DOI: 10.1143/PTP.65.297.
- [64] G. Buchalla and A. J. Buras. “QCD corrections to the sdZ vertex for arbitrary top quark mass”. *Nuclear Physics B* 398.2 (1993), pp. 285–300. DOI: [https://doi.org/10.1016/0550-3213\(93\)90110-B](https://doi.org/10.1016/0550-3213(93)90110-B).
- [65] G. Buchalla and A. J. Buras. “QCD corrections to rare K- and B-decays for arbitrary top quark mass”. *Nuclear Physics B* 400.1 (1993), pp. 225–239. DOI: [https://doi.org/10.1016/0550-3213\(93\)90405-E](https://doi.org/10.1016/0550-3213(93)90405-E).
- [66] G. Buchalla and A. J. Buras. “The rare decays $K \rightarrow \pi\nu\bar{\nu}$, $B \rightarrow X\nu\bar{\nu}$ and $B \rightarrow l^+l^-$: An Update”. *Nucl. Phys. B* 548 (1999), pp. 309–327. DOI: 10.1016/S0550-3213(99)00149-2. arXiv: hep-ph/9901288.
- [67] M. Misiak and J. Urban. “QCD corrections to FCNC decays mediated by Z penguins and W boxes”. *Phys. Lett. B* 451 (1999), pp. 161–169. DOI: 10.1016/S0370-2693(99)00150-1. arXiv: hep-ph/9901278.
- [68] T. Hermann, M. Misiak, and M. Steinhauser. “Three-loop QCD corrections to $B_s \rightarrow \mu^+\mu^-$ ”. *JHEP* 12 (2013), p. 097. DOI: 10.1007/JHEP12(2013)097. arXiv: 1311.1347 [hep-ph].
- [69] M. Beneke, C. Bobeth, and R. Szafron. “Enhanced electromagnetic correction to the rare B-meson decay $B_{s,d} \rightarrow \mu^+\mu^-$ ”. *Phys. Rev. Lett.* 120.1 (2018), p. 011801. DOI: 10.1103/PhysRevLett.120.011801. arXiv: 1708.09152 [hep-ph].
- [70] M. Beneke, C. Bobeth, and R. Szafron. “Power-enhanced leading-logarithmic QED corrections to $B_q \rightarrow \mu^+\mu^-$ ”. *JHEP* 10 (2019), p. 232. DOI: 10.1007/JHEP10(2019)232. arXiv: 1908.07011 [hep-ph].

- [71] H. E. Logan and U. Nierste. “ $B_{s,d} \rightarrow \ell^+ \ell^-$ in a two Higgs doublet model”. *Nucl. Phys. B* 586 (2000), pp. 39–55. DOI: 10.1016/S0550-3213(00)00417-X. arXiv: hep-ph/0004139.
- [72] C. Bobeth, A. J. Buras, F. Krüger, and J. Urban. “QCD corrections to $\bar{B} \rightarrow X_{d,s} \nu \bar{\nu}$, $\bar{B}_{d,s} \rightarrow \ell^+ \ell^-$, $K \rightarrow \pi \nu \bar{\nu}$ and $K_L \rightarrow \mu^+ \mu^-$ in the MSSM”. *Nucl. Phys. B* 630 (2002), pp. 87–131. DOI: 10.1016/S0550-3213(02)00141-4. arXiv: hep-ph/0112305.
- [73] C. Bobeth, T. Ewerth, F. Krüger, and J. Urban. “Analysis of neutral Higgs boson contributions to the decays $\bar{B}(s) \rightarrow \ell^+ \ell^-$ and $\bar{B} \rightarrow K \ell^+ \ell^-$ ”. *Phys. Rev. D* 64 (2001), p. 074014. DOI: 10.1103/PhysRevD.64.074014. arXiv: hep-ph/0104284.
- [74] Heavy Flavor Averaging Group (HFLAV), Y. S. Amhis et al. “Averages of b-hadron, c-hadron, and τ -lepton properties as of 2021”. *Phys. Rev. D* 107.5 (2023), p. 052008. DOI: 10.1103/PhysRevD.107.052008. arXiv: 2206.07501 [hep-ex].
- [75] L. Wolfenstein. “Parametrization of the Kobayashi-Maskawa Matrix”. *Phys. Rev. Lett.* 51 (1983), p. 1945. DOI: 10.1103/PhysRevLett.51.1945.
- [76] UTfit Collaboration, M. Bona et al. “New UTfit Analysis of the Unitarity Triangle in the Cabibbo-Kobayashi-Maskawa scheme”. *Rend. Lincei Sci. Fis. Nat.* 34 (2023), pp. 37–57. DOI: 10.1007/s12210-023-01137-5. arXiv: 2212.03894 [hep-ph].
- [77] A. Crivellin, D. Müller, and C. Wiegand. “ $b \rightarrow s \ell^+ \ell^-$ transitions in two-Higgs-doublet models”. *JHEP* 06 (2019), p. 119. DOI: 10.1007/JHEP06(2019)119. arXiv: 1903.10440 [hep-ph].
- [78] R. S. Chivukula and H. Georgi. “Composite Technicolor Standard Model”. *Phys. Lett. B* 188 (1987), pp. 99–104. DOI: 10.1016/0370-2693(87)90713-1.
- [79] G. D’Ambrosio, G. F. Giudice, G. Isidori, and A. Strumia. “Minimal flavor violation: An Effective field theory approach”. *Nucl. Phys. B* 645 (2002), pp. 155–187. DOI: 10.1016/S0550-3213(02)00836-2. arXiv: hep-ph/0207036.
- [80] M. S. Lang and U. Nierste. “ $B_s \rightarrow \mu^+ \mu^-$ in a Two-Higgs-Doublet Model with flavour-changing up-type Yukawa couplings” (2022). arXiv: 2212.11086 [hep-ph].
- [81] A. J. Buras, P. H. Chankowski, J. Rosiek, and Ł. Ślawniowska. “ $\Delta M_{d,s}, B^0 d, s \rightarrow \mu^+ \mu^-$ and $B \rightarrow X_s \gamma$ in supersymmetry at large $\tan \beta$ ”. *Nucl. Phys. B* 659 (2003), p. 3. DOI: 10.1016/S0550-3213(03)00190-1. arXiv: hep-ph/0210145.
- [82] A. Crivellin and J. Girschbach. “Constraining the MSSM sfermion mass matrices with light fermion masses”. *Phys. Rev. D* 81 (2010), p. 076001. DOI: 10.1103/PhysRevD.81.076001. arXiv: 1002.0227 [hep-ph].
- [83] CMS Collaboration, A. M. Sirunyan et al. “A measurement of the Higgs boson mass in the diphoton decay channel”. *Phys. Lett. B* 805 (2020), p. 135425. DOI: 10.1016/j.physletb.2020.135425. arXiv: 2002.06398 [hep-ex].
- [84] ATLAS Collaboration, G. Aad et al. “Measurement of the Higgs boson mass with $H \rightarrow \gamma \gamma$ decays in 140 fb $^{-1}$ of s=13 TeV pp collisions with the ATLAS detector”. *Phys. Lett. B* 847 (2023), p. 138315. DOI: 10.1016/j.physletb.2023.138315. arXiv: 2308.07216 [hep-ex].

- [85] ATLAS Collaboration, G. Aad et al. “Test of CP-invariance of the Higgs boson in vector-boson fusion production and its decay into four leptons” (2023). arXiv: 2304.09612 [hep-ex].
- [86] CMS Collaboration, A. Tumasyan et al. “Search for CP violation in ttH and tH production in multilepton channels in proton-proton collisions at $\sqrt{s} = 13$ TeV”. *JHEP* 07 (2023), p. 092. DOI: 10.1007/JHEP07(2023)092. arXiv: 2208.02686 [hep-ex].
- [87] ATLAS Collaboration, G. Aad et al. “Probing the CP nature of the top-Higgs Yukawa coupling in $t\bar{t}H$ and tH events with $H \rightarrow b\bar{b}$ decays using the ATLAS detector at the LHC” (2023). arXiv: 2303.05974 [hep-ex].
- [88] CMS Collaboration, A. Tumasyan et al. “Analysis of the CP structure of the Yukawa coupling between the Higgs boson and τ leptons in proton-proton collisions at $\sqrt{s} = 13$ TeV”. *JHEP* 06 (2022), p. 012. DOI: 10.1007/JHEP06(2022)012. arXiv: 2110.04836 [hep-ex].
- [89] ATLAS Collaboration, G. Aad et al. “Measurement of the CP properties of Higgs boson interactions with τ -leptons with the ATLAS detector”. *Eur. Phys. J. C* 83.7 (2023), p. 563. DOI: 10.1140/epjc/s10052-023-11583-y. arXiv: 2212.05833 [hep-ex].
- [90] ATLAS Collaboration, G. Aad et al. “Search for the Higgs boson decays $H \rightarrow ee$ and $H \rightarrow e\mu$ in pp collisions at $\sqrt{s} = 13$ TeV with the ATLAS detector”. *Phys. Lett. B* 801 (2020), p. 135148. DOI: 10.1016/j.physletb.2019.135148. arXiv: 1909.10235 [hep-ex].
- [91] CMS Collaboration, A. M. Sirunyan et al. “Search for lepton-flavor violating decays of the Higgs boson in the $\mu\tau$ and $e\tau$ final states in proton-proton collisions at $\sqrt{s} = 13$ TeV”. *Phys. Rev. D* 104.3 (2021), p. 032013. DOI: 10.1103/PhysRevD.104.032013. arXiv: 2105.03007 [hep-ex].
- [92] CMS Collaboration, A. Hayrapetyan et al. “Search for the lepton-flavor violating decay of the Higgs boson and additional Higgs bosons in the $e\mu$ final state in proton-proton collisions at $\sqrt{s} = 13$ TeV”. *Phys. Rev. D* 108.7 (2023), p. 072004. DOI: 10.1103/PhysRevD.108.072004. arXiv: 2305.18106 [hep-ex].
- [93] ATLAS Collaboration, G. Aad et al. “Searches for lepton-flavour-violating decays of the Higgs boson into $e\tau$ and $\mu\tau$ in $\sqrt{s} = 13$ TeV pp collisions with the ATLAS detector”. *JHEP* 07 (2023), p. 166. DOI: 10.1007/JHEP07(2023)166. arXiv: 2302.05225 [hep-ex].
- [94] ATLAS Collaboration, G. Aad et al. “A detailed map of Higgs boson interactions by the ATLAS experiment ten years after the discovery”. *Nature* 607.7917 (2022). [Erratum: *Nature* 612, E24 (2022)], pp. 52–59. DOI: 10.1038/s41586-022-04893-w. arXiv: 2207.00092 [hep-ex].
- [95] CMS Collaboration, A. Tumasyan et al. “A portrait of the Higgs boson by the CMS experiment ten years after the discovery”. *Nature* 607.7917 (2022), pp. 60–68. DOI: 10.1038/s41586-022-04892-x. arXiv: 2207.00043 [hep-ex].
- [96] CMS Collaboration, A. M. Sirunyan et al. “Evidence for Higgs boson decay to a pair of muons”. *JHEP* 01 (2021), p. 148. DOI: 10.1007/JHEP01(2021)148. arXiv: 2009.04363 [hep-ex].

- [97] LHC Higgs Cross Section Working Group, J. R. Andersen et al. “Handbook of LHC Higgs Cross Sections: 3. Higgs Properties” (2013). DOI: 10.5170/CERN-2013-004. arXiv: 1307.1347 [hep-ph].
- [98] ATLAS Collaboration, G. Aad et al. “Search for boosted diphoton resonances in the 10 to 70 GeV mass range using 138 fb^{-1} of 13 TeV pp collisions with the ATLAS detector”. *JHEP* 07 (2023), p. 155. DOI: 10.1007/JHEP07(2023)155. arXiv: 2211.04172 [hep-ex].
- [99] CMS Collaboration, A. Tumasyan et al. “Search for low-mass dilepton resonances in Higgs boson decays to four-lepton final states in proton–proton collisions at $\sqrt{s} = 13 \text{ TeV}$ ”. *Eur. Phys. J. C* 82.4 (2022), p. 290. DOI: 10.1140/epjc/s10052-022-10127-0. arXiv: 2111.01299 [hep-ex].
- [100] ATLAS Collaboration, G. Aad et al. “Search for resonances decaying into photon pairs in 139 fb^{-1} of pp collisions at $\sqrt{s}=13 \text{ TeV}$ with the ATLAS detector”. *Phys. Lett. B* 822 (2021), p. 136651. DOI: 10.1016/j.physletb.2021.136651. arXiv: 2102.13405 [hep-ex].
- [101] ATLAS Collaboration, G. Aad et al. “Search for Higgs boson pair production in the two bottom quarks plus two photons final state in pp collisions at $\sqrt{s} = 13 \text{ TeV}$ with the ATLAS detector”. *Phys. Rev. D* 106.5 (2022), p. 052001. DOI: 10.1103/PhysRevD.106.052001. arXiv: 2112.11876 [hep-ex].
- [102] CMS Collaboration, A. M. Sirunyan et al. “Search for resonant pair production of Higgs bosons decaying to bottom quark-antiquark pairs in proton-proton collisions at 13 TeV”. *JHEP* 08 (2018), p. 152. DOI: 10.1007/JHEP08(2018)152. arXiv: 1806.03548 [hep-ex].
- [103] CMS Collaboration, A. M. Sirunyan et al. “Search for a new scalar resonance decaying to a pair of Z bosons in proton-proton collisions at $\sqrt{s} = 13 \text{ TeV}$ ”. *JHEP* 06 (2018). [Erratum: *JHEP* 03, 128 (2019)], p. 127. DOI: 10.1007/JHEP06(2018)127. arXiv: 1804.01939 [hep-ex].
- [104] CMS Collaboration, A. M. Sirunyan et al. “Search for a heavy Higgs boson decaying to a pair of W bosons in proton-proton collisions at $\sqrt{s} = 13 \text{ TeV}$ ”. *JHEP* 03 (2020), p. 034. DOI: 10.1007/JHEP03(2020)034. arXiv: 1912.01594 [hep-ex].
- [105] ATLAS Collaboration, *Search for heavy resonances in the decay channel $W^+W^- \rightarrow e\nu\mu\nu$ in pp Collisions at $\sqrt{s} = 13\text{TeV}$ using 139fb^{-1} of data with the ATLAS detector*. Tech. rep. Geneva: CERN, 2022. URL: <https://cds.cern.ch/record/2842518>.
- [106] ATLAS Collaboration, G. Aad et al. “Search for heavy resonances decaying into a pair of Z bosons in the $\ell^+\ell^-\ell'^+\ell'^-$ and $\ell^+\ell^-\nu\bar{\nu}$ final states using 139 fb^{-1} of proton–proton collisions at $\sqrt{s} = 13 \text{ TeV}$ with the ATLAS detector”. *Eur. Phys. J. C* 81.4 (2021), p. 332. DOI: 10.1140/epjc/s10052-021-09013-y. arXiv: 2009.14791 [hep-ex].
- [107] ATLAS Collaboration, M. Aaboud et al. “Search for heavy resonances decaying into WW in the $e\nu\mu\nu$ final state in pp collisions at $\sqrt{s} = 13 \text{ TeV}$ with the ATLAS detector”. *Eur. Phys. J. C* 78.1 (2018), p. 24. DOI: 10.1140/epjc/s10052-017-5491-4. arXiv: 1710.01123 [hep-ex].

- [108] CMS Collaboration, A. M. Sirunyan et al. “Search for a heavy pseudoscalar Higgs boson decaying into a 125 GeV Higgs boson and a Z boson in final states with two tau and two light leptons at $\sqrt{s} = 13$ TeV”. *JHEP* 03 (2020), p. 065. DOI: 10.1007/JHEP03(2020)065. arXiv: 1910.11634 [hep-ex].
- [109] CMS Collaboration, A. Tumasyan et al. “Search for a charged Higgs boson decaying into a heavy neutral Higgs boson and a W boson in proton-proton collisions at $\sqrt{s} = 13$ TeV”. *JHEP* 09 (2023), p. 032. DOI: 10.1007/JHEP09(2023)032. arXiv: 2207.01046 [hep-ex].
- [110] ATLAS Collaboration, G. Aad et al. “Search for heavy resonances decaying into a Z or W boson and a Higgs boson in final states with leptons and b-jets in 139 fb^{-1} of pp collisions at $\sqrt{s} = 13$ TeV with the ATLAS detector”. *JHEP* 06 (2023), p. 016. DOI: 10.1007/JHEP06(2023)016. arXiv: 2207.00230 [hep-ex].
- [111] CMS Collaboration, A. M. Sirunyan et al. “Search for charged Higgs bosons in the $H^\pm \rightarrow \tau^\pm \nu_\tau$ decay channel in proton-proton collisions at $\sqrt{s} = 13$ TeV”. *JHEP* 07 (2019), p. 142. DOI: 10.1007/JHEP07(2019)142. arXiv: 1903.04560 [hep-ex].
- [112] CMS Collaboration, A. M. Sirunyan et al. “Search for charged Higgs bosons decaying into a top and a bottom quark in the all-jet final state of pp collisions at $\sqrt{s} = 13$ TeV”. *JHEP* 07 (2020), p. 126. DOI: 10.1007/JHEP07(2020)126. arXiv: 2001.07763 [hep-ex].
- [113] ATLAS Collaboration, G. Aad et al. “Search for charged Higgs bosons decaying into a top quark and a bottom quark at $\sqrt{s} = 13$ TeV with the ATLAS detector”. *JHEP* 06 (2021), p. 145. DOI: 10.1007/JHEP06(2021)145. arXiv: 2102.10076 [hep-ex].
- [114] ATLAS Collaboration, M. Aaboud et al. “Search for charged Higgs bosons decaying via $H^\pm \rightarrow \tau^\pm \nu_\tau$ in the τ +jets and τ +lepton final states with 36 fb^{-1} of pp collision data recorded at $\sqrt{s} = 13$ TeV with the ATLAS experiment”. *JHEP* 09 (2018), p. 139. DOI: 10.1007/JHEP09(2018)139. arXiv: 1807.07915 [hep-ex].
- [115] ATLAS Collaboration, G. Aad et al. “Search for $t\bar{t}$ resonances in fully hadronic final states in pp collisions at $\sqrt{s} = 13$ TeV with the ATLAS detector”. *JHEP* 10 (2020), p. 061. DOI: 10.1007/JHEP10(2020)061. arXiv: 2005.05138 [hep-ex].
- [116] CMS Collaboration, A. M. Sirunyan et al. “Search for heavy Higgs bosons decaying to a top quark pair in proton-proton collisions at $\sqrt{s} = 13$ TeV”. *JHEP* 04 (2020). [Erratum: *JHEP* 03, 187 (2022)], p. 171. DOI: 10.1007/JHEP04(2020)171. arXiv: 1908.01115 [hep-ex].
- [117] CMS Collaboration, A. M. Sirunyan et al. “Search for beyond the standard model Higgs bosons decaying into a $b\bar{b}$ pair in pp collisions at $\sqrt{s} = 13$ TeV”. *JHEP* 08 (2018), p. 113. DOI: 10.1007/JHEP08(2018)113. arXiv: 1805.12191 [hep-ex].
- [118] CMS Collaboration, A. M. Sirunyan et al. “Search for additional neutral MSSM Higgs bosons in the $\tau\tau$ final state in proton-proton collisions at $\sqrt{s} = 13$ TeV”. *JHEP* 09 (2018), p. 007. DOI: 10.1007/JHEP09(2018)007. arXiv: 1803.06553 [hep-ex].
- [119] ATLAS Collaboration, G. Aad et al. “Search for heavy neutral Higgs bosons produced in association with b-quarks and decaying into b-quarks at $\sqrt{s} = 13$ TeV with the ATLAS detector”. *Phys. Rev. D* 102.3 (2020), p. 032004. DOI: 10.1103/PhysRevD.102.032004. arXiv: 1907.02749 [hep-ex].

- [120] CMS Collaboration, A. Tumasyan et al. “Searches for additional Higgs bosons and for vector leptoquarks in $\tau\tau$ final states in proton-proton collisions at $\sqrt{s} = 13$ TeV”. *JHEP* 07 (2023), p. 073. DOI: 10.1007/JHEP07(2023)073. arXiv: 2208.02717 [hep-ex].
- [121] ATLAS Collaboration, G. Aad et al. “Search for heavy Higgs bosons decaying into two tau leptons with the ATLAS detector using pp collisions at $\sqrt{s} = 13$ TeV”. *Phys. Rev. Lett.* 125.5 (2020), p. 051801. DOI: 10.1103/PhysRevLett.125.051801. arXiv: 2002.12223 [hep-ex].
- [122] ATLAS Collaboration, G. Aad et al. “Combination of searches for resonant Higgs boson pair production using pp collisions at $\sqrt{s} = 13$ TeV with the ATLAS detector” (2023). arXiv: 2311.15956 [hep-ex].
- [123] ATLAS Collaboration, G. Aad et al. “Search for $t\bar{t}H/A \rightarrow t\bar{t}\bar{t}$ production in the multi-lepton final state in proton-proton collisions at $\sqrt{s} = 13$ TeV with the ATLAS detector”. *JHEP* 07 (2023), p. 203. DOI: 10.1007/JHEP07(2023)203. arXiv: 2211.01136 [hep-ex].
- [124] ATLAS Collaboration, G. Aad et al. “Summary plots for beyond Standard Model Higgs boson benchmarks for direct and indirect searches, ATLAS UB note ATL-PHYS-PUB-2022-043.” (2022). URL: <https://cds.cern.ch/record/2827098>.
- [125] L. Maiani, A. D. Polosa, and V. Riquer. “Probing Minimal Supersymmetry at the LHC with the Higgs Boson Masses”. *New J. Phys.* 14 (2012), p. 073029. DOI: 10.1088/1367-2630/14/7/073029. arXiv: 1202.5998 [hep-ph].
- [126] A. Djouadi et al. “The post-Higgs MSSM scenario: Habemus MSSM?” *Eur. Phys. J. C* 73 (2013), p. 2650. DOI: 10.1140/epjc/s10052-013-2650-0. arXiv: 1307.5205 [hep-ph].
- [127] A. Djouadi et al. “Fully covering the MSSM Higgs sector at the LHC”. *JHEP* 06 (2015), p. 168. DOI: 10.1007/JHEP06(2015)168. arXiv: 1502.05653 [hep-ph].
- [128] L. Maiani, A. D. Polosa, and V. Riquer. “Heavier Higgs Particles: Indications from Minimal Supersymmetry”. *Phys. Lett. B* 718 (2012), pp. 465–468. DOI: 10.1016/j.physletb.2012.10.041. arXiv: 1209.4816 [hep-ph].
- [129] A. Djouadi and J. Quevillon. “The MSSM Higgs sector at a high M_{SUSY} : reopening the low $\tan\beta$ regime and heavy Higgs searches”. *JHEP* 10 (2013), p. 028. DOI: 10.1007/JHEP10(2013)028. arXiv: 1304.1787 [hep-ph].
- [130] V. Cacchio, D. Chowdhury, O. Eberhardt, and C. W. Murphy. “Next-to-leading order unitarity fits in Two-Higgs-Doublet models with soft \mathbb{Z}_2 breaking”. *JHEP* 11 (2016), p. 026. DOI: 10.1007/JHEP11(2016)026. arXiv: 1609.01290 [hep-ph].
- [131] D. Chowdhury and O. Eberhardt. “Global fits of the two-loop renormalized Two-Higgs-Doublet model with soft Z_2 breaking”. *JHEP* 11 (2015), p. 052. DOI: 10.1007/JHEP11(2015)052. arXiv: 1503.08216 [hep-ph].
- [132] R. Casalbuoni, D. Dominici, R. Gatto, and C. Giunti. “Strong Interacting Two Doublet and Doublet Singlet Higgs Models”. *Phys. Lett. B* 178 (1986), p. 235. DOI: 10.1016/0370-2693(86)91502-9.

- [133] J. Maalampi, J. Sirkka, and I. Vilja. “Tree level unitarity and triviality bounds for two Higgs models”. *Phys. Lett. B* 265 (1991), pp. 371–376. DOI: 10.1016/0370-2693(91)90068-2.
- [134] S. Kanemura, T. Kubota, and E. Takasugi. “Lee-Quigg-Thacker bounds for Higgs boson masses in a two doublet model”. *Phys. Lett. B* 313 (1993), pp. 155–160. DOI: 10.1016/0370-2693(93)91205-2. arXiv: hep-ph/9303263.
- [135] A. G. Akeroyd, A. Arhrib, and E.-M. Naimi. “Note on tree level unitarity in the general two Higgs doublet model”. *Phys. Lett. B* 490 (2000), pp. 119–124. DOI: 10.1016/S0370-2693(00)00962-X. arXiv: hep-ph/0006035.
- [136] I. F. Ginzburg and I. P. Ivanov. “Tree-level unitarity constraints in the most general 2HDM”. *Phys. Rev. D* 72 (2005), p. 115010. DOI: 10.1103/PhysRevD.72.115010. arXiv: hep-ph/0508020.
- [137] J. Horejsi and M. Kladiva. “Tree-unitarity bounds for THDM Higgs masses revisited”. *Eur. Phys. J. C* 46 (2006), pp. 81–91. DOI: 10.1140/epjc/s2006-02472-3. arXiv: hep-ph/0510154.
- [138] H. E. Haber and D. O’Neil. “Basis-independent methods for the two-Higgs-doublet model III: The CP-conserving limit, custodial symmetry, and the oblique parameters S, T, U”. *Phys. Rev. D* 83 (2011), p. 055017. DOI: 10.1103/PhysRevD.83.055017. arXiv: 1011.6188 [hep-ph].
- [139] B. Grinstein, C. W. Murphy, and P. Uttayarat. “One-loop corrections to the perturbative unitarity bounds in the CP-conserving two-Higgs doublet model with a softly broken \mathbb{Z}_2 symmetry”. *JHEP* 06 (2016), p. 070. DOI: 10.1007/JHEP06(2016)070. arXiv: 1512.04567 [hep-ph].
- [140] L. Durand, J. M. Johnson, and J. L. Lopez. “Perturbative unitarity and high-energy $W(L)_{+-}, Z(L), H$ scattering. One loop corrections and the Higgs boson coupling”. *Phys. Rev. D* 45 (1992), pp. 3112–3127. DOI: 10.1103/PhysRevD.45.3112.
- [141] P. N. Maher, L. Durand, and K. Riesselmann. “Two loop renormalization constants and high-energy $2 \rightarrow 2$ scattering amplitudes in the Higgs sector of the Standard Model”. *Phys. Rev. D* 48 (1993). [Erratum: *Phys.Rev.D* 52, 553 (1995)], p. 1061. DOI: 10.1103/PhysRevD.48.1061. arXiv: hep-ph/9303233.
- [142] L. Durand, P. N. Maher, and K. Riesselmann. “Two loop unitarity constraints on the Higgs boson coupling”. *Phys. Rev. D* 48 (1993), pp. 1084–1096. DOI: 10.1103/PhysRevD.48.1084. arXiv: hep-ph/9303234.
- [143] U. Nierste and K. Riesselmann. “Higgs sector renormalization group in the $\overline{\text{MS}}$ and OMS scheme: The Breakdown of perturbation theory for a heavy Higgs”. *Phys. Rev. D* 53 (1996), pp. 6638–6652. DOI: 10.1103/PhysRevD.53.6638. arXiv: hep-ph/9511407.
- [144] H. Flacher et al. “Revisiting the Global Electroweak Fit of the Standard Model and Beyond with Gfitter”. *Eur. Phys. J. C* 60 (2009). [Erratum: *Eur.Phys.J.C* 71, 1718 (2011)], pp. 543–583. DOI: 10.1140/epjc/s10052-009-0966-6. arXiv: 0811.0009 [hep-ph].

- [145] M. Misiak et al. “Updated NNLO QCD predictions for the weak radiative B-meson decays”. *Phys. Rev. Lett.* 114.22 (2015), p. 221801. DOI: 10.1103/PhysRevLett.114.221801. arXiv: 1503.01789 [hep-ph].
- [146] M. Misiak and M. Steinhauser. “Weak radiative decays of the B meson and bounds on M_{H^\pm} in the Two-Higgs-Doublet Model”. *Eur. Phys. J. C* 77.3 (2017), p. 201. DOI: 10.1140/epjc/s10052-017-4776-y. arXiv: 1702.04571 [hep-ph].
- [147] C. Bobeth, M. Misiak, and J. Urban. “Photonic penguins at two loops and m_t dependence of $BR[B \rightarrow X_s l^+ l^-]$ ”. *Nucl. Phys. B* 574 (2000), pp. 291–330. DOI: 10.1016/S0550-3213(00)00007-9. arXiv: hep-ph/9910220.
- [148] A. J. Buras and M. Misiak. “anti-B \rightarrow X(s gamma) after completion of the NLO QCD calculations”. *Acta Phys. Polon. B* 33 (2002), pp. 2597–2612. arXiv: hep-ph/0207131.
- [149] M. Misiak and M. Steinhauser. “Three loop matching of the dipole operators for $b \rightarrow sy$ and $b \rightarrow sg$ ”. *Nucl. Phys. B* 683 (2004), pp. 277–305. DOI: 10.1016/j.nuclphysb.2004.02.006. arXiv: hep-ph/0401041.
- [150] M. Misiak et al. “Estimate of $\mathcal{B}(\bar{B} \rightarrow X_s \gamma)$ at $O(\alpha_s^2)$ ”. *Phys. Rev. Lett.* 98 (2007), p. 022002. DOI: 10.1103/PhysRevLett.98.022002. arXiv: hep-ph/0609232.
- [151] M. Misiak and M. Steinhauser. “NNLO QCD corrections to the anti-B \rightarrow X(s) gamma matrix elements using interpolation in $m(c)$ ”. *Nucl. Phys. B* 764 (2007), pp. 62–82. DOI: 10.1016/j.nuclphysb.2006.11.027. arXiv: hep-ph/0609241.
- [152] M. Czakon, U. Haisch, and M. Misiak. “Four-Loop Anomalous Dimensions for Radiative Flavour-Changing Decays”. *JHEP* 03 (2007), p. 008. DOI: 10.1088/1126-6708/2007/03/008. arXiv: hep-ph/0612329.
- [153] M. Ciuchini, G. Degrassi, P. Gambino, and G. F. Giudice. “Next-to-leading QCD corrections to $B \rightarrow X_s \gamma$: Standard model and two Higgs doublet model”. *Nucl. Phys. B* 527 (1998), pp. 21–43. DOI: 10.1016/S0550-3213(98)00244-2. arXiv: hep-ph/9710335.
- [154] P. Ciafaloni, A. Romanino, and A. Strumia. “Two loop QCD corrections to charged Higgs mediated $b \rightarrow s$ gamma decay”. *Nucl. Phys. B* 524 (1998), pp. 361–376. DOI: 10.1016/S0550-3213(98)00190-4. arXiv: hep-ph/9710312.
- [155] F. Borzumati and C. Greub. “2HDMs predictions for anti-B \rightarrow X(s) gamma in NLO QCD”. *Phys. Rev. D* 58 (1998), p. 074004. DOI: 10.1103/PhysRevD.58.074004. arXiv: hep-ph/9802391.
- [156] F. Borzumati and C. Greub. “Two Higgs doublet model predictions for anti-B \rightarrow X(s) gamma in NLO QCD: Addendum”. *Phys. Rev. D* 59 (1999), p. 057501. DOI: 10.1103/PhysRevD.59.057501. arXiv: hep-ph/9809438.
- [157] C. Bobeth, M. Misiak, and J. Urban. “Matching conditions for $b \rightarrow sy$ and $b \rightarrow sgluon$ in extensions of the standard model”. *Nucl. Phys. B* 567 (2000), pp. 153–185. DOI: 10.1016/S0550-3213(99)00688-4. arXiv: hep-ph/9904413.
- [158] C. Bobeth, A. J. Buras, and T. Ewerth. “Anti-B \rightarrow X(s) $l^+ l^-$ in the MSSM at NNLO”. *Nucl. Phys. B* 713 (2005), pp. 522–554. DOI: 10.1016/j.nuclphysb.2005.02.011. arXiv: hep-ph/0409293.

- [159] T. Hermann, M. Misiak, and M. Steinhauser. “ $\bar{B} \rightarrow X_s \gamma$ in the Two Higgs Doublet Model up to Next-to-Next-to-Leading Order in QCD”. *JHEP* 11 (2012), p. 036. DOI: 10.1007/JHEP11(2012)036. arXiv: 1208.2788 [hep-ph].
- [160] M. Misiak, A. Rehman, and M. Steinhauser. “Towards $\bar{B} \rightarrow X_s \gamma$ at the NNLO in QCD without interpolation in m_c ”. *JHEP* 06 (2020), p. 175. DOI: 10.1007/JHEP06(2020)175. arXiv: 2002.01548 [hep-ph].
- [161] A. J. Buras and P. H. Weisz. “QCD Nonleading Corrections to Weak Decays in Dimensional Regularization and 't Hooft-Veltman Schemes”. *Nucl. Phys. B* 333 (1990), pp. 66–99. DOI: 10.1016/0550-3213(90)90223-Z.
- [162] A. J. Buras, M. Jamin, and P. H. Weisz. “Leading and Next-to-leading QCD Corrections to ϵ Parameter and $B^0 - \bar{B}^0$ Mixing in the Presence of a Heavy Top Quark”. *Nucl. Phys. B* 347 (1990), pp. 491–536. DOI: 10.1016/0550-3213(90)90373-L.
- [163] A. J. Buras, M. Jamin, M. E. Lautenbacher, and P. H. Weisz. “Effective Hamiltonians for $\Delta S = 1$ and $\Delta B = 1$ nonleptonic decays beyond the leading logarithmic approximation”. *Nucl. Phys. B* 370 (1992). [Addendum: *Nucl.Phys.B* 375, 501 (1992)], pp. 69–104. DOI: 10.1016/0550-3213(92)90345-C.
- [164] M. Gorbahn and U. Haisch. “Effective Hamiltonian for non-leptonic $|\Delta F| = 1$ decays at NNLO in QCD”. *Nucl. Phys. B* 713 (2005), pp. 291–332. DOI: 10.1016/j.nuclphysb.2005.01.047. arXiv: hep-ph/0411071.
- [165] V. A. Khoze and M. A. Shifman. “HEAVY QUARKS”. *Sov. Phys. Usp.* 26 (1983), p. 387. DOI: 10.1070/PU1983v026n05ABEH004398.
- [166] M. A. Shifman and M. B. Voloshin. “Preasymptotic Effects in Inclusive Weak Decays of Charmed Particles”. *Sov. J. Nucl. Phys.* 41 (1985), p. 120.
- [167] V. A. Khoze, M. A. Shifman, N. G. Uraltsev, and M. B. Voloshin. “On Inclusive Hadronic Widths of Beautiful Particles”. *Sov. J. Nucl. Phys.* 46 (1987), p. 112.
- [168] I. I. Y. Bigi and N. G. Uraltsev. “Gluonic enhancements in non-spectator beauty decays: An Inclusive mirage though an exclusive possibility”. *Phys. Lett. B* 280 (1992), pp. 271–280. DOI: 10.1016/0370-2693(92)90066-D.
- [169] I. I. Y. Bigi, N. G. Uraltsev, and A. I. Vainshtein. “Nonperturbative corrections to inclusive beauty and charm decays: QCD versus phenomenological models”. *Phys. Lett. B* 293 (1992). [Erratum: *Phys.Lett.B* 297, 477–477 (1992)], pp. 430–436. DOI: 10.1016/0370-2693(92)90908-M. arXiv: hep-ph/9207214.
- [170] I. I. Y. Bigi et al. “A QCD 'manifesto' on inclusive decays of beauty and charm”. *7th Meeting of the APS Division of Particles Fields.* 1992, pp. 610–613. arXiv: hep-ph/9212227.
- [171] I. I. Y. Bigi, M. A. Shifman, N. G. Uraltsev, and A. I. Vainshtein. “QCD predictions for lepton spectra in inclusive heavy flavor decays”. *Phys. Rev. Lett.* 71 (1993), pp. 496–499. DOI: 10.1103/PhysRevLett.71.496. arXiv: hep-ph/9304225.
- [172] I. I. Y. Bigi and N. G. Uraltsev. “Weak annihilation and the endpoint spectrum in semileptonic B decays”. *Nucl. Phys. B* 423 (1994), pp. 33–55. DOI: 10.1016/0550-3213(94)90564-9. arXiv: hep-ph/9310285.

- [173] M. Gerlach, U. Nierste, V. Shtabovenko, and M. Steinhauser. “Width Difference in the B - B^- System at Next-to-Next-to-Leading Order of QCD”. *Phys. Rev. Lett.* 129.10 (2022), p. 102001. DOI: 10.1103/PhysRevLett.129.102001. arXiv: 2205.07907 [hep-ph].
- [174] G. Isidori and A. Retico. “Scalar flavor changing neutral currents in the large $\tan\beta$ limit”. *JHEP* 11 (2001), p. 001. DOI: 10.1088/1126-6708/2001/11/001. arXiv: hep-ph/0110121.
- [175] A. J. Buras, P. H. Chankowski, J. Rosiek, and Ł. Ślawnianowska. “Correlation between ΔM_s and $B_{s,d}^0 \rightarrow \mu^+ \mu^-$ in Supersymmetry at large $\tan\beta$ ”. *Phys. Lett.* B546 (2002), pp. 96–107. eprint: hep-ph/0207241.
- [176] M. Gorbahn, S. Jäger, U. Nierste, and S. Trine. “The supersymmetric Higgs sector and $B - \bar{B}$ mixing for large $\tan\beta$ ”. *Phys. Rev. D* 84 (2011), p. 034030. DOI: 10.1103/PhysRevD.84.034030. arXiv: 0901.2065 [hep-ph].
- [177] S. Iguro and K. Tobe. “ $R(D^{(*)})$ in a general two Higgs doublet model”. *Nucl. Phys. B* 925 (2017), pp. 560–606. DOI: 10.1016/j.nuclphysb.2017.10.014. arXiv: 1708.06176 [hep-ph].
- [178] A. Buras. *Gauge Theory of Weak Decays*. Cambridge University Press, 2020. DOI: 10.1017/9781139524100.
- [179] A. J. Buras, D. Buttazzo, J. Girschbach-Noe, and R. Kneijens. “Can we reach the Zeptouniverse with rare K and $B_{s,d}$ decays?” *JHEP* 11 (2014), p. 121. DOI: 10.1007/JHEP11(2014)121. arXiv: 1408.0728 [hep-ph].
- [180] Flavour Lattice Averaging Group (FLAG), Y. Aoki et al. “FLAG Review 2021”. *Eur. Phys. J. C* 82.10 (2022), p. 869. DOI: 10.1140/epjc/s10052-022-10536-1. arXiv: 2111.09849 [hep-lat].
- [181] R. J. Dowdall et al. “Neutral B-meson mixing from full lattice QCD at the physical point”. *Phys. Rev. D* 100.9 (2019), p. 094508. DOI: 10.1103/PhysRevD.100.094508. arXiv: 1907.01025 [hep-lat].
- [182] J. F. Gunion and H. E. Haber. “The CP conserving two Higgs doublet model: The Approach to the decoupling limit”. *Phys. Rev. D* 67 (2003), p. 075019. DOI: 10.1103/PhysRevD.67.075019. arXiv: hep-ph/0207010.
- [183] L. Di Luzio, M. Kirk, A. Lenz, and T. Rauh. “ ΔM_s theory precision confronts flavour anomalies”. *JHEP* 12 (2019), p. 009. DOI: 10.1007/JHEP12(2019)009. arXiv: 1909.11087 [hep-ph].
- [184] A. Crivellin, A. Kokulu, and C. Greub. “Flavor-phenomenology of two-Higgs-doublet models with generic Yukawa structure”. *Phys. Rev. D* 87.9 (2013), p. 094031. DOI: 10.1103/PhysRevD.87.094031. arXiv: 1303.5877 [hep-ph].
- [185] LHCb Collaboration, R. Aaij et al. “Improved measurement of CP violation parameters in $B_s^0 \rightarrow J/\psi K^+ K^-$ decays in the vicinity of the $\phi(1020)$ resonance” (2023). arXiv: 2308.01468 [hep-ex].

- [186] CKMfitter Group, J. Charles et al. “CP violation and the CKM matrix: Assessing the impact of the asymmetric B factories”. *Eur. Phys. J. C* 41.1 (2005), pp. 1–131. DOI: 10.1140/epjc/s2005-02169-1. arXiv: hep-ph/0406184.
- [187] CKMfitter Group, J. Charles et al. “Current status of the Standard Model CKM fit and constraints on $\Delta F = 2$ New Physics”. *Phys. Rev. D* 91.7 (2015), p. 073007. DOI: 10.1103/PhysRevD.91.073007. arXiv: 1501.05013 [hep-ph].
- [188] LHCb Collaboration, R. Aaij et al. “Precise determination of the $B_s^0-\bar{B}_s^0$ oscillation frequency”. *Nature Phys.* 18.1 (2022), pp. 1–5. DOI: 10.1038/s41567-021-01394-x. arXiv: 2104.04421 [hep-ex].
- [189] LHCb Collaboration, R. Aaij et al. “Measurement of the CKM angle γ and $B_s^0-\bar{B}_s^0$ mixing frequency with $B_s^0 \rightarrow D_s^\mp h^\pm \pi^\pm \pi^\mp$ decays”. *JHEP* 03 (2021), p. 137. DOI: 10.1007/JHEP03(2021)137. arXiv: 2011.12041 [hep-ex].
- [190] CMS Collaboration, A. M. Sirunyan et al. “Measurement of the CP -violating phase ϕ_s in the $B_s^0 \rightarrow J/\psi \phi(1020) \rightarrow \mu^+ \mu^- K^+ K^-$ channel in proton-proton collisions at $\sqrt{s} = 13$ TeV”. *Phys. Lett. B* 816 (2021), p. 136188. DOI: 10.1016/j.physletb.2021.136188. arXiv: 2007.02434 [hep-ex].
- [191] LHCb Collaboration, R. Aaij et al. “Updated measurement of time-dependent CP -violating observables in $B_s^0 \rightarrow J/\psi K^+ K^-$ decays”. *Eur. Phys. J. C* 79.8 (2019). [Erratum: *Eur.Phys.J.C* 80, 601 (2020)], p. 706. DOI: 10.1140/epjc/s10052-019-7159-8. arXiv: 1906.08356 [hep-ex].
- [192] LHCb Collaboration, R. Aaij et al. “Precision measurement of the $B_s^0-\bar{B}_s^0$ oscillation frequency with the decay $B_s^0 \rightarrow D_s^- \pi^+$ ”. *New J. Phys.* 15 (2013), p. 053021. DOI: 10.1088/1367-2630/15/5/053021. arXiv: 1304.4741 [hep-ex].
- [193] LHCb Collaboration, R. Aaij et al. “Observation of $B_s^0-\bar{B}_s^0$ mixing and measurement of mixing frequencies using semileptonic B decays”. *Eur. Phys. J. C* 73.12 (2013), p. 2655. DOI: 10.1140/epjc/s10052-013-2655-8. arXiv: 1308.1302 [hep-ex].
- [194] CDF Collaboration, A. Abulencia et al. “Observation of $B_s^0 - \bar{B}_s^0$ Oscillations”. *Phys. Rev. Lett.* 97 (2006), p. 242003. DOI: 10.1103/PhysRevLett.97.242003. arXiv: hep-ex/0609040.
- [195] G. Kumar. “Interplay of the charged Higgs boson effects in $R_{D^{(*)}}$, $b \rightarrow s \ell^+ \ell^-$, and W mass”. *Phys. Rev. D* 107.7 (2023), p. 075016. DOI: 10.1103/PhysRevD.107.075016. arXiv: 2212.07233 [hep-ph].
- [196] BaBar Collaboration, J. P. Lees et al. “Evidence for an excess of $\bar{B} \rightarrow D^{(*)} \tau^- \bar{\nu}_\tau$ decays”. *Phys. Rev. Lett.* 109 (2012), p. 101802. DOI: 10.1103/PhysRevLett.109.101802. arXiv: 1205.5442 [hep-ex].
- [197] BaBar Collaboration, J. P. Lees et al. “Measurement of an Excess of $\bar{B} \rightarrow D^{(*)} \tau^- \bar{\nu}_\tau$ Decays and Implications for Charged Higgs Bosons”. *Phys. Rev. D* 88.7 (2013), p. 072012. DOI: 10.1103/PhysRevD.88.072012. arXiv: 1303.0571 [hep-ex].
- [198] Belle Collaboration, M. Huschle et al. “Measurement of the branching ratio of $\bar{B} \rightarrow D^{(*)} \tau^- \bar{\nu}_\tau$ relative to $\bar{B} \rightarrow D^{(*)} \ell^- \bar{\nu}_\ell$ decays with hadronic tagging at Belle”. *Phys. Rev. D* 92.7 (2015), p. 072014. DOI: 10.1103/PhysRevD.92.072014. arXiv: 1507.03233 [hep-ex].

- [199] Belle Collaboration, S. Hirose et al. “Measurement of the τ lepton polarization and $R(D^*)$ in the decay $\bar{B} \rightarrow D^* \tau^- \bar{\nu}_\tau$ ”. *Phys. Rev. Lett.* 118.21 (2017), p. 211801. DOI: 10.1103/PhysRevLett.118.211801. arXiv: 1612.00529 [hep-ex].
- [200] Belle Collaboration, S. Hirose et al. “Measurement of the τ lepton polarization and $R(D^*)$ in the decay $\bar{B} \rightarrow D^* \tau^- \bar{\nu}_\tau$ with one-prong hadronic τ decays at Belle”. *Phys. Rev. D* 97.1 (2018), p. 012004. DOI: 10.1103/PhysRevD.97.012004. arXiv: 1709.00129 [hep-ex].
- [201] Belle Collaboration, G. Caria et al. “Measurement of $\mathcal{R}(D)$ and $\mathcal{R}(D^*)$ with a semileptonic tagging method”. *Phys. Rev. Lett.* 124.16 (2020), p. 161803. DOI: 10.1103/PhysRevLett.124.161803. arXiv: 1910.05864 [hep-ex].
- [202] LHCb Collaboration, R. Aaij et al. “Measurement of the ratios of branching fractions $\mathcal{R}(D^*)$ and $\mathcal{R}(D^0)$ ”. *Phys. Rev. Lett.* 131 (2023), p. 111802. DOI: 10.1103/PhysRevLett.131.111802. arXiv: 2302.02886 [hep-ex].
- [203] LHCb Collaboration, R. Aaij et al. “Test of lepton flavor universality using $B_0 \rightarrow D^* \tau \nu \tau$ decays with hadronic τ channels”. *Phys. Rev. D* 108.1 (2023), p. 012018. DOI: 10.1103/PhysRevD.108.012018. arXiv: 2305.01463 [hep-ex].
- [204] D. Bigi and P. Gambino. “Revisiting $B \rightarrow D \ell \nu$ ”. *Phys. Rev. D* 94.9 (2016), p. 094008. DOI: 10.1103/PhysRevD.94.094008. arXiv: 1606.08030 [hep-ph].
- [205] P. Gambino, M. Jung, and S. Schacht. “The V_{cb} puzzle: An update”. *Phys. Lett. B* 795 (2019), pp. 386–390. DOI: 10.1016/j.physletb.2019.06.039. arXiv: 1905.08209 [hep-ph].
- [206] M. Bordone, M. Jung, and D. van Dyk. “Theory determination of $\bar{B} \rightarrow D^{(*)} \ell^- \bar{\nu}$ form factors at $\mathcal{O}(1/m_c^2)$ ”. *Eur. Phys. J. C* 80.2 (2020), p. 74. DOI: 10.1140/epjc/s10052-020-7616-4. arXiv: 1908.09398 [hep-ph].
- [207] F. U. Bernlochner, Z. Ligeti, M. Papucci, and D. J. Robinson. “Combined analysis of semileptonic B decays to D and D^* : $R(D^{(*)})$, $|V_{cb}|$, and new physics”. *Phys. Rev. D* 95.11 (2017). [Erratum: *Phys.Rev.D* 97, 059902 (2018)], p. 115008. DOI: 10.1103/PhysRevD.95.115008. arXiv: 1703.05330 [hep-ph].
- [208] S. Jaiswal, S. Nandi, and S. K. Patra. “Extraction of $|V_{cb}|$ from $B \rightarrow D^{(*)} \ell \nu_\ell$ and the Standard Model predictions of $R(D^{(*)})$ ”. *JHEP* 12 (2017), p. 060. DOI: 10.1007/JHEP12(2017)060. arXiv: 1707.09977 [hep-ph].
- [209] BaBar Collaboration, J. P. Lees et al. “Extraction of form Factors from a Four-Dimensional Angular Analysis of $\bar{B} \rightarrow D^* \ell^- \bar{\nu}_\ell$ ”. *Phys. Rev. Lett.* 123.9 (2019), p. 091801. DOI: 10.1103/PhysRevLett.123.091801. arXiv: 1903.10002 [hep-ex].
- [210] G. Martinelli, S. Simula, and L. Vittorio. “ $|V_{cb}|$ and $R(D^{(*)})$ using lattice QCD and unitarity”. *Phys. Rev. D* 105.3 (2022), p. 034503. DOI: 10.1103/PhysRevD.105.034503. arXiv: 2105.08674 [hep-ph].
- [211] A. Crivellin, C. Greub, and A. Kokulu. “Explaining $B \rightarrow D \tau \nu$, $B \rightarrow D^* \tau \nu$ and $B \rightarrow \tau \nu$ in a 2HDM of type III”. *Phys. Rev. D* 86 (2012), p. 054014. DOI: 10.1103/PhysRevD.86.054014. arXiv: 1206.2634 [hep-ph].

-
- [212] S. Iguro, T. Kitahara, M. S. Lang, and M. Takeuchi. “Current status of the muon $g-2$ interpretations within two-Higgs-doublet models”. *Phys. Rev. D* 108.11 (2023), p. 115012. DOI: 10.1103/PhysRevD.108.115012. arXiv: 2304.09887 [hep-ph].
- [213] R. E. Cutkosky. “Singularities and discontinuities of Feynman amplitudes”. *J. Math. Phys.* 1 (1960), pp. 429–433. DOI: 10.1063/1.1703676.
- [214] J. C. Romao and J. P. Silva. “A resource for signs and Feynman diagrams of the Standard Model”. *Int. J. Mod. Phys. A* 27 (2012), p. 1230025. DOI: 10.1142/S0217751X12300256. arXiv: 1209.6213 [hep-ph].
- [215] J. Davies, F. Herren, G. Mishima, and M. Steinhauser. “NNLO real corrections to $gg \rightarrow HH$ in the large- m_t limit”. *PoS RADCOR2019* (2019), p. 022. DOI: 10.22323/1.375.0022. arXiv: 1912.01646 [hep-ph].
- [216] K. G. Chetyrkin, J. H. Kühn, and M. Steinhauser. “RunDec: A Mathematica package for running and decoupling of the strong coupling and quark masses”. *Comput. Phys. Commun.* 133 (2000), pp. 43–65. DOI: 10.1016/S0010-4655(00)00155-7. arXiv: hep-ph/0004189.
- [217] F. Herren and M. Steinhauser. “Version 3 of RunDec and CRunDec”. *Comput. Phys. Commun.* 224 (2018), pp. 333–345. DOI: 10.1016/j.cpc.2017.11.014. arXiv: 1703.03751 [hep-ph].
- [218] A. Bazavov et al. “ B - and D -meson leptonic decay constants from four-flavor lattice QCD”. *Phys. Rev. D* 98.7 (2018), p. 074512. DOI: 10.1103/PhysRevD.98.074512. arXiv: 1712.09262 [hep-lat].
- [219] ETM Collaboration, A. Bussone et al. “Mass of the b quark and B -meson decay constants from $N_f=2+1+1$ twisted-mass lattice QCD”. *Phys. Rev. D* 93.11 (2016), p. 114505. DOI: 10.1103/PhysRevD.93.114505. arXiv: 1603.04306 [hep-lat].
- [220] HPQCD Collaboration, R. J. Dowdall et al. “ B -Meson Decay Constants from Improved Lattice Nonrelativistic QCD with Physical u , d , s , and c Quarks”. *Phys. Rev. Lett.* 110.22 (2013), p. 222003. DOI: 10.1103/PhysRevLett.110.222003. arXiv: 1302.2644 [hep-lat].
- [221] C. Hughes, C. T. H. Davies, and C. J. Monahan. “New methods for B meson decay constants and form factors from lattice NRQCD”. *Phys. Rev. D* 97.5 (2018), p. 054509. DOI: 10.1103/PhysRevD.97.054509. arXiv: 1711.09981 [hep-lat].

Acknowledgements

It is a pleasure to thank Prof. Dr. Ulrich Nierste for the possibility to pursue a doctoral degree under his guidance and the collaboration on different flavour topics ever since the beginning of my master's thesis. I owe most of my knowledge of particle physics to him and I am grateful for the numerous discussions that went beyond my own horizon and helped me look at things from a broader perspective.

Prof. Dr. Matthias Steinhauser agreed to be the second reviewer of this thesis and provided valuable comments in the final stages, for which I am much obliged. However, his participation in this thesis far exceeds the typical role of a second reviewer in that he introduced me to the automated computation of (multi-)loop Feynman diagrams by means of the methods outlined in this thesis. I am indebted to him for his endless patience in helping me overcome countless, often self-imposed obstacles and for sharing his experience in these practical matters.

Several members of the institute have been burdened by me with proofreading chapters of the thesis, namely (in alphabetical order) Drs. Florian Herren, Syuhei Iguro, Fabian Lange, and Mustafa Tabet. Their thorough feedback improved this thesis by much, for which I am very grateful. Among them I would like to mention Dr. Syuhei Iguro in particular, who read almost my entire thesis and patiently answered any ignorant question I managed to come up with. Thank you for always knowing exactly where I can find what I need in the literature!

For collaboration on smaller or larger projects I would like to thank Dr. Syuhei Iguro, Dr. Fabian Lange, Pascal Reeck, and in particular Drs. Marvin Gerlach and Florian Herren for the fruitful collaboration on `tapir`!

Next, I would like to thank Dr. Fabian Lange for sharing an office with me for the better part of three years—although we spent a while in home office at the beginning—and for the many interesting discussions about physics or other things we had. For the discussions about all sorts of topics, from missing signs to general aspects of quantum field theory, I would further like to thank (in alphabetical order) Dr. Harun Acaroğlu, Dr. Daniel Baranowski, Dr. Joshua Davies, Manuel Egner, Dr. Marco Fedele, Dr. Marvin Gerlach, Dr. Florian Herren, Dr. Syuhei Iguro, Lucas Kunz, Dr. Matthias Linster, Pascal Reeck, Rebecca von Kuk, and many others.

Dr. Joshua Davies kindly answered many stupid questions about FORM, while Dr. Mustafa Tabet was my go-to Mathematica expert, both of whom I would like to say thank you for this.

I would like to thank my fellow IT admins with whom I shared this responsibility for a long time, Lisa Biermann, Manuel Egner, and Drs. Fabian Lange, Martin Gabelmann, Vitaly Magerya, and Mustafa Tabet for the time spent together in the cluster room and elsewhere. The newer members of the admin team, Sowmiya Balan and Dr. Marco Bonetti, will hopefully have as much fun as I did. Wishes for luck and patience go out to the whole admin team; both are vital lest the machines take control.

The atmosphere at the institute was made pleasant by all members of the TTP, many thanks! In particular, I am grateful to Martina Schorn for taking care of the administrative work. Thanks

also to Manuel Egner, Lucas Kunz, and Tim Kretz for taking care of snacks and drinks, and to my personal Club Mate retailer Pascal Reeck.

Finally, I would like to thank my family and Dr. Sophina Christ, for their continuous support, without which I would not have reached this point.